Modelling the radiation exposure of microorganisms living in naturally radioactive mineral springs

Sofia Kolovi

Université Clermont Auvergne
École Doctorale des Sciences Fondamentales

Thesis

submitted for the degree of

Doctor of Philosophy in Physics

Specialisation: Nuclear physics, Particles, Interactions and Universe

by **Sofia Kolovi**

Physicist, MSc

Laboratoire de Physique de Clermont, CNRS/IN2P3

29 June 2023

Modelling the radiation exposure of microorganisms living in naturally radioactive mineral springs

Thesis Directors

V. BRETON — CNRS, France
L. MAIGNE — UCA, France

Referees

N. ARBOR — IPHC, France
M. DAVIDKOVA — IPN, Czech Republic

Jury members

C. ADAM-GUILLERMIN — IRSN, France
S. INCERTI — LP2IB, France
T.J. MERTZIMEKIS — NKUA, Greece
P. VERNET — UCA, France

Il faut faire de la vie un rêve et faire d'un rêve une réalité.
Pierre Curie

Ἐν πᾶσι γὰρ τοῖς φυσικοῖς ἐνεστὶ τί θαυμαστόν.
Ἀριστοτέλης

Abstract

Radiation has been present on Earth since its origin. The role it may have played in the emergence and evolution of life is still unknown. The earliest traces of terrestrial life are found in the deposits of hydrothermal springs dated 3.7 billion years ago. Mineral springs are isolated ecosystems whose conditions have changed very little over the past centuries, thus offering an exceptional window on the history of life on Earth. In the most radioactive springs, ionizing radiation can be an "abiotic driver" impacting the diversity and structure of microbial communities. However, a major scientific question is to know the dose received by the microorganisms living in the mineral springs. Based on the analytical characterization of selected radioactive mineral springs in the Auvergne region of France, Monte Carlo simulations using GATE were conducted to evaluate the dose rates received by microorganisms from internal and external exposure due to the radioelements present in the mineral springs environment. Radiological analyses of multiple sediment and water samples coming from more than 20 mineral springs have shown that ^{226}Ra in the sediments and ^{222}Rn in the water were the dominant source of radiotoxicity in these ecosystems through their α-decay. DNA damages of microalgae (diatoms) were evaluated using the Geant4-DNA Monte Carlo toolkit. It is shown that in the most radioactive springs radiotoxicity could be an abiotic driver, as the rate of DNA Double Strand Breaks is comparable to diatoms' spontaneous mutation rate. These results should be refined once additional knowledge is acquired about the bioaccumulation of radioelements in the diatoms living in the springs. Additional knowledge is also required on the genome and physiology of diatoms. Finally, the comparison with ERICA, the reference tool for environmental radiation protection, showed that ERICA should be used with great caution when evaluating the radiation exposure of microorganisms in mineral springs. GATE should be seen as the complementary tool to ERICA to characterize, at the micrometric scale, the dose rates to microorganisms in natural ecosystems.

Résumé

La radiation est présente sur Terre depuis son origine. Le rôle qu'elle a pu jouer dans l'émergence et l'évolution de la vie est encore inconnu. Les premières traces de vie terrestre sont trouvées dans les dépôts de sources hydrothermales datant de 3.7 milliards d'années. Les sources minérales sont des écosystèmes isolés dont les conditions ont peu changé au fil des siècles, offrant ainsi une fenêtre exceptionnelle sur l'histoire de la vie sur Terre. Dans les sources les plus radioactives, la radiation ionisante peut être un "facteur abiotique" qui impacte la diversité et la structure des communautés microbiennes. Cependant, une question scientifique majeure est de connaître la dose reçue par les micro-organismes vivant dans les sources minérales. Sur la base de la caractérisation analytique de certaines sources minérales radioactives de la région Auvergne en France, des simulations de Monte Carlo utilisant GATE ont été réalisées pour évaluer les taux de dose reçus par les micro-organismes en raison de l'exposition interne et externe aux radioéléments présents dans l'environnement des sources minérales. Des analyses radiologiques de multiples échantillons de sédiments et d'eau provenant de plus de 20 sources minérales ont montré que le ^{226}Ra dans les sédiments et le ^{222}Rn dans l'eau étaient la source dominante de radiotoxicité dans ces écosystèmes par leur décroissance α. Les dommages à l'ADN des microalgues (diatomées) ont été évalués à l'aide de l'outil de Monte Carlo Geant4-DNA. Il est démontré que dans les sources les plus radioactives, la radiotoxicité pourrait être un facteur abiotique, car le taux de cassures double brin de l'ADN est comparable au taux de mutation spontanée des diatomées. Ces résultats devraient être affinés une fois des connaissances supplémentaires acquises sur la bioaccumulation des radioéléments dans les diatomées vivant dans les sources. Des connaissances supplémentaires sont également nécessaires sur le génome et la physiologie des diatomées. Enfin, la comparaison avec ERICA, l'outil de référence pour la protection de l'environnement contre les radiations, a montré qu'il convient d'utiliser ERICA avec beaucoup de prudence lors de l'évaluation de l'exposition aux radiations des micro-organismes dans les sources minérales. GATE devrait être considéré comme l'outil complémentaire à ERICA pour caractériser, à l'échelle micrométrique, les taux de dose des micro-organismes dans les écosystèmes naturels.

Acknowledgments

First and foremost, I have to thank my supervisors, Vincent Breton and Lydia Maigne, for offering me the opportunity to join this academic journey. I am grateful not only for their guidance, patience and encouragement, but also for giving me the sense of being part of their families. I also wish to deeply thank our laboratory director, Dominique Pallin, for his support and kindness, as well as, the whole LPC for the great hospitality. Moreover, I would like to acknowledge CNRS/IN2P3 for the financial support of this thesis, as well as the Mésocentre Clermont Auvergne University for the supercomputer facilities.

I would like to express my sincere thanks to my thesis committee for accepting to review my work, providing insightful feedback and raising fruitful discussions during my dissertation defense. I wish to thank all the collaborators of the TIRAMISU project for the exchanging and the great moments of field work. I also wish to extend my gratitude to Pierre-Jean Gauthier and Emmanuel Busato for the joyful and productive discussions. I am deeply indebted to Didier Miallier for his trust, kindness and sharing of expertise, as well as, to Ion Stamatelatos and Waclaw Gudowski for their support.

I would like to express my deepest appreciation to my friends and colleagues, Giovanna-Rosa Fois, along with her family, and Patrick Chardon, for sharing their expertise with me, helping, encouraging me and standing by me with a warm smile even during the hard moments. This endeavor would not have been possible without Theo J. Mertzimekis who supported my first research steps, trusted me and stood by me ever after.

I am thankful to Vincent, Ana, Nicoleta, Ziad, Nicole and Jean for the cheerful moments and interest, as well as to Xavier, for the inspiring coffee breaks and help. I would also like to acknowledge the great daily ambience at LPC, especially stemming from Eric, Marine, Geraldine and Cyril.

I would like to thank my office-mates Alexis, Lucas, Sarra and Eloise for the patience and the enjoyable cooperation. Many thanks to Moad and Lennart for the long-standing support, as well as to Gaetan, Nicolas and Ema for the friendly moments and the tolerance of my ups and downs during the redaction of my dissertation. My special thanks to Andreas for the moral support, advice and the unique greek friendship.

I wish to deeply thank Jonathan, Halime, Mike and Theo for the remarkable moments of eating, drinking and discovering Auvergne: we all together managed to go through and, eventually, enjoy this demanding period including CoVid pandemic. I would also like to thank my childhood friends, Gioula and Despoina for their patience, the long discussions and the joyous times, as well as little George and Μπουρμπούλ for the wonderful and carefree moments.

Finally, I would like to thank my whole family for supporting me by any means. I am wholeheartedly grateful to my brother for the emotional support, presence, endless encouragement and delightful jokes. Words cannot express my gratitude to my parents and grandparents. Thank you for embracing my decisions, trusting me and standing by me, helping me and offering me blissful moments.

Contents

List of Figures

List of Tables

List of Abbreviations

ADC Analogue to Digital Converter

ALARA As Low As Reasonably Achievable

bp base pair

CEA Commissariat à l'Energie Atomique

CNRS Centre National de la Recherche Scientifique

CR Concentration Ratio

DBSCAN Density Based Spatial Clustering of Applications with Noise

DCC Dose Conversion Coefficient

DL Detection Limit

DNA DeoxyriboNucleic Acid

DO Dissolved Oxygen

DR Dose Rate

DSB Double Strand Break

ED-XRF Energy Dispersive X-Ray Fluorescence

EDEN Elementary Dose Evaluation for Natural Environments

EPA Environmental Protection Agency

ERICA Environmental Risks from Ionising Contaminants: Assessment and management

FWHM Full Width at Half Maximum

GATE Geant4 Application for Tomographic Emission

Geant GEometry ANd Tracking

HPGe High Purity Germanium

HR-ICP-MS High Resolution Inductively Coupled Plasma Mass Spectroscopy

IAEA International Atomic Energy Agency

ICN Institut de Chimie de Nice

ICP-MS Inductively Coupled Plasma Mass Spectroscopy

ICP-QMS Inductively Coupled Plasma Quadrupole Mass Spectroscopy

ICPE Installations Classées pour la Protection de l'Environnement

ICRP International Commission on Radiological Protection

IRSN Institut de Radioprotection et de Sûreté Nucléaire

ISO International Organization for Standardization

LET Linear Energy Transfer

LM Light Microscopy

LMGE Laboratoire Microorganismes: Génome Environnement

LPC Laboratoire de Physique de Clermont

LTSER Long Term Socio-Ecological Research observatory

MARIS Marine Radioactivity Information System

MC Monte Carlo

MCA Multi-Channel Analyzer

MCCH Monte Carlo Condensed-History

MCDS Monte Carlo Damage Simulation

MCNP Monte Carlo N-Particle

MCTS Monte Carlo Track Structure

NaI Sodium Iodide

NIST National Institute of Standards and Technology

NORM Naturally Occurring Radioactive Materials

NS No Sample

PARTRAC PARticles TRACks

PDB Protein Data Bank

PhSp Phase Space

PITS Positive Ion Track Simulation

RAC Reference Activity Concentration

RAP Reference Animals and Plants

ROS Reactive Oxygen Species

SDR Screening Dose Rate

SEM Scanning Electron Microscope

SSB Single Strand Break

SUBATECH laboratoire de physique SUBatomique et TECHnologies associées

TENORM Technologically Enhanced Naturally Occurring Radioactive Materials

TIRAMISU biodiversiTy in the RAdioactive Mineral Springs in Auvergne

UAC Unit Activity Concentration

UV UltraViolet

WTD Wildlife Transfer Database

XRF X-ray Fluorescence

ZATU Zone-Atelier Territoires Uranifères

INTRODUCTION

For almost 4 billion years, the life on Earth has been developed under a radiation background. A growing pattern of evidence suggests that its current levels may affect the mutational load and, consequently, the genetic composition of plants and animals [1, 2]. The radiation response varies a lot among the different organisms while there is still an open question concerning the radioresistance and the levels of exposure to natural radioactivity [3].

Natural radioactivity has long been puzzling the scientific community on the role that it might have played in the emergence and evolution of life [4, 5]. A main contradiction stems from the fact that although mutagens are considered a drive for biological evolution, it has been documented that significant genetic degeneration is caused by radiation.

Starting with the cosmic rays [6, 7], studies highlight their potential involvement to the formation of life [8, 9] in environments protected, or not, by Earth-wise atmospheres and magnetospheres as well as their effect on the preservation of life in space [10].

The ionizing radiation emitted naturally in bedrocks has already been suggested as a drive of life since it is possible that it has provided the essential energy for chemical and biological reactions [11, 12]. Radioactivity also plays an important role in the evolution of the terrestrial microbial biodiversity. At the bottom of mines or beneath the ocean floor, drillings have revealed the presence of vast communities of microorganisms in the subsurface of our planet where water radiolysis, following the decay of radionuclides, leads to hydrogen (H_2) and oxidants production [13]. This radiolysis could yield enough energy to fuel a large portion of this deep subsurface biome [14].

While ionising radiations have been considered toxic at any level of exposure, experiments at low radiation backgrounds provide a window to explore the adaptive responses of biological systems to radiation. For instance, microbial life is stressed when it is deprived of background levels of radiation [15].

At the same time, studies focus on the correlation of radiation to mutations observed at the microbial life, while others focus on the observation of any chronic effects [16]. Yet, understanding the role of natural radioactivity in the evolution of microbial biodiversity is methodologically challenging. From the need of years-lasting, low level radiation exposure experiments of multiple cell generations, to the complexity of the experimental controls, we also have to encounter the implications due to the mobility of the organisms and other factors, like heavy metals, nitrates, phosphates and UV radiation from the sun, that make every natural ecosystem unique [2].

Radioecology studies the behaviour and the impact of the radionuclides on the environment and the living organisms. From the natural presence of radioactivity to the dispersion of manmade radionuclides in the atmosphere, the biosphere and the geosphere, radioecology studies the mechanisms of the radioisotope transfer, the assessment and evaluation of the potential effects on the flora, fauna and humans and offers a guidance for the radiation protection of the ecosystems. Characterised by multidisciplinarity, this field of research is based on the collaboration among major sciences such as physics, chemistry, biology, geology, and mathematics, to name a few [17, 18].

In this context, the assessment of the radioecological risk to the environment due to ionizing radiation has been traditionally addressed through its biota since it is the sensitive component of the ecosystems. Important initiatives, such as ERICA (Environmental Risks from Ionising Contaminants: Assessment and management) tool, provide a number of assessment components including modelling the transfer of radionuclides through the environment, estimating dose rates to biota from internal and external distributions of radionuclides, and establishing the significance of the dose rates received by organisms [19]. The relevance of ERICA integrated approach has been demonstrated to assess the environmental risks from ionising radiation to macroscopic organisms, but the difficulty of measuring in vivo the dose rates received by biota in the size of a few micrometers, as well as, the assessment of the potential radiation-induced damages at their DNA (nanoscale), makes the use of micro- and nano-dosimetry approaches essential [20, 21].

A common trend in experimental microdosimetry, as applied in a great variety of fields from aviation and space to nuclear installations and radiation therapy, is the validation of the microdetectors performance by Monte Carlo (MC) simulations [22–25]. As it has already been shown in the case of human cells, Monte Carlo simulations are needed for micro- and nano-dosimetric

assessements due to the stochastic nature of the energy depositions at the cell scale [26].

The current thesis is part of the radioecological project TIRAMISU (*biodiversiTy in the RAdioactive Mineral Springs in Auvergne*) which focuses on studying the radiological and radiotoxic effects of natural radioactivity on microorganisms living in mineral springs in the Auvergne region (France). The main goal was to use measured activity concentrations of the radionuclides detected in the mineral springs of Auvergne in order to predict the dose rates and the potential DNA damage received by the microalgae inhabiting these ecosystems using open-source Monte Carlo simulation tools. As it will be detailed later, a certain class of microalgae (diatoms) have drawn the scientific attention due to their peculiar characteristics and wide applications range.

The thesis is divided in five chapters. Chapter 1 introduces the main concepts of this work. Afterwards, three main parts are distinguished: the experimental measurements, addressed in Chapter 2, the simulations which are detailed in Chapters 3 and 4, and the synthesis of the results for the mineral springs in Auvergne presented in Chapter 5.

More specifically, the context, concepts and tools relevant to this multidisciplinary work are addressed in Chapter 1. TIRAMISU project, which inspired the current thesis, mineral springs and diatoms - the peculiar microalgae proliferating in the radioactive aquatic ecosystems of interest- are introduced. Natural radioactivity and the interactions of ionising radiation with the matter, as well as, some basic dosimetric concepts are discussed. In the end, the existing radioecological tools and their limitations are presented, to conclude with the Monte Carlo simulation tools that were used in this work: the GATE platform [27] and Geant4-DNA toolkit [28].

Chapter 2 is dedicated to the characterization of the ecosystems of the mineral springs in Auvergne. An overview of the 26 sampling locations and the methods used to collect water, sediments and diatoms by biologists, geologists, radiochemists and physicists is initially presented. The techniques used for the radiological characterization of water and sediments along with the available information on the diatoms communities in the region are detailed. An overview of the physicochemical properties of the mineral springs is also presented. Dose rates and DNA damage, calculated through simulations, will be scaled to the measured activities presented in this chapter.

Chapter 3 is dedicated to the evaluation of the dose rates received by

microorganisms living in naturally radioactive mineral springs. Two main parts are distinguished: the microdosimetric simulations using GATE and the dose rate evaluations using ERICA radioecological tool [29]. First, the simulation setup using GATE is detailed, a microdosimetric assessment is performed and the results for external and internal radiation exposure are presented. Then, the principles of ERICA tool are presented and a comparison between GATE and ERICA results is shown.

In Chapter 4, the nanoscale simulations performed at the microorganism's nucleus using Geant4-DNA are described. The DNA damage, in terms of Single and Double DNA Strand Breaks (SSB and DSB, respectively), for both internal and external radiation exposure are detailed. Finally, in Chapter 5, the dose rates and DNA damage results for the diatoms in each studied mineral spring in Auvergne are gathered. An overview of the thesis main results, limitations and perspectives is presented in the the last chapter (Conclusion).

Chapter 1

Context, concept and tools for the study of the radioecology of mineral springs

Introduction

In this first chapter, an overview of the essential context covering briefly the many disciplines engaged in this work is provided. It begins with the description of the project that inspired the current thesis in section 1.1, while mineral springs and diatoms are introduced in sections 1.2 and 1.3, respectively.

In section 1.4, natural radioactivity and its basic physics is stated. γ-spectrometry and the interactions of ionising radiation with the matter are presented in sections 1.5 and 1.6, respectively. The chapter continues with the introduction of the basic dosimetric concepts and finishes with an overview of some of the existing radioecological tools in section 1.8 in order to conclude, in section 1.9, with the Monte Carlo simulation tools used in this work.

1.1 The TIRAMISU project

The TIRAMISU (*biodiversiTy in the RAdioactive Mineral Springs in Auvergne*) collaboration gathers expertise from biologists, physicists, radiochemists, geologists, ecologists and sociologists to analyze the response of microorganisms living in naturally radioactive mineral springs. These isolated ecosystems offer a window to the evolution and adaptation of life to chronic radiative environments.

As it will be detailed later in this chapter, Auvergne in Massif Central, France (Fig. 1.1) is a region with a long history in thermo-mineral springs [31]. Zone-Atelier Territoires Uranifères (ZATU) is an observatory expanding over a geographical sector North-East of Clermont Ferrand engaging research groups from french universities, CNRS (Centre National de la Recherche Scientifique), IRSN (Institut de Radioprotection et de Sûreté Nucléaire) and CEA (Commissariat à l'Energie Atomique) [32–35]. Labelled

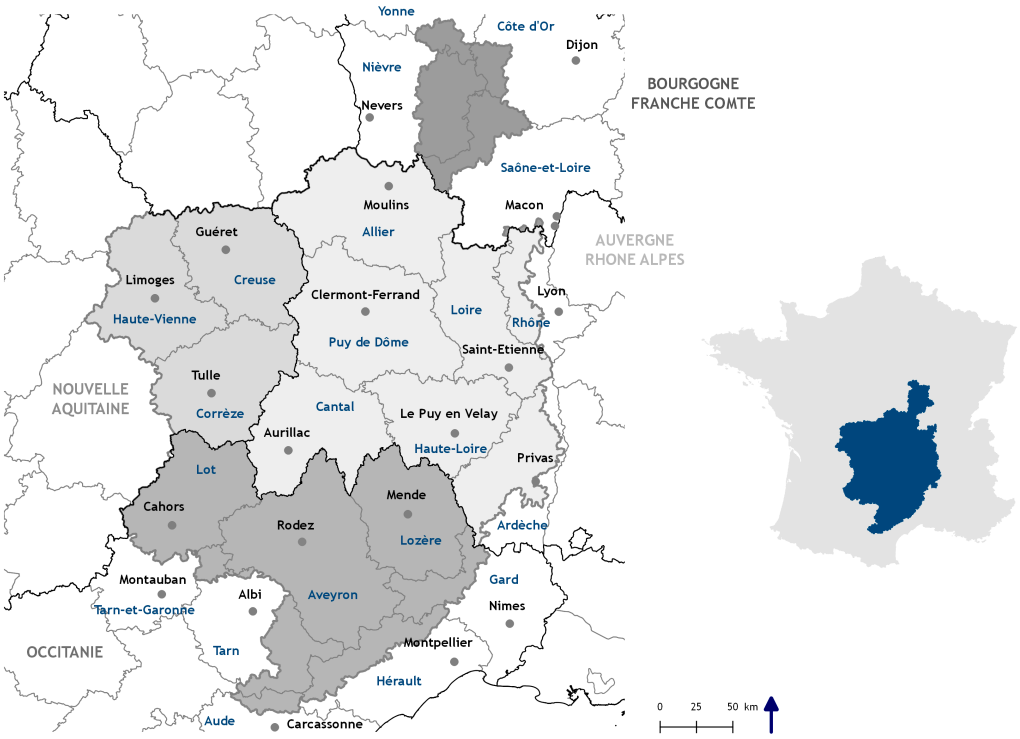

Figure 1.1 Massif Central in France [30]

"Long Term Socio-Ecological Research observatory" (LTSER), ZATU studies the interrelations among ecology, society and radioactivity including the chemical behaviour and interactions of minerals [36, 37] and trace metals (Cu, Pb, Zn) [38, 39] in different environments. The ecological impact of chemical contamination is also explored by the community [40], including the respective effects on biota [41, 42].

Focused studies concerning both Naturally Occurring Radioactive Materials (NORM) and Technologically Enhanced Naturally Occurring Radioactive Materials (TENORM), have revealed important aspects of the chemical behaviour of Uranium (U), Iodine (I) and Chlorine (Cl) radioisotopes [37, 43, 44]. Studies have also focused on the interactions of Uranium and Cesium (Cs) radioisotopes, as well as the interactions of low level background radiation, with the microbial life [16, 45, 46].

The biodiversity of ecosystems is of high interest among the research topics of ZATU LTSER. One of these ecosystems is the wetland area of a former uranium mine (Rophin) situated 55 km North-East of Clermont Ferrand. Rophin was exploited for eight years (1948–1954) and has been classified as ICPE (Installations Classées pour la Protection de l'Environnement) since then [47, 48]. It has been recently placed under monitoring for water level, conductivity and temperature, as well as ^{222}Rn activity in the air, in an effort

to collect data for chemical transport modelization.

With diatoms of Massif Central having received particular attention since 1893 (first study of Auvergne diatoms in 1893 by F.Heribaud) [49], intensive taxonomic studies have also been performed in the local mineral springs [50–53], where natural radionuclides are dissolved in various gradients of activity concentrations. Beginning with the radiological characterization of the mineral springs in Auvergne, the main objectives of the TIRAMISU collaboration are the biodiversity analysis of these ecosystems [51, 54, 55], the modelling of the radiation exposure of the microorganisms inhabiting them and the study of the interactions between the radioelements and the biome [56].

TIRAMISU includes studies of bacterial communities, viruses and diatoms. In a recent study, a negative correlation between ^{222}Rn water activity concentrations and virus abundances in the mineral springs of Auvergne was deduced [57]. Extensive studies on the physicochemical properties of the local springs were also performed, showing their important impact on diatoms taxonomic composition and bacterial communities [52, 55, 58].

New diatom species have also been identified in the recent years in the region (Font-de-Bleix [59], Bard [60] and Sail [61]. In the most radioactive local mineral spring (Montagne), diatoms were found to be highly deformed [62]. This microalgae has long been known as a water quality bioindicator due to its response to environmental stresses, but no link to radioactivity had ever been identified before to the best of our knowledge.

Among the TIRAMISU subdirections dealing with the interactions of the diatoms with radionuclides and their deformations, the current thesis is dedicated to the modelling of the radiation exposure of microorganisms living in naturally radioactive mineral springs.

1.2 Mineral springs

A spring can be identified as a geological formation at the land surface, where groundwater discharges from the aquifer [63, 64]. According to the temperature of the water in comparison to the mean annual temperature of the air of the particular region, we can distinguish cold and thermal springs, heated by geothermal energy. More characteristic to volcanic regions are also the geysers where the heated water is violently ejected accompanied by steam, and, in the case of fumaroles, by other gases like hydrogen sulfide (H_2S).

Mineral springs are small water bodies with waters rich in dissolved

minerals, like silicates, sulfides, carbonates, phosphates and sulfates to name a few. Transferring soluble substances throughout their emergence from great depths, naturally radioactive mineral springs can be described as isolated ecosystems of various physicochemical properties with elevated levels of radionuclide content in comparison to their surroundings, mainly from the three natural decay series (^{238}U, ^{232}Th, ^{235}U). An illustration of mineral springs is presented in Fig. 1.2.

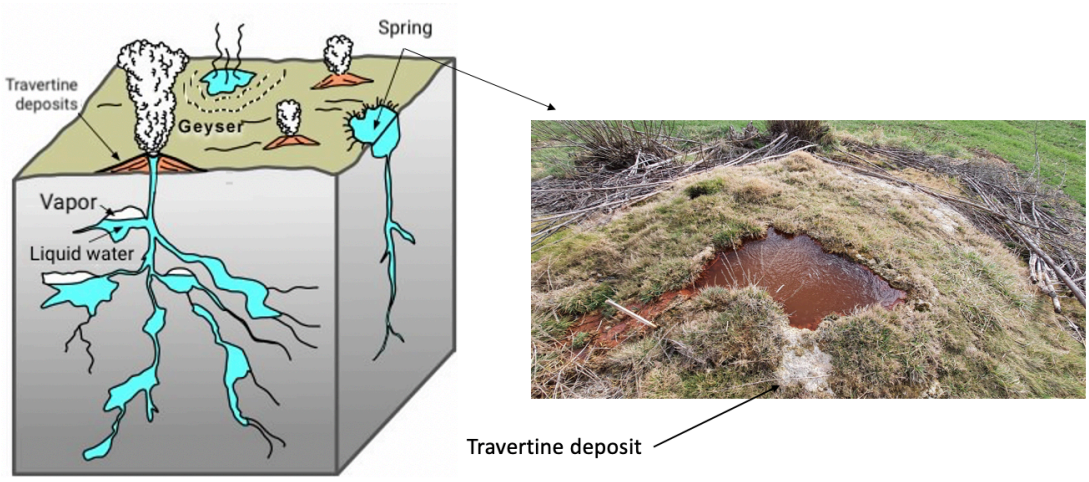

Figure 1.2 Left: Illustration of a mineral spring [65]. Right: Picture of a mineral spring in Auvergne (Daguillon).

Auvergne, situated in Massif Central of France, is a volcanic region rich of 109 mineral springs over the 626 in total registered in France [66, 67]. The geomorphology of the region allows for carbon dioxide (CO_2) emissions from the underground. In turn, this allows the groundwater to flow upwards to the surface through faults in the rocks, getting, simultaneously, enriched in chemical elements. Many of the mineral springs display elevated dissolved CO_2 concentrations, creating travertine deposits of calcium carbonate and iron oxides. Among them, we can find the hottest thermal spring in Europe with a temperature of 82°C [68] ("Par" spring at Chaudes-Aigues - Fig. 1.3).

Figure 1.3 Par: the mineral spring with the highest temperature in Europe (82 °C) situated in Auvergne

Consisting mainly of granitic bedrock, Massif Central is classified as a high natural radiation background area with absorbed dose rates in the air up reaching to 400 nGy/h while the global average due to terrestrial radionuclides is 60 nGy/h [69, 70]. The area has high Uranium content [71], which is correlated to the Radon and Radium activities measured in the local waters and sediments [72, 73]. In Fig. 1.4, the elevated Radon potential in Massif Central in comparison to the rest of France is highlighted.

Radon gas has been a long-standing issue for radioprotection as its inhalation is considered to be the major pathway for dose uptake [75]. In recent years, additional concerns exist for the dose due its presence in drinking water. ^{222}Rn activity concentrations in surface waters is usually $<$ 1 Bq/L, while in groundwaters values of 1000 Bq/L can be reached depending on the surrounding rock morphology, with the highest activity concentration being measured in uranium rich rocks [76]. European Union requires less than 100 Bq/L in drinking water with the ultimate limit of 1000 Bq/L [77].

Mineral springs in Auvergne are characterized by the great heterogeneity of physicochemical properties and their distinctive assemblages of diatom species. With significant gradients in pH, conductivity, bicarbonate (HCO_3^-), temperature and radioactivity, diatoms inhabiting these ecosystems exhibit their adaptability to extreme, and sometimes, hostile conditions. Recently, an

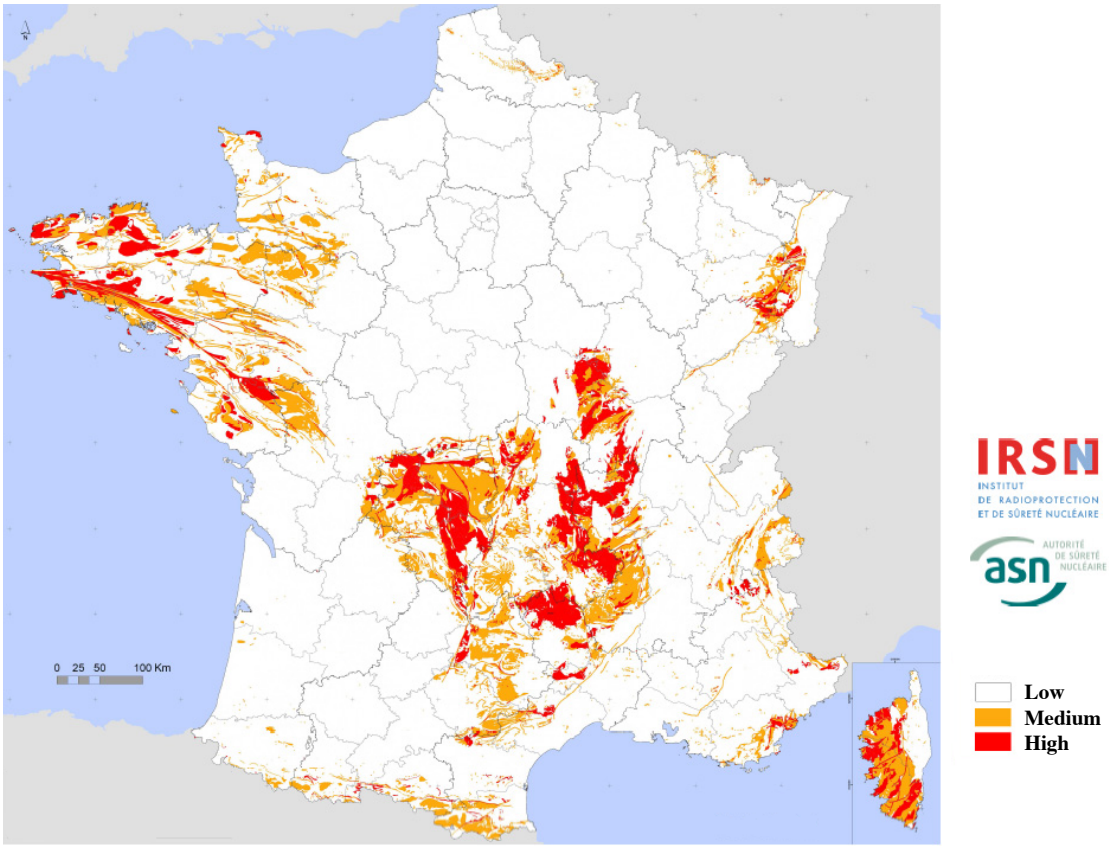

Figure 1.4 Radon potential in France [74]

inventory of 79 mineral springs along with 207 diatom species observed in Massif Central was published [78], including some springs of direct interest for the current thesis (Fig. 1.5 - No 1: Tennis, 7: Rocs bleus, 12: Sail, 13: Saladis, 15: Croizat, 17: Bard1, 18: Bard2, 23: Tete de Lion, 26: Giraudon, 52: Poix, 55: Graviers, 58: Daugillon (Fig. 1.2), 59: Ours, 69: Trois Sauts, 76: Salut). In Fig. 1.6, five of the aforementioned springs studied in the current thesis are shown (Giraudon, Graviers, Ours, Poix, Tennis).

Classified as moderately salty [79] and almost neutral (mean pH = 6.87 ± 0.47), the mean conductivity of these springs is (6073.85 ± 2112) µS/cm with a mean water temperature (16.82 ± 8.24)°C. These levels of mineralization are typical in Auvergne springs except for one outstanding location: Poix. Poix is a bituminous mineral spring with exceptional levels of conductivity, up to 123 200 µS/cm, hosting at least 31 diatom species in a neutral environment with temperatures varying between 10.6°C and 13.6°C [52].

As it will be presented in Chapter 2, 26 mineral springs were studied in the current thesis. Their main physicochemical parameters range is [4, 80]°C, [255, 123200] µS/cm with pH levels ranging between 6.16 and 7.82, hosting more than 60 diatom species [50–53, 55, 57, 60–62].

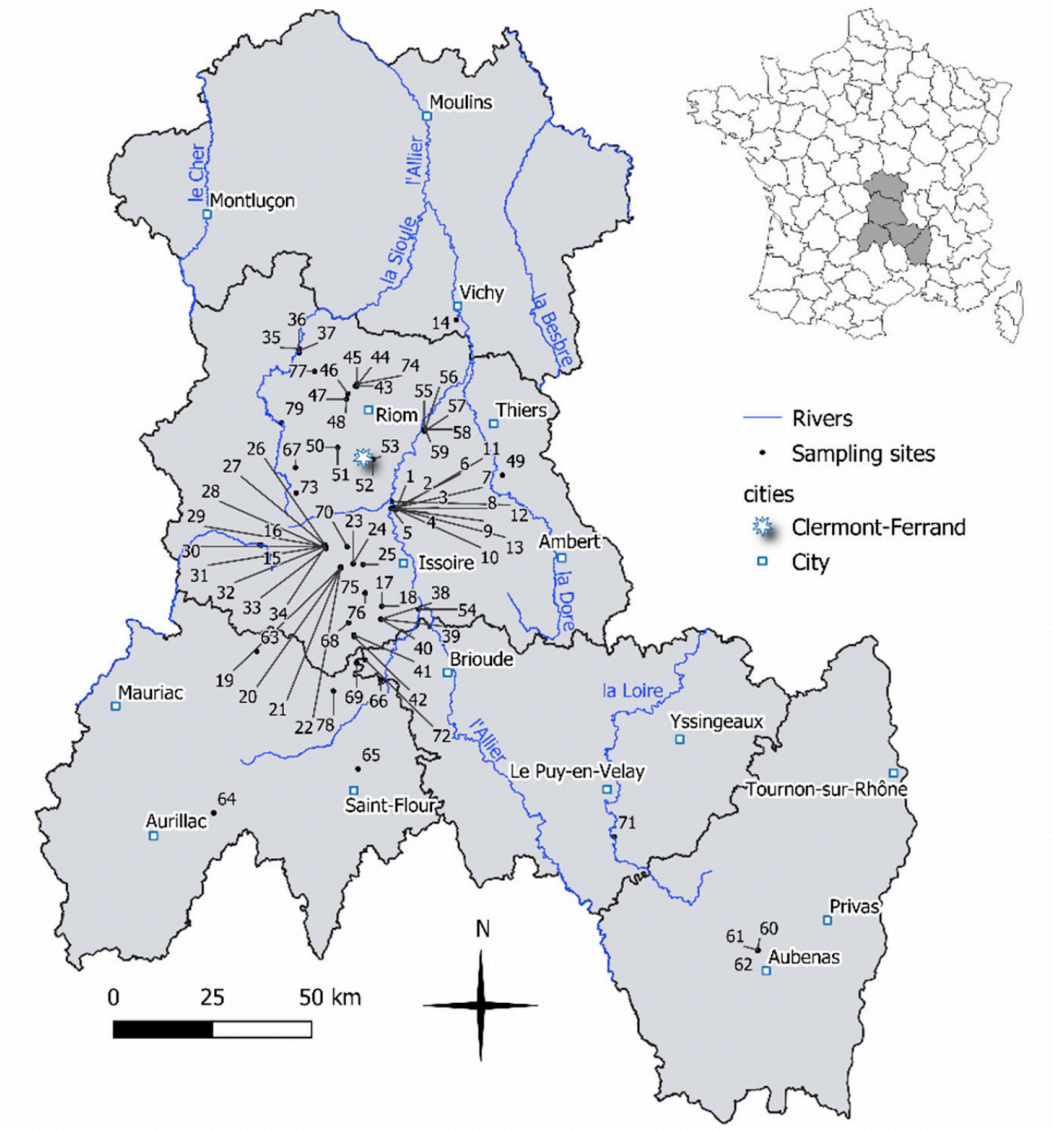

Figure 1.5 Location of 79 mineral springs in Massif Central [78]

1.3 Diatoms

Diatoms, otherwise called Bacillariophyta, are unicellular microalgae living in all aquatic habitats including mineral springs. What makes them unique to be encountered in the living matter is their frustule, a rigid siliceous cell wall that acts as an external skeleton. This peculiar class of microphytoplankton exhibits a great variety of shapes with sizes ranging from a few μm to 2 mm in some rare cases [80]. An example of the diatoms shape diversity is provided in Fig. 1.7 [81].

Figure 1.6 Five of the Auvergne mineral springs studied in the current thesis: Poix, Tennis, Giraudon, Ours, Graviers.

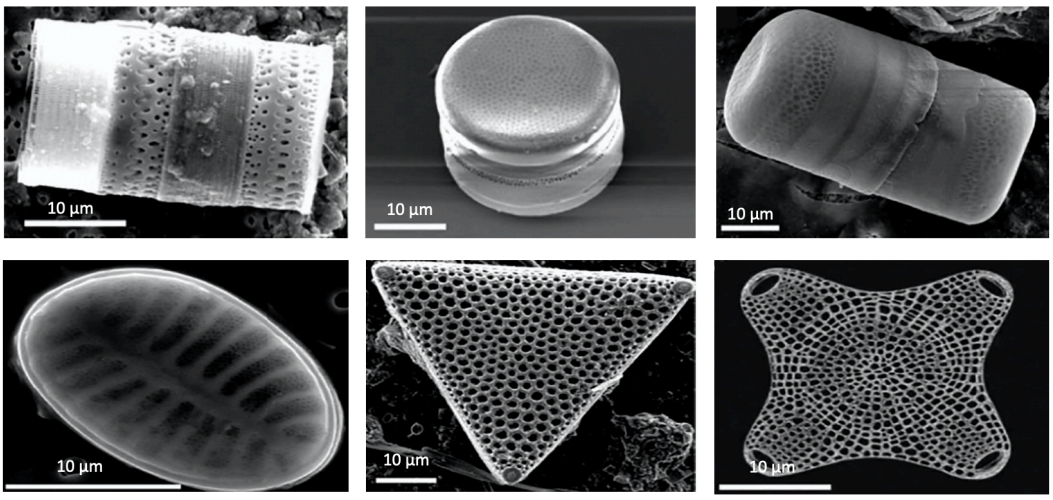

Figure 1.7 Diatom shape diversity: Scanning Electron Microscopy (SEM) images of diatoms frustules [81].

Diatoms can be benthic (live on the bottom of the water body) or live in suspension, representing up to 80% of the phytoplankton and accounting for a great part of the carbon dioxide fixation [82]. They can be found in all kinds of waters: soft and seawater of various gradients of temperature and extreme environmental conditions, as well as, in glaciers [83]. Diatoms play fundamental role in food webs and biochemical cycles such as carbon, silicon, nitrate and iron cycles [84]. Although they are not visible in bare eye, they can be easily detected when in big concentrations. An example is the case of the yellowish-brownish deposit which is formed when thousands of diatoms assembly together.

The first diatoms are believed to have appeared around 200 million years

ago in the oceans, long after the appearance of life on Earth more than 3.5 billion years ago [85, 86]. Considering that the only prokaryotes able to perform photosynthesis are the cyanobacteria, the evolution of photosynthetic eukaryotes is estimated around 1.2 billion years ago as a result of endosymbiotic events between cyanobacteria and prototypic eukaryotes [87]. Diatoms managed to survive the mass extinction event 65 million years ago, diversify and adapt not only in normal, but also extreme environmental conditions. In transitions like this, they are also believed to have invaded freshwaters.

Diatoms started being systematically studied only 200 years ago and despite the fact that new species are discovered every year all around the globe [61, 88–92] only 10 out of an average 200 000 species have their genome fully sequenced up to date, with none of them inhabiting mineral springs. The study of Bhattacharjya et al. [93], summarizing the latest results, reveals a range in DNA size between 27–162 Mbp preserved in nuclei of 1–2 μm diameter [94].

The frustule

Among diatoms' ubiquitous characteristics lays also the ability to metabolise silicon in order to create their rigid siliceous cell walls which allows them to remain well preserved in fossil deposits [95, 96]. Their fossil record permits the performance of studies long after their death providing insights not only on their evolutionary characteristics, but also on their deformations. These silicate (SiO_2) cell walls, resembling glass, are alike two halves valves (*thecae*) which are connected by a girdle to form together the frustule. Fitting into each other like a Petri dish, they are acting like an external skeleton. This characteristic was the foundation of their name originating from the Greek "diatomo" which means "two sectioned parts".

The frustule is rigid, but having pores allows the exchange of essential nutrients and the bioaccumulation of radionuclides [97–100]. It has been suggested, among many other physical and chemical roles, that it serves as a shielding to parasites and abiotic damage. When it comes to the asexual reproduction, diatoms proceed to cell division with the daughter cell keeping one of the parental valves. The other theca, which starts being constructed while in the parent cell, is inevitably slightly reduced in size, resulting in smaller silicified daughter cells. Moving through the generations, the daughter cells will keep decreasing in size until some of them die or reach the phase of the sexual reproduction. In the latter case, the pores of the rigid membrane

are responsible for the exchange of the gametes [101], and the new cells restore the initial size. With relatively small life cycles (ranging from 1 day to several weeks), diatoms can be proliferating for years through mitosis which can last from hours to days but meiosis, when occurring, lasts only a few hours [102].

The great variety of frustule shapes, sculpturing and colours permit their taxonomic analysis. Morphologically, two principal categories can be distinguished: the centric, demonstrating a radial cell wall symmetry, and the pennate which are elongated with a bilateral symmetry [103]. The basic structural components of a raphid pennate diatom are summarized in Fig. 1.8.

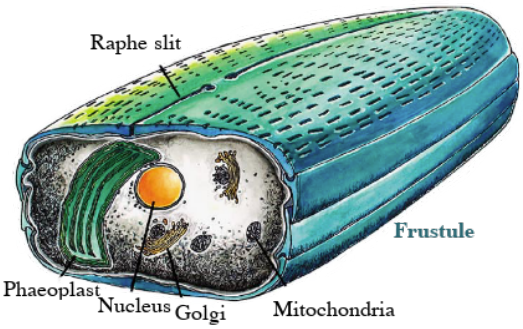

(a) Schematic representation of the basic structure in a raphid pennate diatom [104]

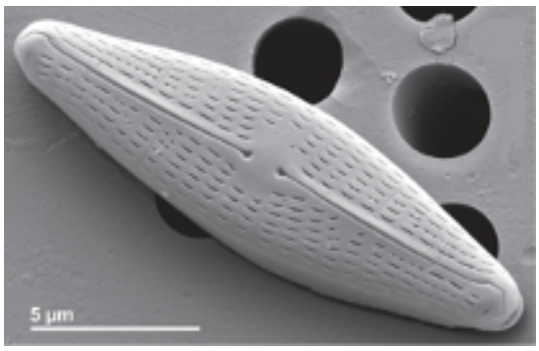

(b) SEM view of *Navicula veneta* [51]

Figure 1.8 Morphology of a diatom

The left part of Fig. 1.8 shows a schematic representation of the rigid frustule with the pores and the characteristic longitudinal fissure (raphe slit), enclosing the nucleus, the Golgi, the mitochondria, and the brown plastid called "phaeoplast". On the right, we can observe the pores and the raphe of the top theca of a pennate diatom as shown through SEM (Scanning Electron Microscope) analysis.

Diatoms' ability to produce biosilica structures (frustules), as well as, the unique mechanical strength and elastic deformable characteristics of the frustules, have placed their utilisation in nanomaterial science and nanotechnology in high rank [105–107]. Another interesting application (biomonitoring) linked to diatoms' frustules, is explored in the following paragraphs.

Biomonitoring and teratological forms

Biomonitoring refers to the use of organisms for tracking changes in the environment. Diatoms can serve as biomonitors due to their response to

environmental alterations, as well as, due to their capacity to accumulate radionuclides.

Beginning with their high bioaccumulation potential, diatoms have recently started being evaluated as radionuclides biomonitors. It is striking that although extensive literature exists over the use of green algae as radionuclide bioaccumulators, little is dedicated to diatoms which distinguish themselves from the rest of phytoplankton due to their frustule. For example, *Coccomyxa actinabiotis* is a green microalga living in the spent fuel cooling pool of a nuclear reactor showing that it can proliferate in hostile radiative environments [108].

Macaskie et al. [109] evaluated diatoms' potential to treat nuclear waste produced from the nuclear fuel cycle. In their study, the marine species *Thalassiosira pseudonana* was found to accumulate ^{241}Am, ^{237}Pu and ^{252}Cf more successfully in comparison to other marine planktonic species, a behaviour presumably attributed to their silicate frustule.

It is now known that diatoms are prone to radionuclides sorption directly from water because they are typically divided on a daily basis and have a large surface to volume ratio [110]. Although this indicates the accumulation of radionuclides on the frustule, it does not reflect the accumulation of the radionuclides inside the diatoms cell: Sansone et al. [111] state that suspended particle adhesion to diatoms is not directly proportional to the uptake rate of radionuclides in the cell and the resulted concentration ratios.

The other biomonitoring application of diatoms stems from their ability to detect and respond to alterations of the environment they inhabit. Their sensitivity to stressful environmental conditions, established diatoms as water quality bio-indicators [112, 113]. Documented stressors include temperature, drought and abnormal silica deposits [114], UV-radiation [115, 116], salinity [117], nutrient rich / depleted conditions [118], as well as, the presence of heavy metals in the habitat [119].

Environmental stresses are known to induce deformations on diatoms morphology. Specifically, the deformations on diatom frustules are defined by abnormal valves, striation patterns (sculpturing) and raphes [116, 120, 121]. The deformities of diatoms are also referred to as 'teratological forms'. An example of a deformed diatom (*Planothidium frequentissimum*) is presented in Fig. 1.9, where the teratological valve is observed via SEM. The deformed valve is characterized by an oversized aperture.

An exceptional abundance of such teratological forms has been recently

observed in the most radioactive springs in Auvergne [62]. *Planothidium frequentissimum* is, along with *Navicula sanctamargaritae* and *Crenotia thermalis* (Fig. 1.10), one of the three most typical species found in the local mineral springs [51, 55, 122]. The study performed by Milan et al. [62] showed that in Montagne spring, where ^{222}Rn activity concentration in water reaches up to 4600 Bq/L, the frustule deformation rates of *P. frequentissimum* were higher than 25%. In another study, various deformation rates (0.5–9 %) were recorded among 58 species identified in 17 local mineral springs with low ^{222}Rn activity concentration in water (10–177 Bq/L) [51].

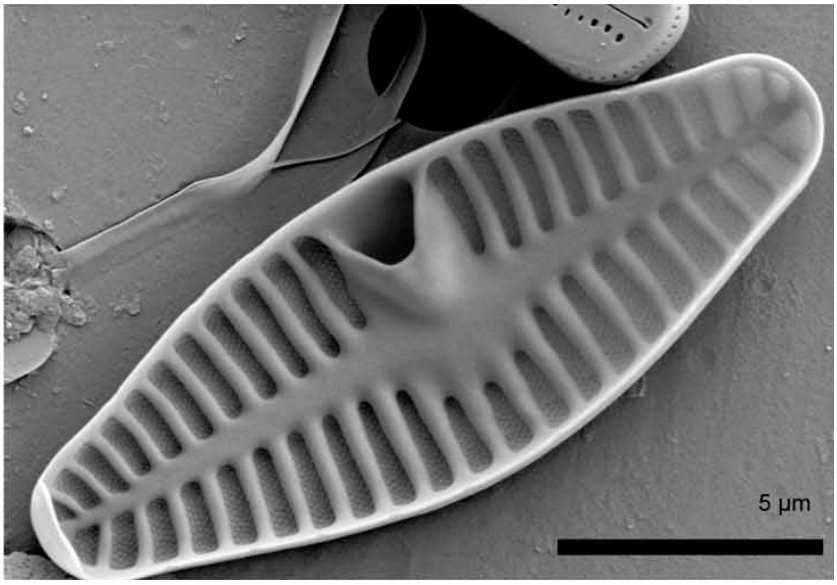

Figure 1.9 Deformed diatom. SEM observation of a teratological valve in *P. frequentissimum* [62]

In unstressed populations, teratological forms are scarce suggesting that even 1% of deformation rates is not negligible [123]. Since these deformities can be attributed to either chemical or physical stresses, radioactivity is considered as a potential stressor.

The studies on the effects of natural radioactivity on benthic diatom communities in the Auvergne mineral springs revealed that some species are particularly abundant in mineral springs with elevated levels of natural radioactivity, proving their tolerance to certain radionuclides. In particular, one of the genetic variants of *P. frequentissimum* seems to be a bio-indicator of ^{238}U in the mineral springs [53].

So far, no correlation has been established between low radioactivity levels and teratological formations [51]. Nevertheless, the high deformation rates observed in the highly radioactive mineral spring in Auvergne allows for radioactivity to be considered as a potential stressor. Such correlations

would require, among others, the genomics sequencing of 'normal' and 'deformed' diatoms. To our knowledge, genomics sequencing has not been performed on the diatoms of the mineral springs in Auvergne. Additionally, no study has been performed to experimentally locate DNA alterations in diatoms and correlate them to natural radiation exposure.

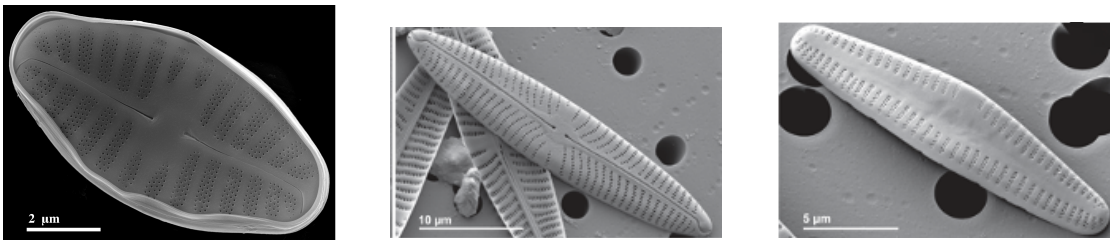

(a) *P. frequentissimum* **(b)** *N. sanctamargaritae* **(c)** *C. thermalis*

Figure 1.10 Three common diatom species in the mineral springs of Auvergne (SEM images)

1.4 Natural Radioactivity

The property of a radionuclide (or radioisotope) to spontaneously emit ionising radiation is called radioactivity. There are two types of radioactivity: natural radioactivity, originating from cosmic radiation, cosmogenic radionuclides and primordial radionuclides, and artificial radioactivity (also known as man-made). Cosmogenic radionuclides are continuously produced due to the interaction of the cosmic rays with stable elements, mainly in the atmosphere. Primordial radionuclides were formed at the primordial phases of the universe during Bing Bang nucleosynthesis and are characterised by half-lives comparable with the age of Earth [124].

Among the primordial radionuclides, we find ^{40}K and the natural decay series of ^{238}U (uranium chain), ^{235}U (actinium chain) and ^{232}Th (thorium chain) which account for a great part of the background radiation since all of them are found in the Earth crust (Fig. 1.11). Radon (Z=86), Radium (Z=88) and Polonium (Z=84) isotopes are produced in these natural decay chains which all end in stable forms of Lead (Z=82) (a periodic table of the chemical elements is provided in Appendix A).

Today, the least prominent among the decay series is that of ^{235}U due to its lower natural abundance (0.719%) in comparison to ^{238}U (99.274%). Although the behaviour of the radionuclides in the environment depends on their chemical properties, the on-site geology and their half-life, some useful widely known characteristics can be pointed out.

Uranium (Z=92) as a chemical element belongs to the actinide family, it

has four possible valences (+III to +VI) and while in the hexavalent form, Uranium is characterized by its highest solubility. Commonly found in high concentrations in granitic soils with a behaviour related to the local redox conditions [125], Uranium can also migrate to waters and deposit to sediments depending mostly on the pH, the redox potential and the salinity conditions [126].

In the ^{238}U decay chain, among the eight α-emitters, we find ^{226}Ra ($t_{1/2}$ = 1600 y) as the parent of ^{222}Rn ($t_{1/2}$= 3.8 d). Radium (Z=88) belongs to the alkaline group and it is generally characterized by moderate solubility so it tends to be accumulated in the terrestrial environment [127]. Its chemistry resembles that of barium (Ba) and it can be sorbed by clay minerals and organic matter.

Radon (Z=86) is a noble gas which can escape from soil to the atmosphere, exhibiting high solubility in water. Characterized as inert, it does not get involved in chemical reactions. Just before the disintegration to the stable ^{206}Pb, we find ^{210}Po which is characterized by low solubility and can be found in higher concentrations in sediments than in water [128].

Thorium (Z=90) concentrations in natural waters are generally low due to its low solubility but it is found in high concentration in the terrestrial environment and in particularly the ones with high mineral content. In the ^{232}Th decay chain we find ^{220}Rn and ^{228}Ra among the six α- and five β-emitters, respectively. Compared to the Radon isotopes in the ^{238}U decay chain (^{222}Rn), ^{220}Rn is less prone to escape in the atmosphere than ^{222}Rn due to its shorter half-life ($t_{1/2}$ = 55.6 s). On the other hand, ^{228}Ra of the ^{232}Th decay chain shows the same geochemical properties as ^{226}Ra of the ^{238}U decay chain [129].

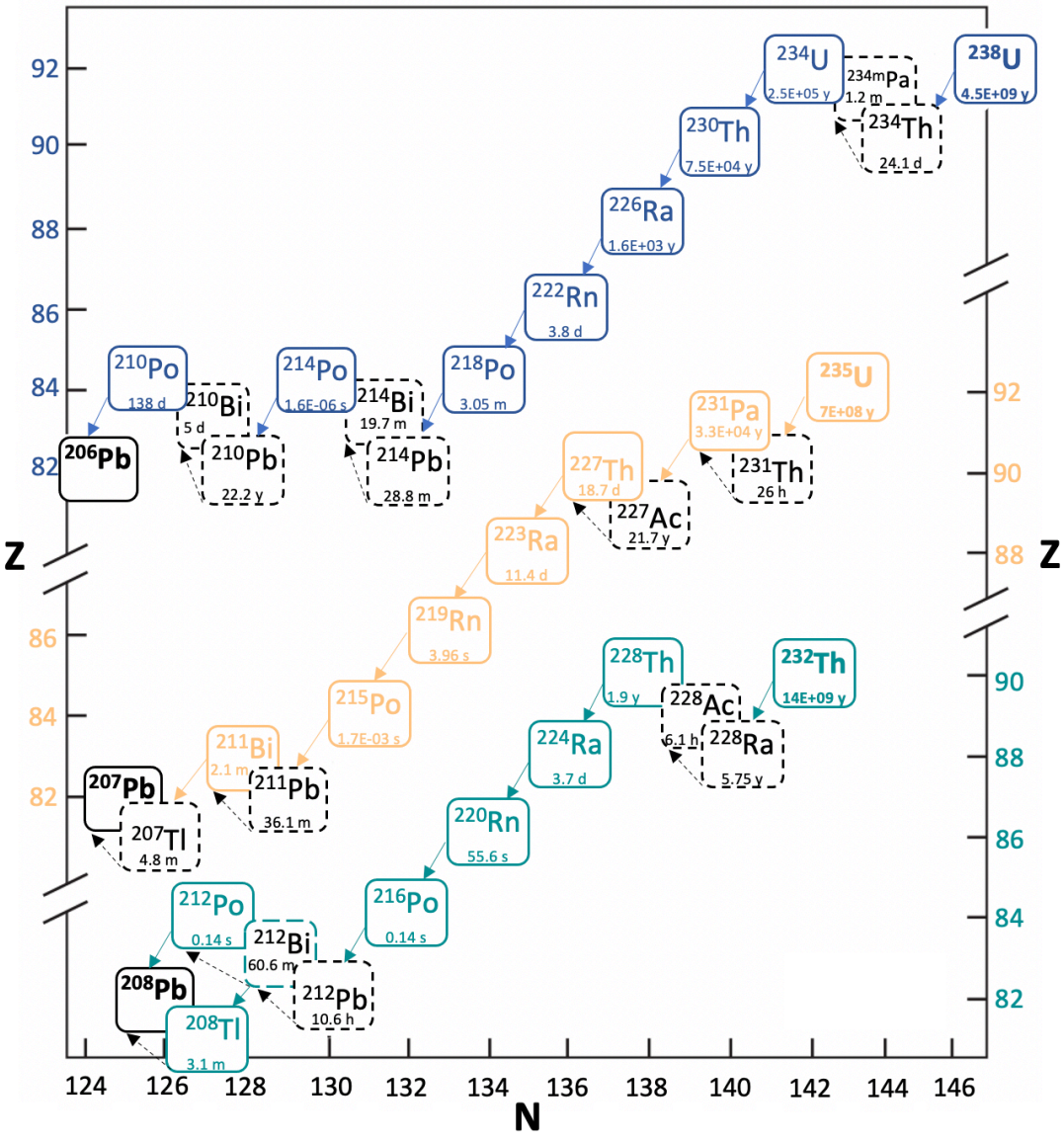

Figure 1.11 Natural decay series. Radioisotopes are provided with their half-lives. Blue: α-emitters of ^{238}U series. Orange: α-emitters of ^{235}U series. Green: α-emitters of ^{232}Th series. Dashed black: β-emitters. Black: stable nuclei (end of decay series).

General principles of radioactivity

Radioactivity is the physical process of the unstable nuclei (radionuclides / radioisotopes) to discard their excess of energy in order to reach stability via spontaneous disintegration. In the nuclear chart (Segre chart) shown in Fig. 1.12, the square pixels represent nuclei: their colour corresponds to the decay mode they undergo during their path to stability. The stable nuclei are coloured with black creating a "valley of stability".

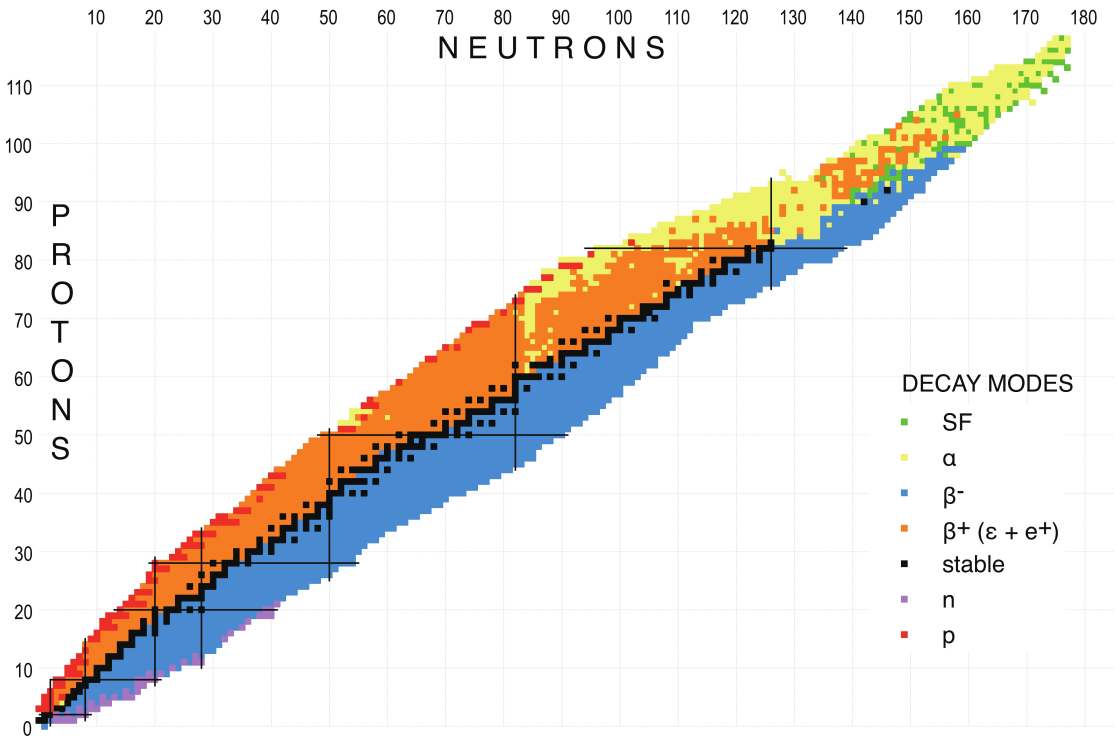

Figure 1.12 Nuclear chart. Black: stable nuclei. The other colours represent unstable nuclei and their decay modes. Green: spontaneous fission, Yellow: α-decay, Blue: β^--decay, Orange: β^+-decay (including electron capture), Magenta: neutron emission, Red: proton emission [130].

The decay processes characterized by the emission of Helium nuclei (α-decay, Eq. 1.1 - favored for isotopes with $A > 150$), the emission of electrons (e^-) or positrons (e^+) (β-decay, Eq. 1.2, 1.3), the electron capture (Eq. 1.4) and the emission of photons (γ-decay, Eq. 1.5) by excited nuclei [131–133] are highlighted. A schematic representation of an α-decay is given in Fig. 1.13 for ^{238}U.

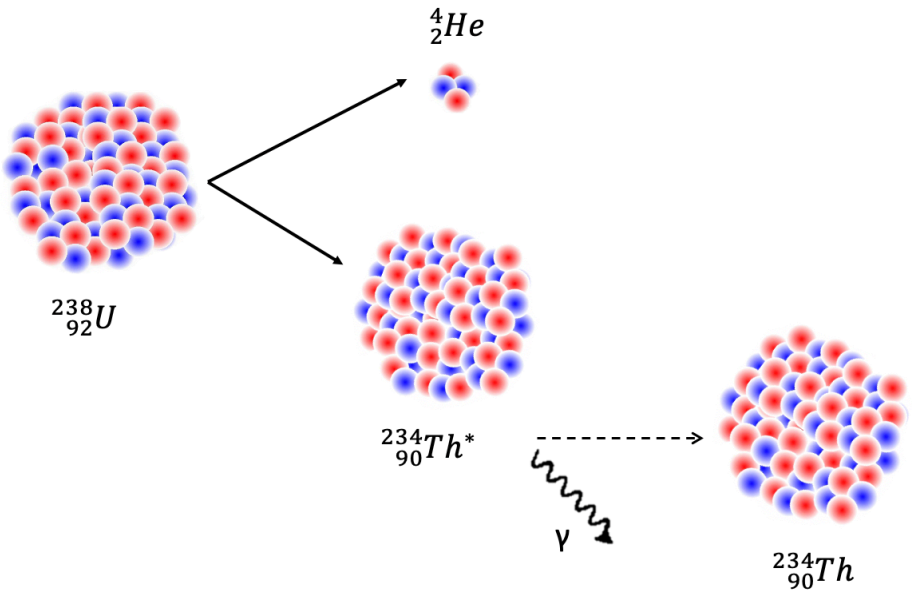

Figure 1.13 Schematic representation of α-decay for ^{238}U followed by the de-excitation of its daughter nucleus (^{234}Th). Red and blue spheres represent protons and neutrons.

$$ {}^{A}_{Z}\mathrm{X} \rightarrow {}^{A-4}_{Z-2}\mathrm{Y} + {}^{4}_{2}\mathrm{He} \tag{1.1} $$

$$ {}^{A}_{Z}\mathrm{X} \rightarrow {}_{Z+1}{}^{A}\mathrm{K} + e^{-} + \bar{\nu}_{e} \tag{1.2} $$

$$ {}^{A}_{Z}\mathrm{X} \rightarrow {}_{Z-1}{}^{A}\mathrm{L} + e^{+} + \nu_{e} \tag{1.3} $$

$$ {}^{A}_{Z}\mathrm{X} + e^{-} \rightarrow {}_{Z-1}{}^{A}\mathrm{L} + \nu_{e} \tag{1.4} $$

$$ {}^{A}_{Z}\mathrm{X}^{*} \rightarrow {}^{A}_{Z}\mathrm{X} + \gamma \tag{1.5} $$

with:

A: mass number (sum of protons and neutrons)

Z: atomic number (number of protons)

ν_e, $\bar{\nu}_e$: electron neutrino, anti-neutrino

${}^{A}_{Z}$X: parent nucleus (* denotes an excited state)

${}^{A-4}_{Z-2}$Y, ${}_{Z+1}{}^{A}$K, ${}_{Z-1}{}^{A}$L : daughter nuclei

γ: photon

The activity (A) (or else decay rate) of a radionuclide is described by the number of disintegrations per unit time (Eq. 1.6). The unit of activity is Becquerel (Bq), defined as one disintegration per second: 1 Bq = 1 s^{-1}. An alternative unit is Curie (Ci) (1 Ci = $3.7 \cdot 10^{10}$ Bq).

$$A = -\frac{dN}{dt} = \lambda N \tag{1.6}$$

with:

A (Bq): activity at a given moment t

λ (s^{-1}): decay constant

N: number of nuclei at a given moment t

The decay constant λ is defined in Eq. 1.7.

$$\lambda = \frac{ln2}{t_{1/2}} = \frac{1}{\tau} \tag{1.7}$$

with:

$t_{1/2}$ (s): half-life (the average time for the radioactive nuclei to halve in number)

τ (s): mean lifetime (the average time for the radioactive nuclei to decrease by 1/e)

The radioactive decay law describes the probability for an unstable nucleus to disintegrate in a given time interval (dt). If N_0 is the initial number of nuclei of the unstable isotope and $N(t)$ is the remaining number of nuclei at a given moment t, then the exponential law of the radioactive decay is given by Eq. 1.8 (as the result of the integration of Eq. 1.6). Proportionally, activity decreases exponentially (Eq. 1.9), too, as shown in Fig. 1.14.

$$N(t) = N_0 e^{-\lambda t} \tag{1.8}$$

$$A(t) = A_0 e^{-\lambda t} \tag{1.9}$$

with:

N(t): number of nuclei which have not disintegrated at a given moment t

N_0: number of nuclei at $t = t_0$

λ: decay constant

A(t): activity at a given moment t

A_0: activity at $t = t_0$

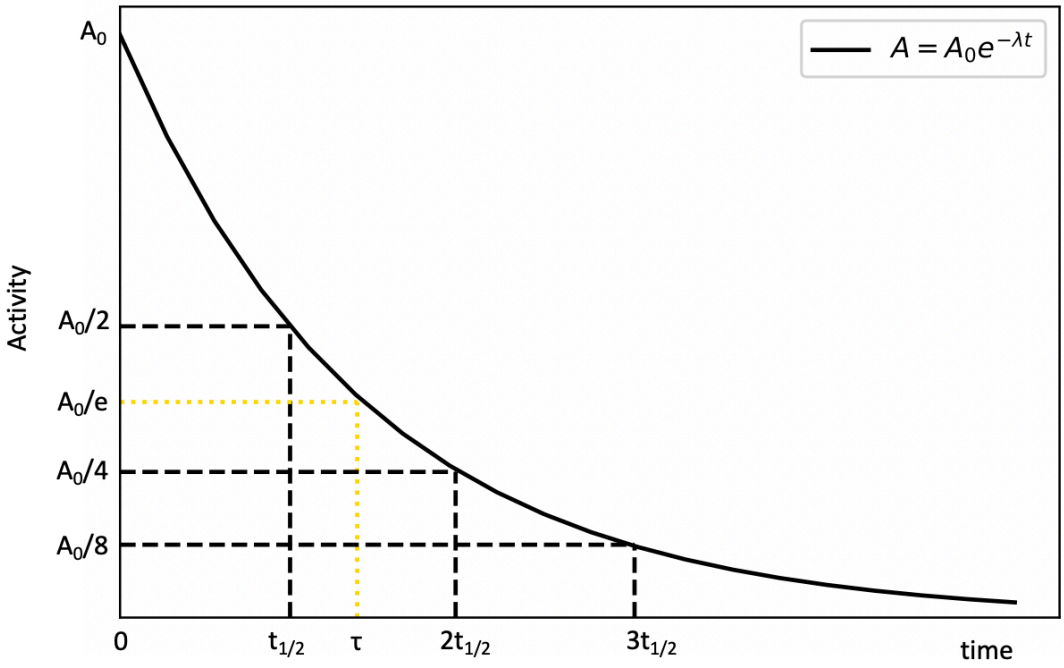

Figure 1.14 Radioactive decay law showing the exponential decrease of an initial activity A_0 as a function of time in terms of half-life ($t_{1/2}$). Yellow indicates the values at $t = \tau$ (mean lifetime).

The sequence of unstable isotopes following the decay of a parent nucleus until stability is called decay chain or decay series. The disintegration of the different isotopes in a decay chain could be schematically described as follows:

$$N_1 \xrightarrow{\lambda_1} N_2 \xrightarrow{\lambda_2} N_3 \xrightarrow{\lambda_3} .... \xrightarrow{\lambda_{k-1}} N_k \tag{1.10}$$

with:

N_k: stable nucleus (end of decay chain)

λ: decay constants

The isotopes of a decay chain are said to be in secular equilibrium when their activities are equal at a given moment (Eq. 1.11). Secular equilibrium can be achieved when an isotope with a very long half-life decays into daughters characterized by shorter half-lives. This is the case for the natural decay chains with the parents' half-lives being in the order of magnitude of 10^8 - 10^{10} years and the daughters half-lives ranging from a few seconds to 10^4 years.

$$\begin{aligned} A_1 = A_2 = A_3 = ... \\ \lambda_1 N_1 = \lambda_2 N_2 = \lambda_3 N_3 = ... \end{aligned} \tag{1.11}$$

Fig. 1.15 shows an example of a daughter nucleus growth (^{222}Rn, $t_{1/2}$ = 3.8 d) following the decay of its parent nucleus (^{226}Ra, $t_{1/2}$ = 1600 y) until they reach secular equilibrium. It is noticed that the secular equilibrium is achieved after approximately 30 days, corresponding to 8 half-lives of ^{222}Rn.

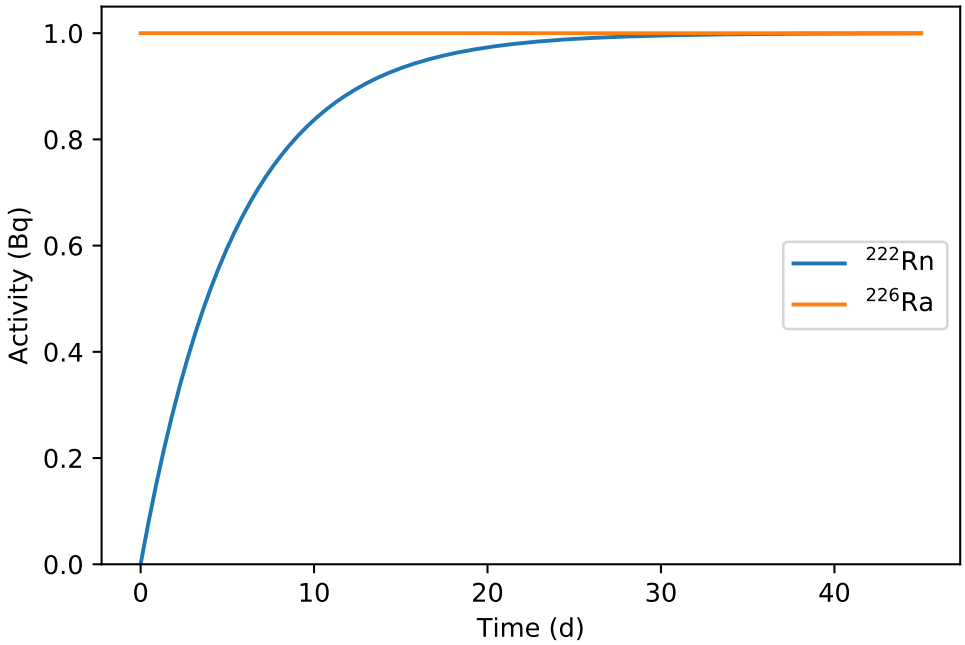

Figure 1.15 Growth of daughter nucleus (^{222}Rn) from long-lived parent (^{226}Ra) until secular equilibrium

The time evolution of the number of nuclei (and consequently the activities) in a decay chain is described by Bateman equations [134]. In the simplest case of a parent nucleus feeding a daughter nucleus, the radioactive decay of the parent nucleus is given by Eq. 1.12, while the time evolution of the daughter nucleus is described by Eq. 1.13 [135,136]. The daughter nucleus is formed at a rate $+\lambda_1 N_1$ (equal to the decay rate of the parent nucleus) and it decays at a rate $-\lambda_2 N_2$.

$$\frac{dN_1(t)}{dt} = -\lambda_1 N_1(t) \tag{1.12}$$

$$\frac{dN_2(t)}{dt} = -\lambda_2 N_2(t) + \lambda_1 N_1(t) \tag{1.13}$$

with:

$N_1(t)$: number of parent nuclei at a given moment t

λ_1: decay constant of parent nucleus

$N_2(t)$: number of daughter nuclei at a given moment t

λ_2: decay constant of daughter nucleus

Eventually, the time evolution of a daughter nucleus is given by Eq. 1.14.

$$N_2(t) = \frac{\lambda_1}{\lambda_2 - \lambda_1} N_1(0) \left(e^{-\lambda_1 t} - e^{-\lambda_2 t} \right) + N_2(0) e^{-\lambda_2 t} \tag{1.14}$$

with:

$N_1(0)$: number of parent nuclei at t = 0

$N_2(0)$: number of daughter nuclei at t = 0

In case that $\lambda_2 \gg \lambda_1$ (corresponding to a daughter nucleus with half-life much smaller than the parent nucleus), Eq. 1.14 simplifies to Eq. 1.15 which for t→∞ describes secular equilibrium.

$$N_2(t) = \frac{\lambda_1}{\lambda_2} N_1(0) e^{-\lambda_1 t} \tag{1.15}$$

1.5 γ-spectrometry

γ-spectrometry is a nuclear, analytical, non-destructive method that allows the detection, identification and quantification of γ-emitting isotopes [137–139]. The principle of any detection is the production of charged particles which are collected and detected through the production of an electrical signal. The γ-spectrometry experimental setup requires at least the detector and its shielding, the acquisition and analysis software, and the interposed electronics (high voltage supply, preamplifier, amplifier, multichannel analyzer) [140]. The main parts of the acquisition chain are summarized in Fig. 1.16.

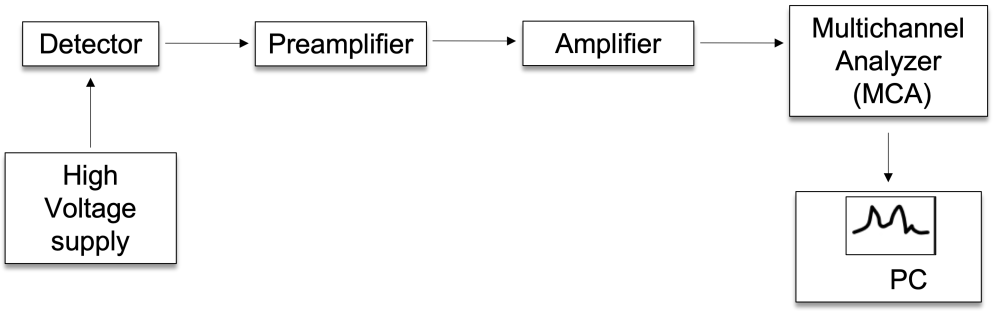

Figure 1.16 Main parts of γ-spectrometry acquisition chain

First, the γ-rays interact with the detector crystal resulting in the creation of electrons that form a signal pulse, which is intensified and shaped through the

preamplifier and the amplifier modules. After the conversion of the pulse from analogue to digital via the ADC (Analogue to Digital Converter), the pulse is sent to the MCA (Multi-Channel Analyzer). With each channel corresponding to a certain energy width (e.g. 0.25 keV/channel), MCAs provide pulse height spectra than can cover all the energy regions of interest. The pulse height spectra are in fact histograms containing the number of pulses registered per energy bin. After applying an energy calibration, we get the energy spectrum of the sample under investigation: the peaks of the histogram correspond now to certain energies to which we are able to attribute the corresponding radionuclides and calculate their activities (A).

The principle of calculating the activity of a radionuclide based on measurements with a detector characterized by an absolute efficiency ϵ_{abs} is described in Eq. 1.16.

$$A = \frac{N}{\epsilon_{abs}\,\Delta t} \tag{1.16}$$

with:

N: number of counts measured at a photopeak during a time interval Δt

ϵ_{abs}: absolute efficiency

Although each radionuclide has its characteristic γ-rays, many radioisotopes share similar γ-rays making, thus, spectrometry a field of expertise on its own. Nevertheless, not all the natural radiosotopes emit intense characteristic γ-rays. As a result, their identification and activity calculation is performed through their parent-nuclides under the hypothesis of secular equilibrium. This method is applied in the γ-spectrometric analyses presented in Chapter 2.

The most common types of detectors used are the scintillators (e.g. NaI - Sodium Iodide) and the solid-state ones (e.g. HPGe - High Purity Germanium). Their main performance differences are their efficiency and energy resolution. In the broad definition, the efficiency is the fraction between the photons detected and the photons emitted, while the energy resolution represents the ability of the detector to distinguish two neighbouring γ-peaks and it is determined via the Full Width at Half Maximum (FWHM) of a photopeak. HPGe detectors are well known for their superior energy resolution, providing sharp, well-defined photopeaks, in comparison to NaI detectors. A comparison between NaI and HPGe spectra depicting the different energy resolutions is shown in Fig. 1.17.

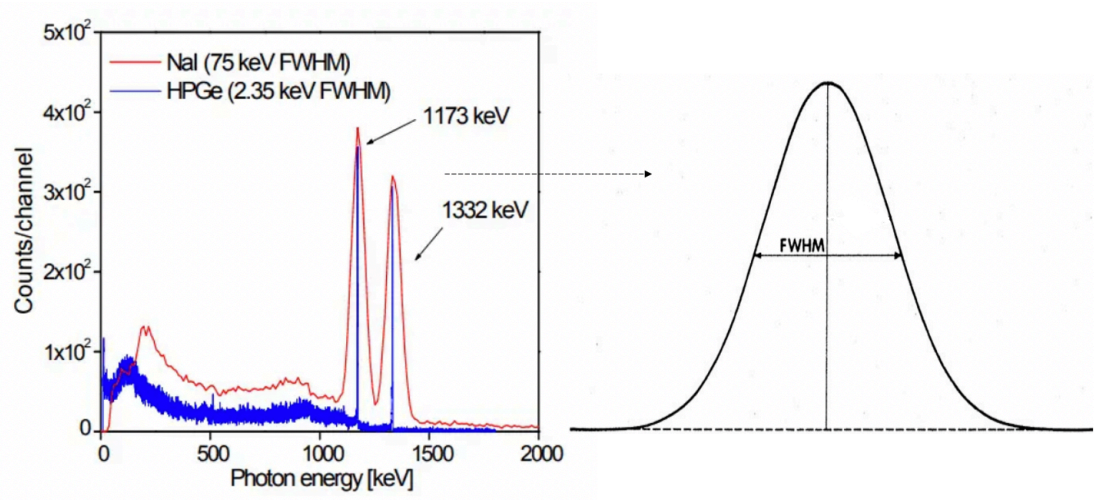

Figure 1.17 Left: Comparison of NaI (red) and HPGe (bleu) spectra for ^{60}Co [141]. Right: schematic representation of the FWHM of a photopeak.

Four different types of efficiency can be attributed to detectors:

1. The *absolute full energy peak (FEP) efficiency* (ϵ_{FEP} - Eq. 1.17) which depends on the geometrical arrangement between the source and the detector and is defined by the ratio between the recorded γ-rays at a photopeak area ($N_{\text{photopeak}}$) and the γ-rays emitted by the source (N_{source}).

$$\epsilon_{FEP} = \frac{N_{\text{photopeak}}}{N_{\text{source}}} \tag{1.17}$$

2. The *absolute total efficiency* (ϵ_{abs} - Eq. 1.18), representing the ratio between the number of counts detected anywhere in the spectrum (N_{spectrum}) and the number of the γ-rays emitted by the source (N_{source}).

$$\epsilon_{abs} = \frac{N_{\text{spectrum}}}{N_{\text{source}}} \tag{1.18}$$

3. The *intrinsic efficiency* (ϵ_{intr} - Eq. 1.19), which is characteristic of a detector and independent of the geometry between source - detector, and it represents the ratio between the number of the counts recorded ($N_{recorded}$) in the spectrum (either at a photopeak or total spectrum) and the number of γ-rays incident to the detector (N_{incident}: not all the γ-rays emitted by the source arrive to the detector).

$$\epsilon_{intr} = \frac{N_{\text{recorded}}}{N_{\text{incident}}} \tag{1.19}$$

4. The *relative efficiency* (ϵ_{rel} - Eq. 1.20) which represents the ratio of the

absolute full-energy peak (FEP) efficiency at 1.33 MeV (^{60}Co) between a standard NaI 3" x 3" detector and the detector of interest (HPGe in the current work) for a source-detector distance of 25 cm.

$$\epsilon_{rel} = \frac{\epsilon_{\mathrm{FEP_{NaI\ standard}}}}{\epsilon_{\mathrm{FEP_{detector}}}} \tag{1.20}$$

As mentioned before, the principle of detection relies on the production of charged particles that are collected and produce an electrical signal. Solid-state detectors, like HPGe, use a semiconductor as diode (Germanium crystal in this case). The principal characteristic of the semiconductors is the low energy required for the creation of electron-holes pairs, thus the lower energy, in comparison to scintillation detectors, to produce electrical signals, resulting in higher resolution spectroscopy.

The measurement of naturally radioactive samples is not expected to induce high counting rates. On the contrary, long counting times are often needed to achieve peaks well distinguished from the background. With the sources of the background radiation ranging from cosmic rays to natural radionuclides embedded in the construction materials of the building itself (such as ^{40}K), the background spectrum is the first to be determined and subtracted from the sample spectrum. In the case of γ-spectrometry, the shielding surrounding the detector serves two roles: primarily, the reduction of the background radiation and secondary, the radioprotection of the people involved in the measurements. Made by high atomic number materials characterized by high attenuation factors, like Pb, the shielding acts as a screening against γ-rays, X-rays and consequently α-particles and electrons (see also Fig. 1.18). Nevertheless, small contributions to the low energy region of the γ-spectrum are also expected from the interaction of the radiation with the shielding and the detector material (X-rays, Bremsstrahlung).

1.6 Interactions of ionising radiation with matter

Ionising radiation is considered to have sufficient energy to ionise matter either directly or indirectly. Charged particles, like betas (e^-, e^+), protons (p), alphas (α) and other ions, can cause direct ionisation. High energy electromagnetic radiation, like photons (γ, X), and neutral particles, such as neutrons (n), can cause indirect ionisation via the production of charged particles.

Due to the different mechanisms of interactions with the matter, each type of ionising radiation can penetrate materials at different depths. In Fig. 1.18, it

is highlighted that α-radiation (heavy charged particles) is easily stopped in a thin paper, while β-radiation (light charged particles) can penetrate paper but it is easily stopped by Aluminum (Al) foils. On the other hand, γ-radiation (photons) can be successfully attenuated by thick layers of Lead (Pb).

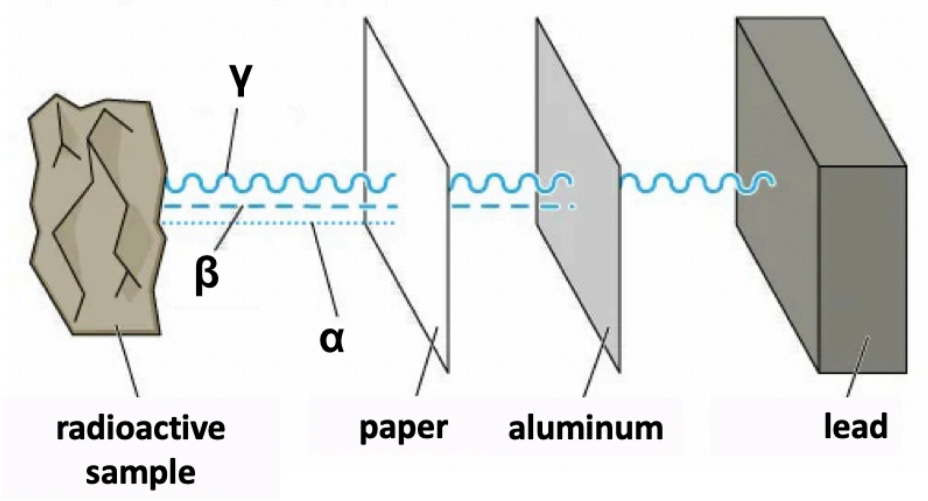

Figure 1.18 Penetration capacity of ionising radiation [142].

Below, the basic interactions of γ-rays with matter are introduced, giving an insight to the principles of γ-ray detection. The main interactions of charged particles with the matter are stated in the next subsection.

Interactions of γ-radiation with matter

As already mentioned, the detection of γ-rays is based on the transfer of the photons energy to the electrons of the detector material. Photons (γ-rays) are governed by the attenuation law when interacting with matter (Eq. 1.21) which describes the decrease of the initial γ-ray intensity (I_0) at a penetration depth x in a material of density ρ with an attenuation coefficient μ [137].

$$I(x) = I_0 e^{-\frac{\mu}{\rho}x} \tag{1.21}$$

with:

I(x): γ-ray intensity at a penetration depth x (cm)

I_0: initial γ-ray intensity (assuming entering the material at depth x = 0 cm)

μ/ρ (cm^2/g): mass attenuation coefficient of material

The main mechanisms of γ-rays interactions with matter, emitted by natural radioisotopes (with energies up to 3.2 MeV - ^{214}Bi), are the Compton scattering, the photoelectric effect and the pair production.

The photoelectric effect dominates in low (incident-photon) energies when the kinetic energy of the incident photon (E_γ) is sufficiently higher than the binding energy of an atomic electron (E_b). The total E_γ gets fully absorbed by the bound electron resulting in its ejection from the atomic shell with a kinetic energy E_{e^-} (Eq. 1.22). The discrete photopeaks observed in γ-ray spectra are the result of the detection of such electrons (often called "photoelectrons").

$$E_{e^-} = E_\gamma - E_b \tag{1.22}$$

with:

E_{e^-}: kinetic energy of ejected electron
E_γ: kinetic energy of incident photon
E_b: binding energy of atomic electron

The Compton effect, otherwise coherent scattering, takes place when a part of the incident photon kinetic energy is transferred to an atomic electron. As a result, the photon is scattered in angle θ with reduced kinetic energy $E_{\gamma'}$, while a recoil electron of an outer shell is ejected with kinetic energy E_{e^-} as described in Eq. 1.23. Thus, the detection of the recoil electrons results in a continuum "Compton area" and a backscatter peak in the γ-ray spectra.

$$E_{e^-} = E_\gamma - E_{\gamma'} = \left\{1 - \frac{1}{[1 + E_\gamma(1 - cos\theta)/m_{e^-}c^2}\right\} \tag{1.23}$$

with:

E_{e^-}: kinetic energy of recoiled electron
E_γ: kinetic energy of incident photon
$E_{\gamma'}$: kinetic energy of scattered photon
θ: scattering angle
m_{e^-}: 0.511 MeV/c^2

For photon incident kinetic energies greater than 1.022 MeV ($2m_ec^2$), the pair production is the dominant interaction mechanism. In this case, the photon interacts with the atom as a whole in a process where the γ-ray energy is transformed into an electron-positron (e^-, e^+) pair in the nucleus field. Their annihilation will produce photons of E_γ= 0.511 MeV, which will further interact with the detector, giving raise to single or double escape peaks in the energy spectrum.

An attenuation coefficient μ, correlated to the respective cross sections (probability of an interaction to take place) depending on the energy of the incident photon and the atomic number of the material, is attributed to each

of the mechanisms described above: $\mu_{Compton}$, $\mu_{Photoelectric}$, $\mu_{PairProduction}$. Thus, the mass attenuation factor (μ/ρ) in Eq. 1.21 is the sum of all the attenuation coefficients divided by the density of the material in the medium. Fig. 1.19 shows the mass attenuation coefficients (μ/ρ) of Germanium (Ge) for photons within the energy range [1 keV, 10 MeV] [143].

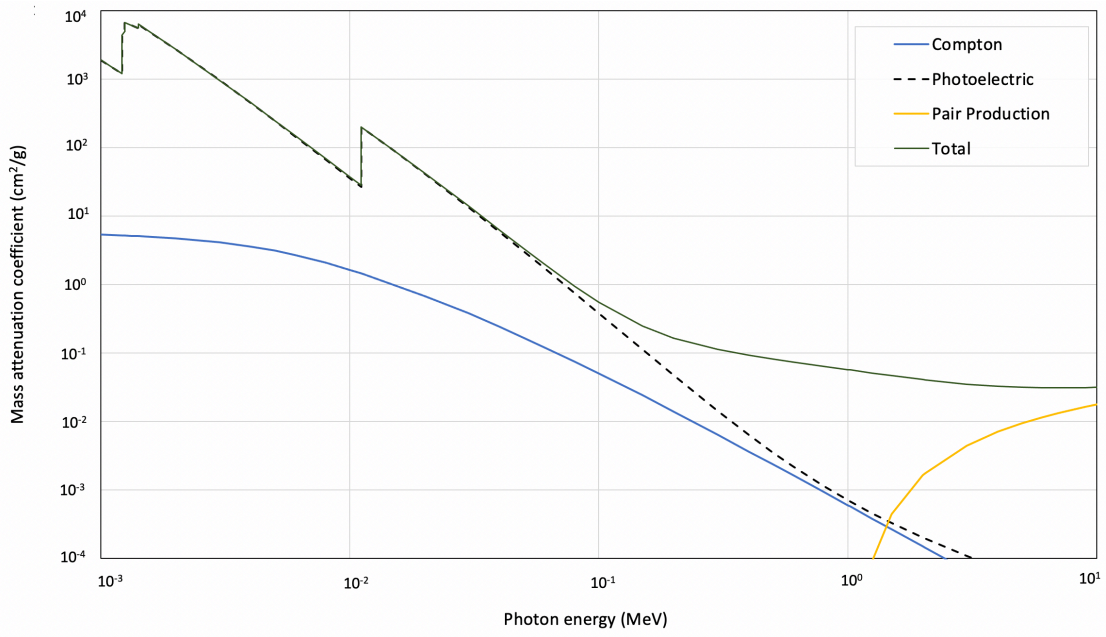

Figure 1.19 Germanium mass attenuation coefficients (μ/ρ) for energies 1 keV to 10 MeV.

Interactions of charged particles with matter

The main energy loss mechanisms of charged particles during their passage through the matter in the energy range of interest in the current study (α-particles up to 8.8 MeV - ^{212}Po and electrons up to 3.3 MeV - ^{214}Bi) are the inelastic collisions with atomic electrons, the elastic scattering from nuclei and the Bremmstrahlung, with the latter being more significant for electrons.

Although interactions with the nucleus are possible (leading to multiple scattering of the charged particle), most of the energy losses of charged particles are due to the collisions with the atomic electrons through Coulomb forces. A simplified explanation is that since atoms are much bigger than nuclei, the collisions of charged particles with atomic electrons are far more probable than the interactions with the nucleus.

An interaction of a charged particle with an orbital electron can either cause the ionisation or excitation of the atom depending on the binding energy of the electron: if the transferred energy is equal to the binding energy of the electron then the latter will escape the Coulomb forces of the nucleus leaving

the atom ionized. In that case, the electrons are called secondary and if they are sufficiently energetic to further cause ionisations they are, then, denoted as 'δ-rays'. Otherwise, the electron can be raised to a higher energy state while still remaining bound to the atom, leaving the latter in an excited state.

Due to these losses, the charged particle will be finally immobilised after many collisions. Since heavy charged particles lose energy in a large number of small steps, they move in almost straight lines. As a result, charged particles are characterized by well defined ranges in a material. For example, the range in water for a 5 MeV α-particle is 37.6 μm, for a 5 MeV proton is 362 μm and for a 5 MeV electron is 2.55 cm [144–146]. Nevertheless, electrons deviate from straight line paths. Especially secondary electrons and δ-rays can transfer energy away from the main path of a heavy charged particle inside the matter.

The rate of energy losses a charged particle encounters during its passage through a material, or else the Stopping Power, dE/dx is described by Bethe-Bloch formula (Eq. 1.24).

$$-\frac{dE}{dx} = \frac{4\pi e^4 z^2}{m_{e^-} u^2} NZ \left[ln\frac{2mu^2}{I} - ln(1-\beta^2) - \beta^2 \right] \tag{1.24}$$

with:

e: electron charge

z: charge of the (moving) charged particle

u: velocity of the (moving) charged particle

m: mass of the (moving) charged particle

N: number of atoms per unit surface in the material

Z: atomic number of the material

I: mean excitation potential of the material

β = u/c

c: speed of light

In the case of the current study, the charged particles have velocities much lower than the speed of light (u $\ll$ c), thus β terms can be ignored. Bethe-Bloch shows that the energy loss rate increases as the particle slows down.

Electrons, too, interact with the matter inducing ionisations and excitations, but since they are light charged particles, they can lose a great part of their kinetic energy during a collision. This explains their deviation from a straight line path in the matter, as mentioned earlier. While moving in the matter, electrons also interact with the Coulomb field of the atomic nuclei of the material. This attractive force results in the decrease of the kinetic energy of the electron leading in the emission of a photon. The

phenomenon is called Bremsstrahlung radiation and it can account for great energy losses at very high energies.

The energy transferred (dE) to a material per unit length (dℓ) of the track of a particle is expressed by LET (Linear Energy Transfer - Eq. 1.25) [147]). LET depends on the type of radiation, as well as, on the medium the radiation interacts with. While X and γ-rays are considered low LET radiations, charged particles are characterised as high-LET radiations.

$$LET = \frac{dE}{d\ell} \tag{1.25}$$

with:

LET (keV/μm): linear energy transfer

E (keV): energy

ℓ (μm): length

Especially α-particles are considered highly ionising particles due to the dense ionising tracks they create through their passage in the matter. For example, the LET in water for a 5 MeV α-particle is 88.6 keV/μm, while for a 5 MeV proton is 7.9 keV/μm and for a 5 MeV electron is 0.197 keV/μm. Table 1.1 summarizes the range and LET values for 5 MeV charged particles in water.

Table 1.1 Range (R) and LET in water for 5 MeV charged particles

Particle	$\mathbf{R}_{water}$ (μm)	$\mathbf{LET}_{water}$ (keV/μm)
α	37.6	88.6
p	362	7.9
e^-	25500	0.197

As a charged particle traverses matter and slows down, its LET varies and the rate of energy transfer to the medium increases. The maximum energy deposition takes place close to the end of the track leading to the characteristic Bragg peak. For example, Fig. 1.20 shows the Bragg peak of a 5 MeV α-particle in water which has range equal to 37.6 μm.

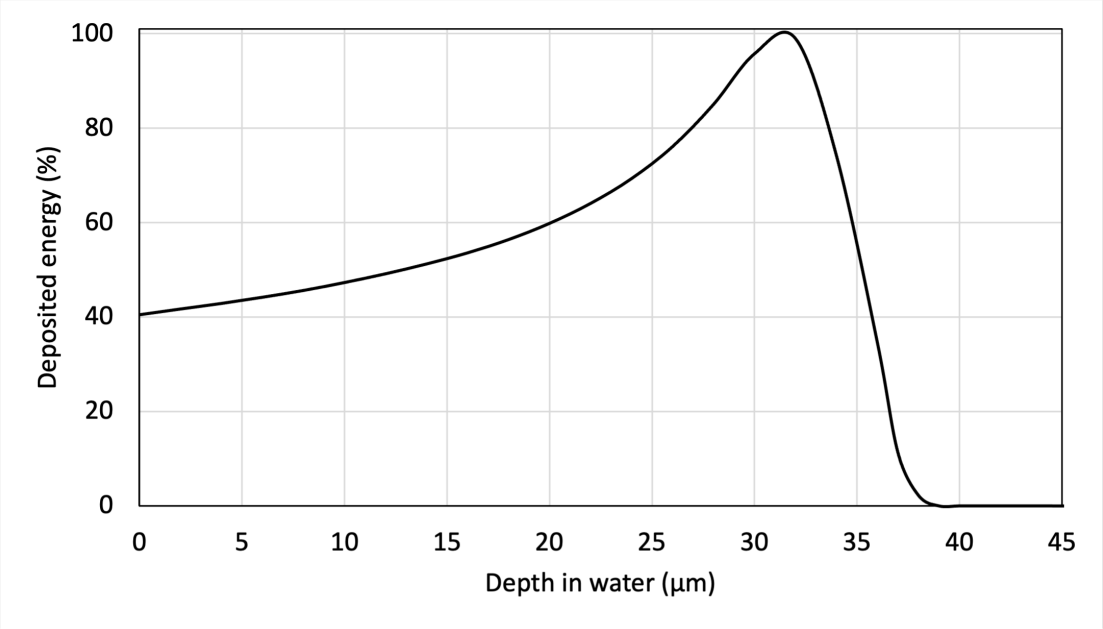

Figure 1.20 Bragg peak of a 5 MeV α-particle in water

The spatial distribution of energy deposition events of high-LET particles is comparable to the dimensions of DNA molecules and other biological molecules. High-LET particles are considered to cause DNA damage less easily repaired, among which, Double Strand Breaks (DSB) [148,149].

Dosimetry basics

A way to quantify the impact of the interaction of radiation with matter is the measurement of the energy absorbed by a target. When normalising this deposited energy with the mass of the target, we get the absorbed (physical) dose (D) received by the irradiated subject (Eq. 1.26). Absorbed (physical) doses are expressed in Gray (Gy). The physical dose can then serve as the basis for calculating equivalent doses (H_T in Sv, Eq. 1.27) and effective doses ($\mathcal{E}$ in Sv, Eq. 1.28) for radiological protection purposes, as briefly described below.

$$D = \frac{E_{dep}}{m} \tag{1.26}$$

where:

D (Gy): absorbed (physical) dose

E_{dep} (J): deposited energy

m (kg): mass

$$H_T = D \times w_R \tag{1.27}$$

where:

H_T (Sv): equivalent dose

D (Gy): absorbed dose

w_R: radiation weighting factor

$$\mathcal{E} = H_T \times w_T \tag{1.28}$$

where:

$\mathcal{E}$ (Sv): effective dose

H_T (Sv): equivalent dose

w_T: tissue weighting factor

The radiation weighting factor w_R varies between 1 and 20 depending on the radiation type and it is used to account for the different radiation types with different level of biological effectiveness [150]. Consequently, the equivalent dose allows the different types of ionising radiation to be considered equally with respect to their potential to cause harm. The tissue weighting factor w_T lays in the range [0.01-0.20] and depicts the different biological response of tissues and organs to ionising radiation [151, 152]. For the purposes of the environmental dosimetry in the current work, only the absorbed dose will be considered [153].

Due to the interest in calculating absorbed doses to microorganisms, the present study focuses on microscale. The stochastic nature of the energy depositions at that scale is handled via microdosimetric approaches which are crucial for the cell and DNA size dosimetry calculations. Microdosimetry eventually studies the probabilities of energy depositions.

At this scale, the energy deposited by a particle and its secondary electrons is called "imparted energy (ε)" which takes place in discrete transfer points, it is considered stochastic and it refers to small volumes of mass m_i. The ratio of imparted energy over the mass at a transfer point is described as "specific energy deposition" (z_i - Eq. 1.29). Fig. 1.21 shows the energy transfer points, the excitations and the positions where δ-rays stop for a 5 MeV α-particle track through water.

$$z_i = \frac{\varepsilon_i}{m_i} = \frac{\varepsilon}{dm} \tag{1.29}$$

where:

z_i (Gy): specific energy deposition

ε (J): imparted energy

m_i (kg): mass

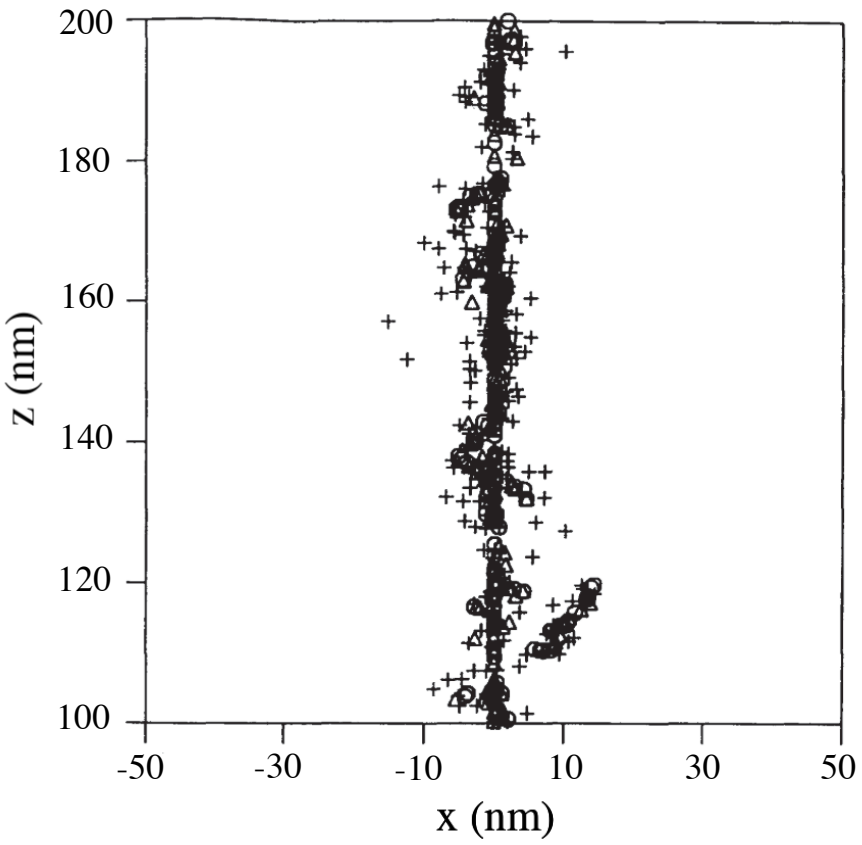

Figure 1.21 A 5 MeV α-particle track in water. Energy transfer points: 'o' ionisations, 'Δ': excitations, '+': positions where secondary electrons (δ-rays) stop [20]

The absorbed dose over the micro- or nano-mass can be denoted as the averaged result of the specific energy depositions in the simplified way shown in Eq. 1.30.

$$z = \sum^{i} z_i \tag{1.30}$$

where:

z (Gy): specific energy

z_i (Gy): specific energy depositions

Nevertheless, due to the stochastic nature of the energy depositions, the probability distribution function $\mathcal{F}(z;D)$ of z at an absorbed dose D and the respective probability density function $f(z;D)$ are described by Eq. 1.31 and

Eq. 1.32 respectively [20, 154].

$$\mathcal{F}(z; D) = P(z' \leq z \mid D) \tag{1.31}$$

$$f(z; D) = \frac{d\mathcal{F}(z; D)}{dz} \tag{1.32}$$

where:

z: specific energy

D: absorbed dose

From the above, it can be deduced that the average specific energy $\bar{z}$ is given by Eq. 1.33. The average specific energy can be equal to the absorbed dose for uniform irradiation of a uniform mass, otherwise $\bar{z}$ corresponds to the average absorbed dose. This interpretation takes us back to the description of the specific energy (z) given in Eq. 1.30.

$$\bar{z} = \int z f(z; D) dz \tag{1.33}$$

1.7 Radiobiology

The sensitive target of the living matter is the genetic material. The genetic material (DeoxyriboNucleic Acid - DNA) is structured in a double helix which is composed by two strands held together by hydrogen bonds. Each DNA strand is composed by alternating sugar and phosphate groups on which a nitrogen base is attached. The four nucleobases (or simply 'bases') involved, namely Adenine (A), Thymine (T), Guanine (G), Cytosine (C) pair up together across the two DNA strands in two unique combinations: A - T and G - C (Fig. 1.22). The sequence of the base pairs (bp) is the genetic code which can be bulky distinguished in two principal categories: the genes, which carry crucial information for the viability of the organism, and the sequence of base pairs for which no known function has been attributed yet (non-coding DNA).

The genetic material follows a well-structured complex organization. What is presented in Fig. 1.22 is the simplest level of organization. The mean distance between two sequent bases is around 0.34 nm, while the distance between the two strands is 2 nm. In the cell, DNA is complexed with histones, proteins that contribute to the formation of nucleosomes (around 147 bp in length). The fold-up of DNA extends to deeper levels of compression and complexity until the formation of chromatides which are the fundamental structures of chromosomes (approximate diameter of 1400 nm) [155]. This

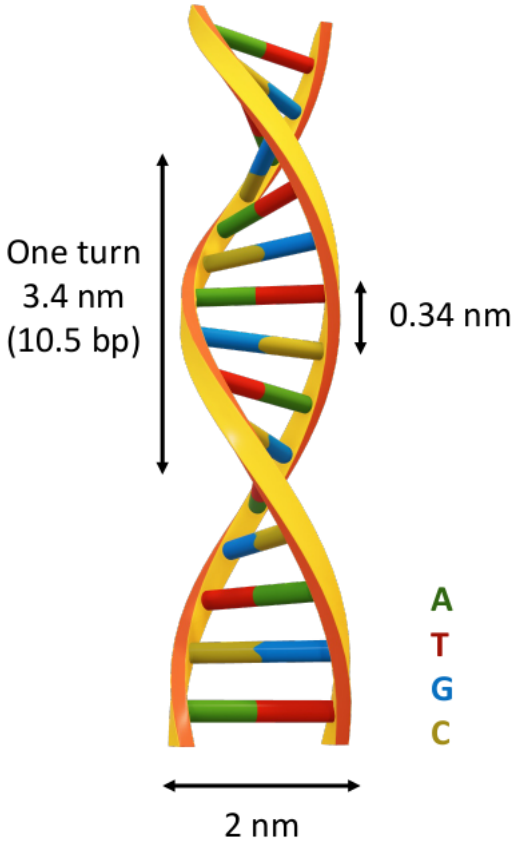

Figure 1.22 DNA double helix. Nucleobases are denoted by colours. Adenine (A): green, Thiamine (T): red, Guanine (G): blue, Cytosine (C): dark yellow.

fold-up is crucial for the conservation of the genetic information in the cell-size. The eukaryotic cells have to preserve enormous sizes of genetic material (nucleic, mitochondrial and/or chloroplast DNA) within a few micrometers. Among the eukaryotes, the genome size can range between 0.38 Mbp (marine protists [156]) to 3.2 Gbp (humans), exhibiting a great variation in comparison to prokaryotic genome sizes which range from 0.5 Mbp to 12 Mbp [157].

Interactions of ionising radiation with the biological matter can lead to DNA damage. Base damages, Single Strand Breaks (SSB) and Double Strand Breaks (DSB) constitute the main types of radiation DNA damage. Misrepair of these damages can lead, among others, to base pair alterations making the genes unable to get expressed. The changes in the DNA sequence are called mutations and in small scale they can be distinguished into point mutations (change of 1 base), substitutions (bases replaced by non-pairable bases), insertions (addition of extra base), deletions (definite removal of a base) and inversions (segments of chromosomes being reversed). Apart from induced, mutations can also be spontaneous and, although traditionally addressed as deleterious for organism, they actually contribute to genetic variation among

species and are considered as an evolution driving-force [158].

Among the biological effects that radiation exposure of an organism can cause are the cell death or even the organism death, associated with the DNA damage. The damage can be caused directly by energy depositions of the ionising radiation and indirectly by the interactions between the radicals produced due to water radiolysis and the DNA molecule [159].

There are three prompt stages of the interaction of ionising radiation with the biological matter which consists mainly of water: the physical, the physicochemical and the chemical stage of water radiolysis [160, 161] (Fig. 1.23). The physical stage takes place immediately after the irradiation and it lasts less than 10^{-15} s leading to the ionisation and excitation of the matter. The free electrons created are then able to interact further with the DNA molecule and the surrounding medium consisting mainly of water. The interaction of a free electron with the DNA can result in the direct breakage of the DNA strand(s). The electrons, the ionised and the excited water molecules proceed to reactions leading to the creation of radicals and solvated electrons during the physico-chemical stage in the timeframe between 10^{-15} and 10^{-12} s. During the chemical stage, which takes place from 10^{-12} to 10^{-6} s after the irradiation, the products of the physico-chemical stage can diffuse in the medium and get involved in chemical reactions, ending up interacting with the DNA molecules.

Among the products, of high importance for provoking DNA damage are the solvated electrons (e^-_{aq}) and the hydroxyl radicals (OH^-) which are one of the many Reactive Oxygen Species (ROS) able to break the chemical bonds of DNA [162,163].

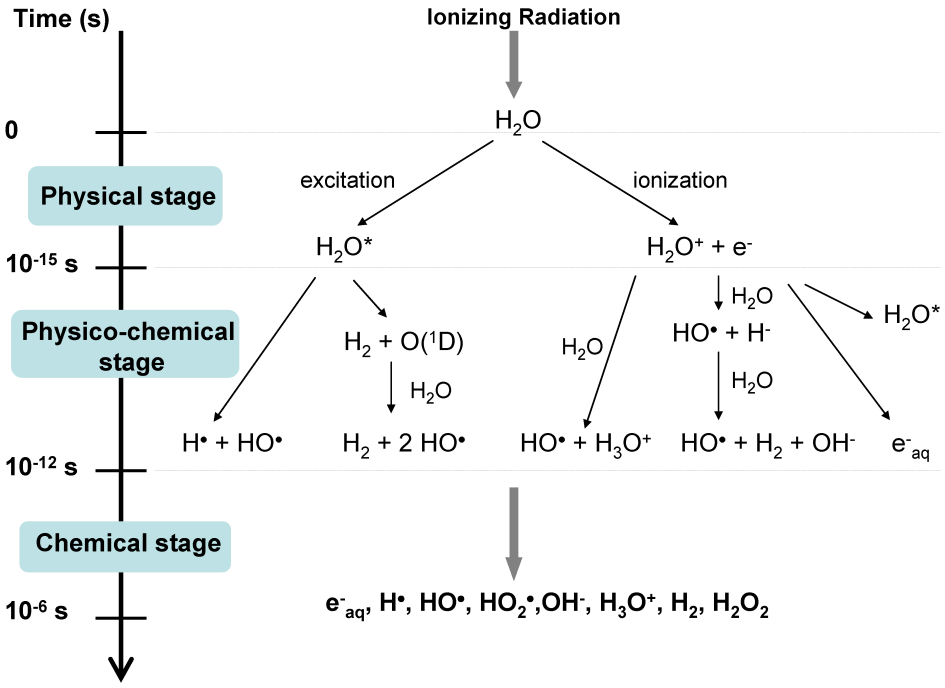

Figure 1.23 The three stages of water radiolysis [161].

1.8 Radioecological tools

The ultimate goal of the protection of the environment is the protection and conservation of non-human species and their biodiversity [164, 165]. When an ecosystem is subject to radiation exposure, the qualitative and quantitative evaluations of the imposed risks are addressed through the performance of risk assessments [166]. In a broad definition, risk is a statistical concept which describes the probability of undesirable effects arising from exposure to contaminants [151]. Radioecological risk assessments for the biota inhabiting environments exposed to ionising radiation provide, among others, estimations of the endpoint biological effects and serve as assisting tools in decision-making procedures [167].

The principal methodology applied in radioecological assessments follows the ICRP (International Commission on Radiological Protection) approach [168–170], which can be defined in a simplified manner as the transformation of radiation exposure to dose received by living matter via the application of Dose Conversion Coefficients (DCC). For a given environmental medium and an organism, the use of DCC for dose rates calculations following this approach can be described in an oversimplified way via Eq. 1.34 and 1.35: DR stands for the dose rate (external and internal, respectively), C_{medium} for the activity concentration of a radionuclide in the environmental medium, C_{org} for the activity concentration of the

radionuclide inside the organism and DCC for the dose conversion coefficient (external and internal, respectively).

$$DR_{ext} = C_{medium} \cdot DCC_{ext} \tag{1.34}$$

with:

DR_{ext}: external dose rate

C_{medium}: activity concentration of a radionuclide in the environmental medium

DCC_{ext}: external exposure dose conversion coefficient

$$DR_{int} = C_{org} \cdot DCC_{int} \tag{1.35}$$

with:

DR_{int}: internal dose rate

C_{org}: the activity concentration of the radionuclide inside the organism

DCC_{int}: internal exposure dose conversion coefficient

Initially, DCC was defined as "A value that enables the dose to an organism to be calculated on the assumption of a uniform distribution of a radionuclide within or external to the organism, assuming simplified dosimetry, in terms of μGy/day per Bq/kg" [171]. Currently, a more detailed definition has been established in ICRP 136, switching the units to μGy/h per Bq/kg for internal exposure cases [172].

The dosimetric approach for environmental protection is based on the use of reference organisms [171, 172] in an effort to cover the vast variety of biota in both aquatic and terrestrial ecosystems. Reference Animals and Plants (RAP) are defined as "Hypothetical entities, with the assumed basic biological characteristics of a particular type of animal or plant, as described to the generality of the taxonomic level of family, with defined anatomical, physiological, and life-history properties, that can be used for the purposes of relating exposure to dose, and dose to effects, for that type of living organism" in ICPR 108 [171]. RAP are modelled as spherical or ellipsoidal volumes for simplification reasons.

This methodology is built upon radionuclide-specific, environment-specific and organism-specific factors. Thus, in the lack of any of these factors, generalizations are implemented. Part of the raised concern due to this generalisation is expected to be addressed by the coordinated research project "Improving External Dosimetry for Terrestrial Animals and Plants" initiated by IAEA (International Atomic Energy Agency) in

December 2022 [173].

ERICA (Environmental Risks from Ionising Contaminants: Assessment and management) open-source tool provides a number of assessment components including modelling the transfer of radionuclides through the environment, estimating dose rates to biota from internal and external distributions of radionuclides, and establishing the significance of the dose rates received by organisms [19,174]. The approach uses simplified organism shapes without considering internal structures (following the RAP approach). No metabolic or biokinetic behaviours of incorporated radionuclides are taken into consideration for the internal exposure calculations.

Developed within the framework of FASSET [175] and EPIC [176] european projects, ERICA offers the opportunity of exploring the outcome of various exposure scenarios ranging from routine to accidental discharges of radioelements to the environment. It is addressed, among others, to stakeholders who need a broad overview of the contamination scenario under study and need assistance for policy decisions.

The tool employs databases of radiological factors and radiation effects for a great variety of radionuclides and model organisms for freshwater, marine and terrestrial environments which are essential for dose rate calculations. The suggested model organisms range from mammals and fish to insects and plants, with the smallest available one being the phytoplankton with mass = $1 \cdot 10^{-6}$ kg. Apart from nuclear industry and medical related radioisotopes, like ^{137}Cs, ^{131}I, ^{239}Pu, ERICA databases include almost all the isotopes of the natural decay chains apart from noble gazes like ^{222}Rn.

In a study performed using ERICA for the evaluation of the radiation doses to aquatic organisms from natural radionuclides [177], the absence of data on the natural decay chains radionuclides in freshwater bodies was highlighted, as well as a deficiency of information on certain model organisms. In cases like this, ERICA suggests the use of the alternative available data. As a result, the provided estimations are qualitative and do not reflect the realistic scenario under study.

Complementary to ERICA, excel-based tools were developed for the evaluation of ^{222}Rn exposure of terrestrial organisms (Rn dose calculator) [178–180], as well as, for the evaluation of the exposure to radionuclides of other noble gases, such as argon (Ar), krypton (Kr) and xenon (Xe), which are produced during nuclear power plants operation (Ar-Xe-Kr calculator) [181]. R&D128 is another excel-based tool targeting

the exposure assessment of non-human biota in coastal, terrestrial and freshwater ecosystems, but with a limited number of reference organisms and radionuclides [182].

A similar to ERICA approach has also been adopted by EDEN software (Elementary Dose Evaluation for Natural Environments) [153,183]. The tool, developed in IRSN (Institut de Radioprotection et de Sûreté Nucléaire, France) for modelling the radiological doses to non-human organisms, allows for the calculation of Dose Conversion Coefficients (DCC). Monte Carlo simulation is used to calculate monoenergetic DCC which are then extrapolated to the energies of interest. The users can create their own ellipsoidal organisms, define the environment by using layers and choose the radiation sources. Among the reference freshwater organisms we find algae with mass = $1.05 \cdot 10^{-13}$ kg. The results include the internal and external DCC and dose rates per nuclide, organism and environmental component. EDEN software is not open-source.

RESRAD-BIOTA code, developed in USA, is another tool targeting aquatic and terrestrial biota dose evaluations. Offering three screening levels, it has a similar approach to ERICA. Radionuclides and organisms are available for two ecosystems (aquatic and terrestrial). The user introduces the activity concentrations in water, sediments and/or soil. Among its features, it provides the user the opportunity to intervene in the radionuclides intake rates, as well as the metabolic characteristics of the organisms [184].

Comparative studies among the tools described above have concluded that ERICA covers most of the radioecological needs. R&D128 is considered as a very basic tool while RESRAD-BIOTA is considered more functional than ERICA in terms of radionuclide transfer within the food chain since it employs dynamic allometric modelling approaches and it does not rely on an "assumed equilibrium ratio approach" like the former [185–187].

Chronic exposure evaluations

Evaluations of natural background radiation exposure to organisms, using ERICA, have revealed variations between 0.01–57 μGy/h. Beresford et al. [188] evaluated the background radiation exposure of terrestrial organisms using ERICA. Focusing on ^{238}U, ^{232}Th decay chains and ^{40}K activity concentrations measured in soils of England and Wales, they showed that the main contributions to the external dose rates come from ^{40}K and ^{226}Ra. In a similar approach, using DCC and activity concentrations of natural radionuclides worldwide, ^{226}Ra and its decay products were shown

to be responsible for a major fraction of the external radiation exposure for terrestrial organisms [189].

Hosseini et al. [190] focused on the background dose rates in aquatic environments using ERICA and observed similar trends. Using wild grass as one of the freshwater reference organisms, they estimated that 55% of the total dose rates were due to internal exposure, dominated by ^{226}Ra contribution. In an analogous study on benthic marine reference organisms, the external dose rates were dominated by ^{226}Ra [191].

Other studies performed for natural radionuclides activity concentrations worldwide report the same trend, while also highlighting the important contribution of ^{226}Ra to the external dose rates for aquatic reference organisms [177].

Calculations performed for freshwater phytoplankton showed that the majority of the total absorbed dose rates are due to internally incorporated ^{226}Ra and ^{210}Po [177]. In the same study, results are provided for bacteria which "because of their small size are assumed to receive the same absorbed dose as the sediments they inhabit". This last clue is representative of the inadequate microdosimetric evaluations using DCC (Dose Conversion Coefficients) and further supports the need for Monte Carlo simulations. Beaugelin-Seiller et al. [192] performed a comparative study between ERICA and EDEN tools in terms of external DCC. Considering an aquatic environment and benthic fish as reference organism exposed to ^{238}U, they found out that the DCC between the two softwares differ by two orders of magnitude. This result is indicative of the importance of the slightly different dosimetric approaches applied.

Moreover, these approaches do not take into consideration the spatial and temporal distribution of absorbed energy in the matter [20, 21] being, thus, also unsuitable for nanodosimetric evaluations.

1.9 Monte Carlo simulation tools

Monte Carlo method can be bulky defined as a statistical approach of solving numerical problems, basically differential equations, by sampling and analysing random numbers/randomly generated events. Governed inherently by randomness, radiation transport is a physical process described by the Boltzmann transfer equation, the solution of which is approached by Monte Carlo (MC) simulations [193]. MNCP, GEANT, FLUKA and PENELOPE are among the most common general-purpose Monte Carlo radiation transport codes.

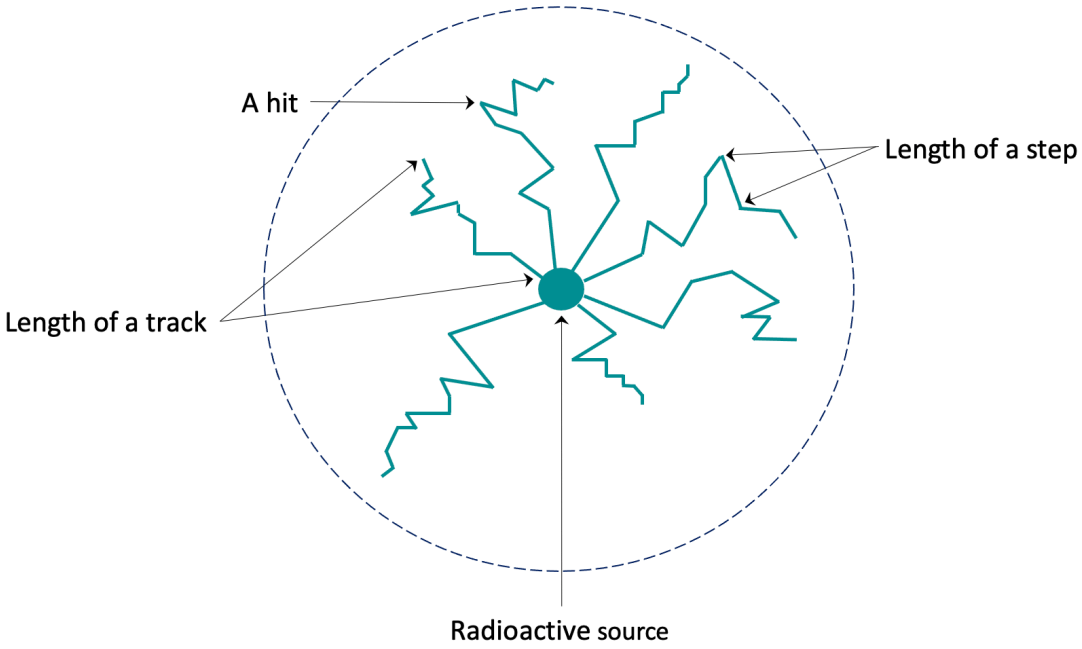

Figure 1.24 Schematic representation of a particle tracking in MC simulations

Monte Carlo simulations for Track Structure (MCTS) provide better accuracy than the respective Condensed-History ones (MCCH) at micro- and nanoscale and low electron energies. While MCTS follows the even-by-event approach and treats in detail all the interactions, MCCH accumulates many physical interactions at every step reducing thus the computational time at the cost of the spatial accuracy of energy depositions [194, 195].

Geant4 and GATE belong to Monte Carlo Track Structure (MCTS) tools. The principle of how a particle is tracked in such approaches is briefly stated below and illustrated in Fig. 1.24. Once a particle is generated, an elementary trajectory step is applied. The particle tracking is achieved through the hits. Hits correspond either to a physical interaction (Photoelectric effect, ionisation, etc) or transportation (process of a particle leaving a volume). During a step, the energy and the momentum of the particle are recalculated according to the processes encountered. When the particle reaches a predefined energy value or crosses predefined space limits, all its history, which is composed by multiple hits, is attributed to a track.

Eventually, why simulation?

As it has already been demonstrated for human cells, MC simulations are needed for micro- and nano- dosimetric assessments due to the stochastic nature of the energy deposition at the cell scale [26]. Furthermore, a common trend in experimental microdosimetry, as applied in a great variety of fields

from aviation and space to nuclear installations and radiation therapy, is the validation of microdosimeters performance by MC simulations [22–25] and vice versa [196].

In macroscale, the efficacy of calculating dose rates using radioecological tools has already been discussed but in the microscale the use MC tools is necessary. For the needs of dose rate simulations on microorganisms, GATE was used and the results were coupled with Geant4-DNA for the prediction of DNA damage.

GATE (Geant4 Application for Tomographic Emission) is an open-source software based on Geant4 libraries, initially dedicated to medical physics [27]. It is a powerful tool, combining the advantages of the Geant4 simulation toolkit with well-validated physics models, sophisticated geometry descriptions and visualization without the need of programming skills by the end-user. GATE has extensively covered simulations from imaging to radiotherapy, dosimetry and radiation protection [197–202] and this work aims at introducing its use to radioecological microdosimetric calculations.

Geant4 (GEometry ANd Tracking) is a MCTS simulation toolkit for the passage of particles through matter [203]. Covering a wide range of applications from radiation protection and medical physics to high energy physics, astrophysics and space science, it offers the ability of modelling and simulating from nanoscale up to macroscale [204–208]. The toolkit, written in C++, provides complete examples covering "basic", "extended" and "advanced" simulation setups which can be modified according to the user's needs [209].

Geant4-DNA software is a low energy extension to Geant4, dedicated to the simulation of the biological damage at the cellular and DNA (nano) scale. Employing physical, chemical and biological models and processes, the mechanistic radiobiological modelling is the principle purpose of the tool. The user can introduce molecular DNA geometries which are either imported from the Protein Data Bank (PDB) [210], generated using external dedicated tools like the DnaFabric software [211] or created within Geant4.

The set of physics processes used here are adapted to micro- and nano-dosimetry in liquid water allowing the tracking of particles down to very low eV energies (~10 eV) [194, 212–214]. With the high accuracy particle tracking, the direct and indirect DNA damages can be explicitly simulated via water radiolysis and direct energy depositions.

Among others, the assessment of the Single and Double DNA Strand Breaks due to the direct and indirect energy deposition of the ionizing particles is

provided through clustering algorithms for DNA structures ranging from the nucleotide level to entire genomes. In this work, the DBSCAN (Density Based Spatial Clustering of Applications with Noise) algorithm [215,216] was used to evaluate the potential DNA damages to microorganisms due to their chronic exposure to natural radioactivity in mineral springs.

Conclusion

In this chapter, the context, concepts and tools relevant for this multidisciplinary work were introduced. Among others, the existing radioecological tools and their limitations were described, as well as, the motivations for micro- and nano-scale Monte Carlo simulations.

In the next chapter, the ecosystems, on which this study focuses, are going to be described. Their characterisation will be presented in detail since they provide the input parameters to the simulations of the current thesis.

Chapter 2

Radiological characterization of the mineral springs

Introduction

The characterization of the ecosystems of the mineral springs is based on the study of water, sediments and diatoms. Sampling campaigns between April 2017 and September 2021 took place in Auvergne as a result of the collective effort of biologists, geologists, radiochemists and physicists from the TIRAMISU collaboration. In this chapter, the sampling sites and methods are first introduced in section 2.1.

Section 2.2 is dedicated to the radiological characterization of the mineral springs waters along with the in-situ ambient dose rate measurements. Details are provided about the γ-spectroscopy studies performed locally at LPC (Laboratoire de Physique de Clermont) for the determination of ^{222}Rn activity concentrations ([^{222}Rn]). The techniques (ICP-MS: Inductively Coupled Plasma Mass Spectroscopy, α-spectroscopy) and the results, obtained for the rest of the radionuclides in water and sediments at the collaborative laboratories are described afterwards.

The radiological characterization of sediments is presented in section 2.3. The main physical and chemical characteristics of the mineral springs are summarized in section 2.4. Using the activity concentrations measured in water and sediments, the distribution coefficients (K_d) of ^{226}Ra and ^{238}Uwere calculated. Then, the elementary composition of dry sediments as determined by XRF (X-ray Fluorescence), as well as, an overview of the main physicochemical properties is presented. Before concluding, the main morphological characteristics of the diatoms inhabiting the under study mineral springs are presented in section 2.5. For clarification reasons, it is stated that the author performed ambient dose rates measurements, collected water during the sampling campaigns and conducted γ-spectrometry, and the subsequent analyses, on the water samples at LPC.

2.1 Sampling

Sampling campaigns were performed for water, sediments and diatoms in 26 mineral springs (Fig. 2.1) corresponding to 24 locations as presented in Table 2.1. For two springs, Bard and Montagne, samples were collected in two locations. In Bard, the two sampling spots correspond το two different emergences (Fig. 2.2). Montagne spring has a peculiar topology that required sampling the same emergence in two locations (Fig. 2.3).

The springs are open for public use and no permit was required to access them and collect samples. The campaigns took place in autumn 2019, summer and autumn 2020, while some specific locations (Montagne and Mariol) were monitored since April 2017 until September 2021. The interest in the long-term monitoring of Montagne and Mariol stems from the study of Millan et al. [62]: ^{222}Rn activity concentration in water was correlated to the percentage of diatoms' deformations during a 1-year survey (May 2018 - March 2019). Moreover, Montagne has been historically known for its elevated radioactivity levels: 3912.75 Bq/L was recorded as early as in 1929 (105.75 mCi/L) [217, 218]. As a consequence, it has been hailed as "the most radioactive spring in France".

For the campaigns performed simultaneously, a certain sampling protocol was followed. Water was first collected in the undisturbed water column in order to avoid any mixing with the rest of the environment. Benthic diatoms were then sampled by the biologists, followed by the collection of sediments.

For the needs of γ-spectroscopic analyses performed at LPC, water was collected according to ISO 5667–1 and ISO 5667–3 standards in 1 L Marinelli style gas-analysis containers (NUVIA Instruments GmbH). The beakers were sealed to avoid any ^{222}Rn leakage. For the needs of ICP-MS analyses, 5 L containers were filled with water.

Site-specific methods were used for the diatom sampling. The main principle is the collection of biofilm which is then processed at the laboratories to isolate and recover diatoms. Biofilms were either retrieved by scraping the surface of the sediments directly with a vial or by using a toothbrush on the surface of travertine deposits. Another method applied was the scrubbing of the surface of rocks recovered from the bottom of the water column. Sediments were collected directly within 50 ml volume capacity vials.

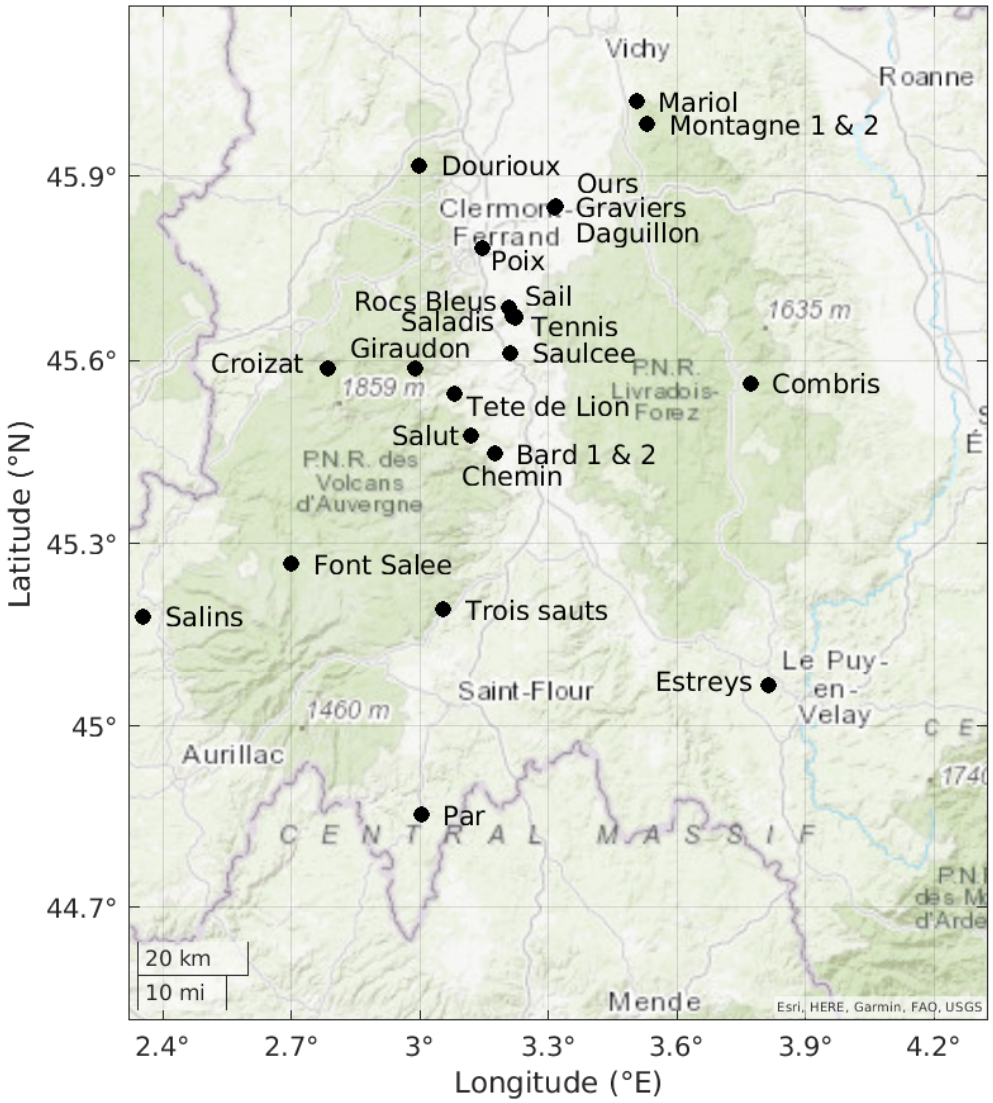

Figure 2.1 Locations of sampled mineral springs in Auvergne (Massif Central)

Table 2.1 Locations of the 26 sampled minerals springs in Auvergne (Massif central)

Spring (Location)	Coordinates	
	North (°)	East (°)
Bard 1 & 2 (Bard)	45.44736	3.174270
Chemin (Ternant les eaux)	45.47718	3.120263
Combris (Ambert)	45.56277	3.771915
Croizat (Mont Dore)	45.58683	2.784650
Daguillon (Joze)	45.85008	3.318260
Dourioux (Dourioux)	45.91756	2.998430
Estreys (Polignac)	45.06771	3.815034
Font Salee (Apchon)	45.26637	2.700802
Giraudon (Saint Nectaire)	45.58755	2.990110
Graviers (Joze)	45.84927	3.313630
Mariol (Mariol)	46.02094	3.505890
Montagne 1 & 2 (Chateldon)	45.98366	3.530788
Ours (Joze)	45.85057	3.317180
Par (Chaudes-Aigues)	44.85348	3.002598
Poix (Clermont-Ferrand)	45.78224	3.146930
Rocs Bleus (Les Martres de Veyre)	45.67163	3.222050
Sail (Mirefleurs)	45.68560	3.207860
Saladis (Les Martres de Veyre)	45.67048	3.215990
Salins (Apcher)	45.17988	2.354711
Salut (Ternant les eaux)	45.47718	3.120395
Saulcee (Coudes)	45.61236	3.212420
Tennis (Saint Marguerite)	45.66862	3.222310
Tete de Lion (Saint Floret)	45.54465	3.081340
Trois sauts (Leyvaux)	45.19130	3.055780

(a) Bard 1

(b) Bard 2

Figure 2.2 Bard 1 and Bard 2

(a) Montagne 1

(b) Montagne 2

Figure 2.3 Montagne 1 and Montagne 2

2.2 Radiological characterization of water

2.2.1 In situ measurements of ambient doses

In situ γ-equivalent dose rate measurements (in nSv/h) were performed during sampling at the water level, as well as, 1 m above the water surface using a portable Geiger-Mueller (VLD Colibri dual sensor survey meter coupled with CsI(Tl), Mirion). Two measurements of Δt = 2 min were conducted each time and their mean values are presented in Tables 2.3 & 2.4. The systematic uncertainty (δDR) is evaluated to 15%, while the provided uncertainties (ΔDR) were calculated according to the common error propagation formula (Eq. 2.1). Local background measurements at the vicinity of the sampling locations (in a radius of 10 m) were in agreement with the typical background levels in Auvergne (150-200 nSv/h).

$$\Delta DR = \frac{1}{2}\sqrt{(\delta DR_1)^2 + (\delta DR_2)^2} \tag{2.1}$$

with:

ΔDR (nSv/h): ambient dose rate uncertainty

δDR (nSv/h): systematic uncertainty of the instrument

Two main points of interest lie in measuring the ambient dose equivalent rates on site. First, it is important to be aware of the levels of radioactivity that we are exposed to during sampling. The duration of this process is commonly around 10–15 min although it is site- and sample-specific. All the sampling sites apart from one (Montagne) are in open space. Considering the three main radioprotection principles (As Low As Reasonably Achievable - ALARA) [165, 219, 220] of maximum distance, minimum time and shielding from a radiation source, the sampling campaigns performed in this work did not raise any concerns. Time restriction (~3 minutes per person) was imposed on the sampling duration inside the building hosting Montagne 1 source.

Second, elevated ambient dose rates in comparison to the background ones are an indication of a radiation source and a potential point of interest. The highest ambient dose rates measured at the water surface and the respective elevated ^{222}Rn concentrations measured in water Dourioux, Montagne 1 and Montagne 2 are highlighted. As shown in Table 2.3, in Dourioux 810 nSv/h and 3110 Bq/L ^{222}Rn in water were measured, in Montagne 1 915 nSv/h and 3452.5 Bq/L ^{222}Rn in water were measured, while the respective values for Montagne 2 are 810 nSv/h and 1127.8 Bq/L. On the other hand, the ambient dose rate on the water surface (210 nSv/h) did not indicate the elevated water ^{222}Rn activity concentration (1272.6 Bq/L) in Estreys. In spite of that, the respective ambient dose rate at 1 m above the water surface was three times higher than on the surface.

The ambient dose rates and ^{222}Rn water activity concentrations measured on the same day in 14 mineral springs are plotted in Fig. 2.4. Pearson coefficients (R) were calculated to evaluate the relationship between ambient dose rates and ^{222}Rn activity concentrations in water. The p-value threshold is set to $p = 0.05$. Positive correlations were found in both cases. The strongest correlation is between the ambient dose rates measured at the water surface and [^{222}Rn] ($R = 0.92$, $p = 3.8 \cdot 10^{-6}$, $N = 14$). The respective positive correlation between the ambient dose rates at 1 m above the water surface and the [^{222}Rn] is weaker ($R = 0.65$, $p = 0.01$, $N = 14$).

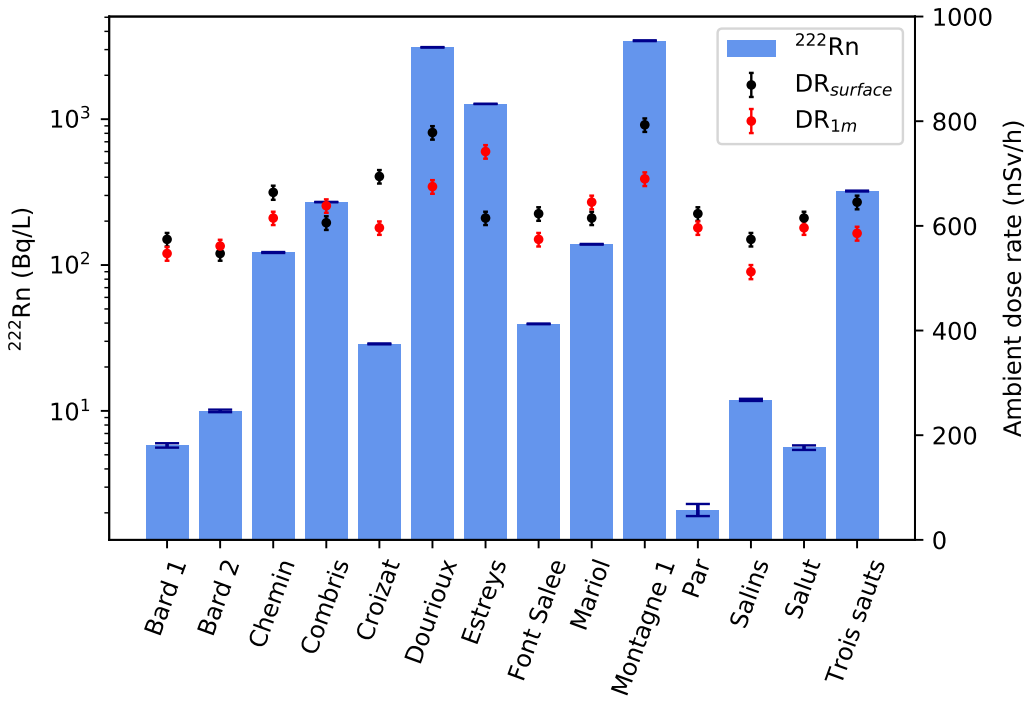

Figure 2.4 Ambient dose rates (DR) and ^{222}Rn activity concentrations in water for 14 mineral springs in Auvergne

Nevertheless, it would be prudent to state no absolute correlation between the ambient dose rates and ^{222}Rn activities in water. Still, ambient dose rates higher than the background ones indicate the existence of a radiation source. In the case of natural radioactivity, this can be correlated to the composition of the environment. In an environment which is naturally rich in Uranium, elevated ambient dose rates stem from the whole decay chain and not exclusively from the ^{222}Rn emanation from water.

2.2.2 Laboratory measurements

γ-spectrometry at LPC

The activity concentrations (in Bq/L) of ^{222}Rn in water were measured by γ-spectrometry according to ISO 13164-2. A High-Purity Germanium (HPGe, 2.56"×2.56") well-type detector (GCW3523, Canberra Inc) of 35% relative efficiency was used, assisted by the Genie2000 software. In Fig. 2.5, the configuration of the well-type detector, placed in its 210 mm width Lead (Pb) shield, before and after placing the water sample is shown. It is highlighted that the geometry of Marinelli beakers allows for the full coverage of the detector.

^{222}Rn activity concentrations were measured within a few hours after the sampling using the 352 keV γ-ray of ^{214}Pb ($t_{1/2}$ = 27.06 min). In this way, ^{222}Rn

dissolved in water which has been carried away from deep underground, along with ^{222}Rn present due to ^{226}Ra decay in the water, was evaluated.

(a) Without sample **(b)** With water sample

Figure 2.5 HPGe detector at LPC

In the absence of a liquid reference source, no efficiency curve was determined for the measurements of the water samples. Instead, a semi-empirical approach based on measurements of solid reference samples and Monte Carlo simulations using Geant4 was considered [221–223]. Corrections were applied for the geometry and the self-absorption of liquid samples. The FWHM of the detector was 1.65 keV at 352 keV. The detector efficiency was checked regularly by comparing the FWHM of control reference samples.

Energy calibration (across 8192 channels) was performed using the 121.8, 244.7, 344.3, 444.6, 778.9, 964.1, 1085.1, 1112.1 and 1408.0 keV photopeaks of the ^{152}Eu source and was evaluated for the low-energy region using the 59.5 keV photopeak of a ^{241}Am source. The applied fit is shown in Eq. 2.2, with A and C being constants determined from the data. The energy calibration is graphically represented in Fig. 2.6.

$$E\ (keV) = A \cdot channel + C \tag{2.2}$$

with:

A = 0.213 ± 0.054 keV/channel

C = -44.22 ± 0.05 keV

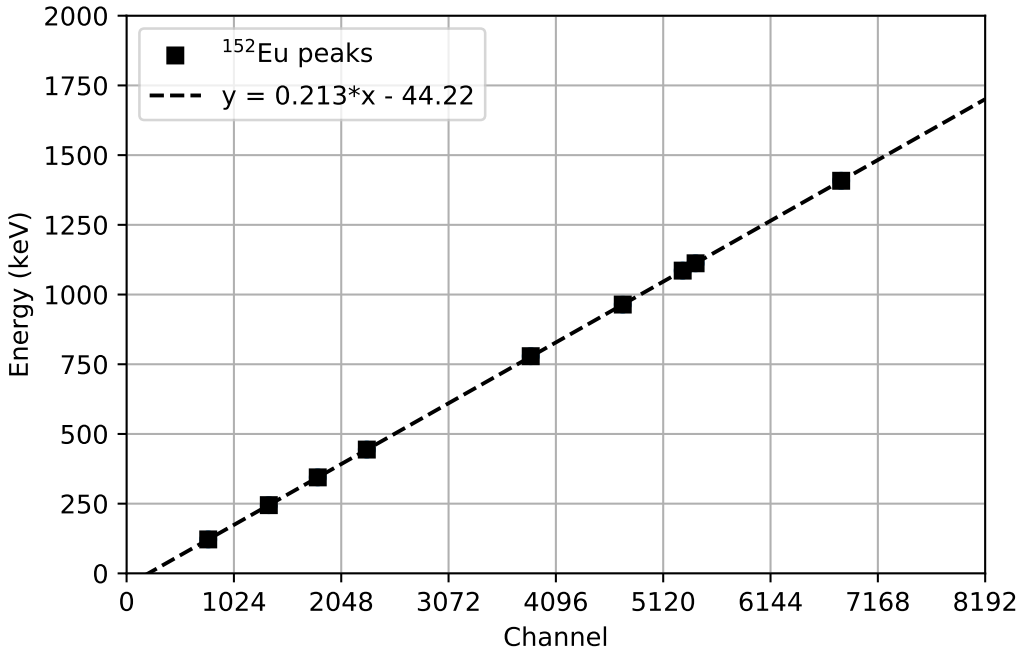

Figure 2.6 Energy calibration using a ^{152}Eu source

The duration of the measurements ranged from a few hours to 2 days according to the counting rate at the photopeak of interest. Tthe ratio $\sqrt{N}/N$ (N: total number of counts) of the 352 keV γ-energy peak was being evaluated, trying to achieve a value lower than 5%. For example, the spectrum shown in Fig. 2.7 corresponds to one of the most active water samples (Montagne spring) with counting rate 15 counts/s and it was measured for 1 & 1/2 h. Apart from the photopeak of interest placed at 352 keV, several γ-peaks of ^{214}Pb and ^{214}Bi are identified in the spectrum, along with Pb X-rays in the low energy region of the spectrum which are summarized in Table 2.2 (the decay schemes can be found in Appendix B). No detection limit has been established for the current measurements but, as it will be discussed later, the very low values of activity concentrations are accompanied by high uncertainties.

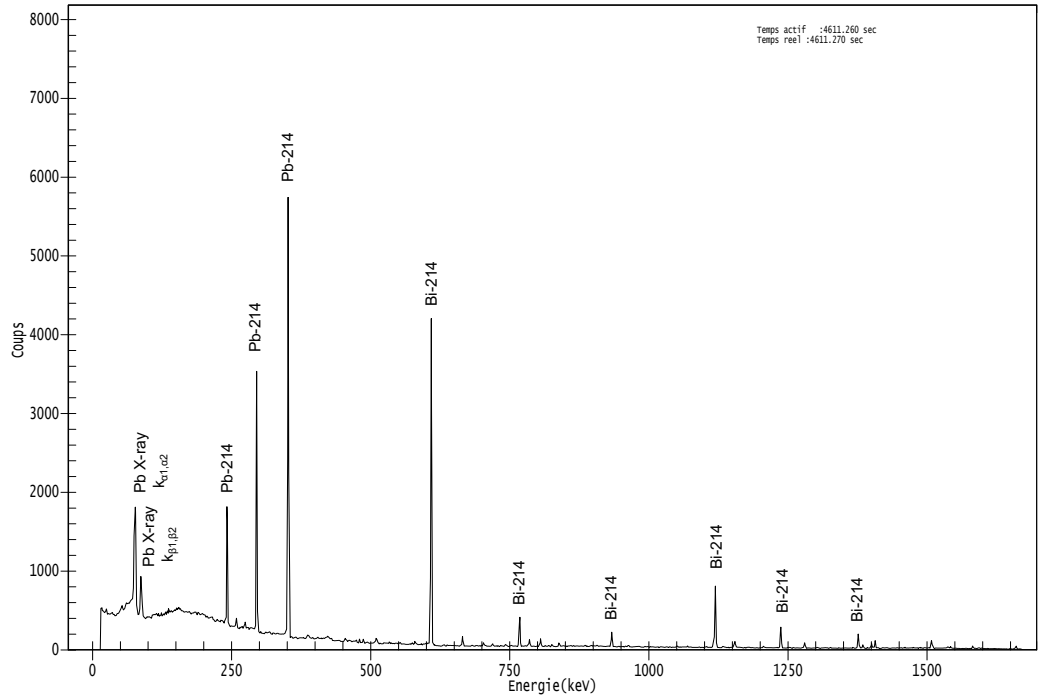

Figure 2.7 γ-spectrum of a mineral spring water sample

Table 2.2 Energy (keV) and emission intensity (%) of the photopeaks in the γ-spectrum of a water sample shown in Fig. 2.7

	Energy (keV)	**Intensity (%)**
Pb $K_{\alpha 2}$ X-ray	74.8	5.1
Pb $K_{\alpha 1}$ X-ray	77.1	8.6
Pb $K_{\beta 1}$ X-ray	87.4	2.0
Pb $K_{\beta 2}$ X-ray	89.8	0.7
^{214}Pb	242.0	7.3
	295.2	18.4
	351.9	35.6
^{214}Bi	609.3	45.5
	768.4	4.9
	934.1	3.1
	1120.3	14.9
	1238.1	5.8
	1408.0	2.4

A correction was applied for the decay of the radionuclides between the sampling moment (t_0) and the beginning of the measurement (t_1). We consider that at t_0, N_0 nuclei of a radiosotope are collected. The measurement starts after a time period $\Delta T = t_1 - t_0$, during which the initial N_0 nuclei have disintegrated following the radioactive decay law. As a result, at the beginning of the measurement, N_1 nuclei are present in the sample, while at the end of the measurement (t_2) N_2 nuclei are left intact. Under the hypothesis of detecting all the emitted nuclei, the number of nuclei measured between t_1 and t_2 (δt) corresponds to "$N_{measured}$" as shown in Fig. 2.8.

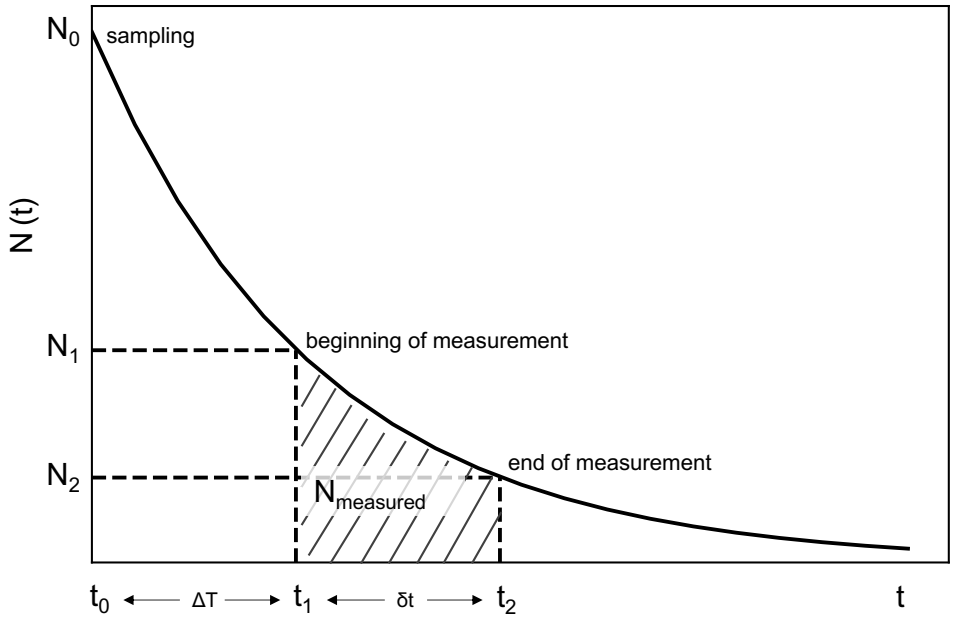

Figure 2.8 Decay curve of a radioactive substance from the sampling moment at the field until the end of the measurement at the laboratory

The differential equation of the activity (A) and the general solutions for a given radionuclide characterized by a decay constant λ are given by Eq. 2.3 - 2.5, respectively.

$$A(t) = -\frac{dN}{dt} = \lambda N(t) \tag{2.3}$$

with:

A(t): activity of a radionuclide at a given moment t

λ: decay constant of the radionuclide

N(t): number of nuclei at a given moment t

$$A(t) = A_0 e^{-\lambda t} \tag{2.4}$$

with:

A(t): activity of a radionuclide at a given moment t

λ: decay constant of the radionuclide

A_0: activity of the radionuclide at t = t_0

$$N(t) = N_0 e^{-\lambda t} \tag{2.5}$$

with:

N(t): number of nuclei which have not disintegrated at a given moment t

(N(t) will be denoted as N onwards in the text for simplification reasons)

λ: decay constant of the radionuclide

N_0: number of nuclei at t = t_0

Integrating Eq. 2.3 between the sampling moment and the moment that the measurement started, we get the number of nuclei N_1 at the beginning of the measurement (Eq. 2.6).

$$\begin{aligned} \int_{N_0}^{N1} \frac{1}{N} dN &= -\int_{t_0}^{t1} \lambda dt \\ &\rightarrow N_1 = N_0 e^{-\lambda \Delta T} \end{aligned} \tag{2.6}$$

Therefore, the disintegration of N_1 nuclei during the measurement is now described by Eq. 2.5 for $N_0 = N_1$. The cumulative number of nuclei corresponding to the total number of counts measured between t_1 and t_2 is calculated via Eq. 2.7.

$$N_{measured} = \int_{t_1}^{t2} N_1 e^{-\lambda t} = \int_{t_1}^{t2} N_0 e^{-\lambda \Delta T} e^{-\lambda t} \tag{2.7}$$

Eventually, the $N_{measured}$ for a radioactive sample collected at the moment t_0 which started being measured at t_1 for a duration δt in the laboratory, is described by Eq. 2.8.

$$N_{measured} = \frac{N_1}{\lambda}(1 - e^{-\lambda \delta t}) \; = \frac{N_0 e^{-\lambda \Delta T}}{\lambda}(1 - e^{-\lambda \delta t}) \tag{2.8}$$

with:

N_0: number of nuclei at the sampling moment

N_1: number of nuclei at the beginning of the measurement

δt: duration of measurement

ΔT: time between sampling moment and beginning of the measurement

λ: decay constant of the radionuclide

The results of ^{222}Rn activity concentrations for the campaign October 2019 - October 2020 are shown in Tables 2.3 & 2.4. The absence of measurements is denoted by "-", while the absence of samples is denoted by "NS" (No Sample). The respective results of the continuous monitoring in Montagne 1 & 2 and Mariol (April 2017 - September 2021) are presented in Table 2.5.

Although no detection limit has been established for the current measurements, it is observed that the lowest value (0.6 Bq/L - measured at Poix) is characterized by 16.7% uncertainty, while the uncertainty for the highest [^{222}Rn] (4600 Bq/L - measured at Montagne 1 in May 2018) is 0.3%. In summary, for [^{222}Rn] $<$ 100 Bq/L the uncertainties vary between 0.5% and 17%, but they stabilize between 0.1% and 1.4% for [^{222}Rn] $\geq$ 100 Bq/L. Although this behaviour is expected due to the increased counting rate, it is reminded that the uncertainties are multi-parametric. They depend on factors which do not fluctuate a lot among the measurements (geometry, physical characteristics of the sample (e.g. density), detector efficiency), so the contribution of the counting rate to the uncertainties is notable for low-activity samples.

^{222}Rn activity concentrations in water vary by 3 orders of magnitude among the mineral springs. During the October 2019 - September 2021 sampling campaign, the lowest [^{222}Rn] measured was 0.6 Bq/L in Poix, while the highest ones correspond to 3852 Bq/L in Dourioux and 3848.5 Bq/L in Montagne 1. Poix is a very peculiar mineral spring. Apart from having very low water flux, imposing difficulties in sampling, Poix is bituminous with very strong hydrogen sulfide (H_2S) odor. This brackish environment is a geological, as well as, an ecological particularity of Massif Central [52].

From Tables 2.3 & 2.4, it is noticed that some repeated measurements can result in very different activity concentrations in some springs (for example in Chemin, Sail, Tennis). The case of Sail is extreme as the spring dries up during summer time and sampling must be interrupted.

Table 2.3 Ambient Dose Rates (DR in nSv/h) & ^{222}Rn activity concentrations (Bq/L) in water
- Part 1

Spring	Sampling date	$DR_{surface}$ (nSv/h)	DR_{1m} (nSv/h)	^{222}Rn (Bq/L)
Bard 1	22/10/2019	150 ± 16	120 ± 13	5.8 ± 0.2
	29/06/2020	-	-	5.9 ± 0.2
Bard 2	22/10/2019	120 ± 13	135 ± 14	10.0 ± 0.2
Chemin	30/10/2019	315 ± 35	210 ± 22	121.9 ± 0.9
	04/08/2020	-	-	10.5 ± 0.2
Combris	25/10/2019	195 ± 21	255 ± 27	270.3 ± 0.6
	16/06/2020	-	-	111.5 ± 0.6
Croizat	30/10/2019	405 ± 43	180 ± 20	28.8 ± 0.2
	29/07/2020	-	-	28.9 ± 0.2
Daguillon	21/10/2019	450 ± 48	345 ± 37	NS
	21/07/2020	-	-	395.6 ± 0.1
	26/10/2020	-	-	545.0 ± 0.3
Dourioux	21/10/2019	810 ± 86	345 ± 37	3110.0 ± 11.0
	02/08/2020	-	-	3852.0 ± 3.7
Estreys	22/10/2019	210 ± 22	600 ± 64	1272.6 ± 1.2
	29/06/2020	-	-	1438.6 ± 1.7
Font Salee	16/10/2019	225 ± 24	150 ± 16	39.5 ± 0.2
	22/06/2020	-	-	33.5 ± 0.3
Giraudon	15/10/2019	390 ± 41	195 ± 21	NS
	27/11/2019	-	-	16.6 ± 0.3
	29/07/2020	-	-	8.2 ± 0.2
Graviers	21/10/2019	330 ± 35	465 ± 50	NS
	21/07/2020	-	-	29.2 ± 0.3
	26/10/2020	-	-	22.1 ± 0.2
Mariol*	21/10/2019	210 ± 22	270 ± 29	138.8 ± 0.7
Montagne 1*	21/10/2019	915 ± 97	390 ± 42	3452.5 ± 20.5
Montagne 2*	13/12/2019	810 ± 86	-	1127.8 ± 5.3
Ours	21/10/2019	405 ± 43	300 ± 32	NS
	21/07/2020	-	-	18.8 ± 0.2
	26/10/2020	-	-	22.1 ± 0.2

Annotations: "-": absence of measurement, "NS": no sample. "*": indicates that the values correspond to the specific sampling dates (the continuous monitoring results are presented in Table 2.5).

Table 2.4 Ambient Dose Rates (DR in nSv/h) & ^{222}Rn activity concentrations (Bq/L) in water
- Part 2

Spring	Sampling date	$DR_{surface}$ (nSv/h)	DR_{1m} (nSv/h)	^{222}Rn (Bq/L)
Par	16/10/2019	225 ± 24	180 ± 19	2.1 ± 0.2
	22/06/2020	-	-	2.2 ± 0.1
Poix	22/10/2019	90 ± 10	75 ± 8	NS
	03/08/2020	-	-	0.6 ± 0.1
Rocs Bleus	15/10/2019	210 ± 22	150 ± 16	NS
	13/11/2019	-	-	11.2 ± 0.2
	10/07/2020	-	-	20.1 ± 0.2
Sail	15/10/2019	270 ± 29	150 ± 16	NS
	13/11/2019	-	-	1006.1 ± 1.6
	10/07/2020	-	-	178.7 ± 1.3
Saladis	15/10/2019	495 ± 53	330 ± 40	NS
	13/11/2019	-	-	10.2 ± 0.2
	10/07/2020	-	-	9.9 ± 0.1
Salins	16/10/2019	150 ± 16	90 ± 10	11.9 ± 0.2
	22/06/2020	-	-	9.1 ± 0.2
Salut	30/10/2019	210 ± 22	180 ± 19	5.6 ± 0.2
	04/08/2020	-	-	6.9 ± 0.2
Saulcee	15/10/2019	375 ± 40	180 ± 19	NS
	27/11/2019	-	-	87.1 ± 0.5
	29/07/2020	-	-	91.7 ± 0.5
Tennis	15/10/2019	390 ± 41	825 ± 88	NS
	13/11/2019	-	-	176.7 ± 0.2
	10/07/2020	-	-	14.9 ± 0.3
Tete de Lion	15/10/2019	465 ± 51	353 ± 38	NS
	27/11/2019	-	-	132.8 ± 0.6
	29/06/2020	-	-	30.1 ± 0.2
Trois sauts	22/10/2019	270 ± 29	165 ± 18	321.6 ± 2.1
	08/08/2020	-	-	578.0 ± 4.7

Annotations: "-": absence of measurement, "NS": no sample

Table 2.5 Monitoring of ^{222}Rn activity concentrations (Bq/L) in Montagne 1, Montagne 2 and Mariol

	^{222}Rn (Bq/L)		
Date	**Montagne 1**	**Montagne 2**	**Mariol**
18/04/2017	4108.0 ± 1.9	NS	NS
30/05/2017	NS	NS	147.0 ± 0.9
16/05/2018	4600.0 ± 10.0	1737.0 ± 13.0	147.0 ± 2.0
18/01/2019	4561.0 ± 13.0	NS	NS
08/04/2019	2780.0 ± 10.0	2100.0 ± 13.0	160.0 ± 2.0
21/10/2019	3452.5 ± 20.5	NS	138.8 ± 0.7
18/11/2019	1662.7 ± 10.3	NS	136.8 ± 0.6
13/12/2019	761.7 ± 3.9	1127.8 ± 5.3	162.2 ± 1.6
10/01/2020	737.4 ± 8.4	1866.1 ± 10.9	134.1 ± 0.4
04/02/2020	796.4 ± 2.0	1338.2 ± 3.9	132.7 ± 0.6
23/06/2020	3746.4 ± 12.8	2177.1 ± 6.8	NS
01/07/2020	NS	NS	139.1 ± 0.4
28/07/2020	NS	1448.7 ± 2.5	NS
16/09/2020	2610.3 ± 4.0	1982.5 ± 1.4	NS
10/02/2021	1344.8 ± 1.5	629.1 ± 0.9	139.2 ± 0.3
22/03/2021	3848.5 ± 15.8	2212.1± 5.3	130.3 ± 0.8
21/04/2021	NS	NS	138.3 ± 0.4
28/05/2021	2721.7 ± 5.6	2440.3 ± 3.6	NS
08/09/2021	1610.3 ± 7.1	2158.4 ± 2.8	NS

Annotations: "NS": no sample

For the mineral springs sampled twice, the measured [^{222}Rn] differed less than 5% in Bard 1, Croizat, Par and Saulcee. In the rest of the locations, the repeated measurements could differ up to a factor 12 (Chemin, Tennis). Consequently, it was considered prudent to not extract mean values of ^{222}Rn activity concentrations in each mineral spring. For the continuously monitored springs, the difference between the maximum and minimum measured [^{222}Rn] was 22% in Mariol, while the maximum and minimum values differed by a factor 4 in Montagne 2 and a factor 6 in Montagne 1. The variations of ^{222}Rn activity concentrations observed in these locations are further discussed later in this chapter.

A conservative approach was adopted for the classification of the mineral springs in three categories (Low, Medium and High level) according to their

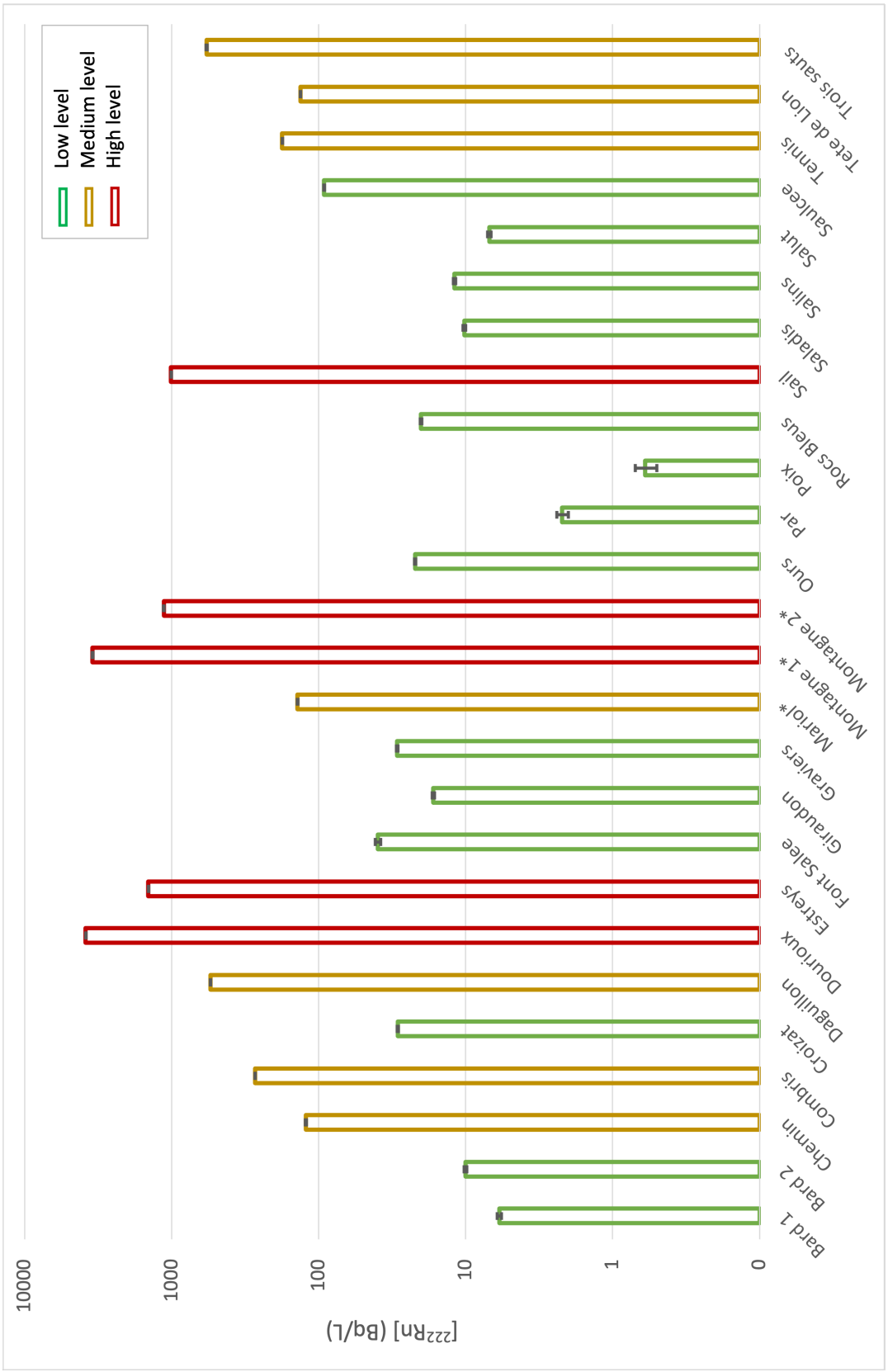

Figure 2.9 ^{222}Rn activity concentration in water ([^{222}Rn]) in 26 mineral springs. Green: Low level ([^{222}Rn] < 100 Bq/L), Orange: Medium level (100 Bq/L ≤ [^{222}Rn] < 1000 Bq/L), Red: High level ([^{222}Rn] ≥ 1000 Bq/L).

water ^{222}Rn activity concentrations. This approach is based on the worst case scenario of radiation exposure for the microorganisms living in these habitats: the higher the [^{222}Rn] is, the greater the radiation exposure is. As a result, the highest [^{222}Rn] measured in each spring was taken into consideration from Tables 2.3-2.5.

As presented in Fig. 2.9, the springs with [^{222}Rn] < 100 Bq/L were classified as Low level (green), the springs with 100 Bq/L ≤ [^{222}Rn] < 1000 Bq/L as Medium level (orange) and the ones with [^{222}Rn] ≥ 1000 Bq/L as High Level (red). The limits of 100 Bq/L and 1000 Bq/L were chosen in accordance to the suggested European Union ^{222}Rn activity concentrations in potable water [77].

According to this classification, the mineral springs with significantly varying ^{222}Rn activity concentrations were initially nominated to be classified in multiple categories. Applying this conservative approach, these springs were finally classified in the highest possible rank. In total, 54% of the sampled locations are categorized as Low level, 27% as Medium level while in 5 out the 26 sampled locations the ^{222}Rn activity concentrations were higher than 1000 Bq/L. The latter include Dourioux, Estreys, Montagne 1 & 2 and Sail.

In Fig. 2.10, the ^{222}Rn activity concentrations in water for the period April 2017 - September 2021 in Montagne 1, Montagne 2 and Mariol are presented graphically. As mentioned before, these locations are of particular interest due to the correlation between ^{222}Rn activity concentrations and diatoms' deformations. Mariol presents a rather steady temporal behaviour with a mean [^{222}Rn] of 142.1 Bq/L and a standard deviation of 10.2 Bq/L, while in Montagne 1 & 2 the ^{222}Rn activity concentrations vary significantly. In Montagne 1, a range of [737.4, 4600.0] Bq/L is observed, with the lowest values measured between December 2019 and February 2020. ^{222}Rn activity concentrations higher than 3000 Bq/L at this location were measured in spring 2017, 2018, 2021, winter and autumn 2019, and summer 2020 (40% of the times). Consequently, no seasonal effect could be directly linked to the [^{222}Rn] variations. The corresponding range in Montagne 2 is [629.1, 2440.3] Bq/L measured in February 2021 and May 2021, respectively.

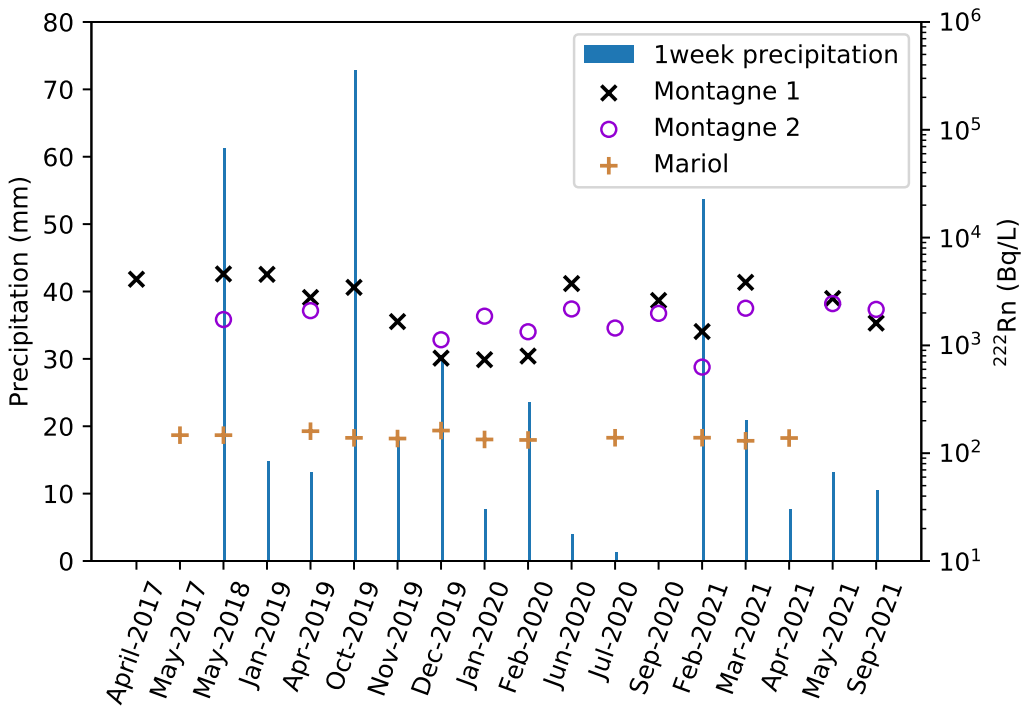

Figure 2.10 ^{222}Rn activity concentration in water and weekly precipitation in Montagne 1, Montagne 2 and Mariol

A preliminary assumption connecting ^{222}Rn water activity concentrations and precipitation levels was made considering that water dilution can be an accountable factor for the phenomenon. Montagne 1 & 2 (45.98366° N, 3.530788° E) and Mariol (46.02094° N, 3.50589° E), are a few kilometers apart. Consequently, they are subject to the same local weather conditions which cannot justify the almost steady [^{222}Rn] in Mariol in contrary to the fluctuating [^{222}Rn] in Montagne locations. However, these springs are subject to different topological arrangements. While Mariol (Fig. 2.11a) emerges in a bowl placed 0.5 m above the ground, Montagne 1 (Fig. 2.11b) is located in a room-sized building presenting stagnant water, with Montagne 2 being located a few meters away, across a small unpaved road. Nonetheless, the water in Montagne 2 is actually a mixture of different springs overflows. The water emerging from this location was exploited until middle '50s: an underground concrete pipe is supposed to connect the two sites. Although the spatial configuration of the two sites is different, both of them are susceptible to precipitation and runoff effects [62].

(a) Mariol **(b)** Montagne 1

Figure 2.11 Mariol and Montagne 1

Pluviometry data were recovered from the nearest meteorological station (46.04 N, 3.61 E) [224] and they are summarized in Appendix C. The daily precipitation levels were first recovered in order to evaluate the local weather conditions 1 week prior to sampling (see Fig. 2.10). Pearson correlations between ^{222}Rn water activity concentrations and the integrated 1-week prior to sampling precipitation levels were conducted. No correlation could be deduced for Montagne 1 ($R = 0.08$, $p = 0.8$, $N = 15$) and Mariol ($R = 0.03$, $p = 0.9$, $N = 12$) while a weak negative correlation was observed for Montagne 2 ($R = -0.55$, $p = 0.06$, $N = 12$).

In the next step, the evaluation was restricted on the total daily precipitation on the sampling dates (Fig. 2.12).

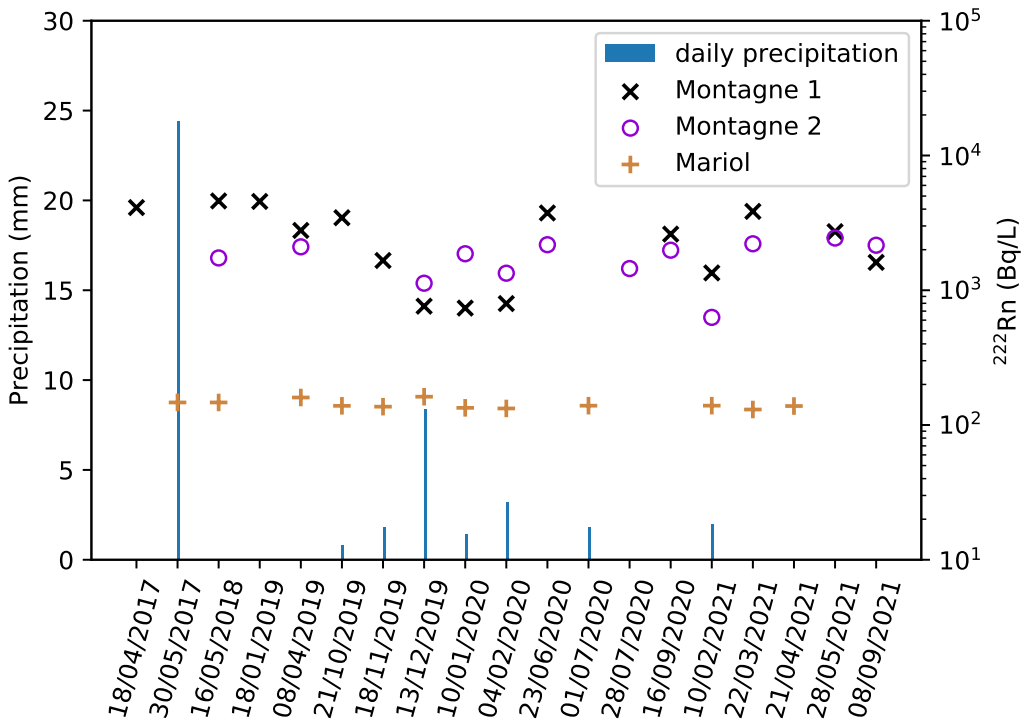

Figure 2.12 ^{222}Rn activity concentration in water and daily precipitation in Montagne 1, Montagne 2 and Mariol

Statistically significant ($p < 0.05$) weak negative correlations between the daily precipitation levels and the ^{222}Rn water activity concentrations were calculated for Montagne 1 ($R = -0.63$, $p = 0.01$, $N = 15$) and Montagne 2 ($R = -0.61$, $p = 0.03$, $N = 12$). On the other hand, no significant correlation could be deduced for Mariol ($R = 0.29$, $p = 0.37$, $N = 12$).

Finally, the study was limited to the available conductivity data (Appendix C). Baker et al. [55] have concluded that there is low correlation between daily precipitation levels and water conductivity in Montagne 1, but significant precipitation events can affect negatively the conductivity levels. In order to evaluate a possible link between ^{222}Rn water activity concentrations and conductivity, Pearson correlations for the three under-study springs were performed. Weak negative correlations were calculated for Montagne 2 ($R = -0.50$, $p = 0.5$, $N = 4$) and Mariol ($R = -0.39$, $p = 0.44$, $N = 6$), while no correlation was found for Montagne 1 ($R = 0.09$, $p = 0.86$, $N = 6$). None of these results are statistically significant ($p_{\text{threshold}} = 0.05$). A summary is provided in Table 2.6.

Therefore, the fluctuating behaviour of Montagne 1 could be possibly attributed to the peculiarity of the sampling site: the mineral spring water flows out from an orifice inside a small building. The building itself allows the accumulation of rainwater and runoffs. Once the level of the

accumulated water increases, it gets mixed with the spring water and there is no way to isolate the spring water from the rainwater.

Table 2.6 Pearson correlation results between ^{222}Rn activity concentration ([^{222}Rn]) in water and one-week precipitation, daily precipitation, conductivity for Montagne 1, Montagne 2 and Mariol

		one-week precipitation			daily precipitation			conductivity		
		R	*p*	*N*	*R*	*p*	*N*	*R*	*p*	*N*
Montagne 1	[^{222}Rn] in water	0.08	0.80	15	-0.63	0.01	15	0.09	0.86	6
Montagne 2		-0.55	0.06	12	-0.61	0.03	12	-0.50	0.50	4
Mariol		0.03	0.90	12	0.29	0.37	12	-0.39	0.44	6

R: Pearson coefficient, *p*: p-value, *N*: number of samples

ICP-MS and α-spectrometry at Subatech and ICN

Water samples were also collected and analysed in SUBATECH (Laboratoire de physique SUBatomique et TECHnologies associées) and ICN (Institut de Chimie de Nice) laboratories for the activity concentrations of ^{238}U, ^{226}Ra, ^{232}Th and ^{210}Po. The samples were filtrated using hydrophile PTFE membrane filters of 0.45 μm pore size, and were chemically purified when needed. ^{238}U and ^{232}Th were measured by ICP-QMS (Xseries 2, Thermo Electron) while HR - ICP - MS (Element XR, Thermo Scientific) was used for ^{226}Ra. ICP-MS (Inductively Coupled Plasma Mass Spectroscopy) is a relative technique requiring liquified samples. The elements of the sample are first ionized and then separated by their mass-to-charge ratio in order for their concentration to be measured (in ppt, ppb, ppq). For each radionuclide, the correlation between the specific activity and the measured concentration allows for the deduction of the activity concentrations (example for ^{226}Ra: specific activity = $3.66 \cdot 10^{10}$ Bq/g, 1 ppq = $1 \cdot 10^{-12}$ g/L, 1 ppq of ^{226}Ra corresponds to $3.07 \cdot 10^{-2}$ Bq/L). The same principle but with higher sensitivity is used by High–Resolution (HR) ICP-MS. ICP-QMS (Inductively Coupled Plasma Quadrupole Mass Spectroscopy) denotes that ICP-MS is performed using a quadrupole magnet.

The activity concentrations of ^{210}Po was measured via dual α-spectrometers (576A, AMETEC-ORTEC) equipped with boron implanted silicon detectors. α-spectroscopy offers high resolution in the low energy region. Due to the short range of α-particles, the technique is performed in vacuum. A thin Silver (Ag) disc is introduced to the water sample. Po is chemically in favor

of Ag, allowing its deposition on the disc. This silver disk is then measured by α - spectroscopy following the principle of transforming the interactions between particles and the detector material to a measurable signal.

The results are presented in Table 2.7. The absence of measurements is denoted by "-". When values are below the detection limit (DL), the value of DL is provided instead (denoted, for example, as "$<2.5 \cdot 10^{-3}$").

There is no spring for which all the radionuclides were simultaneously measured and/or passed the detection limit. In Par, none of the measured radiosotopes was above the detection limit. It is observed that ^{232}Th was above the detection limit (0.001 Bq/L) only in Montagne 2 but still in a very low activity concentration (0.003 ± 0.001 Bq/L). ^{210}Po was above the detection limit (0.01 Bq/L) in nine mineral springs with values ranging between 0.025 ± 0.010 Bq/L (Mariol) and 0.392 ± 0.05 Bq/L (Salins). ^{238}U levels are in the range of [0.003, 0.196] Bq/L with the highest one measured in Salins. ^{226}Ra activity concentration measurements were conducted for 15 locations. Among them, the lowest [^{226}Ra] was measured in Sail with a rather high uncertainty (0.472 ± 0.307 Bq/L) while the highest was measured in Tennis (3.338 ± 0.421 Bq/L).

In Fig. 2.13, the activity concentrations of the radionuclides (^{238}U, ^{226}Ra, ^{222}Rn, ^{210}Po, ^{232}Th) measured in water in each mineral spring are summarized. The absence of measurements is denoted by the absence of the respective radionuclide in each spring (for example, in Trois Sauts, no [^{226}Ra] measurements were performed so the respective bar is missing).

It is observed that ^{222}Rn activity concentrations are 4 to 6 orders of magnitude higher than the other radioisotopes. It is highlighted that [^{226}Ra] are at least 1 order of magnitude lower than [^{222}Rn], making thus ^{222}Rn the dominant radionuclide in water. Wherever ^{238}U and ^{210}Po were both measured, [^{210}Po] was always higher than [^{238}U]. It is reminded that the aforementioned radionuclides are all α-emitters of the ^{238}U decay series apart from ^{232}Th which is the parent nucleus of its decay series. Finally, [^{226}Ra] in water is much higher than [^{238}U], in very good agreement with data from the literature [73].

Table 2.7 Activity concentrations (Bq/L) in water measured by SUBATECH - ICN

	Activity Concentrations (Bq / L)			
Spring	^{238}U	^{226}Ra	^{232}Th	^{210}Po
Bard 1	$<2.5\cdot10^{-3}$	$<4.8\cdot10^{-1}$	$<1.0\cdot10^{-3}$	$<1.0\cdot10^{-2}$
Bard 2	$<2.5\cdot10^{-3}$	0.922 ± 0.326	$<1.0\cdot10^{-3}$	$<1.0\cdot10^{-2}$
Chemin	0.004 ± 0.001	-	$<1.0\cdot10^{-3}$	$<1.0\cdot10^{-2}$
Combris	0.081 ± 0.004	0.853 ± 0.351	$<1.0\cdot10^{-3}$	0.154 ± 0.025
Croizat	0.043 ± 0.003	1.998 ± 0.747	$<1.0\cdot10^{-3}$	0.088 ± 0.015
Daguillon	$<2.5\cdot10^{-3}$	3.221 ± 0.721	$<1.0\cdot10^{-3}$	$<1.0\cdot10^{-2}$
Dourioux	0.008 ± 0.001	-	$<1.0\cdot10^{-3}$	0.030 ± 0.010
Estreys	0.015 ± 0.001	1.204 ± 0.135	$<1.0\cdot10^{-3}$	0.027 ± 0.010
Font salée	$<2.5\cdot10^{-3}$	-	$<1.0\cdot10^{-3}$	$<1.0\cdot10^{-2}$
Giraudon	$<2.5\cdot10^{-3}$	-	$<1.0\cdot10^{-3}$	$<1.0\cdot10^{-2}$
Graviers	$<2.5\cdot10^{-3}$	2.331 ± 0.732	$<1.0\cdot10^{-3}$	$<1.0\cdot10^{-2}$
Mariol	0.012 ± 0.001	2.115 ± 0.359	$<1.0\cdot10^{-3}$	0.025 ± 0.010
Montagne 1	0.046 ± 0.003	$<5.0\cdot10^{-1}$	$<1.0\cdot10^{-3}$	0.195 ± 0.040
Montagne 2	0.109 ± 0.005	1.9 ± 0.2	0.003 ± 0.001	0.066 ± 0.014
Ours	$<2.5\cdot10^{-3}$	2.621 ± 0.454	$<1.0\cdot10^{-3}$	$<1.0\cdot10^{-2}$
Par	$<2.5\cdot10^{-3}$	-	$<1.0\cdot10^{-3}$	$<1.0\cdot10^{-2}$
Poix	0.040 ± 0.002	-	$<1.0\cdot10^{-3}$	0.118 ± 0.025
Rocs Bleus	$<2.5\cdot10^{-3}$	-	$<1.0\cdot10^{-3}$	$<1.0\cdot10^{-2}$
Sail	0.007 ± 0.001	0.472 ± 0.307	$<1.0\cdot10^{-3}$	$<1.0\cdot10^{-2}$
Saladis	$<2.5\cdot10^{-3}$	2.013 ± 0.681	$<1.0\cdot10^{-3}$	$<1.0\cdot10^{-2}$
Salins	0.196 ± 0.009	0.736 ± 0.392	$<1.0\cdot10^{-3}$	0.392 ± 0.050
Salut	$<2.5\cdot10^{-3}$	-	$<1.0\cdot10^{-3}$	$<1.0\cdot10^{-2}$
Saulcée	0.084 ± 0.005	1.438 ± 0.549	$<1.0\cdot10^{-3}$	0.168 ± 0.025
Tennis	0.003 ± 0.001	3.338 ± 0.421	$<1.0\cdot10^{-3}$	$<1.0\cdot10^{-2}$
Tête de lion	0.003 ± 0.001	-	$<1.0\cdot10^{-3}$	$<1.0\cdot10^{-2}$
Trois sauts	0.006 ± 0.001	-	$<1.0\cdot10^{-3}$	$<1.0\cdot10^{-2}$

Annotation: "-": absence of measurement

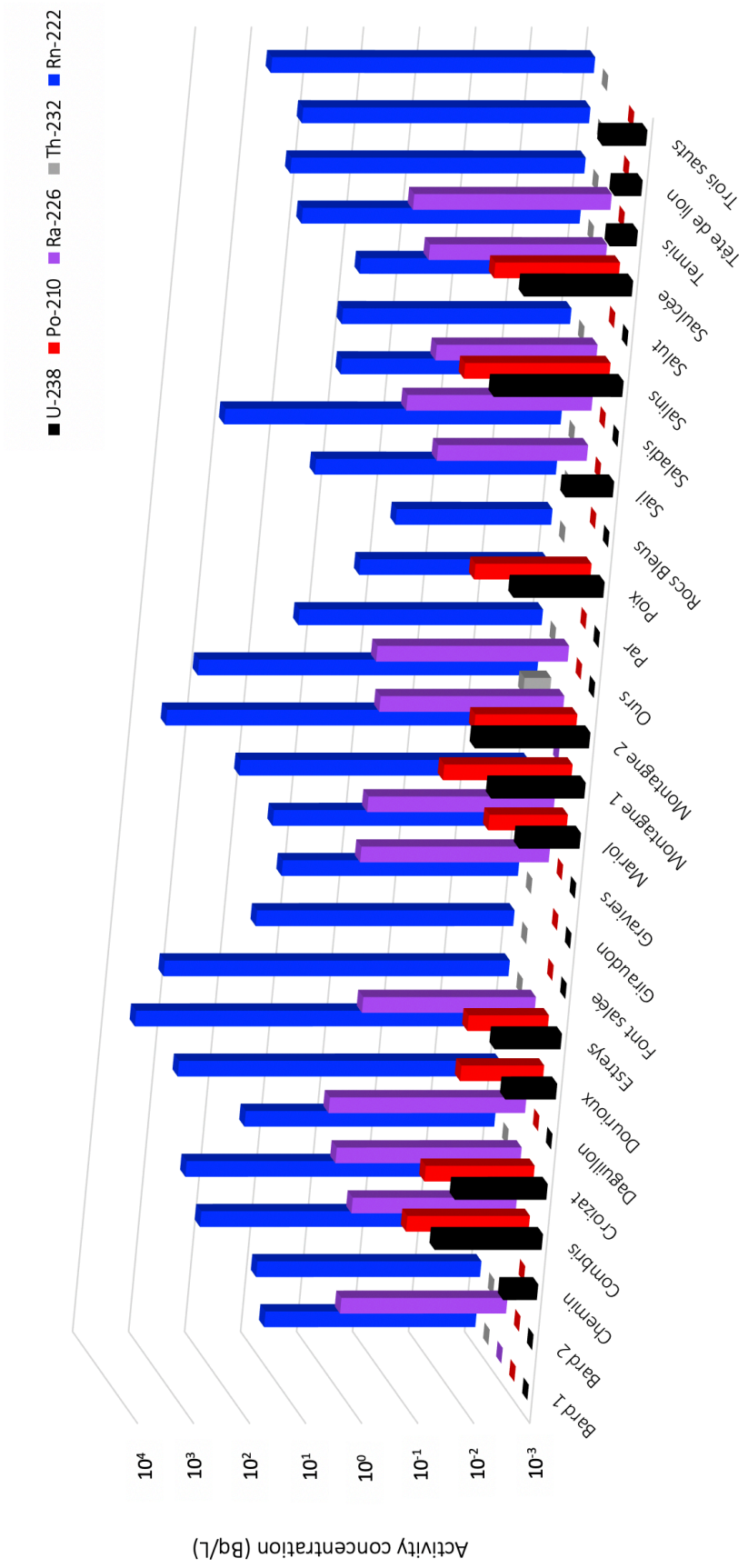

Figure 2.13 Activity concentrations of radionuclides in water in 26 Auvergne mineral springs. Black: ^{238}U, Red: ^{210}Po, Magenta: ^{226}Ra, Grey: ^{232}Th, Blue: ^{222}Rn

2.3 Radiological characterization of sediments

The sediment samples were analyzed in SUBATECH laboratory by means of γ-spectrometry. The samples were sieved to remove parts greater than 2 mm, dried at 105 °C for at least 24 h until constant mass, and finally sealed. By weighting the sediment sample before and after the drying process, the environmental medium was estimated to be a mixture composed by 90% water and 10% dry sediments.

A coaxial HPGe detector of 45% relative efficiency coupled with LabSOCS© calibration software was used for the analyses. The minimum counting time was 28800 s. Efficiency calibration was performed for each sample considering its density, mass and geometry, and a detection limit was attributed to each measurement.

The measurements of ^{226}Ra mass activities were performed at least 4 weeks after the sealing to allow for the secular equilibrium between ^{226}Ra ($t_{1/2}$=1600 y) and ^{222}Rn ($t_{1/2}$=3.82 d), as well as its daughters (^{214}Bi - $t_{1/2}$=19.9 min, ^{214}Pb - $t_{1/2}$=27.06 min). The 352 keV γ-energy peak of ^{214}Pb was used for [^{226}Ra] calculations.

In order to measure the ^{238}U mass activity, the 63 keV of ^{234}Th and 1001 keV of ^{234m}Pa were used. The rest of the radionuclides were quantified by their own γ-peaks as follows: 143 keV of ^{235}U, 46.5 keV of ^{210}Pb, 911 keV of ^{228}Ac, 609 keV of ^{214}Bi and 238 keV of ^{212}Pb.

The results (in kBq/kg) are documented in two tables according to the decay series they belong to: Table 2.8 shows the mass activities of ^{238}U daughter nuclei while in Table 2.9 the results for ^{232}Th daughter nuclei and ^{235}U are presented. Samples were not collected (NS) in Bard 1, Croizat and Par (insufficient quantity of sediments). When values are below the detection limit (DL), the value of DL is provided instead (denoted, for example, as "$< 2.7 \cdot 10^{-1}$"). ^{234m}Pa was not detectable in any spring. As a result, the values of [^{238}U] identify with those of [^{234}Th] (available only for Dourioux and Salins). ^{235}U was also not quantified in any spring.

The measured mass activities vary up to 2 orders of magnitude among the different radionuclides. In the ^{238}U decay series, the mass activity of the least energetic β-emitter (^{210}Pb, Ee^{-}_{max} = 0.0635 MeV) is in the range of [0.02, 8.05] kBq/kg. The corresponding range for the most energetic β-emitter (^{214}Bi, Ee^{-}_{max} = 3.3 MeV) is [0.03, 50.25] kBq/kg. Respectively, the range is 0.03 kBq/kg ≤[^{214}Pb] ≤ 52.13 kBq/kg for ^{214}Pb (Ee^{-}_{max} = 1.018 MeV). The same range applies to ^{226}Ra α-emitter as it is at secular equilibrium with ^{214}Pb. The lowest values were measured in Poix while the highest ones were

measured in Ours. ^{238}U mass activities were measured only in two springs: 0.26 ± 0.07 kBq/kg in Dourioux and 0.30 ± 0.10 kBq/kg in Salins.

Table 2.8 Sediments mass activities (kBq/kg) from ^{238}U decay series

	Mass Activity (kBq / kg)						
Spring	^{238}U	^{234}Th	^{234}mPa	^{226}Ra	^{214}Pb	^{214}Bi	^{210}Pb
Bard 1	NS	NS	NS	NS	NS	NS	NS
Bard 2	$<2.7\cdot10^{-1}$	$<2.7\cdot10^{-1}$	<2.8	2.19 ± 0.27	2.19 ± 0.27	2.04 ± 0.18	1.25 ± 0.37
Chemin	$<3.6\cdot10^{-1}$	$<3.6\cdot10^{-1}$	<6.2	10.78 ± 1.30	10.78 ± 1.30	10.52 ± 0.85	0.32 ± 0.12
Combris	$<2.5\cdot10^{-1}$	$<2.5\cdot10^{-1}$	<2.4	3.86 ± 0.47	3.86 ± 0.47	3.77 ± 0.31	2.34 ± 0.67
Croizat	NS	NS	NS	NS	NS	NS	NS
Daguillon	$<3.1\cdot10^{-1}$	$<3.1\cdot10^{-1}$	<2.7	22.99 ± 2.76	22.99 ± 2.76	22.22 ± 1.70	3.55 ± 1.02
Dourioux	0.26 ± 0.07	0.26 ± 0.07	$<9.9\cdot10^{-1}$	0.60 ± 0.08	0.60 ± 0.08	0.56 ± 0.05	1.44 ± 0.41
Estreys	$<8.6\cdot10^{-2}$	$<8.6\cdot10^{-2}$	<1.1	1.94 ± 0.23	1.94 ± 0.23	1.90 ± 0.16	0.65 ± 0.19
Font salée	$<1.1\cdot10^{-1}$	$<1.1\cdot10^{-1}$	<1.0	0.67 ± 0.08	0.67 ± 0.08	0.64 ± 0.06	0.26 ± 0.09
Giraudon	$<2.4\cdot10^{-1}$	$<2.4\cdot10^{-1}$	<1.9	4.17 ± 0.50	4.17 ± 0.50	4.04 ± 0.33	$<2.1\cdot10^{-1}$
Graviers	$<4.4\cdot10^{-1}$	$<4.4\cdot10^{-1}$	<3.8	26.73 ± 3.21	26.73 ± 3.21	25.75 ± 2.08	3.15 ± 0.90
Mariol	$<1.1\cdot10^{-1}$	$<1.1\cdot10^{-1}$	<3.3	19.58 ± 2.35	19.58 ± 2.35	18.73 ± 1.51	3.74 ± 1.07
Montagne 1	$<2.7\cdot10^{-1}$	$<2.7\cdot10^{-1}$	<2.7	8.61 ± 1.04	8.61 ± 1.04	8.25 ± 0.67	8.06 ± 2.29
Montagne 2	$<1.7\cdot10^{-1}$	$<1.7\cdot10^{-1}$	<1.5	5.97 ± 0.72	5.97 ± 0.72	5.68 ± 0.46	1.54 ± 0.45
Ours	$<4.8\cdot10^{-1}$	$<4.8\cdot10^{-1}$	<3.7	52.13 ± 6.26	52.13 ± 6.26	50.25 ± 4.05	0.90 ± 0.27
Par	NS	NS	NS	NS	NS	NS	NS
Poix	$<7.6\cdot10^{-3}$	$<7.6\cdot10^{-3}$	$<1.2\cdot10^{-1}$	0.03 ± 0.01	0.03 ± 0.01	0.03 ± 0.01	0.02 ± 0.01
Rocs Bleus	$<8.6\cdot10^{-2}$	$<8.6\cdot10^{-2}$	<1.1	0.56 ± 0.07	0.56 ± 0.07	0.54 ± 0.05	0.20 ± 0.07
Sail	$<7.7\cdot10^{-2}$	$<7.7\cdot10^{-2}$	<1.1	0.84 ± 0.10	0.84 ± 0.10	0.81 ± 0.07	0.93 ± 0.27
Saladis	$<7.5\cdot10^{-2}$	$<7.5\cdot10^{-2}$	$<7.5\cdot10^{-1}$	1.19 ± 0.14	1.19 ± 0.14	1.14 ± 0.09	0.85 ± 0.25
Salins	0.30 ± 0.10	0.30 ± 0.10	<2.0	0.75 ± 0.10	0.75 ± 0.10	0.68 ± 0.07	$<1.5\cdot10^{-1}$
Salut	$<3.8\cdot10^{-1}$	$<3.8\cdot10^{-1}$	<3.6	9.51 ± 1.15	9.51 ± 1.15	9.22 ± 0.75	$<3.0\cdot10^{-1}$
Saulcée	$<3.6\cdot10^{-1}$	$<3.6\cdot10^{-1}$	<3.1	19.27 ± 2.31	19.27 ± 2.31	18.63 ± 1.50	1.15 ± 0.36
Tennis	$<2.8\cdot10^{-1}$	$<2.8\cdot10^{-1}$	<2.3	21.64 ± 2.60	21.64 ± 2.60	20.73 ± 1.67	0.26 ± 0.13
Tête de lion	$<3.3\cdot10^{-1}$	$<3.3\cdot10^{-1}$	<2.9	15.87 ± 1.91	15.87 ± 1.91	15.46 ± 1.25	0.85 ± 0.25
Trois sauts	$<2.0\cdot10^{-1}$	$<2.0\cdot10^{-1}$	<2.1	2.08 ± 0.26	2.08 ± 0.26	2.02 ± 0.17	2.94 ± 0.85

Annotation: “NS”: no sample

Table 2.9 Sediments mass activities (kBq/kg) from ^{232}Th and ^{235}U decay series

	^{232}Th **series**		^{235}U **series**
	Mass Activity (kBq / kg)		
Spring	^{228}Ac	^{212}Pb	^{235}U
Bard 1	NS	NS	NS
Bard 2	0.67 ± 0.10	1.10 ± 0.14	$<1.1\cdot10^{-1}$
Chemin	26.16 ± 2.67	11.87 ± 1.45	$<2.3\cdot10^{-1}$
Combris	4.64 ± 0.49	0.97 ± 0.12	$<1.0\cdot10^{-1}$
Croizat	NS	NS	NS
Daguillon	4.65 ± 0.48	3.38 ± 0.41	$<1.1\cdot10^{-1}$
Dourioux	0.11 ± 0.04	0.09 ± 0.01	$<3.6\cdot10^{-2}$
Estreys	$<4.5\cdot10^{-2}$	0.04 ± 0.01	$<4.2\cdot10^{-2}$
Font salée	0.23 ± 0.03	0.19 ± 0.02	$<3.9\cdot10^{-2}$
Giraudon	5.96 ± 0.62	1.24 ± 0.15	$<9.1\cdot10^{-2}$
Graviers	17.97 ± 1.84	9.77 ± 1.19	$<1.6\cdot10^{-1}$
Mariol	15.86 ± 1.62	4.07 ± 0.50	$<1.4\cdot10^{-1}$
Montagne 1	0.84 ± 0.11	0.56 ± 0.07	$<1.0\cdot10^{-1}$
Montagne 2	0.79 ± 0.09	0.46 ± 0.06	$<6.2\cdot10^{-2}$
Ours	28.77 ± 2.94	5.47 ± 0.67	$<1.8\cdot10^{-1}$
Par	NS	NS	NS
Poix	$<4.1\cdot10^{-3}$	$<1.4\cdot10^{-3}$	$<4.2\cdot10^{-3}$
Rocs Bleus	0.09 ± 0.02	0.06 ± 0.01	$<3.5\cdot10^{-2}$
Sail	$<4.3\cdot10^{-2}$	0.03 ± 0.01	$<3.8\cdot10^{-2}$
Saladis	0.12 ± 0.02	0.05 ± 0.01	$<2.9\cdot10^{-2}$
Salins	0.45 ± 0.07	0.10 ± 0.02	$<7.3\cdot10^{-2}$
Salut	12.83 ± 1.22	2.91 ± 0.36	$<1.4\cdot10^{-1}$
Saulcée	11.70 ± 1.20	8.63 ± 1.06	$<1.3\cdot10^{-1}$
Tennis	11.92 ± 1.22	3.81 ± 0.47	$<9.6\cdot10^{-2}$
Tête de lion	12.92 ± 1.32	5.84 ± 0.71	$<1.2\cdot10^{-1}$
Trois sauts	1.14 ± 0.13	0.66 ± 0.08	$<7.9\cdot10^{-2}$

Annotation: “NS”: no sample

In the ^{232}Th decay series, the mass activities of two β-emitters are provided. For ^{228}Ac (Ee^{-}_{max} = 2.134 MeV), the values extend between 0.09 ± 0.02 kBq/kg (Rocs Bleus) and 26.16 ± 2.67 kBq/kg (Chemin). Considering a secular equilibrium between ^{228}Ra (β-emitter, $t_{1/2}$ = 5.75 y, Ee^{-}_{max} = 0.046 MeV) and ^{228}Ac ($t_{1/2}$ = 6.15 h), [^{228}Ac] can be equated to

[^{228}Ra]. The respective minimum and maximum mass activities for ^{212}Pb (Ee^{-}_{max} = 0.569 MeV) are 0.03 ± 0.01 kBq/kg in Sail and 11.87 ± 1.45 kBq/kg in Chemin.

In Fig 2.14, the mass activities of the radionuclides in the sediments are summarized. ^{238}U and ^{234}Th, as well as ^{226}Ra and ^{214}Pb, are plotted together. ^{234m}Pa and ^{235}U are not shown since they did not pass the detection limit threshold in any location. The absence of samples is denoted by the absence of values (Bard 1, Croizat, Par).

Among the α-emitters (^{238}U, ^{226}Ra), the predominance of ^{226}Ra is remarked, as well as, the significant difference between the highest ^{226}Ra mass activity (52.13 kBq/kg - Ours) and the highest ^{238}U mass activity (0.30 kBq/kg - Salins). Except in Dourioux and Salins, ^{238}U activity was below the detection threshold. Among the β-emitters (^{234}Th, ^{210}Pb, ^{228}Ac, ^{212}Pb, ^{214}Pb, ^{214}Bi), the predominance of ^{214}Pb and ^{214}Bi is highlighted since they are in secular equilibrium with ^{226}Ra, followed by accountable mass activities of ^{228}Ac in Chemin and Ours.

In Montagne 1, [^{226}Ra] is 30% higher (8.61 ± 1.04 kBq/kg) than in Montagne 2 (5.97 ± 0.72 kBq/kg). Still, the mass activities of all the radionuclides in the sediments are much lower in both Montagne locations than in Mariol. The respective [^{226}Ra] for the latter is 19.58 ± 2.35 kBq/kg, while the greatest difference is highlighted for [^{228}Ac]: 15.85 ± 1.62 kBq/kg was measured in Mariol, while 0.84 ± 0.11 kBq/kg and 0.79 kBq/kg were measured in Montagne 1 and Montagne 2, respectively.

It is remarked that the mass (or specific) activity is defined as the quotient of the activity over the mass of the sample. Nevertheless, the mass activities will be referred to as "activity concentrations" onwards in the text for simplification.

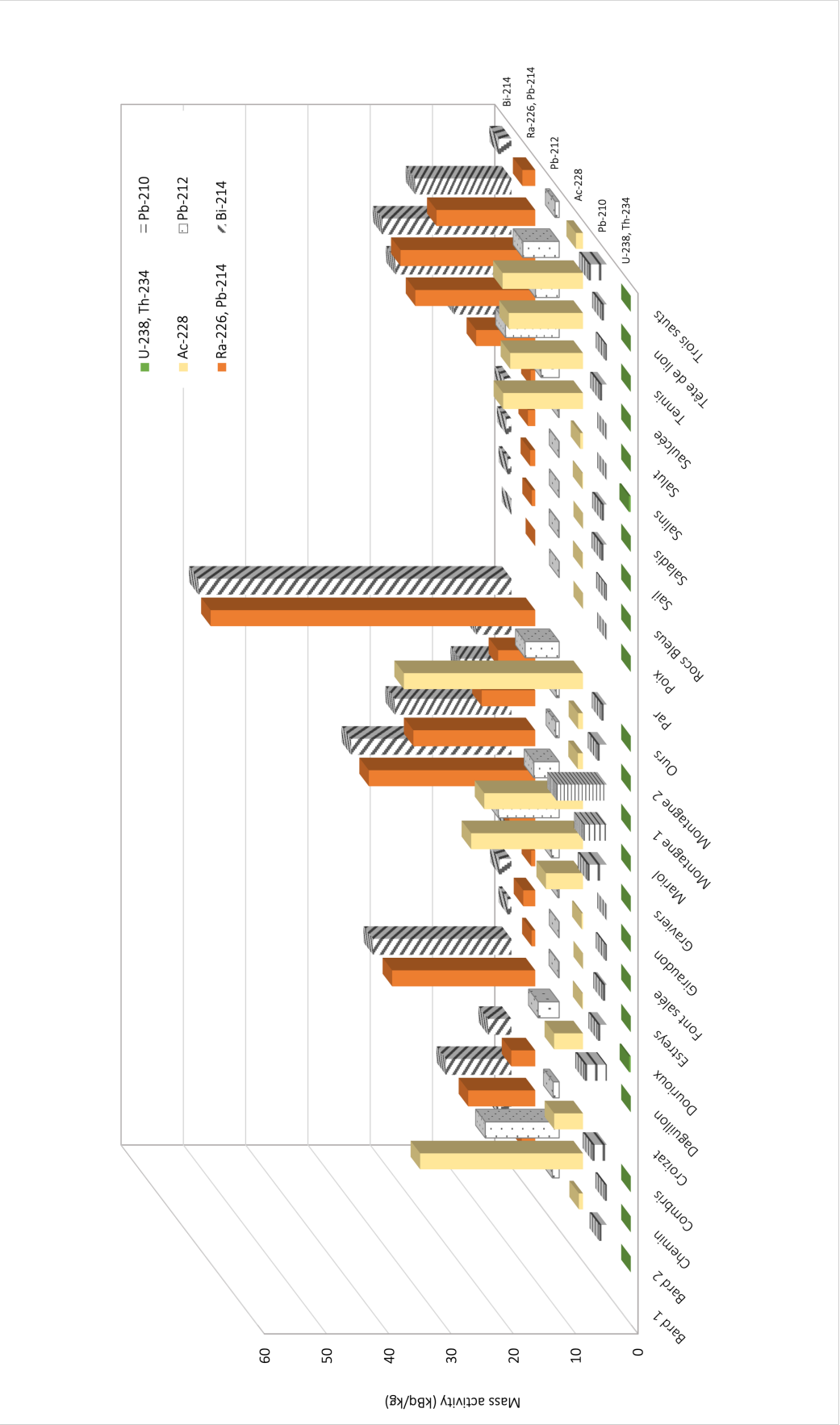

Figure 2.14 Mass activities of radionuclides in sediments in 26 Auvergne mineral springs

2.4 Physical and chemical characteristics

Distribution coefficients in mineral springs

The distribution coefficient K_d is generally defined as the concentration of a chemical species on the solid fraction divided by the concentration in the aqueous phase, assuming a thermodynamic equilibrium between dissolved and particulate phases. In the case of radionuclides, K_d (Eq. 2.9) can be defined as the quotient of the activity concentration per unit mass of sediment (C_{sed}) to the activity concentration per unit mass (or volume) of water (C_{wtr}), assuming respectively, that the exchanges of radionuclides between particles and water are wholly reversible [19, 225]. As deduced from Eq. 2.9, by using K_d , the activity concentration of a radionuclide in water can be determined if its activity concentration in sediments is known and vice versa.

$$K_d = \frac{C_{sed}}{C_{wtr}} \tag{2.9}$$

with: K_d (Bq/L): distribution coefficient

C_{sed} (Bq/kg): sediments activity concentration per unit mass

C_{wtr} (Bq/L): water activity concentration per unit volume

Expressing the mobility of chemical elements between solid and aquatic phases, K_d depends on the sediment type and water chemistry [226]. K_d calculations take into consideration dissolution, precipitation, adsorption and desorption processes. For example, ^{222}Rn K_d cannot be calculated because it migrates as a dissolved gas and all the aforementioned processes are absent [227].

Distribution coefficients are of high importance for understanding the behaviour of radionuclides in environments where solid and aquatic phases are mixed. Their mobility affects, among others, the uptake of the biota and consequenthly the radiation exposure of the biota. Although their behaviour is affected by their chemical form which is out of the context of the current work, K_d is widely used for dosimetric calculations based on the ICRP approach [228, 229].

Moreover, distribution coefficients have been extensively calculated, either in the field or under laboratory conditions, for two main environmental categories: marine and freshwater ecosystems. The latter include lakes and rivers with no specific literature for mineral springs. K_d values are of high interest for both natural and man-made radiosotopes [225, 230, 231].

In an effort to provide an estimation of the distribution coefficients in the

mineral springs, the measured activity concentrations of this work were used to calculate the K_d as the ratio indicated in Eq. 2.9. This simplified approach was also recently applied in marine K_d calculations using IAEA MARIS (Marine Radioactivity Information System) database [232, 233]. Scrutinised K_d calculations taking into consideration the chemistry of the environment are a field of expertise themselves [226, 227, 234–236].

Data for both water and sediment activity concentrations of the same radionuclide are available only for ^{226}Ra in 13 locations and for ^{238}U in 2 locations as indicated in Tables 2.3–2.4 and Tables 2.8–2.9. The calculated K_d values for ^{226}Ra are summarized in Table 2.10 and are graphically represented in Fig. 2.15. For ^{238}U, the respective values of K_d are 32500 ± 9647 L/kg in Dourioux and 1530 ± 515 L/kg in Salins. For the calculation of the K_d uncertainties, Eq. 2.10 was applied.

$$\frac{\delta K_d}{K_d} = \sqrt{\left(\frac{\delta C_{sed}}{C_{sed}}\right)^2 + \left(\frac{\delta C_{wtr}}{C_{wtr}}\right)^2} \tag{2.10}$$

with:

K_d (L/kg): distribution coefficient

δK_d (L/kg): uncertainty of K_d

C_{sed} (Bq/kg): sediments activity concentration per unit mass

δC_{sed} (Bq/kg): uncertainty of C_{sed} measurement

C_{wtr} (Bq/L): water activity concentration per unit volume

δC_{wtr} (Bq/L): uncertainty of C_{wtr} measurement

K_d values vary up to 2 orders of magnitude among the mineral springs, ranging between 591 L/kg in Saladis and almost 20000 L/kg in Ours for ^{226}Ra. With no respective literature for mineral springs to compare the results of the current study to, some available data for rivers, lake and marine environments are presented here.

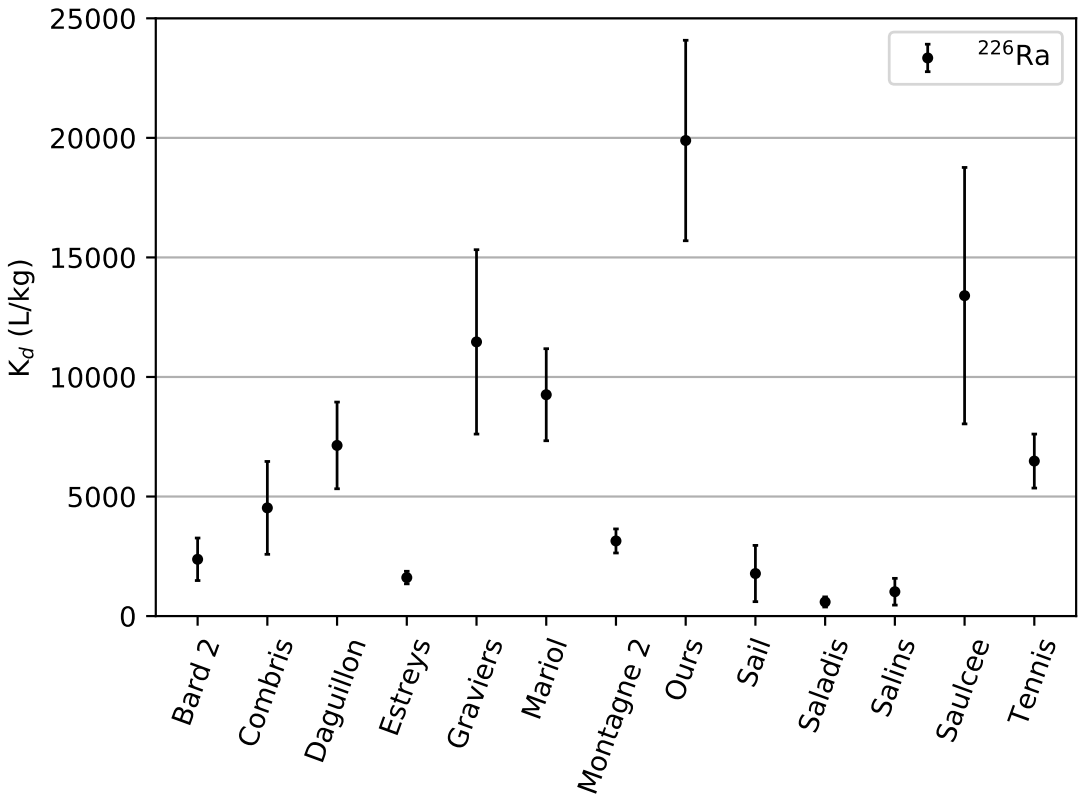

Figure 2.15 Distribution coefficient (K_d) for ^{226}Ra in Auvergne mineral springs

Table 2.10 ^{226}Ra Distribution coefficients (K_d)

Spring	**K_d (L/kg)**
Bard 2	2375 ± 889
Combris	4525 ± 1942
Daguillon	7138 ± 1813
Estreys	1611 ± 263
Graviers	11467 ± 3855
Mariol	9258 ± 1925
Montagne 2	3142 ± 503
Ours	19889 ± 4192
Sail	1780 ± 1178
Saladis	591 ± 212
Salins	1019 ± 559
Saulcée	13401 ± 5362
Tennis	6483 ± 1129

Beginning with the two calculated values for ^{238}U (32500 L/kg in Dourioux and 1530 L/kg in Salins), it was found out that respective calculations were performed near uranium mining sites by Ivanova et al. who computed ^{238}U K_d values varying from 4 L/kg to 1700 L/kg [237]. In a study using a similar calculation approach, ^{238}U K_d values ranged between 500 L/kg and 1400 L/kg [238], while ^{238}U distribution coefficients calculated using water and soil samples in the vicinity of Fukushima Daiichi Nuclear Power Plant ranged between 1000 L/kg and 10000 L/kg [239]. IAEA (International Atomic Energy Agency) recommends K_d = 500 L/kg for open ocean, K_d = 1000 L/kg for coastal environments and provides a range between 20 L/kg and 1000 L/kg for freshwater ecosystems (lakes and rivers) [225, 228]. A general overview shows that the range of ^{238}U distribution coefficients is [<1, $1 \cdot 10^6$] L/kg depending on the pH of the environment under study, showing, thus, how much site-specific K_d values are [225, 227, 230].

A respective overview performed by US EPA (United States Environmental Protection Agency) for ^{226}Ra distribution coefficients concluded that "in the absence of definitive maximum and minimum K_d values for Radium as a function of the key parameters, such as pH, it is suggested that K_d values measured for Radium at site-specific conditions are essential" [240]. In the same report, K_d values for ^{226}Ra exhibit a variation between 10 L/kg to $1 \cdot 10^6$ L/kg depending on the soil type. IAEA recommends K_d = 4000 L/kg for open ocean, K_d = 2000 L/kg for coastal environments and provides a range between 1100 L/kg and 52000 L/kg for freshwater ecosystems (lakes and rivers) [225, 228].

The current work calculations showed significant K_d fluctuations among the mineral springs as it is the case for any other aquatic environment. The existing literature for rivers, lakes and marine environments suggesting mean K_d values is based on multiple independent studies. In the case of the current study, since a very limited number of data is available, extracting a mean value for the mineral springs in Auvergne was not attempted.

Elemental composition of dry sediments and granulometric profiles

ED-XRF analysis (Energy Dispersive X-Ray Fluorescence) was performed for the determination of the mass fraction of the mean elemental composition of the sampled sediments (Table 2.11) using a Niton XL5 analyzer (Thermo Fisher Scientific Inc., Waltham, USA) . XRF is an analytical, non-destructive method used to determine the elemental composition of materials. It is based

on the detection of the discrete, characteristic X-rays emitted by each element following its X-Ray irradiation.

On average, Carbon (C), Oxygen (O), Calcium (Ca) and Silicon (Si) accounted for approximately 95% of the mass fraction with the rest consisting of heavier metals such as Iron (Fe), Aluminum (Al), Potassium (K), Magnesium (Mg), Strontium (Sr) and Titanium (Ti), and a smaller contribution of Chlorine (Cl), Sulfur (S) and Phosphorus (P).

Laser granulometry was also performed on dry sediment samples from Montagne 1 and Mariol. The results showed that Mariol sediments are composed by fine grains (grain size: 17 μm), while the sediments in Montagne 1 are a mixture of small and big grains (grain sizes: 162 μm, 550 μm). These different granulometric profiles indicate the varying structural composition of the sampling sites.

Table 2.11 Dry sediments composition using X-Ray fluorescence analysis

Element	**%**	**Element**	**%**
C & O	60.36	K	0.70
Ca	24.50	Mg	0.53
Si	10.00	Sr	0.50
Fe	1.60	Ti	0.30
Cl	1.40	S	0.30
Al	1.00	P	0.08

Physicochemical properties

The physical and chemical properties of the under study mineral springs were recorded in several campaigns by the biologists [50, 53, 57]. The water temperature, pH and conductivity values along with the bicarbonate (HCO_3^-) concentrations and the percentage of Dissolved Oxygen (DO) are summarized in Table 2.12. These factors, associated with diatoms communities structure, provide among others an overview of the ecosystems acidity and mineralization. The water temperature, conductivity and pH were measured with a WTW probe FC 340i (VWR International, USA). A Hatch carbonate kit was used for HCO_3^- concentrations, while the dissolved oxygen was measured using a Ysi ProODO probe (Yellow Springs Instruments, USA).

Table 2.12 Main water physicochemical properties

Spring	T (°C)	pH	Conductivity (μS/cm)	HCO_3^- (mg/L)	DO (%)	Reference
Bard 1	15.1	6.8	6560	2960	3.5	[57]
Bard 2	14.7	6.8	6380	3010	3.1	[57]
Chemin	-	-	-	-	-	-
Croizat	36.4	6.5	11830	1790	14.2	[57]
Daguillon	13.9	6.6	4030	2140	29.0	[57]
Dourioux	10.7	6.7	255	85	10.1	[57]
Estreys	16.0	6.4	3480	1190	16.4	[57]
Font salee	9.9	6.5	1139	640	4.6	[57]
Giraudon	32.1	7.5	9201	2814	54.0	[53]
Graviers	14.4	6.7	5430	2730	19.5	[57]
Mariol	17.4	6.4	811	442	4.3	[57]
Montagne 1	10.2	6.5	1343	445	6.6	[57]
Montagne 2	9.9	6.6	1625	865	5.4	[57]
Ours	13.7	6.7	5490	2650	13.8	[57]
Par	79.8	6.9	1366	610	-	[50]
Poix	10.6	7.2	123200	4290	6.3	[52]
Rocs bleus	19.2	7.0	8150	2696	9.3	[53]
Sail	16.6	7.0	5390	1150	9.2	[53]
Saladis	16.1	7.8	9680	2928	88.6	[53]
Salins	13.3	6.8	3090	1950	20.1	[57]
Salut	12.1	6.5	5850	2740	11.7	[57]
Saulcee	14.4	6.7	3420	1412	26.0	[57]
Tennis	27.1	7.0	8380	2778	8.9	[57]
Tete de lion	14.4	7.0	4200	2454	18.9	[57]
Trois sauts	13.1	6.7	3890	1940	12.8	[57]

DO: Dissolved Oxygen

The lowest water temperature was measured at Font Salee and Montagne 2 (9.9 °C), while the highest one at Par (79.8 °C). Temperatures higher than 19 °C were recorded in Rocs bleus (19.2 °C), Tennis (27.1 °C), Giraudon (32.1 °C) and Croizat (36.4 °C). In the rest of the springs, the recorded temperatures varied between 10.2 °C (Montagne 1) and 17.4 °C (Mariol).

Excluding the least and most mineralized ones (Estreys with 255 μS/cm and Poix with 123200 μS/cm), the conductivity range for the rest of the mineral

springs was (800, 12000) µS/cm. The most acidic spring is Mariol (pH = 6.4), while Giraudon, Poix and Saladis can be characterized as basic (pH = 7.5 , 7.2 and 7.8 respectively). The rest of the locations exhibit slightly acidic to neutral behaviour (pH = [6.5, 7]).

The bicarbonate concentrations varied between 85 mg/L in Dourioux and 4290 mg/L in Poix. In terms of oxygen levels, at least 10 locations were poorly oxygenated (DO < 10%: Bard, Font Salee, Mariol, Montagne, Ours, Poix, Rocs bleus, Sail and Tennis). Saladis had 89% dissolved oxygen and the rest of the springs varied between 10% and 20%.

2.5 Characterization of local diatoms communities

Diatoms from the 26 under-study mineral springs were collected and studied by the biologists. Benthic diatom species inhabit rocks or sediments of the springs floor but they can also be found in the water column.

Small samples of epipelic and epilithic raw material were prepared for Light Microscopy (LM) observations, morphometric measurements and evaluation of the relative abundance of diatom species at LMGE (Laboratoire Microorganismes: Génome Environnement). Diatoms were imaged using an ultra high-resolution analytical field emission Scanning Electron Microscope (SEM) Hitachi SU-70 (Hitachi High-Technologies Corporation, Japan). SEM images revealed various abnormal forms of diatoms and information concerning their dimensions were used to build a model for the simulation purpose. Ellipsoidal dimensions of individuals varied from 5 µm to 50 µm for the major axis and from 4 µm to 7 µm for the minor axis.

Among the most common species present in the radioactive mineral springs of Auvergne, *Planothidium frequentissimum*, *Navicula sanctamargaritae* and *Crenotia thermalis* (Figure 2.16) exceed an abundance of 60% in some locations [51,55,122].

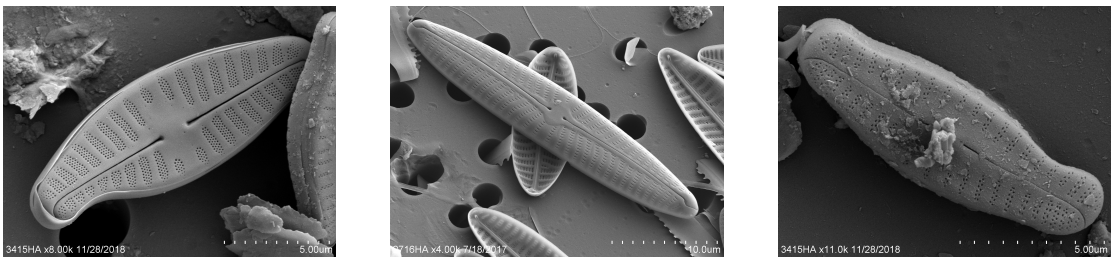

(a) *P. frequentissimum* **(b)** *N. sanctamargaritae* **(c)** *C. thermalis*

Figure 2.16 Abundant diatom species in the Auvergne mineral springs

The same species are observed at Montagne where deformation rates above 25 %, denoted by abnormally shaped frustules, were observed on *Planothidium frequentissimum* [62]. In another study conducted among 58 species identified in 17 local mineral springs, deformation rates were 1% in Tennis and 3% in Rocs Bleus and Saladis [51].

Genomics information for diatoms living in Auvergne mineral springs is currently missing. Indeed, only ten out of the 200 000 currently known diatom species have been completely sequenced up to day, revealing a range in DNA size between 27 and 162 Mbp preserved in 1–2 μm diameter nuclei [93, 241].

Conclusion

In this chapter, the experimental data coming from the analysis of water, sediment and diatom samples collected in 26 mineral springs in Auvergne, France were presented. Positive correlations between ^{222}Rn activity concentrations in water and ambient dose rates at the water surface level and 1 m above it, were calculated. The evaluation of [^{222}Rn] variations in Montagne 1 showed that the observed fluctuating behaviour can be possibly attributed to the peculiarity of the sampling site.

In water, ^{222}Rn activity concentrations ranged between 0.6 Bq/L and 4600.0 Bq/L. The mineral springs were classified according to their [^{222}Rn] (see Fig. 2.17). In 5 out of the 26 springs, the ^{222}Rn activity concentration was above 1000 Bq/L (*High level*).

^{222}Rn is the predominant radionuclide in the waters of the mineral springs since its activity concentrations are 4–6 orders of magnitude higher than the rest of the radionuclides. Small contributions of ^{210}Po and ^{238}U were detected in some locations, while ^{232}Th was above the detection limit only in one mineral spring (Montagne 2). [^{226}Ra] in water ranged between 0.7 Bq/L and 3.4 Bq/L.

In the dry sediments, ^{226}Ra mass activities ranged between 0.03 kBq/kg and 52.13 kBq/kg, making it the predominant radionuclide among the α-emitters. ^{238}U was above the detection limit in only two mineral springs (Dourioux and Salins).

Distribution coefficients were calculated for ^{226}Ra and ^{238}U. The calculations showed significant K_d fluctuations among the different locations, varying up to two orders of magnitude. More specifically, Ra K_d ranged between 591 L/kg in Saladis and almost 20000 L/kg in Ours.

Among the sampled springs, we find the hottest spring in Europe, Par, with 80°C. The rest are characterized by temperatures between 10 °C and 36.4 ° C.

In their majority, the springs are slightly acidic to neutral, and moderately mineralized with the exception of Poix which exhibits a uniquely high value of conductivity: 123 200 μS/cm.

The environment the benthic diatoms inhabit, was evaluated as a mixture composed of 90% water and 10% dry sediments. The latter consists mainly of Carbon and Oxygen, Calcium and Silicon. Ellipsoidal dimensions of diatoms were evaluated between 5 μm and 50 μm for the major axis, and 4 μm to 7 μm for the minor axis.

The experimental results presented in this chapter guide the Monte Carlo simulations for the evaluation of the radiation exposure of microorganisms in radioactive mineral springs presented in the next chapter. The complexity of these ecosystems calls for simplified simulation approaches. Due to the great range of the activity concentration measured experimentally, some Reference Activity Concentrations (RAC) were established for the current studies: [^{222}Rn] = 1000 Bq/L, [^{226}Ra] = 30 kBq/kg, [^{210}Po] = 0.4 Bq/L and [^{238}U] = 0.3 kBq/kg. The RAC for ^{222}Rn and ^{226}Ra stem from their correlation to the high percentage of diatoms deformations observed in the study of Millan et al. [62]. For ^{210}Po and ^{226}Ra, the highest measured activity concentrations were selected as RAC.

In the following chapter (Chapter 3), the mechanistic computation of dose rates to the microorganisms living in naturally radioactive mineral springs is explored.

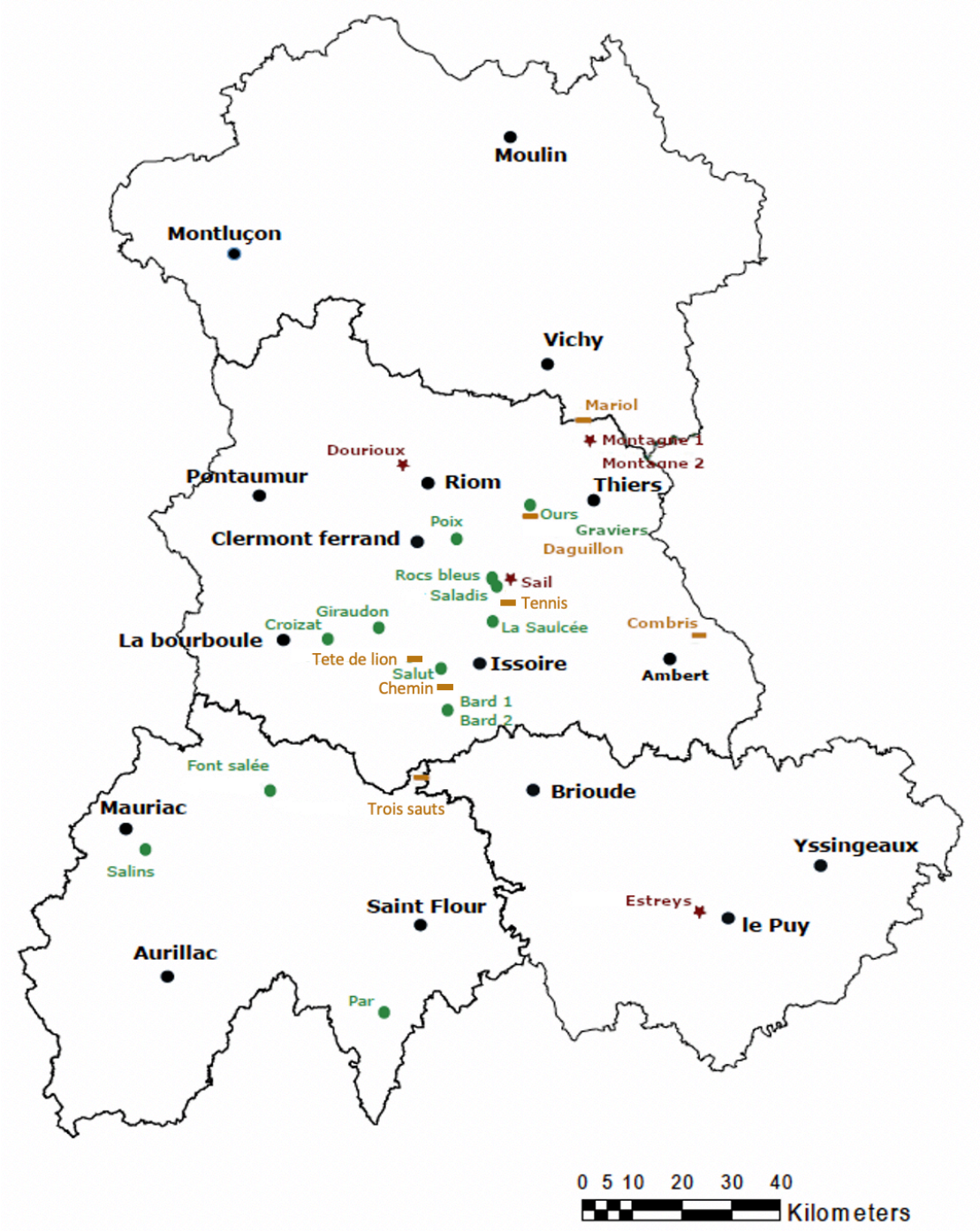

Figure 2.17 Sampled mineral springs in Auvergne classified according to ^{222}Rn activity concentration in water. Green: Low level ([^{222}Rn] < 100 Bq/L), Orange: Medium level (100 Bq/L ≤ [^{222}Rn] < 1000 Bq/L), Red: High level ([^{222}Rn] ≥ 1000 Bq/L).

Chapter 3

Evaluation of dose rates received by microorganisms

Introduction

This chapter is dedicated to the evaluation of the dose rates received by microorganisms living in the ecosystems of naturally radioactive mineral springs. Two distinct dosimetric approaches are possible: the ICRP (International Commission on Radiological Protection) methodology implemented in the current available radioecological tools and Monte Carlo (MC) simulations which allow a more scrutinised dose rate evaluation. An effort to apply both approaches was made using GATE for Monte Carlo simulations and ERICA as a radioecological tool. The studies focused on the predominant α-emitters measured in the environment: ^{222}Rn dissolved in water and ^{226}Ra in the dry sediments. The contribution to the dose rates of ^{210}Po measured in water and ^{238}U in the dry sediments was also evaluated.

The detailed setup of the microdosimetric simulations using GATE is described in section 3.1. Beginning with the microorganisms' external exposure for ^{222}Rn and ^{226}Ra, a comparison among different simulation Physics Lists is presented. Then, an insight to the mechanisms of energy depositions at the microscale is provided. In the following section, the collected dose rates (DR) normalized to Unit Activity Concentrations (UAC - 1 Bq/L for radionuclides measured in water, 1 Bq/kg for radionuclides measured in the dry sediments) and Reference Activity Concentrations (RAC: [^{222}Rn] = 1000 Bq/L, [^{226}Ra] = 30 kBq/kg, [^{210}Po] = 0.4 Bq/L and [^{238}U] = 0.3 kBq/kg) are presented. In the last part of the external exposure results with GATE, the respective impact of the frustule thickness and density on the dose rates was evaluated. The Monte Carlo simulation results are finalised with the internal exposure dose rates presented in section 3.3.

The study performed using ERICA tool is presented in section 3.4. The methodology applied for dose rate calculations in freshwater ecosystems is first described. In section 3.5, the main differences between the two available versions of the tool are highlighted and the respective differences between

the dose rates are explored. Finally, in section 3.6, the internal dose rate calculations using the ICRP approach between ERICA and GATE are explored.

3.1 GATE Simulation setup

Absorbed dose rates to microorganisms have been computed with GATE v9.1 using Geant4 v11.0.0 libraries. The simulation setup is described using macros. The macrofiles contain commands defining the geometry, the materials, the source, the physics lists, the production cuts and the desired outputs (Appendix D). A description of each part is presented in the following subsections. In MC simulations, the tracking of α-particles can be very computationally expensive and thorough consideration was given to the dimensions of the simulated environment, the physics models and the production cuts. The setup of the simulation is summarized in Table 3.3.

Geometry

In the current simulation, the microorganism and its nucleus were modelled as water spheres of 10 μm and 0.5 μm radius respectively. For the modelling of the diatom, a SiO_2 (Silicate) shell of 2 μm thickness was added around the microorganism.

As presented in Chapter 2 (section 2.5), the ellipsoidal dimensions of the local diatom communities range from 5 μm to 50 μm for the major axis, and from 4 μm to 7 μm for the minor axis. The approximation of cell shapes as spherical volumes is well established in microdosimetry though is always investigated. Performing a preliminary simulation, the energy deposited to an ellipsoid water microorganism characterized by 27 μm major axis and 5.5 μm minor axis (mean values of the dimensions of diatoms in the local mineral springs) was compared to a spherical water microorganism characterized by 10 μm radius. It was found out that the energy deposited in the spherical microorganism is on average 10 times higher than in the ellipsoid microorganism, mainly due to their different volumes. This has raised major concerns in internal radiotherapy, especially for β-emitting radionuclides [242, 243].

For the current, the higher values of energy deposition act as a conservative scenario, covering also the great variety of shapes and sizes of diatoms. Nevertheless, when considering the same spherical and ellipsoidal volumes, the difference in the dose rates is less than 10%.

The environment surrounding the microorganism was modelled as a sphere with a radius (r_{env}) calculated according to the empirical Eq. 3.1.

$$r_{env} = (R_{water}^{max} + r_M + F) \times 1.03 \quad (3.1)$$

with:

r_{env} (μm): radius of the simulated spherical environment

R_{water}^{max} (μm): range in water of the most energetic α-particles in the simulation

r_M (μm): radius of the simulated spherical microorganism

F (μm): frustule thickness

1.03: multiplication factor offering an extra 3% space margin

In the current study, the most energetic α-particles in this simulation are those of ^{222}Rn with $E_{\alpha,max}$ = 5.5 MeV corresponding to R_{water}^{max} = 43.44 μm [145]. An OpenGL representation of the GATE modelling is shown in Fig. 3.1.

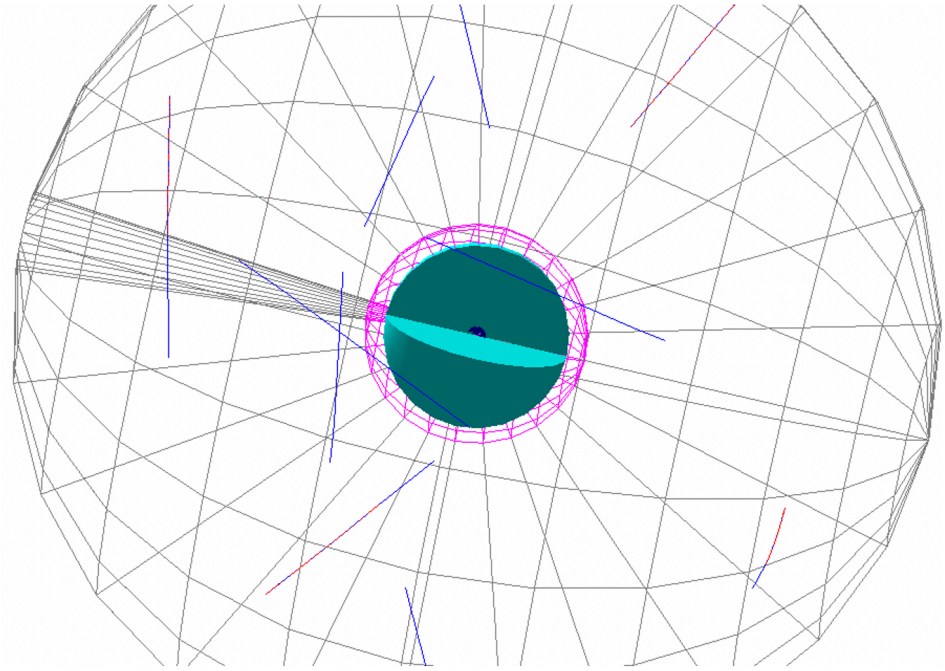

Figure 3.1 OpenGL representation of GATE modelling. From outer to inner shell: environment (grey), frustule (magenta), diatom (green), nucleus (blue). Blue lines represent tracks of α-particles.

Materials

Being the most abundant constituent of cells, liquid water (ρ = 1 g/cm^3) is considered as a surrogate to the biological medium [244, 245] and it is used as the main component of the microorganism (defined as "G4_WATER" NIST material [246]). The rigid shell (frustule) enveloping the water cell in the case of diatom, is composed of silicon dioxide (SiO_2) with a density 2.4 g/cm^3. This composition comes from analysing the literature. The

principal component of frustule is hydrated amorphous silica complemented by organic macromolecules, like proteins and lipids, with densities varying between 0.2 g/cm^3 and 2.5 g/cm^3 [247–250]. In order to evaluate the impact of the frustule on the dose rates received by the microorganism, simulations using modified density values (0.2 g/cm^3 and 1.5 g/cm^3) and various frustule widths (1 μm, 2 μm, 5 μm and 10 μm) were also performed.

The composition of the environment can be either water, dry sediments (Table 2.11) or a homogeneous mixture of water and dry sediments, denoted as "benthic mixture" (BM), excluding thus the grain composition of the dry sediments. A percentage porosity (P), defined in Eq. 3.2, is used to characterize each simulated environment.

$$P = \frac{V_W}{V_{tot}} \times 100 \tag{3.2}$$

with:

P (%): porosity of the environment

V_W (L): water volume

V_{tot} (L): mixture total volume

The study focuses on three porosity values (0%, 90% and 100%) to define the environment. '0%' corresponds to an environment composed only of dry sediments, '100%' of only water (water column), while '90%' porosity refers to the observed conditions at the bottom of the water column where benthic diatoms develop (benthic mixture). According to measurements performed on Auvergne springs, the benthic mixture is typically composed by 90% water and 10% dry sediments, resulting in a density of 1.02 g/cm^3.

Microorganisms living in the water column are exposed to doses corresponding to 100% porosity while the benthic ones, living on the floor of the springs or on rocks, are exposed to the 90% porosity scenario. It is clarified that the dry sediments scenario, corresponding to 0% porosity, does not reflect a relevant environment for diatoms inhabiting mineral springs and it should be considered as an upper limit in this context. However, diatoms have been observed living outside water [251] and some springs dry up during summer seasons. This is the case for Sail spring in Auvergne.

Source

First, ^{222}Rn in water and ^{226}Ra in dry sediments were simulated since their activity concentrations are predominant compared to the rest of the radionuclides measured (Tables 2.3 - 2.4 & 2.7 - 2.9). The simulation was

completed by introducing ^{210}Po measured in water and ^{238}U measured in the dry sediments. Based on the measurements documented in Chapter 2, only the α-particles emitted directly by ^{222}Rn, ^{226}Ra, ^{238}U and ^{210}Po were simulated, without considering their daughter nuclei (Table 3.1).

Before concluding in simulating only α-particles, preliminary simulations were conducted showing that the contribution of β-emitters to the absorbed dose rates could be neglected. In all cases, the contribution of β-emitters to the dose was maximum 0.02% in comparison to the α-emitters. The most and least energetic β-emitting natural radionuclides belong to ^{238}U decay chain: the electrons of ^{214}Bi are characterized by $E_{e^-_{max}}$ = 3.3 MeV with range in water R_{max} = 1.67 cm, while for the ^{210}Pb the respective values are $E_{e^-_{max}}$ = 0.0635 MeV and R_{max} = 68.5 μm. The highest contribution to the dose (0.02%) was recorded for electrons coming from ^{210}Pb.

Table 3.1 Simulated α-particle energies (E_α), intensities and maximum range in water (R^{max}_{water}) for ^{238}U, ^{226}Ra, ^{222}Rn and ^{210}Po [145, 252–255]

Radionuclide	**E_α (MeV)**	**Intensity (%)**	**R^{max}_{water} (μm)**
^{238}U	4.038	$7.80{\cdot}10^{-2}$	28.5
	4.151	21.00	
	4.198	79.00	
^{226}Ra	4.160	$2.70{\cdot}10^{-4}$	35.0
	4.191	$1.00{\cdot}10^{-3}$	
	4.340	$6.50{\cdot}10^{-3}$	
	4.601	6.16	
	4.784	93.84	
^{222}Rn	4.826	$5.00{\cdot}10^{-4}$	43.4
	4.986	$7.80{\cdot}10^{-2}$	
	5.490	99.92	
^{210}Po	4.517	$1.04{\cdot}10^{-3}$	40.5
	5.304	100	

The α-particles were isotropically distributed (4π solid angle) in the spherical volume surrounding the microorganism. Separate simulations were performed for each radionuclide in each environment. For pure dry sediments (0% porosity), ^{226}Ra was the only source of radioactivity, while for pure water (100% porosity) only ^{222}Rn was considered. Both of the radionuclides were present in the benthic mixture (90% porosity). ^{210}Po and ^{238}U were simulated explicitly in the benthic mixture. For the internal exposure, the α-particles of each radionuclide were distributed isotropically

inside the volume of the microorganism composed of water. Fig. 3.2 shows a schematic representation of the distribution of α-particles in the simulated environments. On the left, the random distribution of the α-particles in the environment surrounding the microorganism is depicted. On the right, the α-particles randomly distributed inside the microorganism when simulating the internal exposure is shown. It is remarked that for the internal exposure, the microorganism is modelled as an homogeneous water sphere without the nucleus. The random directions of α-particles emission are highlighted by arrows.

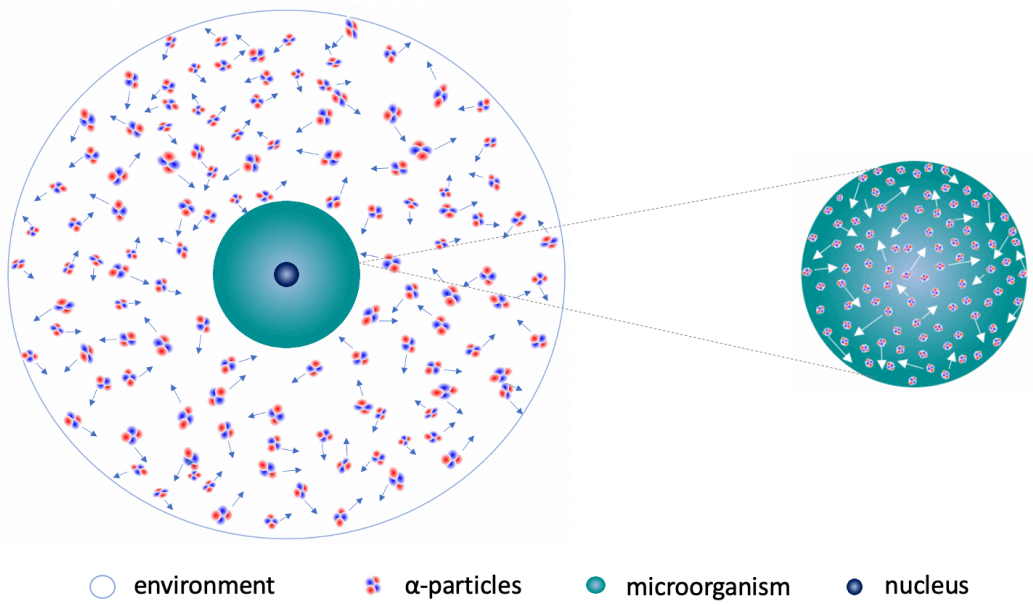

Figure 3.2 Schematic representation of the α-particles distribution in the simulated environments. Left: external exposure. Right: internal exposure. Arrows represent the directions of α-particles. The scale is not representative.

Physics Lists and production cuts

Physics Lists comprise of sets of models appropriate to describe interactions at different energy scales. GATE offers the option of choosing predefined Physics Lists, also called reference Physics Lists, which have been tested, validated and suggested for a variety of applications.

In all simulations, the Geant4 electromagnetic physics list option 4 (emStandard4) was used. It has been designed to provide higher accuracy of electrons, hadrons and ion tracking, combining the most accurate physics models from standard and low energy models. A summary of the Geant4 (G4) models applied in the energy range of the current simulation for electrons and α-particles is presented in Table ??.

Table 3.2 G4 models implemented in emStandard4 Physics List

Particle	G4 Process Name	G4 Model	Energy Range
electrons	e-Multiple Scattering	GoudsmitSaunderson	100 eV - 100 MeV
	e-Ionisation	LivermoreIonisation	0 - 100 keV
		MollerBhabha	100 keV - 100 TeV
	Bremsstrahlung	eBremSB	0 - 1 GeV
	Pair Production	ePairProd	0 - 100 TeV
alphas	Multiple Scattering	UrbanMsc	0 - 100 TeV
	Ion Low Energy Ionisation	BraggIon	0 - 7.9452 MeV
		BetheBloch	7.9452 MeV - 100 TeV
	Nuclear Stopping	ICRU49NucStopping	0 - 1 MeV

Initially, apart from 'emStandard4', the performance of 'emLivermore' and 'emPenelope' from the Low Energy Electromagnetic Physics Lists, and 'QGSP_BIC_EMZ' from the Hadronic Physics Lists, was evaluated. The 'emLivermore' and 'emPenelope' Physics Lists use modified models of 'emStandard4' mainly for the electron ionisation, bremsstrahlung, photoelectric and Compton effect processes. 'emStandard4' is also used as the electromagnetic component of 'QGSP_BIC_EMZ' which has been designed to allow the simulation of high energy hadrons and the following nuclear de-excitations.

Charged particles passing through the matter lose energy due to inelastic collision with the atomic electrons of the material. This energy transfer results in the ionisation or excitation of the atoms of the material. The energy losses due to ionisations are calculated by the Bethe-Bloch formula. In Monte Carlo simulations, the particle energy loss due to ionisation results in production of secondary electrons and is handled by the continuous energy loss approximation.

The application of production cuts avoids the tracking of very low energy secondary particles. Production cuts are specified in units of length which are converted to energy thresholds and they are applicable to electrons, positrons, photons and protons. Once imposed, the generation of secondaries is suppressed according to the defined limit in each part of the geometry. For example, a production cut of 5 cm for electrons in water corresponds to 11.0035 MeV. Once the kinetic energy of a secondary electron reaches this limit, which is reciprocally equivalent to 5 cm range in water, no more secondary electrons are produced. At this point, its energy is locally deposited.

GATE default cuts are set to 1 mm. In this work, the production cuts applied to secondary electrons and gammas were chosen to be 2 orders of magnitude less than the size of the radius of the simulated volumes: 0.1 μm in the environment, 0.01 μm in the diatom (microorganism plus frustule), and 0.001 μm in the nucleus, reaching thus an energy limit of 250 eV. No step limiter was implemented (it allows the limitation of the maximum size of a step).

The interactions of a particle with the simulated medium depend on the cross sections. Cross sections are energy dependent and they are supposed to be approximately constant along a step in Monte Carlo simulations. For the continuous energy loss approximation, tabulated cross section values are interpolated to the energies of interest. Consequently, the steps should be very small in order to achieve high accuracy results. The counterpart of this approach is the increase of the computing time.

GATE can limit the step length with the implementation of the step function. The step function calculates the particle 'step size limit value' at every step. Two parameters are required: the 'Final range' which is a user-defined step size, and the 'Ratio' which is defined as the ratio of the step size over the particle range. For example, the default values for electrons in GATE are: Ratio = 0.2 and Final range = 0.1 mm.

In this way, the continuously calculated 'step size limit value' varies with decreasing energy from the 'Ratio' value to the 'Final range' value. The process stops when the particle range becomes lower than the 'Final range'. The respective default values for α-particles are: Ratio = 0.1 and Final range = 0.02 mm. In this simulation, lower values were tested which resulted in significantly increased computation time. Observing no significant impact on the energy deposition, the usage of the default GATE values for the step function was chosen.

Table 3.3 Summary of GATE simulation characteristics

	environment (frustule*)	**microorganism**	**nucleus**	*** frustule**
Shape	Sphere	Sphere	Sphere	Shell
Size	r_{env}=55 μm (57.1 μm)	r_M=10 μm	r_N=0.5 μm	Width = 2 μm
Material	G4_WATER / dry sediments / mixture	G4_WATER	G4_WATER	Silicate
Density (g/cm^3)	1.00 / 1.20 / 1.02	1.00	1.00	2.40
Cuts (μm)	0.1	0.01	0.001	0.01
Source	^{238}U / ^{226}Ra / ^{222}Rn / ^{210}Po	-	-	-
Physics List	electromagnetic standard option 4			

Output

A "CrystalSD" (sensitive detector) was used to record the energy depositions and the respective physics interactions in the microorganism. Among others, the data which are stored in root files, include also the particle type and position of each hit in the sensitive volume.

In GATE, the tools allowing the interaction with the simulation are called 'actors'. Actors allow the collection of information such as energy deposition, doses, number of particles created in a given volume, information on the kinematics of particles, etc. They can also modify the behaviour of the simulation.

For the needs of tracking and recording the position, the momentum and the kinetic energy of particles entering the different volumes, the 'PhaseSpace actor' was used. This output root file can be used directly as a source in GATE simulations.

When detailed information for the energy deposition were not needed, the 'Dose actor' was engaged. The Dose Actor was attached to the microorganism and the total deposited energy was directly provided in a txt file.

The normalization of the results to unit and reference activity concentrations in each environmental condition was based on the following principle: the radionuclides diluted in water are normalized with respect to the simulated water volume and the radionuclides in dry sediments are normalized with respect to the simulated mass of the dry sediments.

Running the simulation

The different Physics Lists were tested using 10^6 primary α-particles of ^{226}Ra and ^{222}Rn. The energy depositions to the microorganisms due to different physical processes and the duration of each simulation were recorded. After choosing the Physics List (emStandard4), the simulations were launched with 10^8 primary α-particles and they were repeated 10 times in order to evaluate the statistical fluctuations (kept below 1%).

Information concerning particles (energy, position, direction and particle type) entering the microorganism were recorded in a phase space ('PhaseSpace' - 'PhSp') file attached to the external boundary of the microorganism for ^{222}Rn, ^{226}Ra, ^{238}U and ^{210}Po. The phase space retrieved at the boundaries of the microorganism was then used as source for collecting information on α-particles entering the nucleus. The retrieved phase space attached to the nucleus was used as source description for Geant4-DNA simulations. A schematic representation of the sources used in the different

steps of the external exposure simulation is shown in Fig. 3.3.

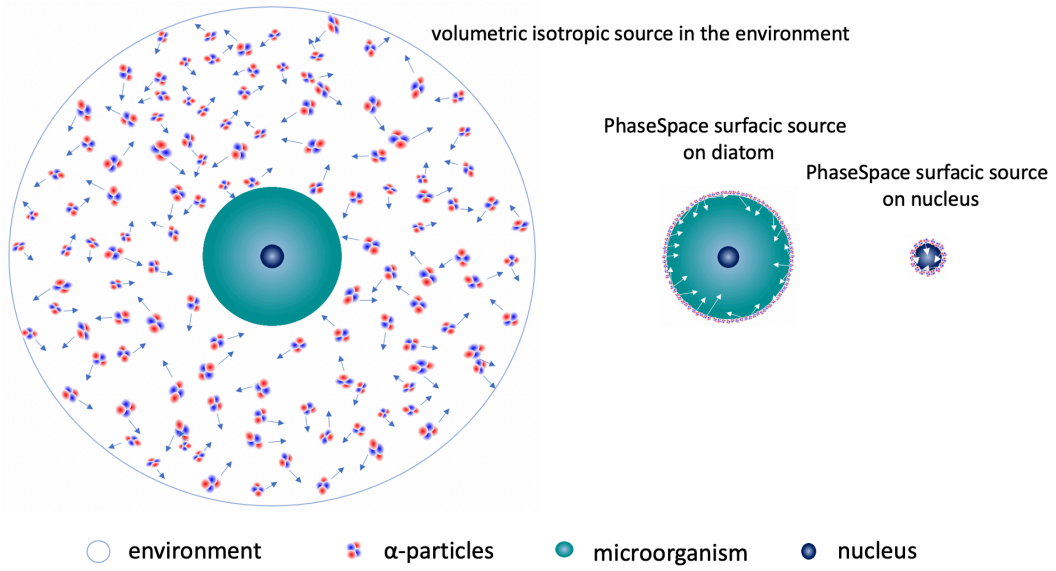

Figure 3.3 Schematic representation of evolution of α-sources in the simulation. Arrows represent the directions of α-particles. The scale is not representative.

At the next step, the energy deposited to the microorganism for each radionuclide was recorded, the contributions of the dominant physical processes were identified, and the total energy depositions were calculated.

Absorbed dose rates to the microorganism in μGy/h were calculated for 0%, 90% and 100% porosity, while the silicate frustule (distinguishing diatoms from other microorganisms) was taken into account only in the simulation of the benthic mixture (90% porosity). In the benthic mixture simulations, ^{238}U and ^{210}Po were also introduced.

It is reminded that Millan et al. [62] established a first correlation between ^{222}Rn activity concentrations measured in water and teratological forms of diatoms. Following their remark concerning the significant deformation rates observed for [^{222}Rn] > 1000 Bq/L in water and [^{226}Ra] > 30 kBq/kg in sediments, these values were kept as major references for the current simulation studies along with the highest measured activity concentrations of ^{210}Po in water and ^{238}U in sediments.

The dose rates were, therefore, scaled to the number of primaries corresponding to Unit (UAC) and Reference (RAC) Activity Concentration values (UAC: 1 Bq/L for radionuclides measured in water, 1 Bq/kg for radionuclides measured in the dry sediments, RAC: [^{222}Rn]= 1000 Bq/L, [^{226}Ra]= 30 kBq/kg, [^{238}U]= 0.3 kBq/kg, [^{210}Po]= 0.4 Bq/L).

An evaluation of the frustule thickness and density impact on the dose rates

was also performed. 1 µm, 2 µm, 5 µm and 10 µm widths of 2.4 g/cm^3 density were considered in the benthic mixture using ^{226}Ra and ^{222}Rn as sources. In the same environmental conditions, two other density values (0.2 g/cm^3 and 1.5 g/cm^3) for a frustule of 2 µm width were simulated.

3.2 Results on the external exposure using GATE

Physics Lists and mechanisms of energy deposition

The energy depositions on diatoms due to different processes were compared for four different Physics Lists in GATE: emStandard4, emLivermore, emPenelope and
QGSP_BIC_EMZ. In Figures 3.4 - 3.5, the deposited energy spectra for ^{226}Ra in the benthic mixture are shown.

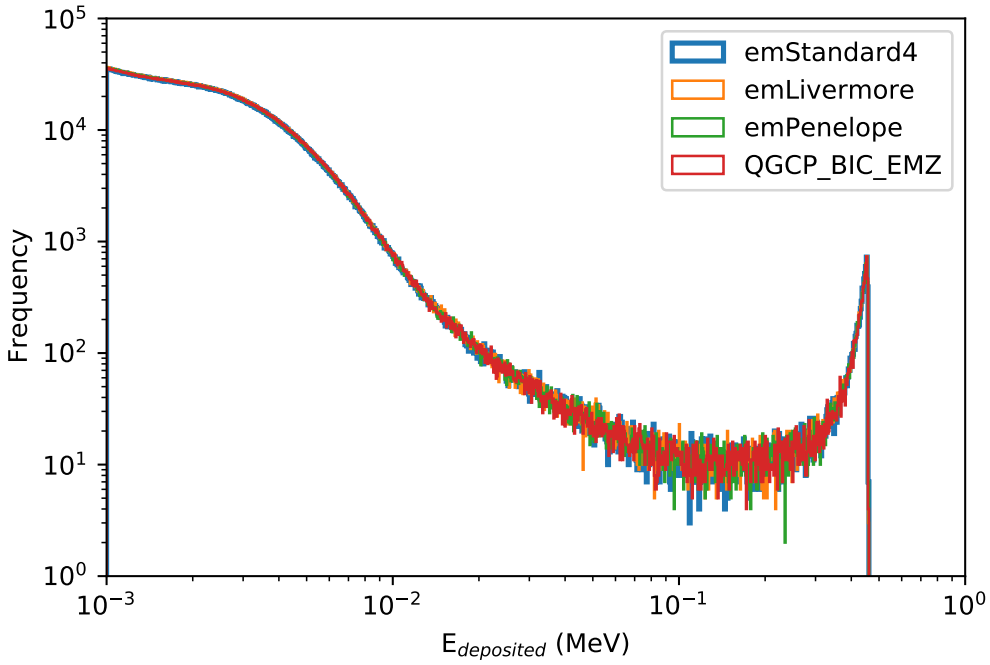

Figure 3.4 Total deposited energy distribution to diatoms for ^{226}Ra in the benthic mixture for different Physics Lists

For the total energy deposition resulting from all the processes (Fig 3.4), no differences are highlighted among the different Physics Lists. Nevertheless, the total energy depositions in emLivermore and emPenelope are 2.4% and 0.76%, respectively, higher than emStandard4, while the opposite trend is observed for QGSP_BIC_EMZ.

In Fig. 3.5, the main processes of energy depositions are shown. The predominance of ion ionisation (Fig. 3.5a) and the much lower contribution

of e- ionisation are highlighted (Fig. 3.5b).

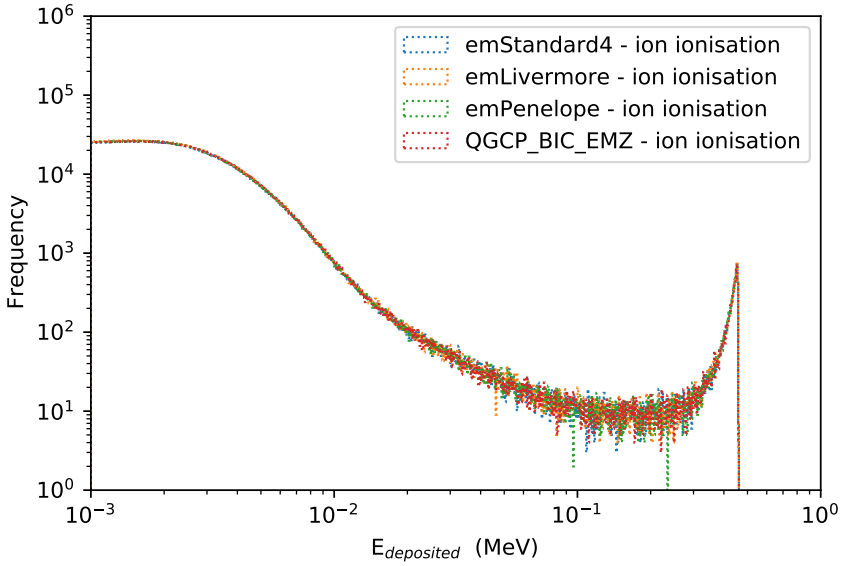

(a) Ion ionisation

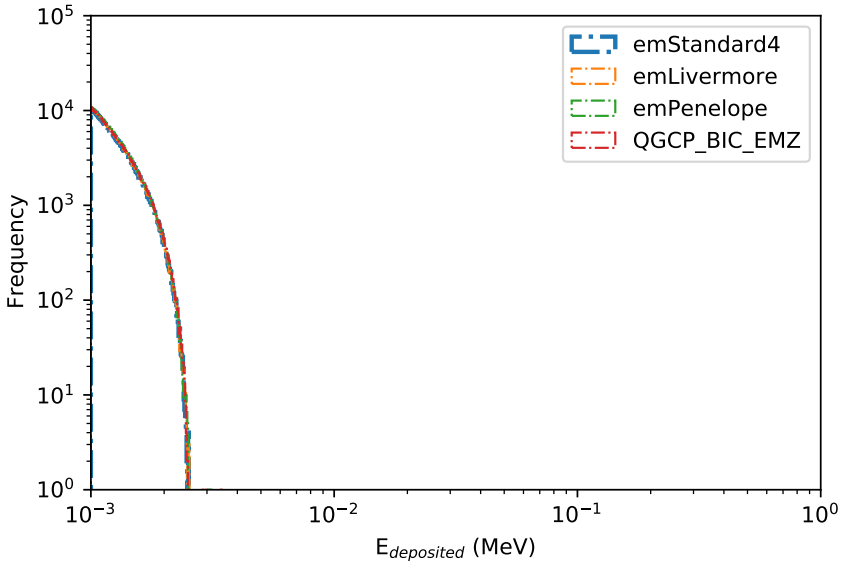

(b) e- ionisation

Figure 3.5 Deposited energy distributions to diatoms for ^{226}Ra in the benthic mixture attributed to electron ionisation and ion ionisation for different Physics Lists

The same behaviour was observed for ^{222}Rn (Appendix E). The same physics processes were activated since the kinetic energy of the α-particles of ^{226}Ra and ^{222}Rn differ less than 0.7 MeV.

In terms of time efficiency, the simulation using emPenelope was 30% slower than emStandard4, while the simulation time using the rest of the

Physics Lists did not differ more than 5%.

Taking into consideration the aforementioned, the rest of the simulations were conducted using the emStandard4 physics list. By recovering the number of particles entering the different volumes, it was observed that only 2% of the primaries emitted in the 55 μm radius environment reached the microorganism. An additional 20% decrease in the number of particles entering the diatom was observed due to presence of the frustule. In Table 3.4, the recorded kinetic energies of the α-particles (primaries) reaching the microorganism for the different simulated environments are summarized. The most energetic primaries have a mean energy of 3.3 MeV coming from ^{222}Rn, which drops by 12% when considering the frustule. A similar trend is observed for ^{226}Ra with a mean energy of 2.5 MeV. The minimum mean kinetic energy of α-particles entering the diatom is 2.1 MeV coming from ^{238}U.

Table 3.4 Kinetic energy of α-particles reaching the microorganism for different simulated environments (when considering frustule, values are provided in the parentheses)

			Kinetic energy (MeV)	
Porosity (%)	**Environment**	**Radionuclide**	**mean**	**maximum**
0	Dry sediments	^{226}Ra	2.8	4.8
90	Benthic Mixture	^{238}U (frustule)	2.4 (2.1)	4.2 (3.9)
		^{226}Ra (frustule)	2.8 (2.5)	4.8 (4.5)
		^{222}Rn (frustule)	3.3 (2.9)	5.5 (5.2)
		^{210}Po (frustule)	3.1 (2.8)	5.4 (5.0)
100	Water	^{222}Rn	3.3	5.5

Fig 3.6 shows the distribution of deposited energies to the diatom from all the processes (total) in the benthic mixture (90% porosity). It is observed that the energy deposited from ^{222}Rn and ^{210}Po is slightly higher than the one from ^{226}Ra and ^{238}U. Since ^{222}Rn and ^{210}Po α-particles are more energetic than ^{226}Ra and ^{238}U ones, they consequently have higher maximum range in water: R^{max}_{water} = 43.4 μm for ^{222}Rn, R^{max}_{water} = 40.5 μm for ^{210}Po, R^{max}_{water} = 35 μm for ^{226}Ra and R^{max}_{water} = 28.5 μm for ^{238}U.

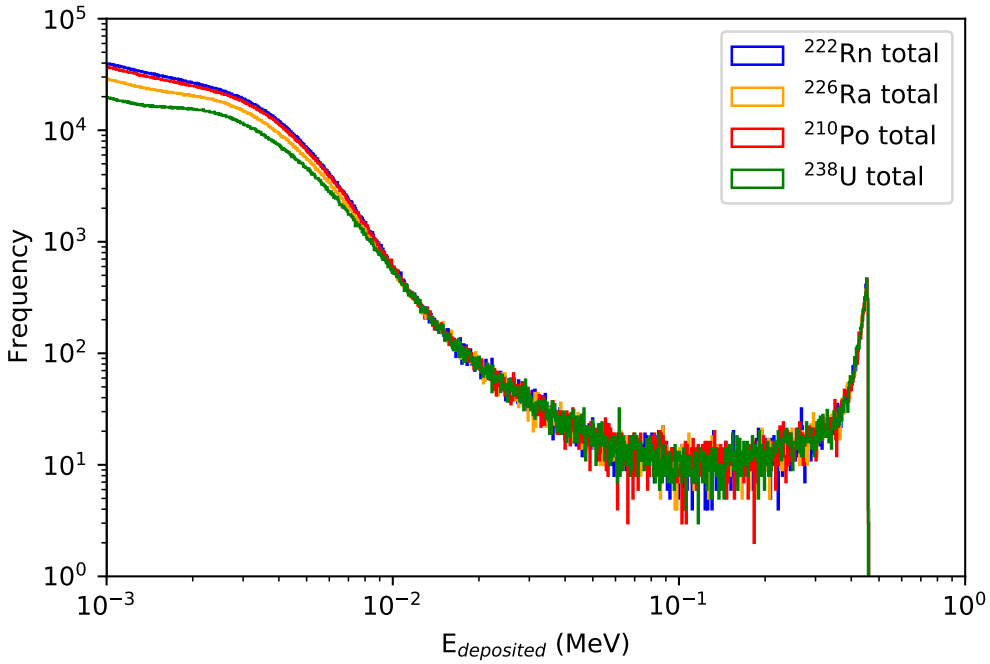

Figure 3.6 Total deposited energy distributions to diatoms in the benthic mixture for ^{226}Ra (orange), ^{222}Rn (blue), ^{210}Po (red) and ^{238}U (green).

In Fig. 3.7, the main physical processes, ion and electron ionisations, involved in the energy depositions for ^{222}Rn (most energetic α-emitter) and ^{238}U (least energetic α-emitter) are shown. Ion ionisation refers to the ionisations caused directly from the α-particle while the electron ionisation refers to the ionisations caused by sufficiently energetic secondary electrons (δ-rays). It is shown that the predominant process is ion ionisation while the mean energy deposition due to electrons ionisation is merely 15 keV. Therefore, the α-particles deposit a great part of their energy inside the microorganism (10 μm radius) through ionisations, reaching the maximum energy deposition at the end of their range (peak observed at higher energies). This results in the absolute doses to the diatom being 59% higher for ^{222}Rn than for ^{238}U when considering the same number of primaries generated for both radionuclides as it will be shown in the next section (Table 3.5).

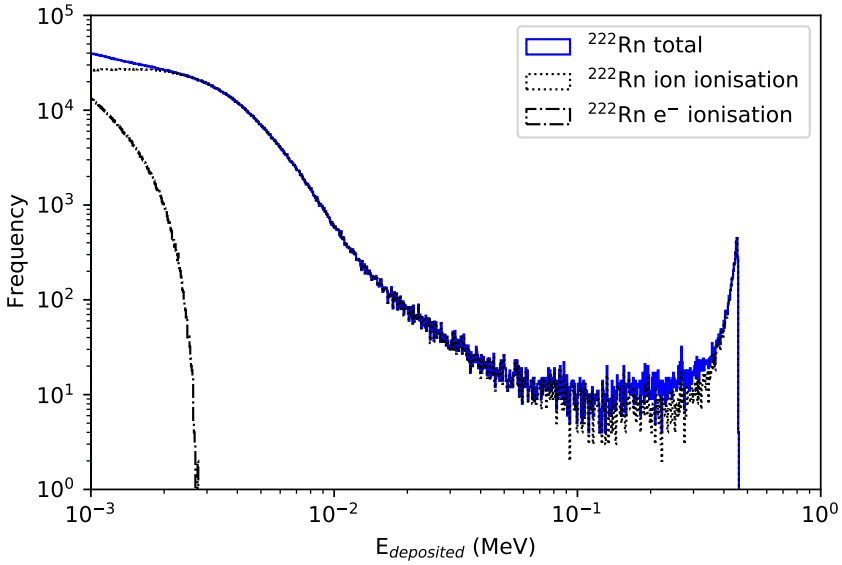

(a) Deposited energy distribution for ^{222}Rn

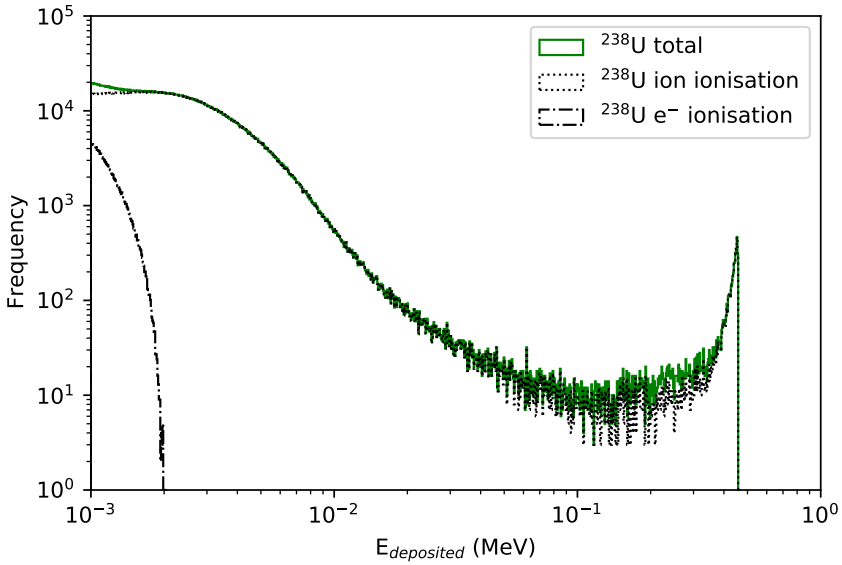

(b) Deposited energy distribution for ^{238}U

Figure 3.7 Deposited energy distributions for ^{222}Rn (a) and ^{238}U (b) in the benthic mixture for diatoms. Solid lines: total deposited energy, Dotted lines: ion ionisation, Dashed lines: electron ionisation.

Dose rates normalized to Unit Activity Concentrations (UAC) and Reference Activity Concentrations (RAC)

First, the external absolute doses for $1{\cdot}10^8$ primaries are presented in Table 3.5. A slightly higher absolute dose for ^{222}Rn in comparison to ^{226}Ra, ^{210}Po and ^{238}U which drops by 21.5% when adding the frustule is observed.

Table 3.5 External absolute doses to microorganisms in all simulated environments (when considering frustule, values are provided in the parentheses)

Porosity (%)	Environment	Radionuclide	Absolute dose ($\times 10^4$ Gy)
0	Dry sediments	^{226}Ra	10.30
90	Benthic mixture	^{238}U (frustule)	6.90 (5.80)
		^{226}Ra (frustule)	9.30 (7.30)
		^{222}Rn (frustule)	11.10 (9.20)
		^{210}Po (frustule)	10.70 (8.70)
100	Water column	^{222}Rn	11.20

Absolute doses correspond to 10^8 primaries.

In Table 3.6, the external dose rates per Unit Activity Concentration (UAC) of the radiative environment are presented. ^{238}U and ^{210}Po were included only in the benthic mixture. Diatoms are distinguished by the inclusion of frustule (values indicated in the parenthesis). The total dose rate when considering Unit Activity Concentrations (UAC) in the benthic environment is $5.4 \cdot 10^{-3}$ μGy/h for the microorganisms and it gets decreased to $4.92 \cdot 10^{-3}$ μGy/h for diatoms (almost -10%).

Table 3.6 External Dose Rates (DR) to microorganisms per Unit Activity Concentration (UAC) in all simulated environments (when considering frustule, values are provided in the parentheses)

Porosity (%)	Environment	Radionuclide	UAC	External DR (μGy/h)
0	Dry sediments	^{226}Ra	1 Bq/kg	$3.08 \cdot 10^{-3}$
90	Benthic mixture	^{238}U (frustule)	1 Bq/kg	$2.30 \cdot 10^{-4}$ ($1.92 \cdot 10^{-4}$)
		^{226}Ra (frustule)	1 Bq/kg	$2.78 \cdot 10^{-4}$ ($2.45 \cdot 10^{-4}$)
		^{222}Rn (frustule)	1 Bq/L	$2.49 \cdot 10^{-3}$ ($2.30 \cdot 10^{-3}$)
		^{210}Po (frustule)	1 Bq/L	$2.40 \cdot 10^{-3}$ ($2.18 \cdot 10^{-3}$)
100	Water column	^{222}Rn	1 Bq/L	$2.79 \cdot 10^{-3}$

It is important to remind that in the benthic mixture, the radionuclides measured in water (^{222}Rn and ^{210}Po) are dissolved in 90% of the mixture volume. Proportionally, the radionuclides measured in the dry sediments (^{226}Ra and ^{238}U) are distributed only in 10% of the mixture volume.

The external dose rates normalized to the reference radiological conditions (RAC: [^{238}U] = 0.3 kBq/kg, [^{226}Ra] = 30 kBq/kg, [^{222}Rn] = 1000 Bq/L, [^{210}Po] = 0.4 Bq/L) are presented in Table 3.7 for the different simulated environments. The results show that a microorganism surrounded only by dry sediments (containing only ^{226}Ra) would be exposed to 92.5 μGy/h whereas in the scenario of a solely aquatic environment containing only ^{222}Rn, the respective value gets reduced to 2.8 μGy/h. In the benthic mixture, the contributions of the different radionuclides to the dose rates differ noticeably. In this case, the dose rates drop by almost 16% for ^{238}U, 12% for ^{226}Ra, 7.6% for ^{222}Rn and 9.4% for ^{210}Po when the frustule is considered.

Table 3.7 External Dose Rates (DR) to microorganisms in all simulated environments normalised to the Reference Activity Concentrations (RAC) (when considering frustule, values are provided in the parentheses)

Porosity (%)	**Environment**	**Radionuclide**	**RAC**	**External DR (μGy/h)**
0	Dry sediments	^{226}Ra	30 kBq/kg	92.46
90	Benthic mixture	^{238}U (frustule)	0.3 kBq/kg	$6.89 \cdot 10^{-2}$ ($5.76 \cdot 10^{-2}$)
		^{226}Ra (frustule)	30 kBq/kg	8.35 (7.35)
		^{222}Rn (frustule)	1000 Bq/L	2.49 (2.29)
		^{210}Po (frustule)	0.4 Bq/L	$9.60 \cdot 10^{-4}$ ($8.70 \cdot 10^{-4}$)
100	Water column	^{222}Rn	1000 Bq/L	2.79

Eventually, when considering the distribution of the radionuclides in the benthic mixture (composed of 90% water and 10% dry sediments), the mean drop in the total dose rate due to the frustule is approximately 11%. Fig 3.8 summarizes the external dose rates normalized to the Reference Activity Concentrations (RAC) for microorganisms (without frustule) and diatoms (with frustule) in the benthic mixture. In total, a microorganism is exposed to 10.9 μGy/h, whereas a diatom to 9.7 μGy/h when considering the Reference Activity Concentrations (RAC). It is highlighted that the dose rates from ^{222}Rn account only for one third of the total ones, while the contributions of ^{238}U and ^{210}Po are less than 0.6%.

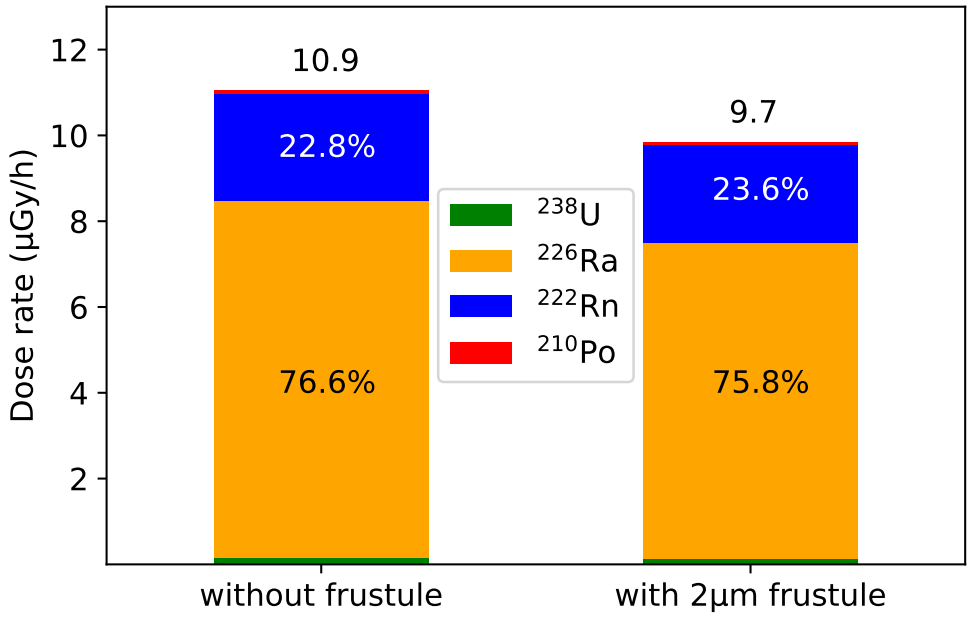

Figure 3.8 External dose rates to microorganisms in the benthic mixture normalized to RAC: [^{238}U]=0.3 kBq/kg, [^{226}Ra]=30 kBq/kg, [^{222}Rn]=1000 Bq/L and [^{210}Po]=0.4 Bq/L. Contribution to dose rates: Blue bar: ^{222}Rn, Orange bar: ^{226}Ra, Green bar: ^{238}U, Red bar: ^{210}Po. Statistical uncertainties < 1 % - not visible.

To our knowledge, dose rates to diatoms have been so far poorly documented: the current study could only be compared to that of Morthekai et al. [256] who investigated luminescence dating on diatom fossils in core sediments of a river and a lake. They obtained dose rates between 0.5 µGy/h and 1 µGy/h due to U, Th and K. Although the environments and radionuclides differ from the current work, Morthekai's values are coherent with the calculations of the present work considering that 1.1 µGy/h is deposited at the frustule in the benthic mixture.

Moreover, it is interesting to compare the simulated dose rate values to the suggested dose rate threshold for the protection of the ecosystems (10 µGy/h) [257, 258] which has also been adopted by ERICA risk assessment tool [19]. The dose rate threshold of 10 µGy/h applies to all the ecosystems and non-human species indicating that the environmental risks are considered negligible below this value. This limit value is almost reached for the benthic conditions considering the reference activity concentration values. For microorganisms living exclusively in the aquatic environment and being exposed only to ^{222}Rn dissolved in water, the dose rates (2.8 µGy/h) are well below the suggested threshold. On the contrary, when

considering microorganisms inhabiting dry sediments and being exposed only to ^{226}Ra, the dose rates (92.5 μGy/h) are almost 10 times higher than the suggested threshold.

Frustule width and density impact

Following the results shown in Fig. 3.8, the impact of different frustule conditions on the microorganism dose rates from ^{226}Ra and ^{222}Rn in the benthic mixture was studied. In Fig. 3.9, the dose rates for various frustule widths for ^{226}Ra and ^{222}Rn normalized to the Reference Activity Concentrations (RAC) are presented.

Although the decreasing trend is obvious for both radionuclides, it is more evident for ^{226}Ra: 1 μm width results in 7.86 μGy/h (7% higher than for 2 μm width), while 10 μm corresponds to 2.64 μGy/h. The respective difference between 1 μm and 10 μm frustule width for ^{222}Rn is -76% (2.39 and 1.36 μGy/h, respectively). It is pointed out here that the most realistic widths are in the range [0,2] μm [248] for the microorganism's size considered in this work. Considering the aforementioned range, it is highlighted that the difference in the total dose rates between a diatom enveloped by 1 μm width frustule and a diatom enveloped by a 2 μm width frustule is 5.8%.

In the next step, the frustule width was kept constant (2 μm) and the dose rates for modified density values were collected. Densities of 0.2 g/cm^3 as measured by Habchi et al. [247] and 1.5 g/cm^3 as suggested by Li et al. [250] were tested. In Table 3.8, the sum of ^{226}Ra and ^{222}Rn dose rates in the benthic mixture, normalized to 30 kBq/kg and 1000 Bq/L respectively, for the different simulated frustule parameters are summarized. It is noticed that between 0.2 g/cm^3 and 2.4 g/cm^3, the dose rates do not vary more than 11%.

In conclusion, the frustule density and width do not critically affect the dose rates received by the microorganisms in the radioactive mineral springs.

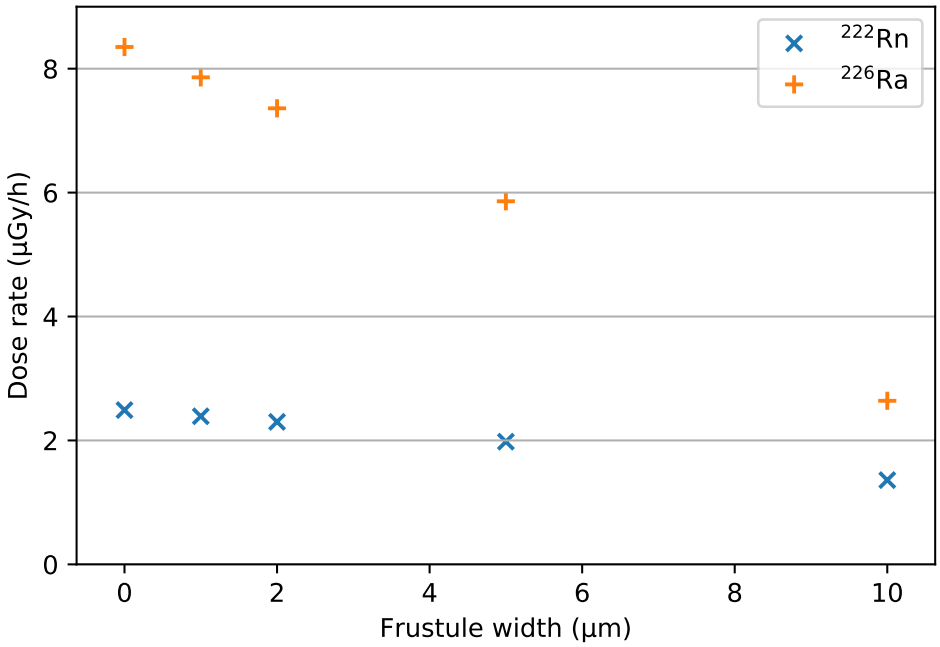

Figure 3.9 External dose rates to microorganisms in the benthic mixture as a function of the frustule width with density 2.4 g/cm^3. Blue: ^{222}Rn, Orange: ^{226}Ra. Dose rates are normalized to RAC: [^{226}Ra] =30 kBq/kg, [^{222}Rn]=1000 Bq/L. Statistical uncertainties: $< 0.5\%$ - not visible.

Table 3.8 Diatom external Dose Rates (DR) normalized to ^{226}Ra and ^{222}Rn Reference Activity Concentrations (RAC) for various frustule conditions in the benthic mixture

Frustule parameters		
Thickness (µm)	**Density (g/cm^3)**	**External DR (µGy/h)**
0	–	10.84
1	2.4	10.25
2	2.4	9.66
	1.5	10.12
	0.2	10.73
5	2.4	7.84
10	2.4	4.00

RAC: [^{222}Rn]=1000 Bq/L, [^{226}Ra]=30 kBq/kg

3.3 Results on the internal exposure using GATE

Apart from the external exposure, additional exposure is expected from the radioelements accumulated on the frustule or internally incorporated in the microorganism [177]. Although diatoms' bioaccumulation capacity, as well as, the adsorption of heavy metals and radionuclides on the frustule have been highlighted in several studies [97, 99, 100, 259], specific data to help the build up the simulation are scarce. As a result, the internal exposure of diatoms for ^{238}U, ^{226}Ra, ^{222}Rn and ^{210}Po was evaluated without considering any explicit mechanisms of radionuclides incorporation.

The dose rates per Unit Activity Concentration (UAC) are in the order of 10^{-4} μGy/h per Bq/kg for each radionuclide. More specifically, $4.85 \cdot 10^{-4}$ for ^{238}U, $4.32 \cdot 10^{-4}$ for ^{226}Ra, $3.84 \cdot 10^{-4}$ for ^{222}Rn and $3.95 \cdot 10^{-4}$ for ^{210}Po, expressed in in μGy/h per Bq/kg, were calculated, summing up to a total $16.96 \cdot 10^{-4}$ μGy/h per Bq/kg.

In Table 3.9, both external and internal dose rates normalized to the respective Reference Activity Concentrations (RAC) for each radionuclide are provided. It is reminded that the external exposure values presented in Table 3.9 refer to the dose rates for diatoms in the benthic mixture. It is also highlighted that ^{238}U and ^{226}Ra account for 10% of the source volume, while ^{222}Rn and ^{210}Po account for 90% of the source volume. Lacking evidence of the realistic incorporation level, the following assumption was considered for the internal dose rate calculations: 0.3 kBq/kg of ^{238}U, 30 kBq/kg of ^{226}Ra, 1000 Bq/L of ^{222}Rn and 0.4 Bq/L ^{210}Po (values corresponding to RAC) are distributed inside the microorganism.

Table 3.9 Diatom external and internal Dose Rates (DR) in the benthic mixture normalized to the Reference Activity Concentrations (RAC)

Radionuclide	**RAC**	**External DR (μGy/h)**	**Internal DR (μGy/h)**
^{238}U	0.3 kBq/kg	$5.76 \cdot 10^{-2}$	$1.46 \cdot 10^{-1}$
^{226}Ra	30 kBq/kg	7.36	12.96
^{222}Rn	1000 Bq/L	2.30	$3.84 \cdot 10^{-1}$
^{210}Po	0.4 Bq/L	$8.70 \cdot 10^{-4}$	$1.58 \cdot 10^{-4}$
Total		9.72	13.49

In Fig. 3.10, the contribution of each radionuclide to the external and the internal diatom dose rates normalized to the Reference Activity Concentrations (RAC) in the benthic mixture are compared graphically in

logarithmic scale. In order to highlight the importance of the activity concentrations, the corresponding dose rates per Unit Activity Concentration (UAC) were plotted in Fig. 3.11. In both Fig. 3.10 and 3.11, the impact of the activity concentrations on the dose rates is observed: both internal and external dose rates normalized to RAC are higher than those normalized to UAC.

Beginning with the external exposure, it is observed that the contribution of the radionuclides to the dose rates are different between Fig. 3.10 and 3.11: the high contribution of ^{226}Ra and ^{222}Rn observed in Fig. 3.10 is not evident in Fig. 3.11. In the radiative environment considered for the external exposure, ^{222}Rn and ^{210}Po are exclusively diluted in water which accounts for 90% of the benthic mixture, whereas ^{238}U and ^{210}Po are distributed in the dry sediments (10% of the benthic mixture). As a result, when all the radionuclides are normalized to UAC (Fig. 3.11), the impact of the mixture composition is more evident: ^{222}Rn and ^{210}Po contribute the most to the dose rates.

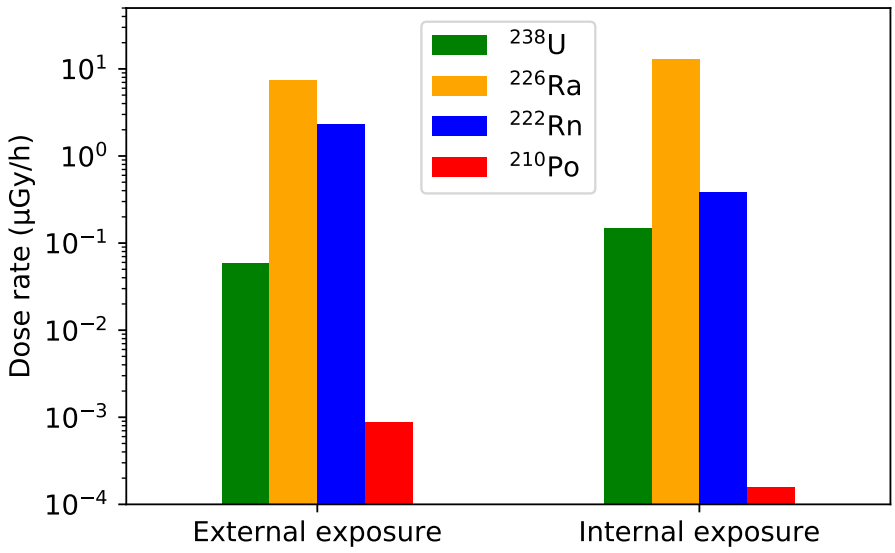

Figure 3.10 External and internal diatom dose rates in the benthic mixture normalized to the Reference Activity Concentrations (RAC). Blue: ^{222}Rn, Orange: ^{226}Ra, Green: ^{238}U, Red: ^{210}Po. RAC: [^{238}U]=0.3 kBq/kg, [^{226}Ra]=30 kBq/kg, [^{222}Rn]=1000 Bq/L and [^{210}Po]=0.4 Bq/L. Statistical uncertainties: $<$ 0.5% - not visible.

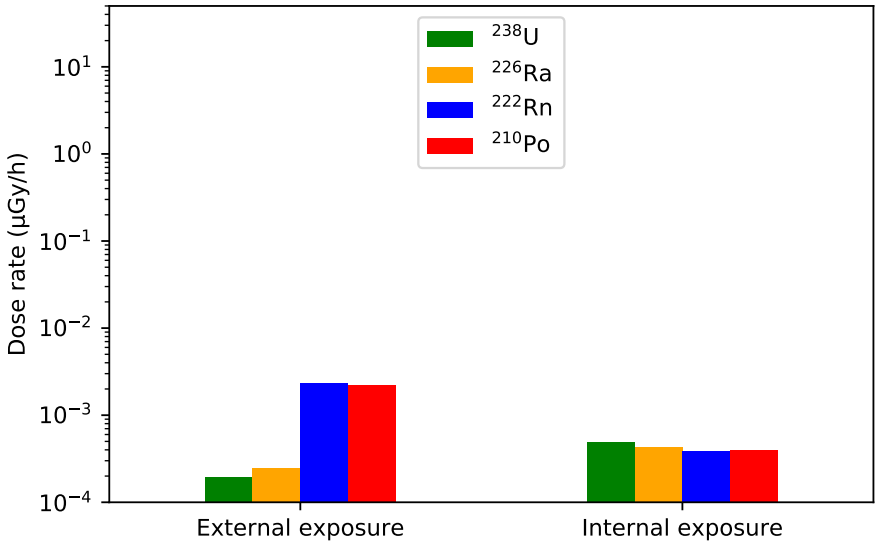

Figure 3.11 External and internal diatom dose rates in the benthic mixture per Unit Activity Concentrations (UAC). Blue: ^{222}Rn, Orange: ^{226}Ra, Green: ^{238}U, Red: ^{210}Po. UAC: [^{238}U]=1 Bq/kg, [^{226}Ra]=1 Bq/kg, [^{222}Rn]=1 Bq/L and [^{210}Po]=1 Bq/L. Statistical uncertainties: $< 0.5\%$ - not visible.

Concerning the internal exposure, the effect of the considered activity concentrations can also be observed by comparing Fig. 3.10 and 3.11. When considering Unit Activity Concentrations (UAC), the internal dose rates from all the considered radionuclides are approximately the same. The small differences of the internal dose rates observed among the different radionuclides in Fig. 3.11 can be attributed to their range in water: these α-emitters are now distributed and enclosed in a 10 µm radius water sphere and their Bragg peak is expected outside the microorganism (^{222}Rn with R^{max}_{water} = 43.4 µm, ^{210}Po with R^{max}_{water} = 40.5 µm, ^{226}Ra R^{max}_{water} = 35 µm and ^{238}U with R^{max}_{water} = 28.5 µm).

It is clarified that it is not claimed that if the activity concentration in the environment is 1 Bq/kg, then the diatom will fully absorb 1 Bq/kg within its cell. The ratio of the absorption of the radionuclides through the diatoms' frustule is still undefined. Nevertheless, when normalising the internal dose rates to the Reference Activity Concentrations (RAC), as shown in Fig. 3.10, it is observed that a high internal exposure is expected from ^{226}Ra, ^{222}Rn and ^{238}U.

In summary, when the α-particles are emitted in the benthic mixture, their interactions with the environment will modulate the energy deposition to the diatoms. On the other hand, when the α-particles are emitted inside the

microorganism, the calculated internal dose rates seem to be similar for the various radioisotopes diluted in identical water volumes.

3.4 ERICA

ERICA, as already introduced in Chapter 1, is an open-source tool for the assessment of radioecological risk. In ERICA, the radiative environment is configured in layers as shown in Fig. 3.12. In principal, this approach is adopted by the radioecological tools since the calculation of dose rates is based on the use of radiological factors that transform activity concentrations measured in the environment to dose rates to the organisms living in this environment. The organism can be placed in any of these layers or a combination of them. As shown in Fig. 3.12, the main difference with the current microdosimetric simulation is that in GATE the environment is modelled as an homogeneous sphere surrounding the microorganism.

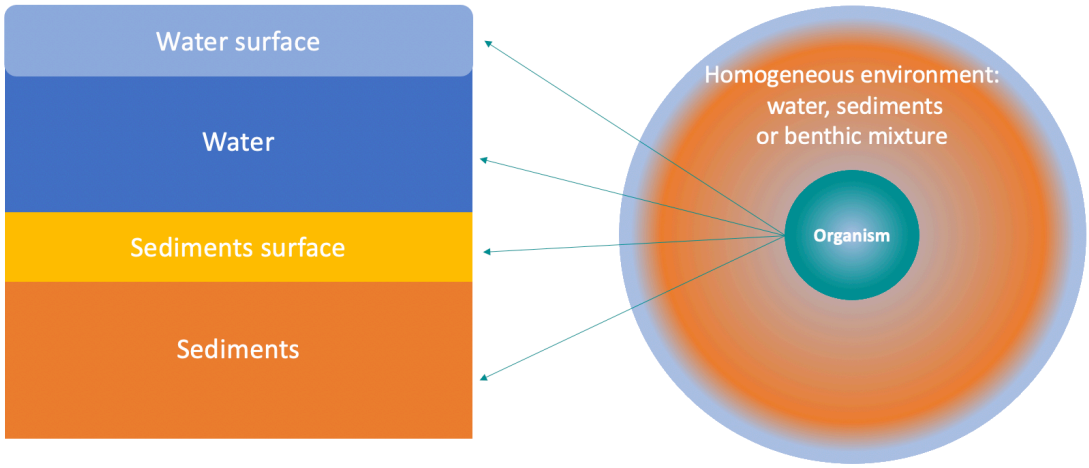

Figure 3.12 Configuration of the radiative environment in ERICA (left) and GATE (right). Left: the environment is separated in layers where the organism can be placed. Right: the environment is homogeneous and surrounds the microorganism.

The approach adopted by ERICA for risk assessments, introduces 3 tiers of incremental detail. At Tier 1 level, the user chooses the environment (terrestrial, marine or freshwater) and the radionuclides of interest, while in Tier 2 and Tier 3 the user also selects the organisms of interest. The main idea of Tier 1 is to provide the user with a conservative evaluation of the scenario under study using only the radionuclides activity concentration values. At the end of this step, the user will be either recommended to proceed to Tier 2 for a more detailed evaluation or the current evaluation

can be considered finalised if no radioecological impact on any non-human biota is predicted. In Tier 2, the model organism is selected and the output, including dose rate and risk quotient calculations, is considered as the complete assessment. Tier 3 is designed for probabilistic and sensitivity analyses using Monte Carlo simulations to complement the assessment acquired in Tier 2. The output of Tier 3 includes probability dose rate distributions and correlations of radiological factors with the dose rates but no risk assessment is provided.

Based on the ICRP dosimetric calculation approach, ERICA employs databases of radiological factors and radiation effects (FREDERICA database [260]) for a great variety of radionuclides and model organisms from freshwater, marine and terrestrial environments. The databases include, among others, distribution coefficients (K_d), equilibrium Concentration Ratios (CR) and Dose Conversion Coefficients (DCC), which are essential for dose rate calculations in aquatic environments and they will be detailed in the following paragraphs. The suggested model organisms range from mammals and fishes to insects and plants, with the smallest available one being the phytoplankton. Apart from nuclear industry and medical related radioisotopes, like ^{137}Cs, ^{131}I, ^{239}Pu, ERICA databases include almost all the isotopes of the natural decay chains apart from noble gazes like ^{222}Rn.

The latest version (v2.0) of ERICA assessment tool became available to the public in November 2021. In this work, radiological evaluations for freshwater biota were initially performed using ERICA v1.3 and repeated using ERICA v2.0. The latest release (v2.0) incorporates updated databases and modifications on the approaches used for the dose rate calculations. Below, the principal approaches adopted for freshwater ecosystems by ERICA v2.0 are descibed. In the end, the main differences between the two versions are briefly reported and an example of their impact on the results is provided.

In an effort to evaluate ERICA for microorganisms, Tier 2 approach was adopted for phytoplankton in a freshwater aquatic ecosystem. In ERICA documentation, phytoplankton corresponds to a water sphere of 50 μm radius and a mass of $1 \cdot 10^{-6}$ kg, the only freshwater reference organism resembling diatoms size. As described in detail below, the constants used for the calculations of the Dose Conversion Coefficients (DCC) are extrapolated from already tabulated values using the BiotaDC tool [261]. The software is developed on behalf of ICRP [262] making use of the ICRP-07 data files for organisms with masses in the range $[1 \cdot 10^{-6}, 1 \cdot 10^{3}]$ kg. This lowest bound

of the dosimetric extrapolation tool ($1 \cdot 10^{-6}$ kg) corresponds to an accreted mass of phytoplankton cells in ERICA and it replaced the old value of $2.05 \cdot 10^{-12}$ kg corresponding to FASSET freshwater phytoplankton [263].

Dose rate calculations in freshwater ecosystems

A simplified schema summarizing the dosimetric approach of ERICA is provided in Fig. 3.13 for both internal and external exposure cases. It is reminded that the methodology is based on the ICRP approach described by Eq. 1.34 and 1.35 in Chapter 1 which uses Dose Conversion Coefficients (DCC) to transform activity concentrations to dose rates.

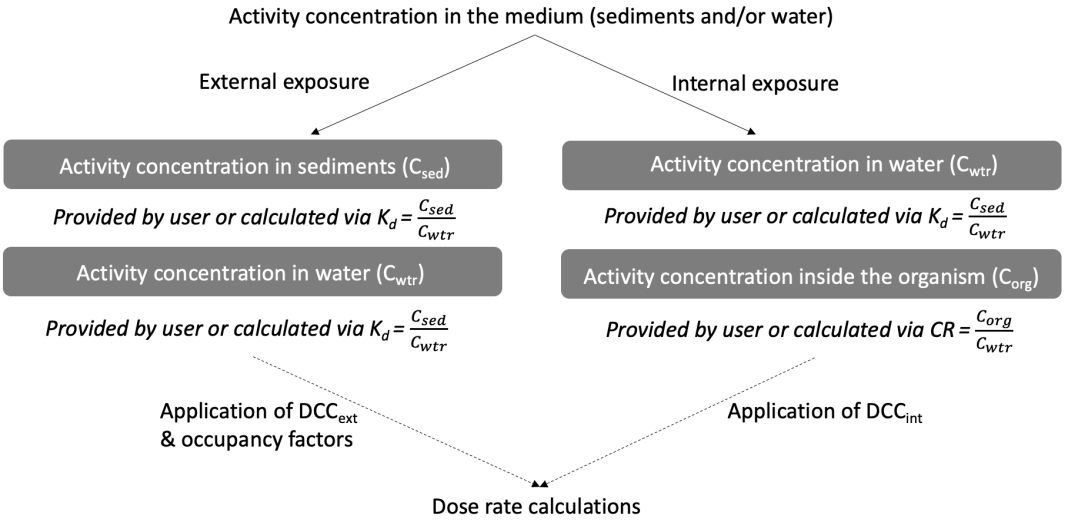

Figure 3.13 The pathway to calculate dose rates from activity concentrations in the medium (sediments and/or water)

After the choice of the ecosystem, radionuclide and organism of interest, the user should introduce at least one activity concentration measured in the environmental medium (water or/and sediments). As shown in Fig. 3.13, the tool needs both the activity concentration in sediments (C_{sed}) and in water (C_{wtr}) for the external dose rate calculations, while for the internal dose rate calculations only (C_{wtr}) is needed. In the absence of any of these two values, the tool uses distribution coefficients (K_d) to calculate the missing activity concentration. As defined earlier in Chapter 2, K_d (Eq. 3.3) can be used to derive the activity concentration of a radionuclide in water if the activity concentration of the radionuclide in sediments is known, and vice versa.

$$K_d = \frac{C_{sed}}{C_{wtr}} \tag{3.3}$$

with:

K_d (L/kg): distribution coefficient

C_{sed} (Bq/kg): sediments activity concentration per unit mass

C_{wtr} (Bq/L): water activity concentration per unit volume

For the internal exposure dose rate calculations, the activity concentration of a radionuclide inside the organisms needs to be known first. The applied methodology makes use of tabulated equilibrium Concentration Ratios (CR) which allow the derivation of the activity concentrations inside the organisms (C_{org}). CR (Eq. 3.4) is defined as the ratio of the activity concentration of a radionuclide inside the organism (C_{org} in Bq/kg of fresh weight) per activity concentration of the radioduclide in aqueous phase (C_{wtr} in Bq/L). The application of CR for internal dose rate calculations is based on the assumption that the organism is in biochemical equilibrium with its surroundings [19, 225, 229]. The tabulated concentration ratios are taken from the Wildlife Transfer Database (WTD) [264].

$$CR = \frac{C_{org}}{C_{wtr}} \tag{3.4}$$

with:

CR (Bq/kg per Bq/L): concentration ratio

C_{org} (Bq/kg): activity concentration of the radionuclide inside the organism

C_{wtr} (Bq/L): activity concentration of the radioduclide in water

As shown in Eq. 3.5, for the internal dose rate (DR_{int}) calculations ERICA uses the activity concentration of the radionuclide in the organism (C_{org} as derived by Eq. 3.4), the internal exposure dose conversion coefficient (DCC_{int}) specific to the radionuclide and the organism, as well as, the weighting factor (w_R) specific to the radiation type (for example, w_R=10 for α-particles concerning non-human biota [263, 265]). In this work, non-weighted results (w_R=1) are provided.

$$DR_{int} = C_{org} \times DCC_{int} \times w_R \tag{3.5}$$

with:

DR_{int} (μGy/h): internal dose rate

C_{org} (Bq/kg): activity concentration of the radionuclide inside the organism

DCC_{int} (μGy/h per Bq/kg): internal exposure dose conversion coefficient

w_R: weighting factor specific to the radiation type

ERICA incorporates BiotaDC tool for the derivation of Dose Conversion Coefficients (DCC). BiotaDC extrapolates DCC for both internal and external exposure which have been calculated by Monte Carlo simulations for certain geometries (resembling organisms), energies and particle types [266]. DCC have already been introduced in Chapter 1 as coefficients which allow the dose calculation to an organism for given radionuclide activity concentrations. In a more detailed definition, considering DCC as the absorbed dose rates per activity concentration in an organism or a medium (expressed in μGy/h per Bq/kg), the DCC for a certain radiation type can be defined as a function of the absorbed fraction φ(E) in the simplified way shown in Eq. 3.6 (for internal exposure) and Eq. 3.7 (for external exposure) [267]. In this case, φ(E) (which will be annotated as φ onwards in the text) is the fraction of the energy emitted by a radiation source that is absorbed within the organism, and $C = 5.767 \cdot 10^{-4}$ is the unit conversion constant.

$$DCC_{int}(E) = C \times E \times \phi(E) \tag{3.6}$$

$$DCC_{ext}(E) = C \times E \times (1 - \phi(E)) \tag{3.7}$$

with:

DCC_{int} (μGy/h per Bq/kg): internal exposure dose conversion coefficient

DCC_{ext} (μGy/h per Bq/kg): external exposure dose conversion coefficient

$C = 5.767 \cdot 10^{-4}$: unit conversion constant

E (MeV): energy of incident radiation

φ(E): absorbed energy fraction

Although ERICA provides directly the DCC, the user can easily find the extrapolated φ values for energies of α, β-γ radiation and low-energy β particles (as well as fission fragments which are out of the scope of the current work) corresponding to the organism and the radionuclide of interest online [261]. The absorbed energy fractions φ and the DCC for ^{226}Ra and ^{222}Rn provided by BiotaDC for ERICA freshwater phytoplankton reference organism (water sphere with a mass of $1 \cdot 10^{-6}$ kg) are presented in Tables 3.10 and 3.11. Nevertheless, ERICA does not include ^{222}Rn in the aquatic ecosystems. The values provided in Table 3.10 follow the ICRP136 methodology taking into account the radioactive progeny for a period for T = 365.24 days. The values provided in Table 3.11 follow the ICRP108 methodology taking into account only radioactive progeny with half-lives

less than 10 days. It is observed that the energy absorbed fractions φ for α-particles, as well as the DCC, do not differ notably between the two approaches.

Table 3.10 BiotaDC parameters for a spherical freshwater reference organism with mass = $1{\cdot}10^{-6}$ kg following ICRP136

		^{226}Ra	^{222}Rn
Absorbed energy fraction	φ_{α}	$97.12{\cdot}10^{-2}$	$96.85{\cdot}10^{-2}$
	$\varphi_{low\ \beta-\gamma}$	$15.65{\cdot}10^{-5}$	$19.37{\cdot}10^{-5}$
	$\varphi_{high\ \beta-\gamma}$	$10.62{\cdot}10^{-3}$	$13.18{\cdot}10^{-3}$
Dose Conversion Coefficient (μGy/h per Bq/kg)	$\mathbf{DCC}_{external}$	$13.90{\cdot}10^{-4}$	$14.10{\cdot}10^{-4}$
	$\mathbf{DCC}_{internal}$	$14.10{\cdot}10^{-3}$	$11.50{\cdot}10^{-3}$

Values consider the contribution of radioactive progeny using ratios of integral activities for T = 365.24 d (ICRP 136) [261].
Ratios for ^{226}Ra: 1 × ^{226}Ra, 0.9849 × ^{222}Rn, 0.984892 × ^{218}Po, 0.984622 × ^{214}Pb, 0.000197 × ^{218}At, 0.984764 × ^{214}Bi, 0.000207 × ^{210}Tl, 0.984557 × ^{214}Po, 0.014990 × ^{210}Pb, 0.014402 × ^{210}Bi, 0.005762 × ^{210}Po.
Ratios for ^{222}Rn: 1 × ^{222}Rn, 1 × ^{218}Po, 0.9998 × ^{214}Pb, 0.0002 × ^{218}At, 1 × ^{214}Bi, 0.00021 × ^{210}Tl, 0.99979 × ^{214}Po, 0.030278 × ^{210}Pb, 0.029679 × ^{210}Bi, 0.015806 × ^{210}Po.

Table 3.11 BiotaDC parameters for a spherical freshwater reference organism with mass = $1{\cdot}10^{-6}$ kg following ICRP108

		^{226}Ra	^{222}Rn
Absorbed energy fraction	φ_{α}	$97.12{\cdot}10^{-2}$	$96.86{\cdot}10^{-2}$
	$\varphi_{low\ \beta-\gamma}$	$15.65{\cdot}10^{-5}$	$17.99{\cdot}10^{-5}$
	$\varphi_{high\ \beta-\gamma}$	$10.62{\cdot}10^{-3}$	$13.03{\cdot}10^{-3}$
Dose Conversion Coefficient (μGy/h per Bq/kg)	$\mathbf{DCC}_{external}$	$14.10{\cdot}10^{-4}$	$11.40{\cdot}10^{-4}$
	$\mathbf{DCC}_{internal}$	$14.20{\cdot}10^{-3}$	$11.40{\cdot}10^{-3}$

Values consider the contribution of radioactive progeny using ICRP108 method (decay chain cut-off at half-life longer than 10 days) [261].
Ratios for ^{226}Ra: 1 × ^{226}Ra, 1 × ^{222}Rn, 1 × ^{218}Po, 0.9998 × ^{214}Pb, 0.0002 × ^{218}At, 1 × ^{214}Bi, 0.00021 × ^{210}Tl, 0.999790 × ^{214}Po.
Ratios for ^{222}Rn: 1 × ^{222}Rn, 1 × ^{218}Po, 0.9998 × ^{214}Pb, 0.0002 × ^{218}At, 1 × ^{214}Bi, 0.00021 × ^{210}Tl, 0.999790 × ^{214}Po.

The respective calculations of the external dose rates (Eq. 3.8) follow a

similar logic. Here, the external dose rate depends on the activity concentration of the radionuclide in the environmental medium (water: C_{wtr} and sediments: C_{sed}), the external dose conversion coefficient (DCC_{ext}) specific to the radionuclide and the organism, as well as, the occupancy factor (ν). The latter expresses the fraction of time the organism spends in each of the environmental layers shown earlier in Fig. 3.12 (water surface, water, sediments surface, sediments) [19].

$$DR_{ext,v} = C_{media} \times DCC_{ext} \times v \tag{3.8}$$

with:

$DR_{ext,v}$ (μGy/h): external dose rate

C_{medium} (Bq/kg): activity concentration of the radionuclide in the medium

DCC_{ext} (μGy/h per Bq/kg): external exposure dose conversion coefficient

ν: occupancy factor

In the frame of the current work, considering that a microorganism can spend 90% of its life in the water and 10% on the sediments surface, the external dose rate due to a certain radionuclide can be expressed by Eq. 3.9.

$$DR_{ext} = C_{sed} \times DCC_{ext,sed} \times 0.1 + C_{wtr} \times DCC_{ext,wtr} \times 0.9 \tag{3.9}$$

Summarizing the approach of ERICA tool for the dose rate calculations, it should be first highlighted that once the user inputs water activity concentration data, these values are used for the calculation of the rest missing data via multiplication with the appropriate tabulated K_d or CR, with the latter being used only in the case of internal exposure. A second keypoint is that the extrapolated DCC have been calculated for a range of monoenergetic radiation types and reference organisms in the shape of spheres or ellipsoids. Another assumption is the uniform distribution of radionuclides in the organisms without considering their metabolic functions. These simplifications are necessary to cover the vast variety of biota and offer a first order approximation of exposure scenarios.

For the risk assessment in freshwater ecosystems, the dose rates from each radionuclide are first compared to the Screening Dose Rate (SDR) in order to calculate the expected risk quotient for the selected organism (R_{org}) as shown in Eq. 3.10. The suggested SDR for chronic exposure is equal to 10 μGy/h reflecting a threshold for the protection of the structure and function of ecosystems [257, 258, 268]. This value (10 μGy/h) has also been adopted in this work as a threshold dose rate.

$$R_{org} = \frac{DR_{org}}{SDR} \quad (3.10)$$

with:

R_{org}: risk quotient for organism

DR_{org} (μGy/h): dose rate to organism

SDR (μGy/h): screening dose rate

In Eq. 3.10, the dimensionless risk quotient acts a as a screening method to easily identify if the calculated dose rates exceed the SDR (R_{org}>1) or not (R_{org}<1). Since risk assessment is not in the context of this work, no further information will be provided for the methodology adopted by ERICA for the risk assessment. Nevertheless, it is stated that, according to FREDERICA radiation effects database, the concept of risk for phytoplankton should be interpreted as the risk of a negative effect on the growth ability with a morbidity endpoint [260, 268].

Main differences between ERICA v1.3 and v2.0

In ERICA v2.0, the values of K_d and CR have been updated. The dosimetric methodology of v1.3 complied with ICRP 108 [171] while the current methodology is consistent with ICRP 136 [172]. Using BiotaDC to supply the DCC databases, v2.0 has adopted a new approach for the dose rate calculations of short-lived radioactive progeny in decay chains. In the current work, the short-lived progeny were not taken into consideration, in compliance with the methodology used in Monte Carlo simulations showed in section 3.1. The option to perform Radon internal dosimetry for terrestrial organisms was also added in v2.0. The approach is based on inhalation models, thus it has been excluded from this work. In Table 3.12, the set of parameters for ^{226}Ra in the freshwater ecosystem concerning phytoplankton in both versions is shown.

The suggested K_d values for ^{226}Ra in freshwater ecosystems concern rivers and lakes. In Chapter 2 (section 2.4), the respective K_d values for 13 Auvergne mineral springs (where data was available) were calculated. As shown in Table 2.10, K_d for ^{226}Ra are in the range [591, 19889] L/kg. Showing significant variations from site to site, a mean K_d value for the mineral springs was not calculated. Comparing the minimum and maximum calculated K_d to the values suggested by ERICA (14035 L/kg [228] in v1.3 and 8466 L/kg [230] in v2.0), it could be argued that ERICA tool is not appropriate for dose rate calculations in mineral springs using the default K_d

values for freshwater ecosystems. Knowledge of the specific K_d for each mineral spring is needed.

Table 3.12 Default parameters for ^{226}Ra and phytoplankton in ERICA

		version 1.3	**version 2.0**
Distribution coefficient (L/kg)	**Kd**	14035	8466
Concentration ratio (Bq/kg per Bq/L)	**CR**	551	517
Dose Conversion Coefficient (µGy/h per Bq/kg)	$\mathbf{DCC}_{internal,low\,\beta}$	$1.63{\cdot}10^{-6}$	$2.04{\cdot}10^{-6}$
	$\mathbf{DCC}_{internal,\beta-\gamma}$	$1.50{\cdot}10^{-4}$	$1.50{\cdot}10^{-4}$
	$\mathbf{DCC}_{internal,\alpha}$	$1.38{\cdot}10^{-2}$	$1.39{\cdot}10^{-2}$
	$\mathbf{DCC}_{external,low\,\beta}$	$1.73{\cdot}10^{-12}$	not provided
	$\mathbf{DCC}_{external,\beta-\gamma}$	$1.42{\cdot}10^{-3}$	not provided
	$\mathbf{DCC}_{external}$	not provided	$1.39{\cdot}10^{-3}$

CR default values are taken from the Wildlife Transfer Database (WTD) for freshwater phytoplankton and Radium [228, 264, 269]. Microalgae accumulate radionuclides more than other aquatic organisms, and especially diatoms are prone to adsorption of radioactive heavy metals (for example ^{210}Pb, ^{210}Po, ^{241}Am) on their frustule but with a small uptake inside the cell [97, 100, 270]. Existing bibliography is limited to marine phytoplankton and does not provide explicit CR values [99, 271]. Some other studies state that the uptake of Radium is very low but they indicate that the biological uptake of ^{226}Ra is still a significant process [259, 272]. In conclusion, the applicability of the default CR values for phytoplankton in freshwater ecosystems on diatoms in mineral springs requires further investigation.

3.5 ERICA results

Dose rate calculations were conducted for the reference activity concentration of ^{226}Ra in the sediments (30 kBq/kg) using ERICA tool v1.3 and v2.0. As described earlier, 30 kBq/kg ^{226}Ra and 1000 Bq/L ^{222}Rn in water correspond to reference values for the Monte Carlo simulations of the current study. Due to the absence of ^{222}Rn parameters in ERICA, the dose rates on phytoplankton reference organism were evaluated only for ^{226}Ra and then compared to GATE results.

The assessment was performed in Tier 2 selecting the aquatic freshwater ecosystem and phytoplankton. 30 kBq/kg of ^{226}Ra were introduced in the

sediments and the phytoplankton was placed in 4 different positions represented by the corresponding occupancy factors. The four evaluation scenarios correspond to the organism living exclusively in water, exclusively on the sediments surface, exclusively in sediments or spending 10% of its lifetime on the sediments surface and 90% in water.

The ERICA default parameters for both versions are summarized in Table 3.12. It is remarked that there is no distinction among the four scenarios for the parameters. For the current assessment, it is highlighted that the impact of v2.0 approach concerning the contribution of the under-study radionuclide (^{226}Ra) daughters with $t_{1/2} > 10$ d is not presented. It is just stated that in all cases, the daughter nuclei with $t_{1/2} > 10$ d accounted for less than 0.2% of the total dose rates calculated by ERICA.

Dose rates

The dose rate results for internal and external exposure due to 30 kBq/kg ^{226}Ra are presented in Table 3.13. Four scenarios are considered and compared between the two versions for the phytoplankton: it is always submerged in water (Scenario 1), it lives on the sediments surface (Scenario 2), it is submerged in the sediments (Scenario 3), or it spends 90% of its lifetime in water and 10% on the sediments surface (Scenario 4).

Table 3.13 ERICA dose rates due to 30 kBq/kg ^{226}Ra in sediments

	Scenario 1		**Scenario 2**		**Scenario 3**		**Scenario 4**	
	v1.3	**v2.0**	**v1.3**	**v2.0**	**v1.3**	**v2.0**	**v1.3**	**v2.0**
DR$_{ext}$ (μGy/h)	0.0030	0.0049	21.28	20.82	42.56	41.64	2.13	2.09
DR$_{int}$ (μGy/h)	16.44	25.78	16.44	25.78	16.44	25.78	16.44	25.78

In all scenarios apart from Scenario 3 (organism submerged in the sediments), the default K_d (Table 3.12) is used to compute the ^{226}Ra activity concentration in water (Eq. 3.3). Respectively, the default CR (Table 3.12) are used to compute the activity concentration of ^{226}Ra inside the organism (Eq. 3.4) for the needs of internal dose rate calculations.

The external dose rates of the different scenarios depict the involvement of the occupancy factor in the external dosimetric calculations. For v1.3, the external dose rates are on average 2% higher than for v2.0 for all scenarios apart from Scenario 1 (phytoplankton constantly submerged in water). The internal dose rates are constant in each version no matter the considered scenario: 16.44 μGy/h in v1.3 and 25.75 μGy/h in v2.0 (36% higher compared to v1.3).

3.6 ERICA v2.0 vs GATE internal exposure dose rate calculations

Under the initial scope of evaluating the dose rates in the mineral springs using ERICA v2.0, several tests were performed in order to comprehend the impact of K_d , CR and occupancy factors on the dose rates calculations. A comparative study between another Monte Carlo simulation tool (MCNPX) and ERICA, for a macrometric marine reference organism showed a satisfactory agreement between the two tools [273]. In that case, K_d was known and the CR was provided by ERICA database. On the contrary, in the absence of K_d and CR for the mineral springs, the evaluation of the dose rates using ERICA is not an added value. In order to avoid using random values for K_d and CR, it was decided to examine an internal exposure scenario in which K_d is not needed and CR is equal to unit. Performing so, the internal dose rate calculations between ERICA v2.0 and GATE for 1 Bq/L ^{226}Ra were compared. The calculations assume a uniform distribution of the radionuclide within the organism.

For ERICA v2.0 the freshwater phytoplankton was selected (documented as a water sphere of 50 μm radius) and two new organisms of 10 μm and 621 μmd radii were created. The water sphere of 10 μm radius corresponds to the diatom modelled in the Monte Carlo simulation of the current study. Since the phytoplankton reference organism in ERICA is described as a water sphere of 50 μm radius but the mass limitations imposed by the tool do not permit masses less than $1{\cdot}10^{-6}$ kg, it was calculated that a spherical mass = $1 \cdot 10^{-6}$ kg and density = 1 g/cm^3 corresponds to a radius = 621 μm. In BiotaDC, the user is able to introduce only the mass (limited by 10^{-6} kg) and the shape of the organism but not the dimensions of the organism. As a result, no matter the radii of the spherical masses (10 μm, 50 μm, 621 μm radius) introduced in ERICA, BiotaDC does not take them into consideration.

In GATE, three water spheres were, respectively, modelled. The α-emitters of ^{226}Ra were placed randomly inside the water volumes, which represent the microorganisms, following a uniform distribution. Absorbed energy fractions for the α-particles ($\varphi_{\alpha,GATE}$ - Eq. 3.11), internal Dose Conversion Coefficients ($DCC_{int,GATE}$ - Eq. 3.12) and internal Dose Rates ($DR_{int,GATE}$) were calculated in each case using GATE. Internal DCC and DR ($DCC_{int,BiotaDC}$, $DCC_{int,ERICA}$, $DR_{int,ERICA}$), as well as, $\varphi_{\alpha,BiotaDC}$ from BiotaDC and ERICA were also retrieved. A summary of the data is provided in Table 3.14.

$$\phi_{\alpha,GATE} = \frac{E_{dep}}{E_{emit}} \tag{3.11}$$

with:

$\phi_{\alpha,GATE}$: absorbed energy fraction for α-particles calculated with GATE

E_{dep}: energy deposited to the organism

E_{emit}: energy emitted by the source

$$DCC_{int,GATE} = \frac{DR_{int,GATE}}{C_{org}} \tag{3.12}$$

with:

$DCC_{int,GATE}$ (μGy/h per Bq/kg): internal dose conversion coefficient using GATE

$DR_{int,GATE}$ (μGy/h): internal dose rate

C_{org} (Bq/kg): activity concentration of radionuclide inside the organism

Table 3.14 ERICA vs GATE for 1 Bq/L ^{226}Ra internal exposure

	Radius (μm)	**10**	**50**	**621**
Absorbed energy fraction for α-particles	$\varphi_{\alpha,BiotaDC^*}$	0.9712	0.9712	0.9712
	$\varphi_{\alpha,GATE}$	0.1568	0.7110	0.9773
Internal Dose Conversion Coefficient (μGy/h per Bq/kg)	$\mathbf{DCC}_{int,BiotaDC}$	$1.41{\cdot}10^{-2}$	$1.41{\cdot}10^{-2}$	$1.41{\cdot}10^{-2}$
	$\mathbf{DCC}_{int,ERICA}$	$1.39{\cdot}10^{-2}$	$1.39{\cdot}10^{-2}$	$1.39{\cdot}10^{-2}$
	$\mathbf{DCC}_{int,GATE}$	$4.23{\cdot}10^{-4}$	$1.96{\cdot}10^{-3}$	$2.69{\cdot}10^{-3}$
Internal Dose Rate (μGy/h)	$\mathbf{DR}_{int,ERICA}$	$1.41{\cdot}10^{-2}$	$1.41{\cdot}10^{-2}$	$1.41{\cdot}10^{-2}$
	$\mathbf{DR}_{int,GATE}$	$4.23{\cdot}10^{-4}$	$1.96{\cdot}10^{-3}$	$2.69{\cdot}10^{-3}$

$\varphi_{\alpha,BiotaDC^*}$: BiotaDC takes as inputs only the mass and the shape of the organism, but not its dimensions.

The constant φ values provided by BiotaDC and the differences compared to GATE are first highlighted. It is reminded that the only parameter calculated by MC simulation in BiotaDC is the absorbed energy fraction φ.

Focusing on the column concerning the 621 μm radius in Table 3.14, it is observed that although the φ values are in excellent agreement between GATE and BiotaDC, the corresponding DCC values and dose rates differ by 1 order of magnitude. A further step was taken to evaluate the discrepancy between $DCC_{BiotaDC}$ and DCC_{GATE}: a validation of the applicability of Eq. 3.6 (calculation of DCC using absorbed energy fractions) on the Monte Carlo simulation results of the current study was performed. Both $DCC_{BiotaDC}$ and DCC_{GATE} were successfully reproduced by applying Eq. 3.6 to the respective

$\varphi_{\alpha,BiotaDC}$ and $\varphi_{\alpha,GATE}$ values. It was found out that the deviation of DCC_{GATE} from $DCC_{BiotaDC}$ (a correction factor 5.2) is attributed to the energies of the radionuclides considered in the calculations: in GATE, only ^{226}Ra was considered while BiotaDC takes into account the emissions of ^{226}Ra and its daughter nuclei with half-lives less than 10 days as shown before in Table 3.11: ^{222}Rn, ^{218}Po, ^{214}Pb, ^{214}Bi and ^{210}Tl.

Additionally, the suggested, by Ulanovsky et al. [266], methodology for extrapolating DCC to masses lower than the ERICA limit value ($1{\cdot}10^{-6}$ kg) was evaluated using Eq. 3.13.

$$DCC_{int}(m) = DCC_{int}(m_0) \times \frac{m}{m_0} \tag{3.13}$$

with:

$DCC_{int}(m)$: internal exposure DCC for an organism of mass $m < m_0$

m: mass of organism

$m_0 = 1 \cdot 10^{-6}$ kg

It was calculated that for m = $4.189{\cdot}10^{-12}$ kg, which corresponds to the diatom modelled as a sphere of 10 μm radius composed by water of ρ = 1. g/cm^3, the extrapolated dose conversion coefficient would be $DCC_{int} = 5.95 \cdot 10^{-8}$ μGy/h per Bq/kg. The respective DCC calculated using GATE is $DCC_{int,GATE} = 4.23 \cdot 10^{-4}$ μGy/h per Bq/kg (see Table 3.14 - column corresponding to radius = 10 μm). Taking into consideration the correction for the energies described in the previous paragraph, the final discrepancy between the suggested extrapolated DCC value and the calculated $DCC_{int,GATE}$ corresponds to 3 orders of magnitude.

Although, an earlier study by Pappa et al. [273] showed a satisfactory agreement between ERICA (v1.3) and MCNPX for a macroscopic organism, the current study showed that the results are greatly affected by the mass limitations on ERICA organisms. These results justify the statement in the work of Ulanovsky et al. [266] where the methodology to extrapolate DCC to masses lower than ERICA limit value ($1{\cdot}10^{-6}$ kg) is suggested: "these extrapolations may be inappropriate for very small organisms (e.g. bacteria) because the sizes and the masses of these organisms are close to the limits of conventional dosimetry".

It was concluded that the lack of the appropriate K_d and CR for the mineral springs, as well as, the imposed mass limit does not allow for the performance of risk assessment using ERICA tool.

Conclusion

In this chapter, the dose rates received by the microorganisms living in the ecosystem of naturally radioactive mineral springs were calculated. Two approaches were implemented: direct microdosimetric calculations using GATE and the ICRP dosimetric approach followed by ERICA.

The calculations of external and internal dose rates on microorganisms were based on the experimental measurements performed in Chapter 2. The study focused on α-emitting radionuclides (^{222}Rn, ^{226}Ra, ^{210}Po and ^{238}U) and three external exposure environments in GATE: dry sediments, water column and a benthic homogeneous mixture where benthic diatoms are found to spend the great majority of their life.

For the external dose rates normalized to the Reference Activity Concentrations (RAC: [^{238}U]= 0.3 kBq/kg, [^{226}Ra]= 30 kBq/kg, [^{222}Rn]= 1000 Bq/L, [^{210}Po] = 0.4 Bq/L), it was shown that the microorganisms living in the dry sediments are exposed to 33 times higher dose rates in comparison to those living solely in water (92.46 μGy/h and 2.79 μGy/h, respectively). For those living in the benthic mixture, the total dose rate is 10.9 μGy/h which drops to 9.72 μGy/h for diatoms with a frustule of 2 μm thickness and density equal to 2.4 g/cm^3. The dose rates at the benthic mixture are comparable to the 10 μGy/h dose rate threshold suggested for the protection of the ecosystems. It is highlighted that the main contributions to the dose rates originate from the high activity concentration of ^{226}Ra in the dry sediments and ^{222}Rn in water, while the contributions from ^{238}U and ^{210}Po are almost negligible (less than 0.6%).

The internal exposure was evaluated under the assumption of homogeneous distribution of α-emitters inside the microorganism and without considering their metabolic and biokinetic behaviour. For diatoms in the benthic mixture characterized by the Reference Activity Concentrations (RAC), the current work predicts an internal exposure (13.5 μGy/h) higher than the external one (9.72 μGy/h).

The evaluation of ERICA efficacy on calculating dose rates for microorganisms in radioactive mineral springs showed that the tool is not suitable for microdosimetric assessments. In particular, it was concluded that the absence of essential parameters that get involved in the calculations, namely the distribution coefficient (K_d) and the equilibrium concentration ratios (CR), for the mineral springs does not allow the performance of risk assessment using ERICA. It is also evident that a full assessment cannot be performed if the user cannot provide site specific K_d values for all the

radionuclides of interest. Additionally, the inability of calculating K_d for ^{222}Rn due to its chemical inertia makes ICRP approach unsuitable for dose rate calculations using the ICRP approach for microorganisms in aquatic environments. As a result, the initial intention of running an assessment using ERICA tool for all the measured radiosotopes in the mineral springs in Auvergne was not feasible.

After the evaluation of the dose rates received by microorganisms in the naturally radioactive mineral springs using GATE in the current chapter, nanodosimetric simulations were performed to assess the respective DNA damage as described in Chapter 4.

Chapter 4

Nanodosimetry and prediction of DNA damage

Introduction

Following the external exposure scenarios described in Chapter 3 for ^{222}Rn, ^{226}Ra, ^{210}Po and ^{238}U, the specific energy distributions were collected in nanometric targets resembling nucleosomes. The simulation was based on "dnaphysics" open-access advanced example provided within the Geant4 toolkit [194, 274].

DNA damage was evaluated for both external and internal exposure scenarios for the microorganisms living in naturally radioactive mineral springs. The calculations of Single and Double DNA Strand Breaks (SSB and DSB, respectively) were performed using the DBSCAN (Density Based Spatial Clustering of Applications with Noise) algorithm after the respective Geant4-DNA example [212, 275].

In Section 4.1, the description of the simulation setup begins with the presentation of the common parameters used in both examples. Then, it is divided in two main parts dedicated respectively to each Gean4-DNA example the current simulation was based on. For each case, the modifications performed, the resulted geometry and the output are presented.

The results are divided in two parts. In section 4.2, the specific energy distributions attributed to different mechanisms for electrons and Helium (He) ions are presented for nucleosomes. In section 4.3, the validation of DBSCAN clustering algorithm for α-particles against the available bibliography is first shown. Then, the SSB and DSB were evaluated for the external exposure normalized to Unit Activity Concentrations (UAC: 1 Bq/L for radionuclides measured in water, 1 Bq/kg for radionuclides measured in the dry sediments). Respective calculations were performed for the external exposure normalized to the Reference Activity Concentrations (RAC: [^{222}Rn]= 1000 Bq/L, [^{226}Ra]= 30 kBq/kg, [^{210}Po]= 0.4 Bq/L, [^{238}U]= 0.3 kBq/kg). In the end, the evaluation of DNA damage due to internal exposure was also attempted.

4.1 Geant4-DNA simulation setup

Geant4-DNA based on Geant4 version 11.0.0 was used to simulate track structure of particles inside the microorganism's nucleus from the phase space ('PhaseSpace' - 'PhSp') file produced with GATE (Chapter 3). The genetic material, considered only in the nucleus in the current study, is known to be the sensitive target of ionising radiation.

The current simulations are based on dnaphysics [274] and clustering [275] advanced examples provided by the Geant4-DNA collaboration. Geant4 is written in C++ and follows the common structure of headers and source files. As shown in Fig. 4.1, the common principal source files of the code include the geometry modelling (DetectorConstruction.cc), the description of the source - particles (PrimaryGeneratorAction.cc) and the physics processes (PhysicsLists.cc), as well as, the description and record of the parameters of the desired output (RunAction.cc and SteppingAction.cc).

The launch of the simulation is called via the ActionInitialization.cc. A new feature had to be implemented (G4UserPhaseSpaceReader.cc) allowing the reading of HDF5 (.h5) files [276]. This work was performed by MSc student Sarra Lanouar and it is briefly described below. A summary of the Geant4-DNA simulation setup is presented in Table 4.2.

```
ActionInitialization.cc
DetectorConstruction.cc
DetectorMessenger.cc
G4UserH5PhaseSpaceReader.cc
PhysicsList.cc
PrimaryGeneratorAction.cc
RunAction.cc
SteppingAction.cc
```

(a) Source files of dnaphysics

```
ActionInitialization.cc
ClusteringAlgo.cc
ClusteringAlgoMessenger.cc
ClusterSBPoints.cc
CommandLineParser.cc
DetectorConstruction.cc
EventAction.cc
G4UserH5PhaseSpaceReader.cc
PhysicsList.cc
PrimaryGeneratorAction.cc
RunAction.cc
RunActionMessenger.cc
RunInitObserver.cc
SBPoint.cc
SteppingAction.cc
```

(b) Source files of clustering

Figure 4.1 Geant4 source files in (a) dnaphysics code and (b) clustering code

Common parameters

The simulations focus on the nucleus which is modelled as a water ("G4_WATER" [246]) sphere of 0.5 μm radius. "G4EmDNAPhysics_option4" physics list was used in all cases because it includes an upgraded energy-loss model for water molecules ionisation and

excitation due to low energy electrons (below 10 keV) which has been thoroughly validated by Geant4-DNA collaboration [277]. In Geant4-DNA, all interactions are simulated explicitly and no production cuts are applied. As shown in Table 4.1, where the different models applied for electrons and α-particles are summarized, electrons are transported down to 10 eV approximating the ionization threshold of water in the liquid phase [278].

Table 4.1 G4-DNA models implented in emDNA4 Physics List

Particle	G4-DNA Process Name	G4-DNA Model	Energy Range
electron	e-_G4DNAElectronSolvation	DNAOneStepThermalization	0 - 10 eV
	e-_G4DNAElastic	DNAUeharaScreenedRutherfordElastic	0 - 1 MeV
	e-_G4DNAExcitation	DNAEmfietzoglouExcitation	0 - 10 keV
	e-_G4DNAIonisation	DNAEmfietzoglouIonisation	0 - 10 keV
alpha	alpha_G4DNAElastic	DNAIonElastic	0 - 1 MeV
	alpha_G4DNAExcitation	DNAMillerGreenExcitation	0 - 400 MeV
	alpha_G4DNAIonisation	DNARuddIonisation	0 - 400 MeV
	alpha_G4DNAChargeDecrease	DNADingfelderChargeDecrease	0 - 400 MeV

The different simulated environments (dry sediments: 0% porosity, benthic mixture: 90% porosity, water column: 100% porosity) are represented by the respective phase space (PhSp) files collected with GATE. Their initial format is root which is then transformed to h5 through a python script. The introduced G4UserH5PhaseSpaceReader header and source files, as well as the modified PrimaryGeneratorAction.cc are provided in Appendix F.

Using the phase space files, the particles are shot isotropically from the surface of the nucleus (radius= 0.5 μm). In Fig. 4.2, an OpenGL representation of the simulated water nucleus crossed by an α-particle of 2.5 MeV kinetic energy emitted from the surface towards the center the sphere is shown. The track of the α-particle itself is an almost straight line accompanied by the tracks (red lines) of the secondary electrons. These low energy secondary electrons are responsible for a great part of the energy deposition along the track of the α-particle. In this illustration, only a small part of the interactions taking place in the first 1 μm of the total 14.3 μm long track of the 2.5 MeV α-particle in the water can be seen. The interactions taking place in the water medium outside the 1 μm diameter nucleus are not shown in this OpenGL view. As it will shown later (Table 4.3), the 2.5 MeV is representative of the kinetic energy of α-particles reaching the nucleus after their initial emission in the environment.

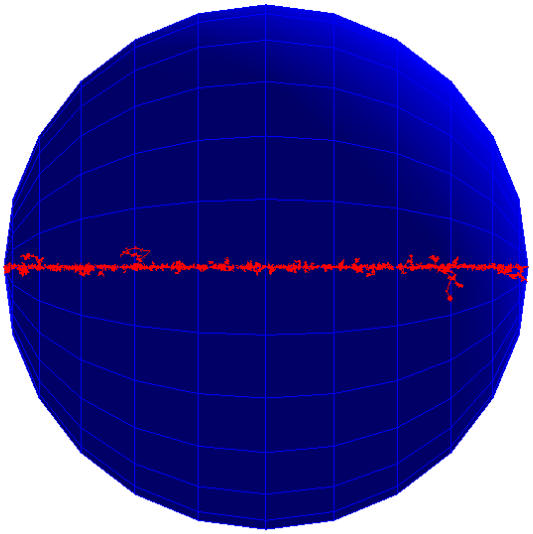

Figure 4.2 OpenGL representation of a track belonging to a 2.5 MeV α-particle emitted from the surface of the 1 μm diameter water nucleus with direction towards the center of the nucleus. Red lines represent the tracks of the secondary electrons. The interactions outside the nucleus are not shown.

Specific energy distributions

Using the α-particles generated from the phase space file as source, the distribution of deposited energies using the simplified model suggested by D.E. Charlton [279] were collected. 30000 water cylinders were simulated, representing nucleosomes (approximately 147 base pairs each) of 10 nm diameter and 5 nm height made of water. They were generated in random positions in the spherical nucleus of the microorganism. In Fig 4.3, one of the 30000 simulated cylinders (green) is depicted. The red lines represent the tracks of the secondary electrons produced due to the interactions of a 2.5 MeV α-particle (blue line) with the nucleus (water).

Energy depositions were collected in the randomly distributed cylindrical targets and the probability distributions of the specific energies (dP/dz) over all the nucleosomes were calculated. Specific energies usually result from several energy transfers in a given nanometric target and therefore from several physical processes. A physical process can, however, be assigned to to each specific energy by considering the dominant process which leads to the largest contribution of energy deposition. This allows the study of the total specific energy spectra and the different contributions from dominant processes.

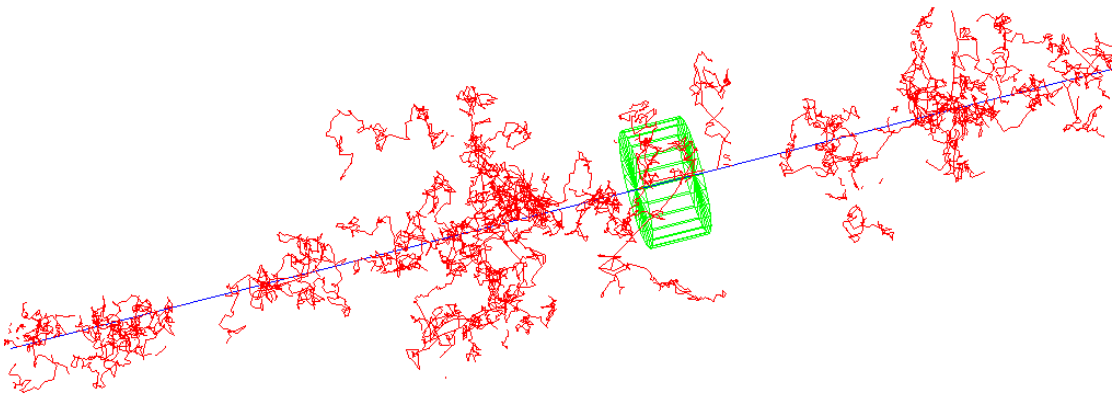

Figure 4.3 OpenGL representation of 1 cylinder representing a nucleosome traversed by a 2.5 MeV α-particle in water (blue line). Red lines represent the tracks of secondary electrons.

Single and Double DNA Strand Breaks

The assessment of radiation induced SSBs and DSBs was performed by the DBSCAN clustering algorithm [215]. It is based on the assumption that the nucleus is occupied by uniformly distributed DNA molecules, which is actually indicative of diatoms presenting an active metabolic activity [280]. Thus, it makes it possible to predict the potential DNA damage without the use of sophisticated DNA geometry. Such geometry is not available for the diatoms inhabiting the mineral springs because their genome has not been sequenced yet. For this reason, the assumption of a 1 μm diameter nucleus enclosing 27.4 Mbp of genetic material was made. The generation time considered for diatoms was 24 hours (1 day) following the study of Krasovec et al. [281].

The formation of SSB in this algorithm is a function of the energy deposited following a probability distribution function. For deposited energies (E_{dep}) below 5 eV the damage probability is considered zero while it increases linearly up to 37.5 eV. For $E_{dep} \geq 37.5$ eV the algorithm considers that all the events can cause SSB. The minimum number of SSB to form a DSB is set to 2 within a radius of 3.3 nm, representing roughly the distance between 10 DNA base pairs. The indirect DNA damage due to the radicals formation after water radiolysis is taken into consideration in the free parameter 'SPointProb'. It describes the probability that an interaction point is located in a sensitive area, composed by the DNA helix and a virtual aura, where both direct and indirect

DNA damages can occur.

The example provided by Geant4-DNA collaboration was initially validated for protons using as source an external beam irradiating a water cube of 0.5 μm edge. For the needs of the current work, the geometry of the target was modified to a water sphere of 0.5 μm radius to resemble the microorganism's nucleus and the source was placed on its surface. Among the main assumptions, a 27.4 Mbp genetic material was considered for the model microorganism in the lack of genomic information concerning the diatoms of the local mineral springs (see Section 2.5). The selected DNA length is consistent with the widely used as model diatom *Phaeodactylum tricornutum* [282–287].

Strong correlations between the genome size and phenotypic characteristics, such as nuclear and cell volume, are abundantly documented in the literature for eukaryotes [288]. As a consequence, the 'SPointProb' parameter is not expected to change significantly among eukaryotes. Still, different values of the free parameter 'SPointProb' were tested in order to validate the algorithm against simulation and experimental data from the literature.

The prediction of SSB and DSB was performed for both external and internal exposure scenarios using the respective phase space files as source (Fig. 4.4). For the evaluation of the DNA damage due to the external exposure, the phase space collected at the boundary of the nucleus, recording particles initially emitted in the different simulated environments, was used.

For the needs of the evaluation of the DNA damage due to internal exposure, the microorganism was modelled with its nucleus, the primary α-particles were distributed uniformly inside the microorganism and the phase space of the α-particles entering the nucleus was collected. This phase space was then used as a surfacic source for the irradiation of the nucleus.

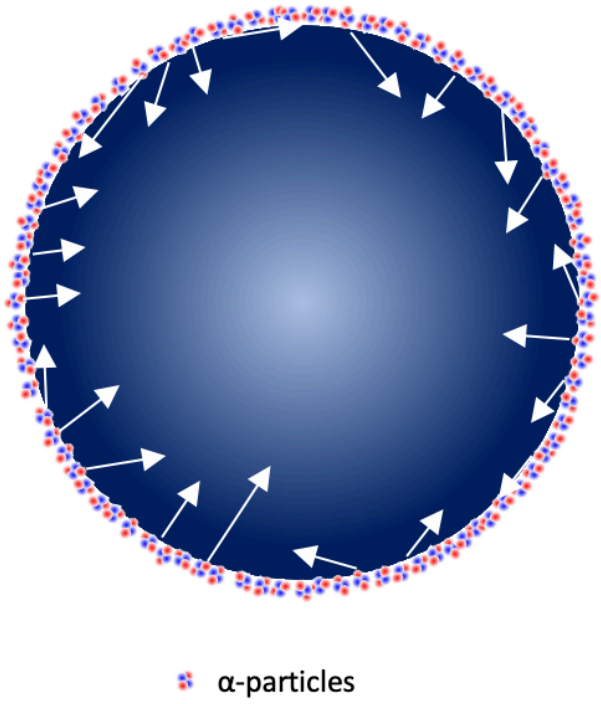

Figure 4.4 Schematic representation of PhaseSpace source placed on the surface of the nucleus for the DNA damage simulation. Blue sphere represents the nucleus. Arrows represent the directions of α-particles. The scale is not representative.

Table 4.2 Summary of Geant4-DNA simulation characteristics

	nucleus	**nucleosomes**
Dimensions	radius: 500 nm	diameter: 10 nm height: 5 nm
Material	G4_WATER	
Density (g/cm^3)	1.00	
Source	α-particles from PhaseSpace	
Physics Lists	G4EmDNAPhysics_option4	

4.2 Specific energy distributions - Results

From the 10^8 primaries initially emitted in the environment, only very few alphas reached the nucleus ($2{\cdot}10^3$ - $3{\cdot}10^3$). In Table 4.3, the mean and maximum kinetic energies of the α-particles entering the nucleus for the different simulated environments are presented. Whatever the considered environment, the mean energy of α-particles reaching the nucleus is around 2.3 MeV corresponding to a range of 13 µm, 13 times higher than the

nucleus diameter considered (1 μm). Consequently, a very small fraction of energy (around 0.07%) is deposited to the nucleus.

The α-particles of ^{226}Ra reach the nucleus with an average 22% reduced mean energy compared to their initial emission in the environment, while with the frustule the loss is about 27%. A similar trend is observed for ^{222}Rn and ^{210}Po with 20% losses on average. The least energetic α-particles come from ^{238}U with an initial maximum kinetic energy of 4.2 MeV emitted in the environment. When entering the nucleus of the microorganism, their mean kinetic energy has dropped to 1.7 MeV and it gets further decreased to 1.4 MeV in the case of diatoms (microorganism surrounded by frustule). As a result, ^{238}U α-particles have the shortest range in the water accounting for an average 8.5 μm.

Table 4.3 Kinetic energy of α-particles reaching the nucleus for the different simulated environments (when considering frustule, values are provided in the parentheses)

			Kinetic energy (MeV)	
Porosity (%)	**Environment**	**Radionuclide**	**mean**	**maximum**
0	Dry sediments	^{226}Ra	2.1	3.9
90	Benthic Mixture	^{238}U (frustule)	1.7 (1.4)	3.2 (2.8)
		^{226}Ra (frustule)	2.1 (1.9)	3.9 (3.5)
		^{222}Rn (frustule)	2.7 (2.4)	4.9 (4.4)
		^{210}Po (frustule)	2.5 (2.3)	4.5 (4.1)
100	Water	^{222}Rn	2.7	4.9

The specific energy probability distributions collected for the nucleosomes of diatoms in the benthic mixture (90% porosity considering the frustule) are presented in Figures 4.5 - 4.7. For the nanodosimetric assessment, ^{222}Rn, ^{226}Ra, ^{238}U and ^{210}Po are no further distinguished in the benthic mixture.

Fig 4.5 presents the total specific energy probability distribution, while Fig 4.6 and 4.7 present the distributions associated to the main physical processes. It is highlighted that the main contributions come from He ions and electrons. The different ionised states of He are a result of the passage of α-particles though the matter. The α-particles represent the doubled ionised state of He atoms. Among their other interactions with the surrounding, α-particles attract and acquire electrons. Initially, they get transformed to He^+ by acquiring one electron. When He^+ acquire the second electron which makes them neutral, they are denoted as He atoms.

The terminology used by Geant4 concerning the mechanisms describing

the energy depositions was also adopted in the current work. In Fig 4.6, the distribution of the energy deposited to the nucleosomes attributed to He ions "ionisations" is shown. In Geant4-DNA, when He ions reach very low kinetic energy thresholds (<1 keV) their tracking is stopped and their energy is deposited locally. Thus, the mechanisms shown in Fig 4.6 corresponds to the energy deposited locally by He ions of low kinetic energies.

The distribution of specific energy deposition to the nucleosomes attributed to electrons are shown in Fig. 4.7. The major energy-loss mechanisms of α-particles are electronic excitation and ionisation. As described for He ions, when the kinetic energy of these electrons falls below very low values, they are no further tracked and their energy is deposited locally. These energy depositions are annotated as "e^- Excitation" and "e^- Ionisation", respectively. Similarly, the term "e^- Solvation" refers to the thermalization of secondary electrons.

Particularly solvated electrons, known to play an important role in the damaging effects to the DNA [162,163], contribute to 15% of the total specific energy, while the contributions of ionised and excited electrons, as well as α-particles, to the total specific energy are 32.5% and 19.6% respectively.

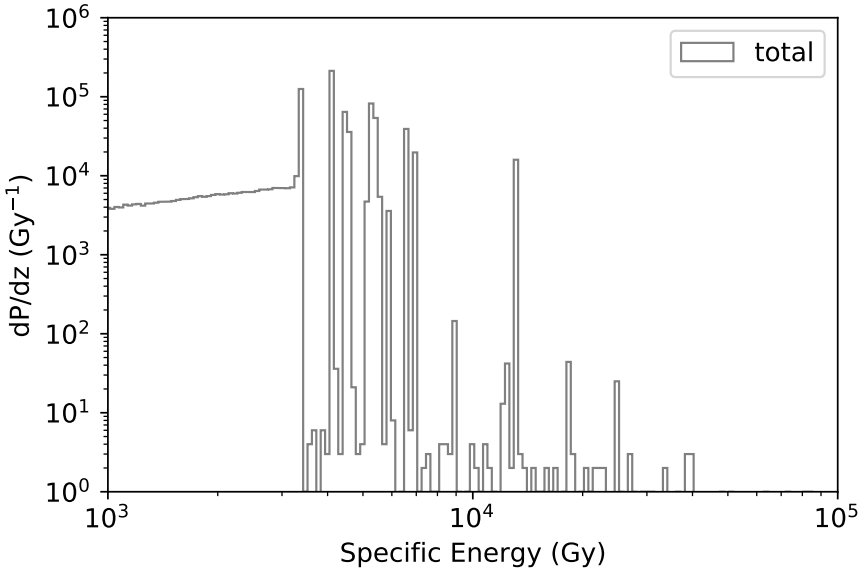

Figure 4.5 Total specific energy probability distribution for diatom nucleosomes in the benthic mixture (90% porosity). Grey: All processes.

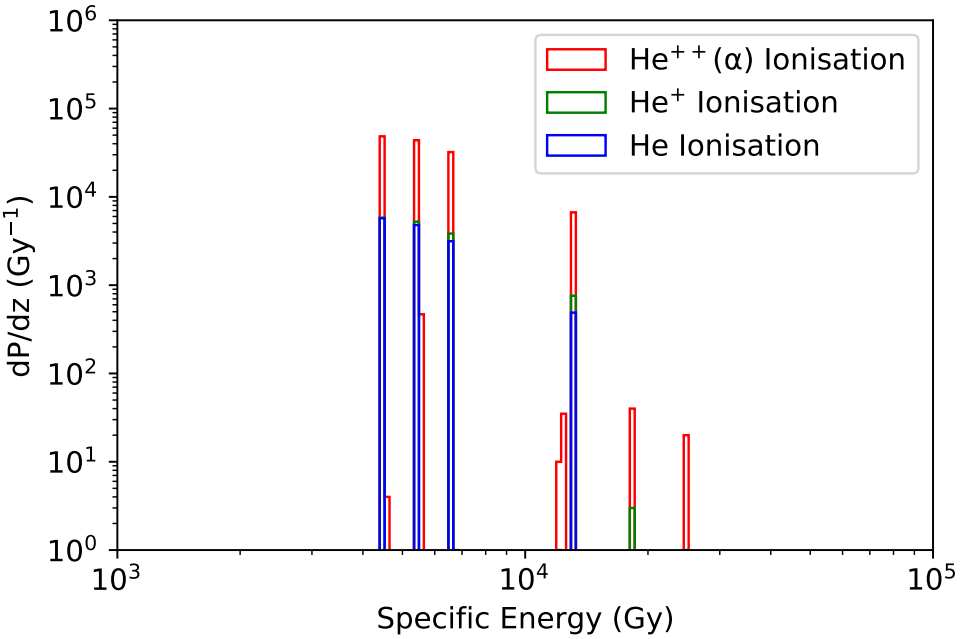

Figure 4.6 He ions specific energy probability distributions for diatom nucleosomes in the benthic mixture (90% porosity). Red: α-particles (He^{++}), Green: He^+, Blue: He atom.

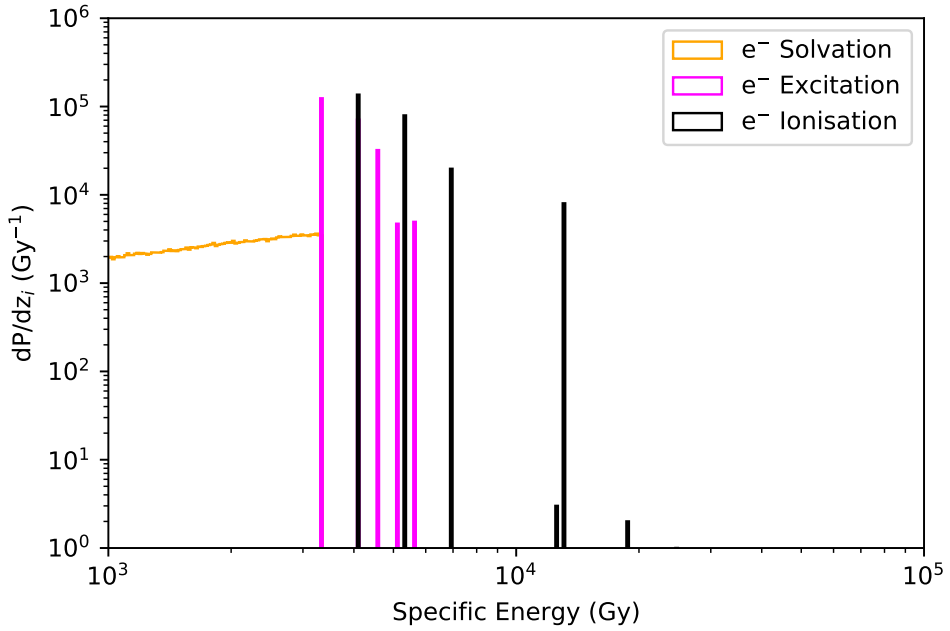

Figure 4.7 Electrons specific energy probability distributions for diatom nucleosomes in the benthic mixture (90% porosity). Orange: electrons solvation, Purple: electrons excitation, Black: electrons ionisation.

4.3 Single and Double DNA Strand Breaks - Results

Validation of DBSCAN algorithm for α-particles

The DSB/Gy/Mbp for four different SPointProb values of the free parameter in the DBSCAN algorithm for monoenergetic α-particles are plotted against the available literature in Fig 4.8. The algorithm has already been validated for protons using 16% [215] and 20% SPointProb [212] to fit respective experimental and simulation data. For α-particles in the energy range of 2 MeV-10 MeV, 20%, 16%, 12% and 8% SPointProb were tested in an effort to best fit the results of the present work with Moeini et al. and the references included in that article [289].

The available bibliography for α-particles included different simulation codes, clustering algorithms and geometries, as well as, experimental data. None of them used Geant4-DNA coupled with the DBSCAN algorithm as performed in the current study.

Moeini et al. [289] performed simulations with Geant4-DNA using 216 bp long double DNA helix. Nikjoo et al. [290] used the same model but employed PITS (Positive Ion Track Simulation) Monte Carlo code. Friedland et al [291] used PARTRAC (PARticles TRACks) Monte Carlo code to simulate DSB at the nucleus of human fibroblast cells. Semenenko et al. [292] implemented their own algorithm (MCDS Monte Carlo Damage Simulation [293]) on DNA segments.

The three available experimental datasets concern DNA extracted from T7 bacteriophage (Neary et al. [294]), from human skin fibroblasts (Frankenberg et al. [295]) and V79-4 mammalian cells (Jenner et al. [296]).

As shown in Fig. 4.8, the predicted values of the current work are in fair agreement with the experimental and other simulation results using different Monte Carlo codes. The overprediction of DSBs when using the suggested values of 16% [215] and 20% [212] smooths when lowering the value. 12% offers a good agreement with Moeini et al. [289] but the SpointProb equal to 8% was finally selected due to the better agreement with the experimental results, too.

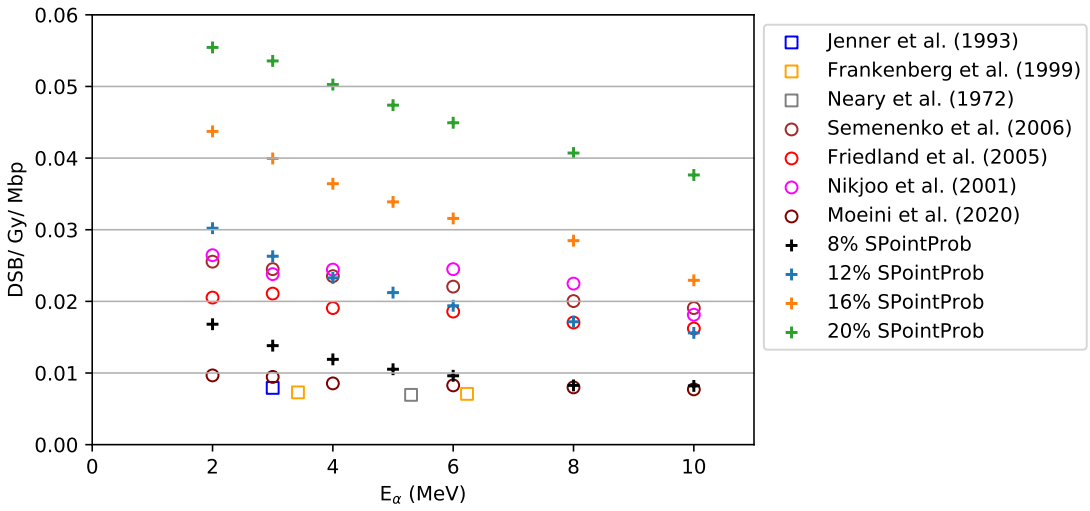

Figure 4.8 Number of DSB per Gray per Mbp as a function of the energy of α-particles
(+): different values of the SPointProb parameter in the current work,
(○): simulations using other codes found in the literature [289–292],
(□): experiments found in the literature [294–296]. Statistical uncertainties: current work : $<$ 1% - not visible, literature: not provided.

DNA damage due to external exposure

In Table 4.4, the SSB and DSB obtained per Gray and per Mbp using the DBSCAN clustering algorithm (8% SPointProb) for the different simulated environments are listed. Assuming one generation of the microorganisms per day, the SSB and DSB per generation normalised to 27.4 Mbp and, to 1 day-exposure to unity (UAC) and reference activity concentrations (RAC: [^{222}Rn]=1000 Bq/L, [^{226}Ra]=30 kBq/kg, [^{210}Po]=0.4 Bq/L, [^{238}U]=0.3 kBq/kg) are present in the same table. The dose rates to the microorganisms are also provided (GATE results in Chapter 3). The assumption of one microorganism generation per day is based on the study of Krasovec et al. [281]. For the results in the benthic mixture, the contribution of all the simulated radionuclides are summed.

It is observed that the highest number of SSB/Gy/Mbp and DSB/Gy/Mbp is predicted for the benthic mixture (0.30 and 0.07, respectively), while the frustule decreases the values by 6%. The number of SSB/Gy/Mbp originating solely from ^{222}Rn in the water is 14% higher than from ^{226}Ra in the dry sediments, while DSB/Gy/Mbp is 0.02 in both cases. It should be highlighted here, that according to Table 4.3 and Fig. 4.8, the predicted DSB values of the present work correspond to α-particles with kinetic energies lower than 2 MeV.

Table 4.4 SSB and DSB due to external exposure (when considering frustule, values are provided in the parentheses)

Porosity (%)	**0**	**90**	**100**
Environment	**Dry sediments**	**Benthic Mixture**	**Water column**
Radionuclide	^{226}Ra	^{238}U, ^{226}Ra, ^{222}Rn & ^{210}Po (frustule)	^{222}Rn
SSB/Gy/Mbp	0.07	0.30 (0.29)	0.08
DSB/Gy/Mbp	0.02	0.07 (0.07)	0.02
Results per Unit Activity Concentrations (UAC)			
External DR (μGy/h)	$3.08{\cdot}10^{-3}$	$5.40{\cdot}10^{-3}$ ($4.92{\cdot}10^{-3}$)	$2.79{\cdot}10^{-3}$
SSB/generation/UAC	$1.50{\cdot}10^{-7}$	$2.80{\cdot}10^{-7}$ ($2.48{\cdot}10^{-7}$)	$1.47{\cdot}10^{-7}$
DSB/generation/UAC	$3.54{\cdot}10^{-8}$	$5.85{\cdot}10^{-8}$ ($5.45{\cdot}10^{-8}$)	$2.98{\cdot}10^{-8}$
Results per Reference Activity Concentrations (RAC)			
External DR (μGy/h)	92.51	10.92 (9.72)	2.83
SSB/generation/RAC	$4.50{\cdot}10^{-3}$	$5.45{\cdot}10^{-4}$ ($4.70{\cdot}10^{-4}$)	$1.47{\cdot}10^{-4}$
DSB/generation/RAC	$1.06{\cdot}10^{-3}$	$1.22{\cdot}10^{-4}$ ($1.12{\cdot}10^{-4}$)	$2.98{\cdot}10^{-5}$

External DR: External Dose Rates to microorganisms (section 3.2).
The calculations are performed for 1-day internal exposure to UAC, RAC, considering 1 generation/day and 27.4 Mbp DNA length.
RAC: [^{226}Ra] = 30 kBq/kg, [^{222}Rn] = 1000 Bq/L, [^{238}U] = 0.3 kBq/kg, [^{210}Po] = 0.4 Bq/L.

When normalizing to the Unit Activity Concentrations (UAC), the number of strand breaks per generation are in the order of magnitude of 10^{-7} for SSB and 10^{-8} for DSB, respectively. Focusing on the DSB/generation normalized to the Reference Activity Concentrations (RAC), it is observed that the highest values are predicted for the dry sediments environment ($1.06{\cdot}10^{-3}$ DSB/generation/RAC corresponding to 92.5 μGy/h due to ^{226}Ra). On the other hand, the predicted DSB/generation/RAC for microorganisms without frustule exposed to 2.8 μGy/h due to ^{222}Rn is approximately $3{\cdot}10^{-5}$.

Considering that the most realistic exposure scenario is represented by the simulated benthic mixture, it is noticed that the DSB/generation between microorganisms and diatoms do not differ noticeably ($1.22{\cdot}10^{-4}$ DSB/generation/RAC and $1.12{\cdot}10^{-4}$ DSB/generation/RAC, respectively). The predicted value of DSB/generation for diatoms in the current work is 2 orders of magnitude lower than the estimated spontaneous mutation rate indicated in the study of Krasovec et al. [281]. Their research focused on the experimental determination of the spontaneous base-substitution and base-insertion-deletion mutation rate in the genome of *P. tricornutum*.

According to their results, the spontaneous mutation rate per generation is approximately $1.29 \cdot 10^{-2}$.

When Lampe et al. [297] conducted similar studies for the DNA damage induced on the prokaryotic *Escherichia coli* due to the natural background radiation, they observed that it was responsible for $2.8 \cdot 10^{-8}$ DSB/day. They also estimated that the total dose rate corresponding to the background radiation (^{40}K, terrestrial γ-background, cosmic neutrons and muons) was 0.23 μGy/h [298]. As *E. coli* spontaneous mutation rate from endogenous causes is 5 orders of magnitude higher ($1 \cdot 10^{-3}$/genome/generation) [299], they concluded that the radiation background likely had only a very small mutational effect on the biological system under study. It is worth mentioning that the results of the current work for microorganisms (without frustule) in the benthic mixture, normalized to Unit Activity Concentrations (UAC) for ^{222}Rn, ^{226}Ra, ^{210}Po and ^{238}U, are in the same order of magnitude with the Lampe et al. prediction (10^{-8} DSB/generation/UAC considering 1 generation/day).

The results of the current study could also be related to the observed correlation between natural bedrock radioactivity and the mutation rate of waterlices living in subterranean habitants [2]. This result suggests that natural radioactivity can be an important abiotic driver of the evolution of microorganisms living in mineral springs. The comparison has of course some limitations. First, laboratory conditions impose their own sources of stress with a potential effect on the mutation rates. As a consequence, differences are expected between the experimental mutation rates and the long-term average mutation rates in the natural environment. The other limitation lies in the comparison between radiation induced damages and spontaneous mutation rates: between these two, the complete cell repair process lies.

For the needs of comparing the current work to other studies, the predicted DNA Double Strand Breaks (DSB) were juxtaposed to mutation rates. It is important to clarify that the existence of DSB does not correspond to a fixed mutation but to a potential mutation. Any change that occurs to a DNA sequence is called mutation. The following small scale mutations can be highlighted: the 'point' ones which refer to the change of one base in the DNA sequence, the 'substitution' ones which take place when one or more bases in the DNA sequence is replaced by the same number of bases, the 'insertion' ones which refer to the addition of a base to the sequence, and the 'deletion' which denotes the deletion of one base from the DNA

sequence. DNA Double Strand Breaks caused by ionising radiation can lead to mutations if they are not properly repaired. Spontaneous mutations occur without any exposure to environmental stresses as opposed to induced mutations (due to exposure to chemicals, ionising radiation, UV-radiation, etc) [300, 301]. Specific attention is paid to DNA Double Strand Breaks because they are considered highly mutagenic lesions which can lead to base substitutions, deletions and chromosomal rearrangements (mutations) if misrepaired [149]. The main repair mechanisms of DNA Double Strand Breaks are namely 'Homologous Recombination (HR)' and 'Non-Homologous End Joining (NHEJ)' [302]. Detailed account of these mechanisms falls beyond the scope of the present work.

DNA damage due to internal exposure

In an effort to evaluate the impact of the internal exposure on the prediction of DNA strand breaks, the primary α-particles were distributed uniformly directly inside the diatom and the phase space of the α-particles entering the nucleus was recorded in each case. This phase space was then placed at the borders of the nucleus and used as a source. The results are summarized in Table 4.5 where the contribution of all the simulated radionuclides are summed.

In Table 4.5, the SSB and DSB obtained per Gray and per Mbp are first shown. Assuming one generation of diatoms per day [281], the SSB and DSB per generation normalised to 27.4 Mbp DNA length and, to 1 day-exposure to Unit (UAC) and Reference Activity Concentrations (RAC: [^{222}Rn]=1000 Bq/L, [^{226}Ra]=30 kBq/kg, [^{210}Po]=0.4 Bq/L, [^{238}U]=0.3 kBq/kg) are presented. The internal dose rates to the diatoms, calculated with GATE in Chapter 3, are also provided.

It is noticed that the DNA damage due to the external exposure in the benthic mixture for diatoms (Table 4.4) and the DNA damage due to the internal exposure (Table 4.5) are in the same orders of magnitude. The distribution of the radionuclides in the environment (external exposure) results in $5.45 \cdot 10^{-8}$ DSB/generation/UAC and $1.12 \cdot 10^{-4}$ DSB/generation/RAC, while the distribution of radionuclides inside the diatom (internal exposure) results in $2.51 \cdot 10^{-8}$ DSB/generation/UAC and $2.00 \cdot 10^{-4}$ DSB/generation/RAC.

According to the calculations of the present study, the internal exposure contributes to the formation of DNA Double Strand Breaks (DSB) as much as the external exposure does. Nevertheless, lacking evidence of the proper mechanisms of accumulation of radionuclides inside the diatoms, it could only

be assumed that the incorporation of radiosotopes can account for a great part of their DNA damage.

Table 4.5 SSB and DSB due to internal exposure

Radionuclides	^{238}U, ^{226}Ra, ^{222}Rn & ^{210}Po
SSB/Gy/Mbp	0.42
DSB/Gy/Mbp	0.04
Results per Unit Activity Concentrations (UAC)	
Internal DR (μGy/h)	$1.70 \cdot 10^{-5}$
SSB/generation/UAC	$1.48 \cdot 10^{-7}$
DSB/generation/UAC	$2.51 \cdot 10^{-8}$
Results per Reference Activity Concentrations (RAC)	
Internal DR (μGy/h)	13.50
SSB/generation/RAC	$1.17 \cdot 10^{-3}$
DSB/generation/RAC	$2.00 \cdot 10^{-4}$

Internal DR: Internal Dose Rates to diatoms (section 3.3).
The calculations are performed for 1-day internal exposure to UAC, RAC, considering 1 generation/day and 27.4 Mbp DNA length.
RAC: [^{226}Ra] = 30 kBq/kg, [^{222}Rn] = 1000 Bq/L, [^{238}U] = 0.3 kBq/kg, [^{210}Po] = 0.4 Bq/L.

Conclusion

This chapter focused on the nucleus of the microorganisms living in naturally radioactive aquatic ecosystems. Geant4-DNA was used for nanodosimetric simulations and the assessment of DNA damage caused by α-emitting natural radionuclides (^{222}Rn, ^{226}Ra, ^{238}U, ^{210}Po).

Specific energy distributions collected on nano-sized geometries resembling nucleosomes of 147 bp length each, showed that the energy depositions come primarily from low energy He ions and electrons.

For the DNA damage, the DBSCAN algorithm was used to calculate Single (SSB) and Double (DSB) DNA Strand Breaks. SSB and DSB were calculated for both internal and external radiation exposure of the microorganisms. For the external exposure, it was observed that the number of DSB per microorganism generation per Unity Activity Concentration (UAC) do not differ noticeably among the different simulated environments with values in the order of magnitude of 10^{-8} DSB/generation/UAC. A small decrease of 7% was observed when the frustule was considered (exclusively

in the benthic mixture), indicating that the frustule does not provide significant protection against the ionising radiation.

Considering the Reference Activity Concentrations (RAC) of radionuclides in the mineral springs (RAC: [^{226}Ra] = 30 kBq/kg, [^{222}Rn] = 1000 Bq/L, [^{238}U] = 0.3 kBq/kg, [^{210}Po] = 0.4 Bq/L), the respective number of DSB per diatom generation is 4 orders of magnitude higher ($1.12 \cdot 10^{-4}$ DSB/generation/RAC) than the DSB/generation/UAC.

Since mutation rates can be affected by environmental stresses [303, 304], the comparison of the current work predicted diatom DSB per generation due to external exposure to the spontaneous mutation rates experimentally evaluated in laboratory conditions ($1.29 \cdot 10^{-2}$ mutations per generation [281]), could only suggest that, in the natural environment, DSB could be significantly higher and potentially contribute to radiation induced mutations.

The calculations of the current study for microorganisms (without frustule) could also be parallelized to the study of Lampe et al. [297] who concluded that natural background radiation would have a very small mutational impact on bacteria.

Lastly, an evaluation of the DNA damage due to the internal exposure of microorganisms to α-emitters found in the radioactive mineral springs was performed. The number of DSB/generation are comparable to those attributed to external exposure. Without data on diatoms' bioaccumulation for radionuclides in the mineral springs, the hypothesis that the activity concentrations were equal inside and outside diatoms was made. Considering this approximation valid, it could only be suggested that internal exposure can account for a great part of their DNA damage.

In the next chapter, the microdosimetric results and the predicted DNA damage corresponding to the radiological conditions of each mineral spring involved in the current thesis are discussed.

Chapter 5

Diatoms radiation exposure and DNA damage prediction in the mineral springs of Auvergne

Introduction

This final chapter is dedicated to the diatoms radiation exposure and the DNA damage corresponding to the radiological conditions of each Auvergne mineral spring studied in the current thesis. The results of experimental measurements from Chapter 2, the dose rate results from Chapter 3 and DNA damage predicted in Chapter 4 are gathered in order to calculate the diatom dose rates and the DNA Double Strand Breaks (DSB) according to the activity concentrations of ^{222}Rn, ^{226}Ra, ^{238}U and ^{210}Po measured in each mineral spring.

The simulation results concerning the microorganism with frustule (diatom) in the benthic mixture (composed by 90% water and 10% dry sediments) are extracted. In section 5.1, the dose rates calculated with GATE for each mineral spring due to the internal and external exposure are detailed. The diatoms DNA Double Strand Breaks (DSB) due to the external exposure for each mineral spring are presented in section 5.2. Before concluding, a discussion is performed on the assumptions upon which the simulation was built for the evaluation of the radiation exposure on microorganisms in mineral springs in section 5.3.

5.1 Diatoms dose rates

In this study, the environment the diatoms inhabit is approached by the simulated homogeneous benthic mixture. The simulated dose rates are scaled to the measured activity concentrations in the mineral springs for a microorganism (water sphere of radius = 10 μm) enveloped by a 2 μm width frustule of 2.4 g/cm^3 density. As shown before (Fig 3.8), the external dose rates are expected to be on average 10% higher in the absence of frustule.

The external dose rates to diatoms for ^{222}Rn measured in water (values taken from Tables 2.3 & 2.4), ^{210}Po measured in water (values taken from

Table 2.7), ^{226}Ra and ^{238}U measured in dry sediments (values taken from Table 2.8) are presented in Table 5.1. The respective internal dose rates are presented in Table 5.2, while both external and internal dose rates to diatoms in all the mineral springs are shown in Fig. 5.1. Tables presenting the measured activity concentrations and the corresponding dose rates are provided in Appendix ??.

As discussed earlier in Chapter 3, the internal dose rate calculations must be renormalized to account for the bioaccumulation of radionuclides. The case of ^{222}Rn is peculiar: ^{222}Rn is absorbed in the microorganism through water exchange between the environment and the microorganism. As a noble gas, ^{222}Rn is not involved in chemical reactions and its concentration should be the same inside and outside the diatom. The internal dose rate results presented in Fig. 5.1 show that in case that the same amount of radionuclides present in the environment are distributed inside the diatom, then the internal exposure can already be above 10 μGy/h.

The external diatom dose rates in the mineral springs range from $5{\cdot}10^{-3}$ μGy/h (in Par) to 12.8 μGy/h (in Ours). From Table 5.1 and Fig. 5.1, it is observed that the external dose rates to diatoms are above the suggested threshold for the protection of ecosystems (10 μGy/h [257,258]) in Montagne 1 (10.1 μGy) and Ours (12.8 μGy/h), while Dourioux (9.06 μGy/h) is very close to the threshold. It is remarked that Montagne 1 and Dourioux are classified as High level activity springs in Chapter 2 since their ^{222}Rn activity concentrations measured in water are higher than 1000 Bq/L (3452 Bq/L in Montagne 1 and 3852 Bq/L in Dourioux). On the contrary, Ours is classified as Low level activity spring since its [^{222}Rn] = 22 Bq/L. It is also noticed that the other springs classified as High level activity, Estreys, Montagne 2 and Sail, are well below the dose rate threshold of 10 μGy/h.

It is clear that in each mineral spring, the external dose rates received by diatoms living at the benthic mixture depend highly on the activity concentrations of radionuclides present in the sediments. In Fig. 5.2, the contribution of water and sediment dose rates to the total diatom external dose rate for each spring is shown. It is reminded that the dose rates coming from the radionuclides measured in the water (^{222}Rn and ^{210}Po) correspond to 90% of the simulated benthic mixture, while the dose rates rates coming from the radionuclides measured in the sediments (^{226}Ra and ^{238}U) correspond to 10% of the simulated benthic mixture.

As shown in Fig. 5.2, the contribution to the total diatom dose rates of each compartment of the simulated environment (water or sediments with

the respective radionuclides) varies in each spring. For example, it is evident that the sole contribution to the diatom dose rate comes from water in Bard 1, Croizat and Par. Apart from ^{222}Rn in water, no other radionuclides were measured in water and in sediments in Bard 1 and Par, while in Croizat ^{222}Rn and ^{210}Po were measured in water but no ^{226}Ra or ^{238}U was measured in the sediments.

On the contrary, the highest contribution to the external dose rates to diatoms comes from the sediments in Ours, where the ^{222}Rn activity concentration in water is 22 Bq/L and the ^{226}Ra activity concentration in sediments is 52 kBq/kg resulting in 12.8 μGy/h total diatom dose rate.

In Dourioux, where the total diatom dose rate is 9.06 μGy/h, the contribution of the radionuclides measured in water dominates: [^{222}Rn]=3852 Bq/L and [^{210}Po]=0.03 Bq/L were measured in water, while [^{226}Ra]=0.6 kBq/kg and [^{238}U]=0.26 kBq/kg were measured in sediments.

In Fig. 5.2, the higher contribution of the radionuclides measured in water in comparison to sediments in Montagne 1 can also be remarked. The calculated diatom dose rates correspond to [^{222}Rn]=3452 Bq/L and [^{210}Po]=0.195 Bq/L measured in water, and to [^{226}Ra]=8.61 kBq/kg measured in the sediments.

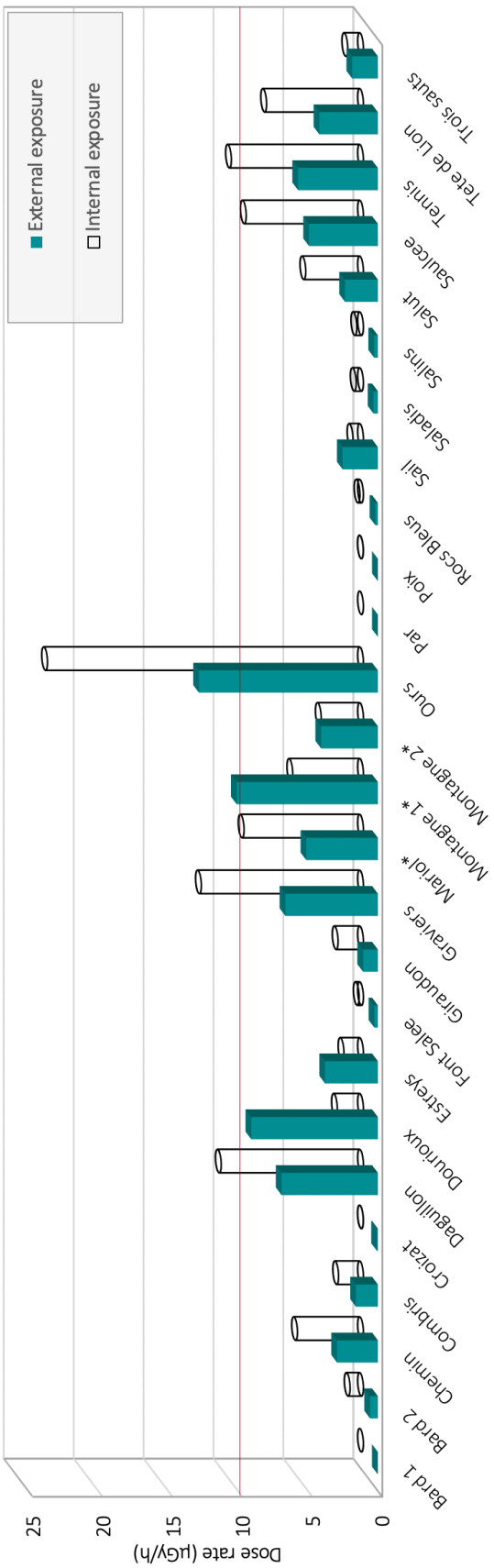

Figure 5.1 Diatom simulated external and internal dose rates in Auvergne mineral springs. Red line: 10 µGy/h - threshold for the protection of the ecosystems. Statistical uncertainties : $< 0.5\%$ - not visible.

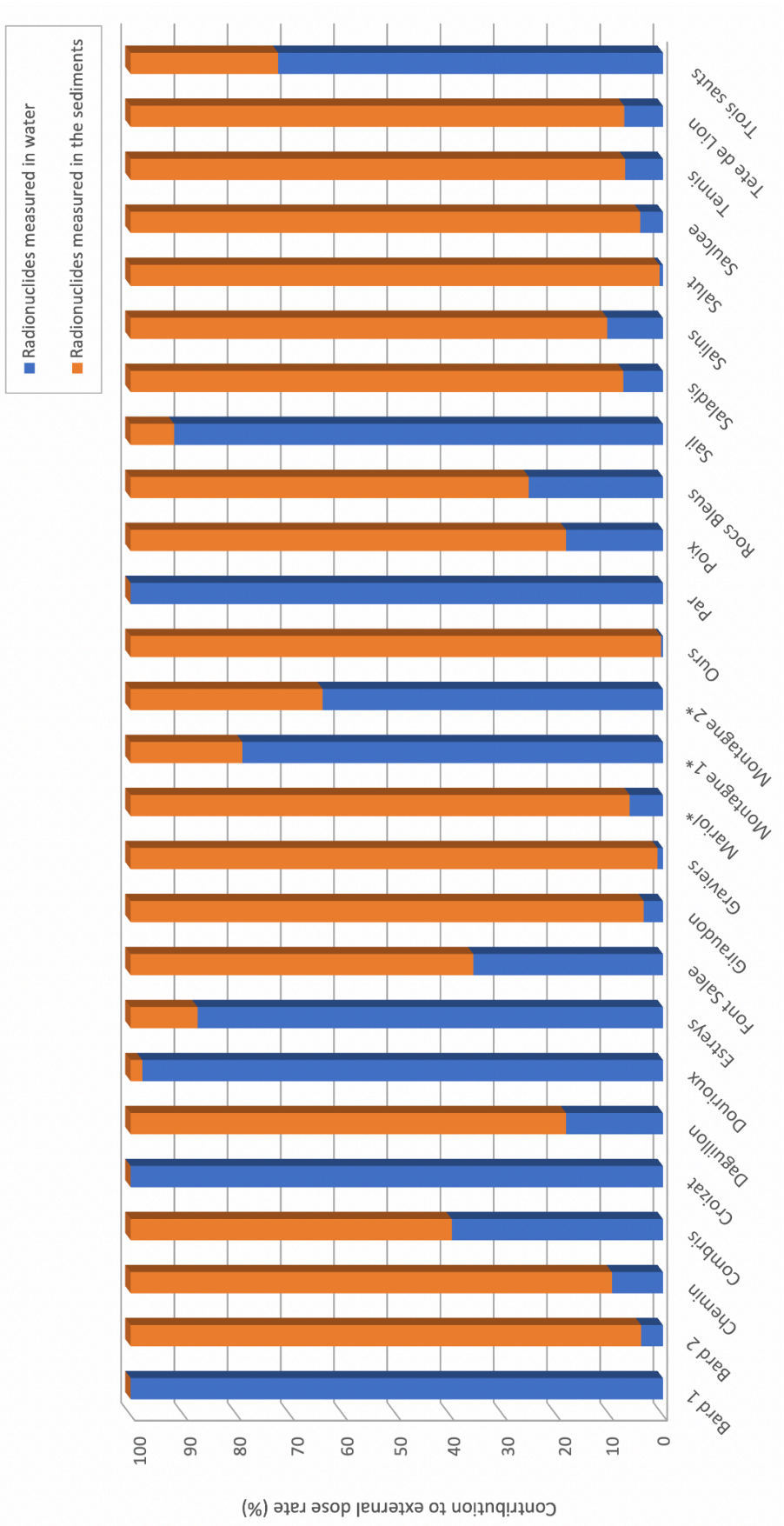

Figure 5.2 Contribution of radionuclides in water (blue) and sediments (orange) to diatoms external dose rates in Auvergne mineral springs

Table 5.1 Diatom simulated external Dose Rates (DR) normalized to the measured activity concentrations in the mineral springs

	Diatom simulated external DR (μGy/h)				
Spring	^{222}Rn	^{226}Ra	^{210}Po	^{238}U	**Total**
Bard 1	$1.36 \cdot 10^{-2}$	-	-	-	$1.36 \cdot 10^{-2}$
Bard 2	$2.30 \cdot 10^{-2}$	$5.37 \cdot 10^{-1}$	-	-	$5.60 \cdot 10^{-1}$
Chemin	$2.80 \cdot 10^{-1}$	2.64	-	-	2.92
Combris	$6.22 \cdot 10^{-1}$	$9.46 \cdot 10^{-1}$	$3.35 \cdot 10^{-4}$	-	1.57
Croizat	$6.65 \cdot 10^{-2}$	-	$1.91 \cdot 10^{-4}$	-	$6.67 \cdot 10^{-2}$
Daguillon	1.25	5.63	-	-	6.89
Dourioux	8.86	$1.47 \cdot 10^{-1}$	$6.53 \cdot 10^{-5}$	$4.99 \cdot 10^{-2}$	9.06
Estreys	3.31	$4.75 \cdot 10^{-1}$	$5.87 \cdot 10^{-5}$	-	3.78
Font Salee	$9.09 \cdot 10^{-2}$	$1.64 \cdot 10^{-1}$	-	-	$2.55 \cdot 10^{-1}$
Giraudon	$3.82 \cdot 10^{-2}$	1.02	-	-	1.06
Graviers	$6.72 \cdot 10^{-2}$	6.55	-	-	6.62
Mariol*	$3.19 \cdot 10^{-1}$	4.80	$5.44 \cdot 10^{-5}$	-	5.12
Montagne 1*	7.94	2.11	$4.24 \cdot 10^{-4}$	-	10.10
Montagne 2*	2.59	1.46	$1.44 \cdot 10^{-4}$	-	4.06
Ours	$5.08 \cdot 10^{-2}$	12.77	-	-	12.80
Par	$5.06 \cdot 10^{-3}$	-	-	-	$5.06 \cdot 10^{-3}$
Poix	$1.40 \cdot 10^{-3}$	$7.35 \cdot 10^{-3}$	$2.57 \cdot 10^{-4}$	-	$9.01 \cdot 10^{-3}$
Rocs Bleus	$4.62 \cdot 10^{-2}$	$1.37 \cdot 10^{-1}$	-	-	$1.83 \cdot 10^{-1}$
Sail	2.31	$2.06 \cdot 10^{-1}$	-	-	2.52
Saladis	$2.35 \cdot 10^{-2}$	$2.92 \cdot 10^{-1}$	-	-	$3.15 \cdot 10^{-1}$
Salins	$2.74 \cdot 10^{-2}$	$1.84 \cdot 10^{-1}$	$8.53 \cdot 10^{-4}$	$5.76 \cdot 10^{-2}$	$2.70 \cdot 10^{-1}$
Salut	$1.59 \cdot 10^{-2}$	2.33	-	-	2.35
Saulcee	$2.11 \cdot 10^{-1}$	4.72	$3.65 \cdot 10^{-4}$	-	4.93
Tennis	$4.06 \cdot 10^{-1}$	5.30	-	-	5.71
Tete de Lion	$3.05 \cdot 10^{-1}$	3.89	-	-	4.19
Trois sauts	1.33	$5.10 \cdot 10^{-1}$	-	-	1.84

Table 5.2 Diatom simulated internal Dose Rates (DR) normalized to the measured activity concentrations in the mineral spring.

	Diatom simulated internal DR (μGy/h)				
Spring	^{222}Rn	^{226}Ra	^{210}Po	^{238}U	**Total**
Bard 1	$2.27 \cdot 10^{-3}$	-	-	-	$2.27 \cdot 10^{-3}$
Bard 2	$3.84 \cdot 10^{-3}$	$9.49 \cdot 10^{-1}$	-	-	$9.53 \cdot 10^{-1}$
Chemin	$4.68 \cdot 10^{-2}$	4.67	-	-	4.72
Combris	$1.04 \cdot 10^{-1}$	1.67	$6.08 \cdot 10^{-5}$	-	1.78
Croizat	$1.11 \cdot 10^{-2}$	-	$3.48 \cdot 10^{-5}$	-	$1.11 \cdot 10^{-2}$
Daguillon	$2.09 \cdot 10^{-1}$	9.96	-	-	10.20
Dourioux	1.48	$2.60 \cdot 10^{-1}$	$1.19 \cdot 10^{-5}$	$1.27 \cdot 10^{-1}$	1.87
Estreys	$5.52 \cdot 10^{-1}$	$8.41 \cdot 10^{-1}$	$1.07 \cdot 10^{-5}$	-	1.39
Font Salee	$1.52 \cdot 10^{-2}$	$2.90 \cdot 10^{-1}$	-	-	$3.06 \cdot 10^{-1}$
Giraudon	$6.37 \cdot 10^{-3}$	1.81	-	-	1.81
Graviers	$1.12 \cdot 10^{-2}$	11.60	-	-	11.60
Mariol*	$5.33 \cdot 10^{-2}$	8.48	$9.88 \cdot 10^{-6}$	-	8.54
Montagne 1*	1.33	3.73	$7.70 \cdot 10^{-5}$	-	5.06
Montagne 2*	$4.33 \cdot 10^{-1}$	2.59	$2.61 \cdot 10^{-5}$	-	3.02
Ours	$8.49 \cdot 10^{-3}$	22.59	-	-	22.60
Par	$8.45 \cdot 10^{-4}$	-	-	-	$8.45 \cdot 10^{-4}$
Poix	$2.30 \cdot 10^{-4}$	$1.30 \cdot 10^{-2}$	$4.66 \cdot 10^{-5}$	-	$1.33 \cdot 10^{-2}$
Rocs Bleus	$7.72 \cdot 10^{-3}$	$2.43 \cdot 10^{-1}$	-	-	$2.50 \cdot 10^{-1}$
Sail	$3.86 \cdot 10^{-1}$	$3.64 \cdot 10^{-1}$	-	-	$7.50 \cdot 10^{-1}$
Saladis	$3.92 \cdot 10^{-3}$	$5.16 \cdot 10^{-1}$	-	-	$5.20 \cdot 10^{-1}$
Salins	$4.57 \cdot 10^{-3}$	$3.25 \cdot 10^{-1}$	$1.55 \cdot 10^{-4}$	$1.46 \cdot 10^{-1}$	$4.76 \cdot 10^{-1}$
Salut	$2.65 \cdot 10^{-3}$	4.12	-	-	4.12
Saulcee	$3.52 \cdot 10^{-2}$	8.35	$6.64 \cdot 10^{-5}$	-	8.39
Tennis	$6.79 \cdot 10^{-2}$	9.38	-	-	9.45
Tete de Lion	$5.10 \cdot 10^{-2}$	6.88	-	-	6.93
Trois sauts	$2.22 \cdot 10^{-1}$	$9.01 \cdot 10^{-1}$	-	-	1.12

5.2 Diatoms DNA Double Strand Breaks (DSB)

In Fig. 5.3, the simulated DNA Double Strand Strand Breaks (DSB) per diatom generation due to the external exposure and the total external dose rates to diatoms in each spring are presented. The diatom DSB/generation vary between $5.5{\cdot}10^{-8}$ in Par to $1.5{\cdot}10^{-4}$ in Ours corresponding to $5.06{\cdot}10^{-3}$ μGy/h and 12.8 μGy/h diatom external dose rates, respectively.

As shown earlier, the highest contribution to the diatom dose rate in Ours comes from the sediments, where the highest ^{226}Ra activity concentration in sediments was measured among the springs (52 kBq/kg). In Montagne 1, the highest contribution to the diatom dose rate comes from water, where the highest ^{222}Rn activity concentration in water are typically measured among the springs.

Recalling the fluctuations of [^{222}Rn] in water measured in Montagne 1 during the monitoring period (April 2017 - September 2021), the corresponding simulated DSB/generation attributed only to the external exposure due to ^{222}Rn measured in water was plotted in Fig. 5.4. It is observed that the external dose rates due to ^{222}Rn in water, vary between 1.7 μGy/h and 10.6 μGy/h corresponding to the lowest and highest ^{222}Rn activity concentrations measured in water (737 Bq/L in January 2020 and 4600 Bq/L in May 2018, respectively). The DSB/generation vary respectively between $1.86{\cdot}10^{-5}$ and $1.16{\cdot}10^{-4}$. It is recalled that the 4600 Bq/L of ^{222}Rn activity in May 2018 corresponds to the study of Millan et al. [62] where the deformation rates of diatoms was found higher that 25%.

The importance of Fig. 5.4 is highlighted: it shows the radiation pressure on diatoms in Montagne 1 spring exclusively from ^{222}Rn in water which accounts for 90% of the benthic mixture volume. Although the chemical toxicity of the radionuclides which can contribute to additional DNA damage is out of the context of this work, it is remarked that ^{222}Rn is a noble gas and consequently chemically inert. As a result, the damage induced by ^{222}Rn on microorganisms is purely due to radiation and no additional damages are expected due to chemical interactions.

In Table 5.3, the summed total external and internal dose rates to diatoms for ^{222}Rn, ^{210}Po, ^{226}Ra and ^{238}U, along with the respective DSB per diatom generation are presented.

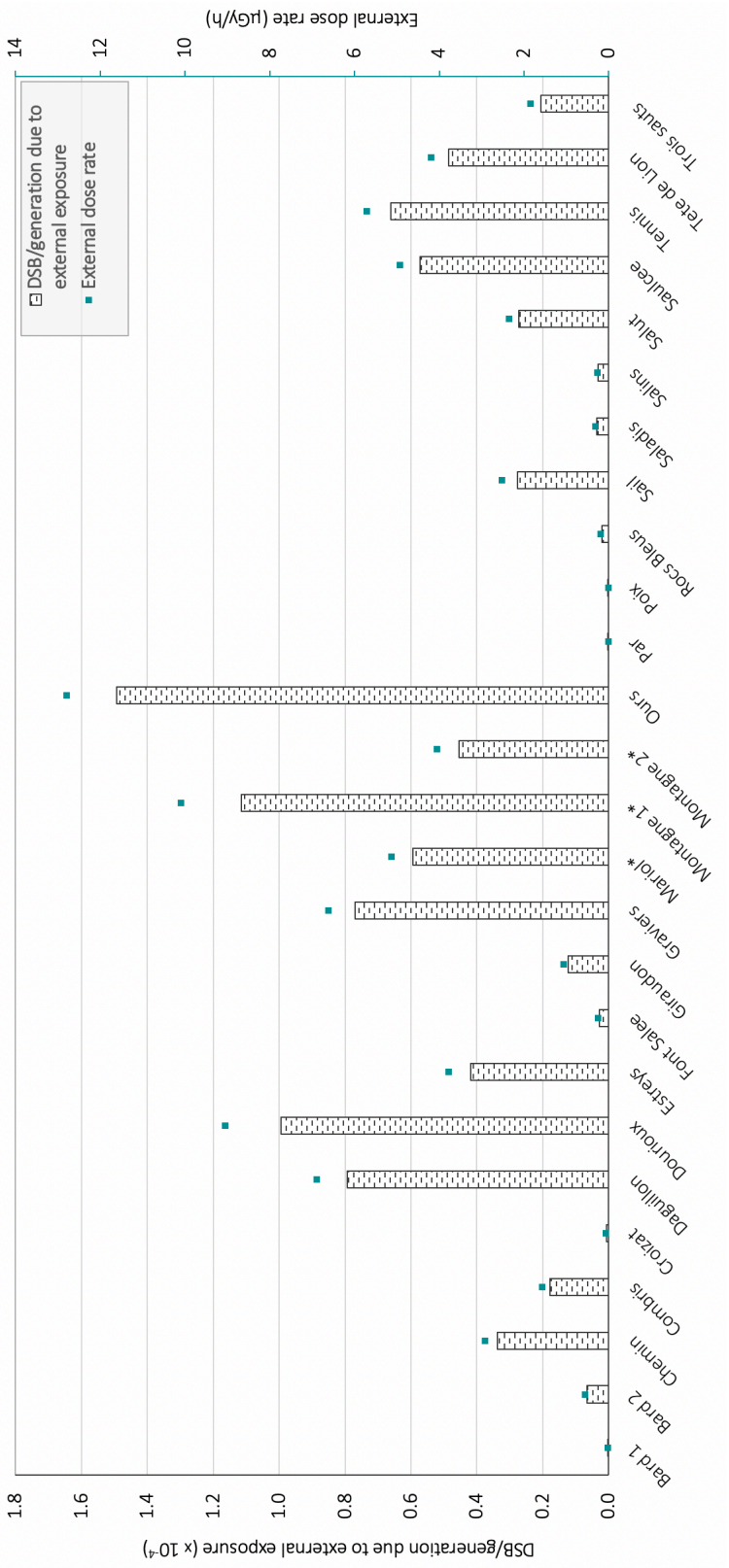

Figure 5.3 Simulated diatom DNA Double Strand Breaks (DSB) in Auvergne mineral springs due to external exposure. Green: simulated external dose rates to diatoms.

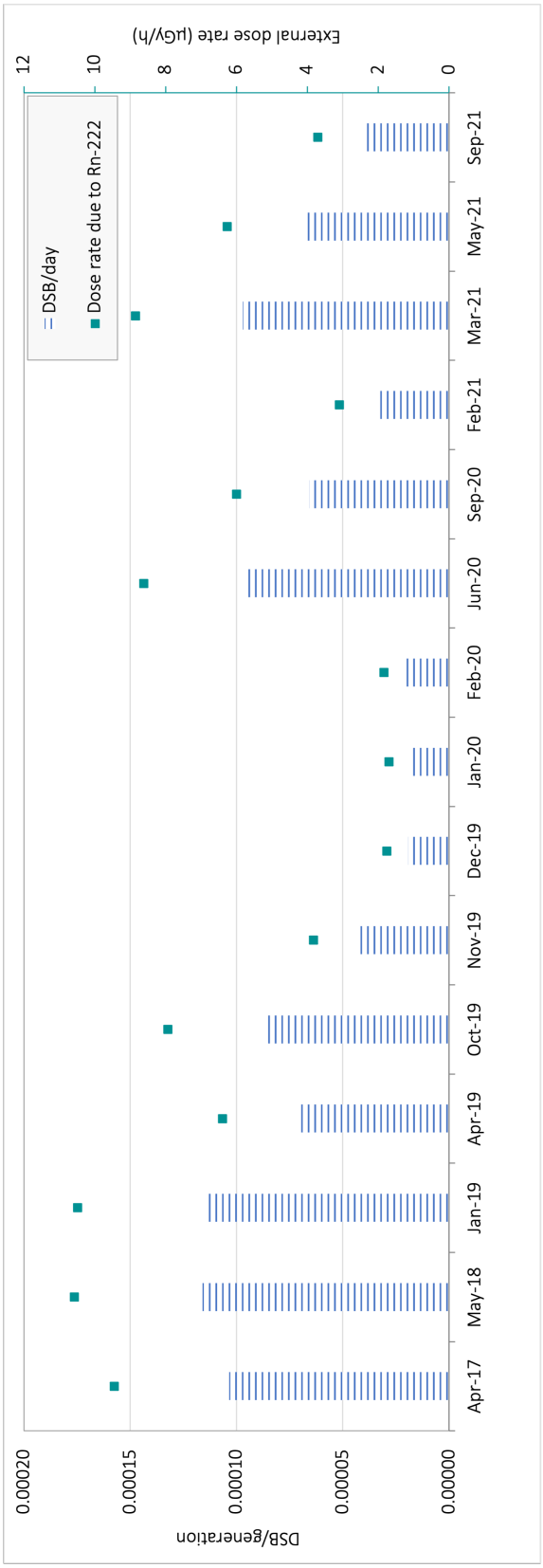

Figure 5.4 Simulated diatom DNA Double Strand Breaks (DSB) at Montagne 1 due to external exposure to ^{222}Rn in water. Green: simulated external dose rates to diatoms due to ^{222}Rn in water.

Table 5.3 Diatom simulated Dose Rates (DR) and DNA Double Strand Breaks (DSB) due to external and internal exposure in Auvergne mineral springs

	Diatoms external exposure		Diatoms internal exposure		
Spring	**DR (μGy/h)**	**DSB/generation**	**DR (μGy/h)**	**DSB/generation**	**Total DSB/generation**
Bard 1	$1.36 \cdot 10^{-2}$	$1.49 \cdot 10^{-7}$	$2.27 \cdot 10^{-3}$	$3.15 \cdot 10^{-8}$	$1.80 \cdot 10^{-7}$
Bard 2	$5.60 \cdot 10^{-1}$	$6.50 \cdot 10^{-6}$	$9.53 \cdot 10^{-1}$	$1.41 \cdot 10^{-5}$	$2.06 \cdot 10^{-5}$
Chemin	2.92	$3.38 \cdot 10^{-5}$	4.72	$7.00 \cdot 10^{-5}$	$1.04 \cdot 10^{-4}$
Combris	1.57	$1.78 \cdot 10^{-5}$	1.78	$2.63 \cdot 10^{-5}$	$4.41 \cdot 10^{-5}$
Croizat	$6.67 \cdot 10^{-2}$	$7.30 \cdot 10^{-7}$	$1.11 \cdot 10^{-2}$	$1.55 \cdot 10^{-7}$	$8.85 \cdot 10^{-7}$
Daguillon	6.89	$7.93 \cdot 10^{-5}$	10.20	$1.51 \cdot 10^{-4}$	$2.30 \cdot 10^{-4}$
Dourioux	9.06	$9.94 \cdot 10^{-5}$	1.87	$2.65 \cdot 10^{-5}$	$1.26 \cdot 10^{-4}$
Estreys	3.78	$4.18 \cdot 10^{-5}$	1.39	$2.02 \cdot 10^{-5}$	$6.19 \cdot 10^{-5}$
Font Salee	$2.55 \cdot 10^{-1}$	$2.91 \cdot 10^{-6}$	$3.06 \cdot 10^{-1}$	$4.52 \cdot 10^{-6}$	$7.43 \cdot 10^{-6}$
Giraudon	1.06	$1.23 \cdot 10^{-5}$	1.81	$2.69 \cdot 10^{-5}$	$3.92 \cdot 10^{-5}$
Graviers	6.62	$7.70 \cdot 10^{-5}$	11.60	$1.72 \cdot 10^{-4}$	$2.49 \cdot 10^{-4}$
Mariol*	5.12	$5.94 \cdot 10^{-5}$	8.54	$1.27 \cdot 10^{-4}$	$1.86 \cdot 10^{-4}$
Montagne 1*	10.10	$1.12 \cdot 10^{-4}$	5.06	$7.38 \cdot 10^{-5}$	$1.85 \cdot 10^{-4}$
Montagne 2*	4.06	$4.54 \cdot 10^{-5}$	3.02	$4.44 \cdot 10^{-5}$	$8.99 \cdot 10^{-5}$
Ours	12.8	$1.49 \cdot 10^{-4}$	22.60	$3.35 \cdot 10^{-4}$	$4.85 \cdot 10^{-4}$
Par	$5.06 \cdot 10^{-3}$	$5.54 \cdot 10^{-8}$	$8.45 \cdot 10^{-4}$	$1.18 \cdot 10^{-8}$	$6.72 \cdot 10^{-8}$
Poix	$7.61 \cdot 10^{-3}$	$1.04 \cdot 10^{-7}$	$1.30 \cdot 10^{-2}$	$1.97 \cdot 10^{-7}$	$3.00 \cdot 10^{-7}$
Rocs Bleus	$1.83 \cdot 10^{-1}$	$2.10 \cdot 10^{-6}$	$2.50 \cdot 10^{-1}$	$3.71 \cdot 10^{-6}$	$5.81 \cdot 10^{-6}$
Sail	2.52	$2.77 \cdot 10^{-5}$	$7.50 \cdot 10^{-1}$	$1.08 \cdot 10^{-5}$	$3.85 \cdot 10^{-5}$
Saladis	$3.15 \cdot 10^{-1}$	$3.65 \cdot 10^{-6}$	$5.20 \cdot 10^{-1}$	$7.71 \cdot 10^{-6}$	$1.14 \cdot 10^{-5}$
Salins	$2.70 \cdot 10^{-1}$	$3.18 \cdot 10^{-6}$	$4.76 \cdot 10^{-1}$	$7.22 \cdot 10^{-6}$	$1.04 \cdot 10^{-5}$
Salut	2.35	$2.73 \cdot 10^{-5}$	4.12	$6.12 \cdot 10^{-5}$	$8.85 \cdot 10^{-5}$
Saulcee	4.93	$5.73 \cdot 10^{-5}$	8.39	$1.24 \cdot 10^{-4}$	$1.82 \cdot 10^{-4}$
Tennis	5.71	$6.62 \cdot 10^{-5}$	9.45	$1.40 \cdot 10^{-4}$	$2.06 \cdot 10^{-4}$
Tete de Lion	4.19	$4.86 \cdot 10^{-5}$	6.93	$1.03 \cdot 10^{-4}$	$1.51 \cdot 10^{-4}$
Trois sauts	1.84	$2.05 \cdot 10^{-5}$	1.12	$1.65 \cdot 10^{-5}$	$3.70 \cdot 10^{-5}$

The calculations are performed for 1-day external and internal exposure to the measured activity concentrations of ^{222}Rn, ^{226}Ra, ^{238}U and ^{210}Po, considering 1 diatom generation/day and 27.4 Mbp DNA length.

The predicted total DSB/generation (due to internal and external exposure) for diatoms in the mineral springs in this work are 2 to 5 orders of magnitude lower than the diatoms spontaneous rates experimentally determined by Krasovec et al. [281] ($1.29 \cdot 10^{-2}$ mutations per generation). Spontaneous mutation rates determine the frequency of new DNA alterations (that have not been present in previous generations) introduced into a population. Since mutation rates can be affected by environmental stresses [303, 304], Krasovec et al. [281] state that 'experimental mutation rates may differ from the long-term average mutation rate in the natural environment'.

In the most radioactive springs, the rate of total DSB per diatom generation reaches $5 \cdot 10^{-4}$ according to the current estimates. It is important to stress that for the internal exposure calculations, the same activity concentrations of radionuclides at the environment and inside the diatom have been considered. In case of high bioaccumulation, the rates of DSB due to internal exposure will grow proportionally.

Another important remark is that in the current simulations, the α-particles of ^{222}Rn, ^{226}Ra, ^{238}U and ^{210}Po were explicitly considered, without taking into account the additional energy deposited by their progeny. As shown earlier in Chapter 3 (section 3.6), when comparing the Dose Conversion Coefficients (DCC), and consequently the dose rate calculations of this work, to BiotaDC and ERICA, it was found out that the daughter nuclei with half-lives less than 10 days can be taken into account by applying some correction factors. These correction factors correspond to the ratio between ERICA and GATE dose rates.

As presented in Table 3.11, the contribution of radioactive progeny using ICRP108 method (decay chain cut-off at half-life longer than 10 days) [261] are considered by applying the following ratios to the energy spectra of the radionuclides:

- for ^{226}Ra dose rate calculations : $1 \times {}^{226}$Ra, $1 \times {}^{222}$Rn, $1 \times {}^{218}$Po, $0.9998 \times {}^{214}$Pb, $0.0002 \times {}^{218}$At, $1 \times {}^{214}$Bi, $0.00021 \times {}^{210}$Tl, $0.999790 \times {}^{214}$Po, resulting in a correction factor 5.2
- for ^{222}Rn dose rate calculations: $1 \times {}^{222}$Rn, $1 \times {}^{218}$Po, $0.9998 \times {}^{214}$Pb, $0.0002 \times {}^{218}$At, $1 \times {}^{214}$Bi, $0.00021 \times {}^{210}$Tl, $0.999790 \times {}^{214}$Po, resulting in a correction factor 3.5

The application of these correction factors (5.2 for ^{226}Ra and 3.5 for ^{222}Rn) to the dose rates and DNA damage calculations can provide a gross estimation of the contribution of the daughter nuclei (which were not considered in

the current simulations) to the results of the present work. An example is provided in Table 5.4 for Ours and Montagne 1 mineral springs where the highest ^{226}Ra activity concentration (in sediments) and the highest ^{222}Rn activity concentration (in water), were respectively measured. The 5.2-fold increase for ^{226}Ra calculations results in total diatom DSB/generation in the order of magnitude 10^{-3} which is comparable to the diatoms spontaneous mutation rate ($1.29{\cdot}10^{-2}$ mutations per generation [281]). This last remark indicates that radiation can be an abiotic drive in the naturally radioactive mineral springs even without considering the proper bioaccumulation.

Table 5.4 Diatom Dose Rates (DR) and DNA Double Strand Breaks (DSB) due to external and internal exposure in Ours and Montagne 1 corrected for daughter nuclei with $t_{1/2} \leq 10$ d

	Ours	**Montagne 1**
Radionuclide	^{226}Ra	^{222}Rn
Activity concentration	52.1 kBq/kg	4600 Bq/L
Diatom external DR (μGy/h)	66.58	37.10
Diatom DSB/generation due to external exposure	$7.75{\cdot}10^{-4}$	$4.06{\cdot}10^{-4}$
Diatom internal DR (μGy/h)	117	6.20
Diatom DSB/generation due to internal exposure	$1.74{\cdot}10^{-3}$	$8.61{\cdot}10^{-5}$
Total diatom DSB/generation	$2.52{\cdot}10^{-3}$	$4.92{\cdot}10^{-4}$

Applied correction factors: ^{226}Ra: 5.2, ^{222}Rn: 3.5

5.3 Discussion

The complexity of the ecosystems of the mineral springs required a simplified simulation approximation. The simulation of the environment of the mineral springs where microorganisms inhabit was built upon the experimental measurements.

Two main factors were taken into consideration for the size of the simulated environment: the size of the microorganism and the range of the radionuclides of interest in the water. Both sizes are in the microscale. As a result, the simulation setup corresponds to microdosimetric configurations.

The composition of the benthic environment where the microorganisms of interest develop was evaluated as 90% water and 10% dry sediments. The realistic living conditions of diatoms are not represented by well separated layers of dry sediments covered by a water column: their environment resembles a mixture.

One of the main assumptions made for the simulation of the benthic mixture is its homogeneity. In reality, the dry sediments in each mineral spring have different granulometric profiles. For instance, in Mariol the dry sediments are composed by fine grains of a few micrometers size, while in Montagne fine grains are mixed with grains of a few hundred micrometers size. The impact of the distribution of radionuclides in the dry sediments on the dose rates received by the biota is currently under study. As a first step, the benthic environment was simulated as a homogeneous sphere.

The spherical approach was adopted for the simulation of the microorganism, too. According to the dimensions of the diatoms in the mineral springs in Auvergne, provided by the biology laboratory, and the bibliography for cell-sized dosimetric simulations, spheres can be used to fairly represent the microorganisms. Similarly, assumptions had to be made for the DNA size of the diatoms due to the lack of genomic information for diatoms in the local mineral springs. A 27.4 Mbp genetic material which is consistent with the DNA length of the marine model diatom *Phaeodactylum tricornutum* was considered.

Concerning the sources of radioactivity, the radiation exposure coming from the α-emitting radionuclides in the environment was evaluated. The dominant α-emitters were simulated in accordance with the measured activity concentrations in the water and the sediments of the mineral springs. No precipitation or mobility mechanisms between the two environmental compartments were taken into consideration. Any daughter nuclei which were not measured in the environment were also excluded. Dose rates calculations for β-emitters were not performed since they contribute less than 0.2% to the total dose rates according to the preliminary simulations.

Moreover, the lack of bioaccumulation factors for diatoms in the mineral springs did not allow for robust internal exposure evaluations. For the internal dose rate calculations, the basic assumption was that the same amount of radionuclides present in the environment, are uniformly diluted inside the microorganism. Consequently, the internal dose rate results should be treated as a qualitative representation of the internal exposure.

As a result, the simulated dose rates in this work should be interpreted

as a lower estimate of the radiation exposure expected by α-radioisotopes in the mineral springs. Nevertheless, all the results of the current study will be easily scaled up once the missing information is available: for instance, the bioaccumulation of radioelements inside the diatoms.

Conclusion

In this chapter, the diatoms radiation exposure and DNA damage corresponding to the radiological conditions in the Auvergne mineral springs studied in the current thesis was evaluated. In each mineral spring, the radiation pressure is different and it depends on the activity concentrations of the radionuclides present in the environment. The simulated external diatom dose rates in the mineral springs range from $5{\cdot}10^{-3}$ μGy/h (in Par) to 12.8 μGy/h (in Ours).

It was shown that only in 3 (Dourioux, Montagne 1, Ours) out of the 26 mineral springs, the simulated external dose rates to diatoms are close to or just above the suggested threshold for the protection of the ecosystems (10 μGy/h). Each of these three mineral springs has different radionuclide content: Dourioux, with 9.06 μGy/h diatom external dose rate belongs to High activity level springs according to the present work ^{222}Rn water activity concentration classification. The dose rate results in Dourioux are dominated by the contribution of ^{222}Rn, small contributions come from ^{226}Ra and ^{238}U in the sediments, while the contribution of ^{210}Po in water can be considered negligible.

In Ours, where the highest ^{226}Ra activity concentration in sediments was measured, the external dose rates (12.8 μGy) are dominated by the contribution of ^{226}Ra, while a small contribution to the diatom dose rates stems from ^{222}Rn in water.

In Montagne 1, where the highest ^{222}Rn activity concentrations in water are typically measured among the springs, ^{222}Rn contributes 78.61% to the diatom external dose rates (10.10 μGy/h), ^{210}Po 0.5% and ^{226}Ra 20.89%. It was also evaluated that during the monitoring period (April 2017 - September 2021), the external dose rates to diatoms due to ^{222}Rn varied between 1.7 μGy/h and 10.6 μGy/h. It is highlighted that the highest ^{222}Rn activity concentration in Montagne 1 (resulting in 10.6 μGy/h diatom external dose rate) corresponds to the study of Millan et al. [62] where the deformation rates of diatoms was found higher that 25%.

The total diatom DSB/generation vary between $7{\cdot}10^{-8}$ in Par to $5{\cdot}10^{-4}$ in Ours. Considering that in the most radioactive mineral springs the total

diatom DSB/generation are in the order of 10^{-4} without taking into account explicit bioaccumulation factors or the energy deposited by the daughter nuclei of the simulated radioelements, it may be considered that the radiation induced DNA Double Strand Breaks in the real environment of the mineral springs could be significantly higher than the predictions of the current work. It is reminded that experimentally determined spontaneous mutation rates for diatoms were recently calculated in the order of magnitude 10^{-2} mutations per generation [281].

CONCLUSIONS

The goal of this PhD was to develop a multiscale simulation to study the impact of ionizing radiation on microorganisms living in naturally radioactive mineral springs. This work is, to our knowledge, the first attempt of implementing a micro- and nano-scale Monte Carlo simulation of the radiation exposure of microorganisms living in naturally radioactive aquatic ecosystems. It is built upon the radiological characterization of mineral springs in Auvergne using the GATE and Geant4-DNA Monte Carlo simulation toolkits.

After introducing the context, the concepts and the tools in Chapter 1, the first task described in Chapter 2, was to conduct an extensive characterization of more than 20 mineral springs from the Auvergne region in France. The springs, characterized through γ-spectrometry, have varying ^{222}Rn activity concentrations in water, ranging from a few to more than 4000 Bq/L. One of those (identified as Montagne 1 in this manuscript) is the most radioactive mineral spring in the region, with ^{222}Rn activity concentration in water reaching 4600 Bq/L and a fluctuating behaviour possibly attributed to the peculiarity of the sampling site.

It was observed that the dominant radioelements in water and sediments are those of the ^{238}U decay chain: ^{226}Ra decay is the dominant source of irradiation in the sediments, while ^{222}Rn decay is the dominant source of irradiation in spring waters, both through their α-decay. Small contributions of ^{210}Po and ^{238}U were detected in some locations. Based on the measured activity concentrations in the sediments and water, the site-specific distribution coefficients (K_d) for ^{226}Ra in the mineral springs were also calculated.

In Chapter 3, GATE Monte Carlo platform was used to simulate the microorganisms and their environment at the micrometric scale using standard approximations: water as surrogate for biological medium and simplified spherical geometry for microorganisms.

Based on the radiological analyses of the springs (Chapter 2), microdosimetric simulations were performed considering ^{222}Rn and ^{210}Po in the water, and ^{226}Ra and ^{238}U in the sediments. It was shown that the dose rates received by the microorganisms living in the springs come mainly from

the α-emitters of the ^{238}U decay chain, in particular ^{226}Ra in the sediments and ^{222}Rn in water. By studying the energy deposited inside microorganisms surrounded by a silicate exoskeleton (frustule - the characteristic feature of diatoms), it was observed that the frustule reduced the received dose rates by approximately 10%. It was also evaluated that the frustule density variations (between 0.2 g/cm^3 and 2.4 g/cm^3) would not significantly affect the absorbed dose rates to diatoms (differences less than 11%).

In the absence of radionuclides bioaccumulation information for the microorganisms in the mineral springs, the internal exposure dose rate calculations were performed under the assumption that the radionuclides concentrations are equal inside and outside the organism, showing that the internal exposure can be significant. The comparison with ERICA, the reference tool for environmental radiation protection, showed that it has to be used with caution to assess dose rates to microorganisms, especially in mineral springs.

First, it was shown that the distribution coefficient K_d which links the activity concentration of a radioelement in water to its activity concentration in sediments, varies by several orders of magnitude among the mineral springs studied in this thesis. Another point of vigilance is the bioaccumulation factor (or equilibrium Concentration Ratio - CR) provided for phytoplankton. ERICA's default value for CR is very high (500) which means that the activity concentration inside the microorganisms is 500 times higher than outside. This average value is based on a set of publications, but the bioaccumulation varies considerably from one microorganism to another. To this day, relevant bioaccumulation factors for diatoms in mineral springs are not available.

Finally, the biggest limit in using ERICA for microorganisms is that the tool does not consider organisms weighting less than $1{\cdot}10^{-6}$ kg with spherical dimensions smaller than 600 μm radius. GATE is therefore an utterly complementary tool to ERICA to characterize, at the micrometric scale, the dose rates to microorganisms in naturally radioactive ecosystems.

In Chapter 4, the DNA damage to diatoms was studied. The genome of the vast majority of microorganisms living in mineral springs is not yet known. Therefore, no explicit DNA geometry was modelled but a clustering algorithm was rather used. This algorithm attributes Single and Double DNA Strand Breaks due to energy depositions in a fraction of the core volume (nucleus assimilated to water). The free parameters of the algorithm were adjusted based on the universality of the genomic density in eukaryotic cells. The

main result is that the DNA Double Strand Break rate is comparable to the only known spontaneous mutation rate published for a marine diatom species (*P. tricornutum*).

In Chapter 5, the diatoms radiation exposure and the DNA damage corresponding to the radiological conditions in the Auvergne mineral springs studied in the current thesis was evaluated. It was shown that the dose rates to diatoms are site-specific and they depend on the radionuclides and the respective activity concentrations. It was observed that only in 3 (Dourioux, Montagne 1, Ours) out of the 26 mineral springs, the simulated external dose rates to diatoms are close to or just above the suggested threshold for the protection of the ecosystems (10 μGy/h). The DNA Double Strand Breaks per diatom generation in each mineral spring was also evaluated. The results of the current thesis indicate that ionizing radiation could be an abiotic driver in the Auvergne radioactive mineral springs.

This thesis work opens short term perspectives:

- Prokaryotic organisms, as bacterial communities (cyanobacteria), are often present and studied in hydrothermal ecosystems: their genome are well known and the damage through radiation could be precisely simulated and compared to what obtained with diatoms.

- α-particle interactions are significantly impacted by the medium considered: simulations performed in this thesis could be refined by considering sediment heterogeneity.

- When bioaccumulation of certain radioelements in the microorganism' organelles or frustule will be measured, then calculated internal dose rates will be refined and renormalized accordingly.

- Travertine cores have already been sampled in Ours and Montagne mineral springs: their radiological characterization needs to be performed which would enable to refine the simulation in terms of the radionuclides mobility and distribution in the mineral springs ecosystems.

- Finally, based on this PhD work, an open source database of mean dose rates per unit of activity, calculated with the GATE platform, is being implemented for different spherical microorganisms sizes (from 10 to 150 μm in diameter) and for alpha emitters from the ^{238}U and ^{232}Th decay series present in water and sediments of different porosities and densities. This work will be a new building block in the development of predictive open source toolkits for radioprotection purposes.

In a longer term, the following perspectives have been identified:

- It has to be noticed that this PhD work focused on the radiotoxicity of radioelements. If Radon has no chemical activity because it is a noble gas, the other radioelements and, in particular Uranium, can induce chemical toxicity. With the ongoing PhD work of Yihua Hé (SUBATECH - Radiochemistry department) concerning the understanding of the role of the diatom on the Uranium speciation: simulations could be refined accordingly by taking into account radiochemistry data (presence, location and chemical form of radionuclides measured in the environment and inside microorganisms) and metabolism information to improve the realistic assessment of radiation-induced DNA damage.
- Preliminary irradiation tests were conducted on diatoms using a low energy X-ray irradiator (X-Rad320) in the objective to assess the response of the microalgae to radiation. As soon as the protocol for irradiation is set-up, diatoms will be also irradiated using the IBA Cyclotron Cyclone 70 from ARRONAX (Nantes) producing some MeV Helium ions.

Résumé analytique

Pendant près de 4 milliards d'années, la vie sur Terre s'est développée sous un fond de radiation. Un schéma de preuves croissant suggère que ses niveaux actuels peuvent affecter la charge mutationnelle et, par conséquent, la composition génétique des plantes et des animaux [1, 2]. La réponse à la radiation varie beaucoup parmi les différents organismes, alors qu'il existe encore une question ouverte concernant la radio-résistance et les niveaux d'exposition à la radioactivité naturelle [3].

La radioactivité naturelle a longtemps intrigué la communauté scientifique sur le rôle qu'elle pourrait avoir joué dans l'émergence et l'évolution de la vie [4]. Une contradiction principale découle du fait que bien que les mutagènes soient considérés comme un moteur de l'évolution biologique, il a été documenté que des dégénérescences génétiques significatives sont causées par la radiation.

En commençant par les rayons cosmiques [6, 7], des études mettent en évidence leur potentiel rôle dans la formation de la vie [8, 9] dans des environnements protégés, ou non, par des atmosphères et une magnétosphère terrestres, ainsi que leur effet sur la préservation de la vie dans l'espace [10].

La radiation ionisante émise naturellement dans les roches a déjà été suggérée comme étant un moteur de la vie, car il est possible qu'elle ait fourni l'énergie essentielle pour des réactions chimiques et biologiques [11, 12]. La radioactivité joue également un rôle important dans l'évolution de la biodiversité microbienne terrestre. Au fond des mines ou sous le plancher océanique, des forages ont révélé la présence de vastes communautés de micro-organismes dans le sous-sol de notre planète, où la radiolyse de l'eau, suite à la désintégration de radionucléides, entraîne la production d'hydrogène (H_2) et d'oxydants [13]. Cette radiolyse pourrait produire suffisamment d'énergie pour alimenter une grande partie de ce biome profond du sous-sol [14].

Bien que les radiations ionisantes aient été considérées comme toxiques à n'importe quel niveau d'exposition, les expériences menées à des niveaux

de radiation faibles offrent une fenêtre pour explorer les réponses adaptatives des systèmes biologiques à la radiation. Par exemple, la vie microbienne est stressée lorsqu'elle est privée de niveaux de radiation de fond [15].

Dans le même temps, des études se concentrent sur la corrélation entre la radiation et les mutations observées dans la vie microbienne, tandis que d'autres se concentrent sur l'observation de tout effet chronique [16]. Cependant, comprendre le rôle de la radioactivité naturelle dans l'évolution de la biodiversité microbienne est méthodologiquement difficile. De la nécessité d'expériences d'exposition à des niveaux faibles de radiation durant plusieurs générations de cellules, à la complexité des contrôles expérimentaux, nous devons également prendre en compte les implications liées à la mobilité des organismes et à d'autres facteurs perturbateurs, tels que les métaux lourds, les nitrates, les phosphates et la radiation UV du soleil, qui rendent chaque écosystème naturel unique [2].

La radioécologie étudie le comportement et l'impact des radionucléides sur l'environnement et les organismes vivants. De la présence naturelle de la radioactivité à la dispersion des radionucléides artificiels dans l'atmosphère, la biosphère et la géosphère, la radioécologie étudie les mécanismes de transfert des radioisotopes, l'évaluation et l'évaluation des effets potentiels sur la flore, la faune et les humains, et offre des orientations pour la protection contre les radiations des écosystèmes. Caractérisé par la multidisciplinarité, ce domaine de recherche est basé sur la collaboration entre les principales sciences telles que la physique, la chimie, la biologie, la géologie et les mathématiques, pour n'en citer que quelques-unes [17,18].

Dans ce contexte, l'évaluation du risque radioécologique pour l'environnement dû aux rayonnements ionisants a traditionnellement été abordée à travers sa biote car elle est le composant sensible des écosystèmes. Des initiatives importantes, telles que l'outil ERICA (Environmental Risks from Ionising Contaminants: Assessment and management), fournissent un certain nombre de composantes d'évaluation, notamment la modélisation du transfert des radionucléides dans l'environnement, l'estimation des taux de dose pour la biote à partir des distributions internes et externes des radionucléides, et l'établissement de la signification des taux de dose reçus par les organismes [19].

La pertinence de l'approche intégrée d'ERICA a été démontrée pour évaluer les risques environnementaux liés aux rayonnements ionisants pour les organismes macroscopiques, mais la difficulté de mesurer in vivo les taux de dose reçus par la biote à l'échelle de quelques micromètres, ainsi que

l'évaluation des dommages potentiels induits par les radiations à leur ADN (à l'échelle nanométrique), rendent l'utilisation d'approches de micro- et nano-dosimétrie essentielle [20, 21].

Une tendance commune en microdosimétrie expérimentale, appliquée dans une grande variété de domaines allant de l'aviation et de l'espace aux installations nucléaires et à la thérapie par rayonnement, est la validation des performances des microdétecteurs par des simulations de Monte Carlo (MC) [22–25]. Comme cela a déjà été démontré dans le cas des cellules humaines, les simulations Monte Carlo sont nécessaires pour les évaluations micro- et nano-dosimétriques en raison de la nature stochastique du dépôt d'énergie à l'échelle cellulaire [26].

La thèse actuelle fait partie du projet radioécologique TIRAMISU (*biodiversiTy in the RAdioactive Mineral Springs in Auvergne*) qui se concentre sur l'étude des effets radiologiques et radiotoxiques de la radioactivité naturelle sur les microorganismes vivant dans les sources minérales de la région d'Auvergne (France). L'objectif principal était d'utiliser les valeurs de concentration d'activité mesurées des radionucléides détectés dans les sources minérales d'Auvergne pour prédire les taux de dose et les dommages potentiels de l'ADN reçus par les microalgues habitant ces écosystèmes en utilisant des outils de simulation Monte Carlo open source. Une certaine classe de microalgues (les diatomées) ont attiré l'attention scientifique en raison de leurs caractéristiques particulières et de leur large gamme d'applications.

Une simulation multi-échelle a eté développée pour étudier l'impact des rayonnements ionisants sur les micro-organismes vivant dans des sources minérales naturellement radioactives. Ce travail est, à notre connaissance, la première tentative de mettre en œuvre une simulation de Monte Carlo à l'échelle micro- et nano-métrique de l'exposition aux radiations des micro-organismes vivant dans des écosystèmes aquatiques naturellement radioactifs. Il est basé sur la caractérisation radiologique des sources minérales en Auvergne en utilisant les outils de simulation de Monte Carlo GATE et Geant4-DNA.

Le mémoire est divisé en cinq chapitres. Le Chapitre 1 présente les principaux concepts de ce travail. Ensuite, trois parties principales sont distinguées : les mesures expérimentales, abordées dans le Chapitre 2, les simulations qui sont détaillées dans les Chapitres 3 et 4, et la synthèse des résultats pour les sources minérales en Auvergne présentée dans le Chapitre 5.

Plus spécifiquement, dans le Chapitre 1, le contexte, les concepts et les outils pertinents à ce travail multidisciplinaire sont abordés. Le projet TIRAMISU qui a inspiré cette thèse, les sources minérales et les diatomées - les microalgues particulières qui prolifèrent dans les écosystèmes aquatiques radioactifs d'intérêt sont présentés. En plus, la radioactivité naturelle et des interactions des rayonnements ionisants avec la matière, ainsi que les concepts dosimétriques de base sont discutées. Enfin, les outils radioécologiques existants et leurs limites sont présentés, pour conclure avec les outils de simulation Monte Carlo qui ont été utilisés dans cette travail : la plateforme GATE [27] et la trousse d'outils Geant4-DNA [28].

Le Chapitre 2 est dédié à la caractérisation des écosystèmes des sources minérales en Auvergne. Une vue d'ensemble des 26 sites d'échantillonnage et des méthodes utilisées pour collecter l'eau, les sédiments et les diatomées par des biologistes, géologues, radiochimistes et physiciens est présentée en premier lieu. Les techniques utilisées pour la caractérisation radiologique de l'eau et des sédiments sont détaillées ainsi que les informations disponibles sur les communautés de diatomées dans la région. Un aperçu des propriétés physico-chimiques des sources minérales est également présenté. Les débits de dose et les dommages à l'ADN, calculés par simulation, sont ajustés aux activités mesurées présentées dans ce chapitre.

Les sources, caractérisées par spectrométrie γ, ont des concentrations d'activité de ^{222}Rn variables dans l'eau, allant de quelques dizaines à plus de 4000 Bq/L. L'une d'entre elles (identifiée dans ce manuscrit sous le nom de Montagne 1) est la source minérale la plus radioactive de la région, avec une concentration d'activité de ^{222}Rn dans l'eau atteignant 4600 Bq/L et un comportement fluctuant pouvant être attribué à la particularité du site d'échantillonnage.

Il a été observé que les radioéléments dominants dans l'eau et les sédiments sont ceux de la chaîne de désintégration de l'uranium: la désintégration du ^{226}Ra est la source dominante d'irradiation dans les sédiments, tandis que la désintégration du ^{222}Rn est la source dominante d'irradiation dans les eaux des sources, toutes deux par leur décroissance alpha. De petites contributions de ^{210}Po et d'^{238}U ont été détectées dans certains endroits. En fonction des concentrations d'activité mesurées dans les sédiments et l'eau, les coefficients de distribution spécifiques au site (K_d) pour le ^{226}Ra dans les sources minérales ont également été calculés.

Le Chapitre 3 est dédié à l'évaluation des taux de dose reçus par les microorganismes vivant dans les sources minérales naturellement

radioactives. Deux parties principales sont distinguées: les simulations microdosimétriques utilisant GATE et les évaluations des taux de dose en utilisant l'outil radioécologique ERICA [29]. Tout d'abord, la configuration de simulation utilisant GATE est détaillée, une évaluation microdosimétrique est effectuée et les résultats pour l'exposition aux rayonnements externes et internes sont présentés. Ensuite, les principes de l'outil ERICA sont présentés et une comparaison entre les résultats de GATE et ERICA est présentée.

La plateforme de simulation Monte Carlo GATE a été utilisée pour simuler les micro-organismes et leur environnement à l'échelle micrométrique en utilisant des approximations standard: l'eau comme substitut pour le milieu biologique et une géométrie sphérique simplifiée pour les micro-organismes.

Basant sur les analyses radiologiques des sources (Chapitre 2), des simulations microdosimétriques ont été effectuées en considérant le ^{222}Rn et le ^{210}Po dans l'eau, et le ^{226}Ra et l'U dans les sédiments. Il a été montré que les doses reçues par les microorganismes vivant dans les sources proviennent principalement des émetteurs alpha de la chaîne de désintégration de l'U, en particulier le ^{226}Ra dans les sédiments et le ^{222}Rn dans l'eau. En étudiant l'énergie déposée à l'intérieur des microorganismes entourés d'une exosquelette de silicate (frustule - la caractéristique distinctive des diatomées), il a été observé que le frustule réduisait les taux de dose reçus d'environ 10%. Il a été également évalué que les variations de densité du frustule (entre 0.2 g/cm^3 et 2.4 g/cm^3) n'affecteraient pas de manière significative les taux de dose absorbés par les diatomées (différences inférieures à 11%).

En l'absence d'informations sur la bioaccumulation des radionucléides pour les microorganismes dans les sources minérales, les calculs de dose d'exposition interne ont été effectués en supposant que les concentrations de radionucléides sont égales à l'intérieur et à l'extérieur de l'organisme, montrant que l'exposition interne peut être significative. La comparaison avec ERICA, l'outil de référence pour la protection contre les rayonnements environnementaux, a montré qu'il doit être utilisé avec prudence pour évaluer les doses reçues par les microorganismes, en particulier dans les sources minérales.

En premier lieu, il a été montré que le coefficient de distribution K_d , qui relie la concentration d'activité d'un radioélément dans l'eau à sa concentration d'activité dans les sédiments, varie de plusieurs ordres de

grandeur parmi les sources thermales étudiées dans cette thèse. Un autre point de vigilance est le facteur de bioaccumulation (ou rapport de concentration à l'équilibre - CR) fourni pour le phytoplancton. La valeur par défaut de CR d'ERICA est très élevée (500), ce qui signifie que la concentration d'activité à l'intérieur des microorganismes est 500 fois plus élevée qu'à l'extérieur. Cette valeur moyenne est basée sur un ensemble de publications, mais la bioaccumulation varie considérablement d'un microorganisme à l'autre. À ce jour, des facteurs de bioaccumulation pertinents pour les diatomées dans les sources thermales ne sont pas disponibles.

Enfin, la plus grande limite de l'utilisation d'ERICA pour les microorganismes est qu'elle ne prend pas en compte les organismes ayant un poids inférieur à $1{\cdot}10^{-6}$ kg et des dimensions sphériques inférieures à 600 μm de rayon. GATE est donc un outil complémentaire indispensable à ERICA pour caractériser, à l'échelle micrométrique, les taux de dose pour les microorganismes dans les écosystèmes naturellement radioactifs.

Dans le Chapitre 4, les simulations à l'échelle nanométrique effectuées au niveau du noyau des micro-organismes à l'aide de Geant4-DNA sont décrites. Les dommages à l'ADN sont détaillés, en termes de cassures simples et doubles de brins d'ADN (SSB et DSB, respectivement), pour l'exposition aux radiations internes et externes. En raison du fait que la majorité des microorganismes vivant dans les sources minérales ont un génome inconnu, la géométrie de l'ADN n'a pas été simulée, mais on avait plutôt utilisé un algorithme de regroupement dans lequel seules les dépôts d'énergie dans une fraction du volume nucléaire (le noyau assimilé à de l'eau) peuvent générer des cassures simples et doubles de brins d'ADN. Les paramètres libres de l'algorithme ont été ajustés en fonction de l'universalité de la densité génomique dans les cellules eucaryotes. Le principal résultat est que le taux de cassures doubles de brins d'ADN est comparable au seul taux connu de mutation spontanée publié pour une espèce de diatomée marine (*P. tricornutum*).

Dans le Chapitre 5, les résultats des taux de dose et des dommages à l'ADN pour les diatomées dans chaque source minérale que nous avons étudiée en Auvergne sont rassemblés. Il a été montré comment les taux de dose sont spécifiques à chaque site pour les diatomées, dépendent des radionucléides et de leurs concentrations d'activité. il a été observé que seules dans 3 sources (Dourioux, Montagne 1, Ours) sur les 26 étudiées, les taux de dose externes simulés pour les diatomées sont proches ou juste au-dessus du seuil suggéré pour la protection des écosystèmes (10 μGy/h).

Les cassures double-brin de l'ADN par génération de diatomées dans chaque source ont également été évaluées. Les résultats indiquent que les radiations ionisantes pourraient être un facteur abiotique dans les sources minérales radioactives.

Ce travail de thèse ouvre des perspectives à court terme:

- Les organismes procaryotes, tels que les communautés bactériennes (cyanobactéries), sont souvent présents et étudiés dans les écosystèmes hydrothermaux: leur génome est bien connu et les dommages dus aux radiations pourraient être précisément simulés et comparés à ceux obtenus avec les diatomées.

- Les interactions des particules alpha sont significativement affectées par le milieu considéré : les simulations effectuées dans cette thèse pourraient être affinées en considérant l'hétérogénéité des sédiments.

- Lorsque la bioaccumulation de certains radioéléments dans les organites ou la frustule des micro-organismes sera mesurée, alors les taux de dose internes calculés seront affinés et renormalisés en conséquence.

- Des carottes de travertin ont déjà été prélevées dans les sources minérales d'Ours et de Montagne : leur caractérisation radiologique doit être effectuée afin de raffiner la simulation en termes de mobilité et de distribution des radionucléides dans les écosystèmes des sources minérales.

- Enfin, sur la base de ce travail de doctorat, une base de données open source de taux de dose moyens par unité d'activité, calculés avec la plateforme GATE, est en cours d'implémentation pour différentes tailles de microorganismes sphériques (de 10 à 150 μm de diamètre) et pour les émetteurs alpha des séries de désintégration ^{238}U et ^{232}Th présents dans l'eau et les sédiments de différentes porosités et densités. Ce travail sera un nouveau bloc de construction dans le développement d'outils open source prédictifs pour des fins de radioprotection.

À plus long terme, les perspectives suivantes ont été identifiées :

- Il convient de noter que ce travail de doctorat s'est concentré sur la radiotoxicité des radioéléments. Si le radon n'a pas d'activité chimique car c'est un gaz noble, les autres radioéléments et, en particulier l'uranium, peuvent induire une toxicité chimique. Avec le travail de

doctorat en cours de Yihua Hé (département de radiochimie de SUBATECH) sur la compréhension du rôle de la diatomée dans la spéciation de l'uranium : les simulations pourraient être affinées en prenant en compte les données de radiochimie (présence, emplacement et forme chimique des radionucléides mesurés dans l'environnement et à l'intérieur des microorganismes) et les informations sur le métabolisme pour améliorer l'évaluation réaliste des dommages à l'ADN induits par les radiations.

- Des tests d'irradiation préliminaires ont été effectués sur des diatomées à l'aide d'un irradiateur à rayons X à faible énergie (X-Rad320) dans le but d'évaluer la réponse des microalgues aux radiations. Dès que le protocole d'irradiation sera établi, les diatomées seront également irradiées à l'aide du cyclotron Cyclone 70 d'IBA chez ARRONAX (Nantes), produisant des ions d'hélium de quelques MeV.

Bibliography

[1] Moller AP, Mousseau TA. The effects of natural variation in background radioactivity on humans , animals and other organisms. Biological Reviews. 2012;88:226–254. doi:10.1111/j.1469-185X.2012.00249.x.

[2] Saclier N, Chardon P, Malard F, Konecny-Dupré L, Eme D, Bellec A, et al. Bedrock radioactivity influences the rate and spectrum of mutation. eLife. 2020;9:1–20. doi:10.7554/eLife.56830.

[3] Baumstark-Khan C, Facius R. Life under Conditions of Ionizing Radiation. Astrobiology. 2002; p. 261–284. doi:10.1007/978-3-642-59381-9_18.

[4] Haldane J. Radioactivity and the origin of life in Milne's cosmology. Nature. 1944;153:555–556. doi:https://doi.org/10.1038/153555a0.

[5] Zagórski ZP, Kornacka EM. Ionizing Radiation: Friend or Foe of the Origins of Life? Origins of Life and Evolution of Biospheres. 2012;42(5):503–505. doi:10.1007/s11084-012-9314-1.

[6] Todd P. Cosmic radiation and evolution of life on earth: Roles of environment, adaptation and selection. Advances in Space Research. 1994;14(10):305–313. doi:10.1016/0273-1177(94)90483-9.

[7] Dartnell LR. Ionizing radiation and life. Astrobiology. 2011;11(6):551–582. doi:10.1089/ast.2010.0528.

[8] Rodgers-Lee D, Vidotto AA, Taylor AM, Rimmer PB, Downes TP. The Galactic cosmic ray intensity at the evolving Earth and young exoplanets. Monthly Notices of the Royal Astronomical Society. 2020;499(2):2124–2137. doi:10.1093/mnras/staa2737.

[9] Abplanalp MJ, Gozem S, Krylov AI, Shingledecker CN, Herbst E, Kaiser RI. A study of interstellar aldehydes and enols as tracers of a cosmic ray-driven nonequilibrium synthesis of complex organic molecules. Proceedings of the National Academy of Sciences of the United States of America. 2016;113(28):7727–7732. doi:10.1073/pnas.1604426113.

[10] Horneck G, Klaus DM, Mancinelli RL. Space Microbiology. Microbiology and Molecular Biology Reviews. 2010;74(1):121–156. doi:10.1128/mmbr.00016-09.

[11] Atri D. On the possibility of galactic cosmic ray-induced radiolysis-powered life in subsurface environments in the Universe. Journal of the Royal Society Interface. 2016;13(123). doi:10.1098/rsif.2016.0459.

[12] Garzón L, Garzón ML. Radioactivity as a significant energy source in prebiotic synthesis. Origins of Life and Evolution of the Biosphere. 2001;31(1-2):3–13. doi:10.1023/A:1006664230212.

[13] Blair CC, D'Hondt S, Spivack AJ, Kingsley RH. Radiolytic hydrogen and microbial respiration in subsurface sediments. Astrobiology. 2007;7(6):951–970. doi:10.1089/ast.2007.0150.

[14] Sherwood Lollar B, Heuer VB, McDermott J, Tille S, Warr O, Moran JJ, et al. A window into the abiotic carbon cycle – Acetate and formate in fracture waters in 2.7 billion year-old host rocks of the Canadian Shield. Geochimica et Cosmochimica Acta. 2021;294:295–314. doi:10.1016/j.gca.2020.11.026.

[15] Castillo H, Schoderbek D, Dulal S, Escobar G, Wood J, Nelson R, et al. Stress induction in the bacteria Shewanella oneidensis and Deinococcus radiodurans in response to below-background ionizing radiation. International Journal of Radiation Biology. 2015;91(9):749–756. doi:10.3109/09553002.2015.1062571.

[16] Lampe N. The long term impact of ionising radiation on living systems. Nuclear Experiment. 2017; p. 210.

[17] Gilbin R, Arnold T, Beresford NA, Berthomieu C, Brown JE, de With G, et al. An updated strategic research agenda for the integration of radioecology in the european radiation protection research. Journal of Environmental Radioactivity. 2021;237. doi:10.1016/j.jenvrad.2021.106697.

[18] Institut De Protection Et De Sûreté Nucléaire. Radioecology IPSN booklets; 2001.

[19] Brown JE, Alfonso B, Avila R, Beresford NA, Copplestone D, Pröhl G, et al. The ERICA Tool. Journal of Environmental Radioactivity. 2008;99(9):1371–1383. doi:10.1016/j.jenvrad.2008.01.008.

[20] Rossi HH, Zaider M. Microdosimetry and Its Applications. Springer; 1996.

[21] Rabus H. Nanodosimetry – on the "tracks" of biological radiation effectiveness. Zeitschrift fur Medizinische Physik. 2020;30(2):91–94. doi:10.1016/j.zemedi.2020.01.002.

[22] Waker AJ. Techniques for radiation measurements: Microdosimetry and dosimetry. Radiation Protection Dosimetry. 2006;122(1-4):369–373. doi:10.1093/rpd/ncl497.

[23] Payervand F, Raisali GR, Hajiesmaeilbaigi F, Saramad S. Determination of dose-equivalent response of a typical diamond microdosimeter in space radiation fields. Iranian Journal of Medical Physics. 2018;15(1):39–47. doi:10.22038/ijmp.2017.24503.1242.

[24] Braby LA. Experimental microdosimetry: History, applications and recent technical advances. Radiation Protection Dosimetry. 2015;166(1-4):3–9. doi:10.1093/rpd/ncv137.

[25] Guardiola C, Fleta C, Quirion D, Pellegrini G, Gómez F. Silicon 3D microdetectors for microdosimetry in hadron therapy. Micromachines. 2020;11(12):1–20. doi:10.3390/mi11121053.

[26] Huang CY, Guatelli S, Oborn BM, Allen BJ. Microdosimetry for targeted alpha therapy of cancer. Computational and Mathematical Methods in Medicine. 2012;2012. doi:10.1155/2012/153212.

[27] The GATE Collaboration;. online. Available from: `https://gate.uca.fr/`.

[28] The Geant4-DNA collaboration. Geant4-DNA;. online. Available from: `http://geant4-dna.org/`.

[29] ERICA tool;. online. Available from: `https://erica-tool.com/`.

[30] Massif Central - Le territoire;. online. Available from: `http://www.massif-central.eu/le-massif/le-territoire/`.

[31] Cross R. Auvergne: its thermo-mineral springs, climate and scenery: a salutary resort for invalids. London: Hardwicke, provided by the University of Glasgow; 1867.

[32] Bretagnolle V, Benoit M, Bonnefond M, Breton V, Church JM, Gaba S, et al. Action-orientated research and framework: insights from the French longterm social-ecological research network. Ecology and Society. 2019;24(3). doi:10.5751/ES-10989-240310.

[33] CNRS. *Centre national de la recherche scientifique*;. online. Available from: https://www.cnrs.fr/fr.

[34] IRSN. *Institut de Radioprotection et de Sûreté Nucléaire*;. online. Available from: https://www.irsn.fr.

[35] CEA. *Commissariat à l'Energie Atomique*;. online. Available from: https://www.cea.fr.

[36] Xie M, Mayer KU, Claret F, Alt-Epping P, Jacques D, Steefel C, et al. Implementation and evaluation of permeability-porosity and tortuosity-porosity relationships linked to mineral dissolution-precipitation. Computational Geosciences. 2015;19(3):655–671. doi:10.1007/s10596-014-9458-3.

[37] Chagneau A, Tournassat C, Steefel CI, Bourg IC, Gaboreau S, Esteve I, et al. Complete restriction of 36Cl- diffusion by celestite precipitation in densely compacted illite. Environmental Science and Technology Letters. 2015;2(5):139–143. doi:10.1021/acs.estlett.5b00080.

[38] Fleury G, Del Nero M, Barillon R. Molecular fractionation of a soil fulvic acid (FA) and competitive sorption of trace metals (Cu, Zn, Cd, Pb) in hematite-solution systems: Effect of the FA-to-mineral ratio. RSC Advances. 2017;7(68):43090–43103. doi:10.1039/c7ra06838g.

[39] Walaszek M, Del Nero M, Bois P, Ribstein L, Courson O, Wanko A, et al. Sorption behavior of copper, lead and zinc by a constructed wetland treating urban stormwater. Applied Geochemistry. 2018;97(January):167–180. doi:10.1016/j.apgeochem.2018.08.019.

[40] Dumas E, Giraudo M, Goujon E, Halma M, Knhili E, Stauffert M, et al. Fate and ecotoxicological impact of new generation herbicides from the triketone family: An overview to assess the environmental risks. Journal of Hazardous Materials. 2017;325:136–156. doi:10.1016/j.jhazmat.2016.11.059.

[41] Rossi F, Artigas J, Mallet C. Structural and functional responses of leaf-associated fungal communities to chemical pollution in streams. Freshwater Biology. 2017;62(7):1207–1219. doi:10.1111/fwb.12937.

[42] Sletten S, Bourgeon S, Bårdsen BJ, Herzke D, Criscuolo F, Massemin S, et al. Organohalogenated contaminants in white-tailed eagle (Haliaeetus albicilla) nestlings: An assessment of relationships to immunoglobulin levels, telomeres and oxidative stress. Science of the Total Environment. 2016;539:337–349. doi:10.1016/j.scitotenv.2015.08.123.

[43] Jin Q, Su L, Montavon G, Sun Y, Chen Z, Guo Z, et al. Surface complexation modeling of U(VI) adsorption on granite at ambient/elevated temperature: Experimental and XPS study. Chemical Geology. 2016;433:81–91. doi:10.1016/j.chemgeo.2016.04.001.

[44] Razafindratsima S, Péron O, Piscitelli A, Gégout C, Schneider V, Barbecot F, et al. Transport properties of iodide in a sandy aquifer: Hydrogeological modelling and field tracer tests. Journal of Hydrology. 2015;520:61–68. doi:10.1016/j.jhydrol.2014.11.021.

[45] Theodorakopoulos N, Chapon V, Coppin F, Floriani M, Vercouter T, Sergeant C, et al. Use of combined microscopic and spectroscopic techniques to reveal interactions between uranium and Microbacterium sp. A9, a strain isolated from the Chernobyl exclusion zone. Journal of Hazardous Materials. 2015;285:285–293. doi:10.1016/j.jhazmat.2014.12.018.

[46] Hazotte AA, Peron O, Abdelouas A, Montavon G, Lebeau T. Microbial mobilization of cesium from illite: The role of organic acids and siderophores. Chemical Geology. 2016;428:8–14. doi:10.1016/j.chemgeo.2016.02.024.

[47] ANDRA-*Agence nationale pour la gestion des déchets radioactifs*. Inventaire National Des Matieres et Déchets Radioactifs;. online. Available from: `https://inventaire.andra.fr/site/rophin-mine`.

[48] AREVA. DREAL Auvergne-Rhône-Alpes, *Direction régionale de l'environnement, de l'aménagement et du logement*;. online. Available from: `https://www.auvergne-rhone-alpes.developpement-durable.gouv.fr/IMG/pdf/bilan_annuel_rophin_2010.pdf`.

[49] Taylor FB. The Literature of Diatoms. Transactions of the American Microscopical Society. 1921;40(4):187–194. doi:10.2307/3221973.

[50] Beauger A, Wetzel CE, Voldoire O, Garreau A, Ector L. Morphology and ecology of Craticula lecohui sp. nov. (Bacillariophyceae) from

hydrothermal springs (Puy-de-Dôme, Massif Central, France) and comparison with similar Craticula species. Nova Hedwigia, Beihefte. 2018;146(October):7–22. doi:10.1127/1438-9134/2017/007.

[51] Beauger A, Voldoire O, Wetzel CE, Allain E, Millan F, Breton V, et al. Biodiversity and ecology of diatoms in mineral springs of the area of of Sainte Marguerite (Saint-Maurice-ès-Allier, Massif central, France). BIOM. 2020;1:21–34. doi:10.18145/biom.v1i1.250.

[52] Baker LA, Beauger A, Wetzel CE, Voldoire O, Blavignac C, Allain E, et al. Brackish diatom species observed at the bituminous Poix spring: an island of curiosity. BIOM - Revue scientifique pour la biodiversité du Massif central. 2022;3(1):40–51.

[53] Baker LA, Beauger A, Kolovi S, Voldoire O, Allain E, Breton V, et al. Diatom DNA metabarcoding to assess the effect of natural radioactivity in mineral springs on ASV of benthic diatom communities. Science of the Total Environment. 2023;873(September 2022). doi:10.1016/j.scitotenv.2023.162270.

[54] Beauger A, Baker La, Wetzel CE, Ector L, Biron D. Thermo-Mineral Springs , Old and Unique Aquatic Ecosystems to Survey and Preserve. Biodiversity Online Journal. 2021;1(4). doi:BOJ.000519.2021.

[55] Baker LA, Biron DG, Millan F, Voldoire O, Breton V, Allain E, et al. The substrate, a key factor or not, to explain the species diversity of diatom communities in mineral springs. Botany Letters. 2022;169(2):155–165. doi:10.1080/23818107.2022.2028186.

[56] Breton V, et al. Impact of radioactivity on microorganisms living in mineral springs. Radiation Protection Dosimetry. 2022;Under review.

[57] Baker LA, Biron DG, Beauger A, Kolovi S, Colombet J, Allain E, et al. Virus-to-prokaryote ratio in spring waters along a gradient of natural radioactivity. Hydrobiologia. 2023;850(0123456789). doi:10.1007/s10750-023-05146-1.

[58] Holub G, et al. Bacterial communities in different natural radioactive mineral sources: how can the physico-chemical parameters structure these communities? Science of the Total Environment. 2023;To be submitted.

[59] Beauger A, Wetzel CE, Voldoire O, Garreau A, Ector L. Sellaphora labernardierei (Sellaphoraceae, Bacillariophyta), A new epilithic species from French spring and four new combinations within the genus Sellaphora. Phytotaxa. 2016;260(3):235–246. doi:10.11646/phytotaxa.260.3.3.

[60] Beauger A, Wetzel CE, Voldoire O, Ector L. Pseudostaurosira bardii (Fragilariaceae, Bacillariophyta), a new species from a saline hydrothermal spring of the Massif Central (France). Botany Letters. 2018;166(1):3–13. doi:10.1080/23818107.2018.1460278.

[61] Beauger A, Wetzel CE, Allain E, Bertin C, Voldoire O, Breton V, et al. Chamaepinnularia salina (Bacillariophyta), a new diatom species from French mineral springs (Massif Central). Phytotaxa. 2022;538(1):55–73. doi:10.11646/phytotaxa.538.1.5.

[62] Millan F, Izere C, Breton V, Voldoire O, Biron DG, Wetzel CE, et al. The effect of natural radioactivity on diatom communities in mineral springs. Botany Letters. 2020;167(1):95–113. doi:10.1080/23818107.2019.1691051.

[63] Kresic N. Types and classifications of springs. 1st ed. Elsevier Inc.; 2009.

[64] Bryan K. DigitalCommons at University of Nebraska - Lincoln Classification Of Springs. The Journal of Geology. 1919;27(7):522–561.

[65] Bourque PA. Planète Terre. Laval University, Department of Geology;. online. Available from: `http://www2.ggl.ulaval.ca/personnel/bourque/s3/eaux.souterraines.html`.

[66] Lecoq H. Les Eaux minérales considérées dans leurs rapports avec la chimie et la géologie. Paris: Rothchild, Source gallica.bnf.fr / BnF; 1864.

[67] Surmely F. Les sources minérales oubliées du Massif Central. Editions des monts d'Auvergne; 2004.

[68] Bérard P, Loizeau M, Rouzaire D, Vigouroux P. Amélioration de la connaissance des ressources en eau souterraine des sites thermaux en Auvergne, Site de Chaudes-Aigues (15). BRGM RF'-51722-FR. 2002;(15):152.

[69] Nations U, Committee S, Radiation A, Assembly G, Annexes S. SOURCES AND EFFECTS United Nations Scientific Committee on the Effects of Atomic Radiation. vol. I. UN; 2008.

[70] UNSCEAR. Sources, effects and risks of ionizing radiation. United Nations Scientific Committee on the Effects of Atomic Radiation.. vol. I. UN; 2008.

[71] Ielsch G, Cuney M, Buscail F, Rossi F, Leon A, Cushing ME. Estimation and mapping of uranium content of geological units in France. Journal of Environmental Radioactivity. 2017;166:210–219. doi:10.1016/j.jenvrad.2016.05.022.

[72] Ielsch G, Thiéblemont D, Labed V, Richon P, Tymen G, Ferry C, et al. Radon (222Rn) level variations on a regional scale: Influence of the basement trace element (U, Th) geochemistry on radon exhalation rates. Journal of Environmental Radioactivity. 2001;53(1):75–90. doi:10.1016/S0265-931X(00)00106-5.

[73] Rihs S, Condomines M, Fouillac C. U- and Th-series radionuclides in CO2-rich geothermal systems in the French Massif Central. Journal of Radioanalytical and Nuclear Chemistry. 1997;226(1-2):149–157. doi:10.1007/BF02063640.

[74] IRSN. *Cartographie du potentiel radon des formations géologiques*;. online. Available from: `https://is.gd/pOPIWp`.

[75] The United Nations scientific committee on the effects of atomic radiation. UNSCEAR 2008 Sources and effects of ionizing radiation; 2010.

[76] World Health Organization (WHO). Guidelines for Drinking-Water Quality, 3rd edition. WHO; 2008.

[77] European Parliament. Council Directive 2013/51/EURATOM laying down requirements for the protection of the health of the general public with regard to radioactive substances in water intended for human consumption. Official Journal of the European Union. 2013;.

[78] Beauger A, Voldoire O, Allain E, Gosseaume P, Blavignac C, Baker LA, et al. Biodiversity and Environmental Factors Structuring Diatom Assemblages of Mineral Saline Springs in the French Massif Central. Diversity. 2023;15(2). doi:10.3390/d15020283.

[79] Krieger RA. The chemistry of saline waters. Groundwater. 1963;1(4):7–12.

[80] Malviya S, Scalco E, Audic S, Vincent F, Veluchamy A, Poulain J, et al. Insights into global diatom distribution and diversity in the world's ocean. Proceedings of the National Academy of Sciences of the United States of America. 2016;113(11):E1516–E1525. doi:10.1073/pnas.1509523113.

[81] De Tommasi E, Gielis J, Rogato A. Diatom Frustule Morphogenesis and Function: a Multidisciplinary Survey. Marine Genomics. 2017;35(2017):1–18. doi:10.1016/j.margen.2017.07.001.

[82] Field C, Behrenfeld M, Randerson J, Falkowski P. Primary production of the biosphere: integrating terrestrial and oceanic components. Science. 1998;281:237–240. doi:10.1042/bst0040954.

[83] Sanyal A, Larsson J, van Wirdum F, Andrén T, Moros M, Lönn M, et al. Not dead yet: Diatom resting spores can survive in nature for several millennia. bioRxiv. 2019; p. 285122.

[84] Smol JP, Stoermer EF. The Diatoms: Applications for the Environmental and Earth Sciences. Cambridge University Press; 2010.

[85] Dodd MS, Papineau D, Grenne T, Slack JF, Rittner M, Pirajno F, et al. Evidence for early life in Earth's oldest hydrothermal vent precipitates. Nature. 2017;543(7643):60–64. doi:10.1038/nature21377.

[86] Betts HC, Puttick MN, Clark JW, Williams TA, Donoghue PCJ, Pisani D. Integrated genomic and fossil evidence illuminates life's early evolution and eukaryote origin. Nature Ecology and Evolution. 2018;2(10):1556–1562. doi:10.1038/s41559-018-0644-x.

[87] Benoiston AS, Ibarbalz FM, Bittner L, Guidi L, Jahn O, Dutkiewicz S, et al. The evolution of diatoms and their biogeochemical functions. Philosophical Transactions of the Royal Society B: Biological Sciences. 2017;372(1728). doi:10.1098/rstb.2016.0397.

[88] Mora D, Stancheva R, Jahn R. Cocconeis czarneckii sp. nov. (Bacillariophyta): a new diatom species from Lake Okoboji (Iowa, USA), based on the strain UTEX FD23. Phycologia. 2022;61(1):60–74. doi:10.1080/00318884.2021.2003684.

[89] Stanek-Tarkowska J, Czyż E, Rybak M. Description of a new diatom species—Microcostatus dexteri sp. nov.—from terrestrial habitats in southern Poland. Phytotaxa. 2021;509. doi:10.11646/phytotaxa.509.2.7.

[90] Roy S, Radhakrishnan C, Taylor JC, Kulikovskiy MS, Karthick B. Encyonema keshrii, sp. nov.: A New Diatom Species (Cymbellales, Bacillariophyceae) from the Indian Subcontinent. Cryptogamie, Algologie. 2020;41(2):7–17. doi:10.5252/cryptogamie-algologie2020v41a2.

[91] Mihalić KC, Galović I, Wetzel CE, Ector L, Ilijanić N, Miko S, et al. Envekadea vranaensis sp. Nov. a new diatom species (bacillariophyta) from the lacustrine holocene sediments of Lake Vrana, Croatia. Nova Hedwigia. 2020;110(1-2):1–9. doi:10.1127/nova_hedwigia/2019/0561.

[92] Ajani PA, Verma A, Lassudrie M, Doblin MA, Murray SA. A new diatom species P. Hallegraeffii sp. Nov. Belonging to the toxic genus Pseudo-nitzschia (Bacillariophyceae) from the East Australian Current. PLoS ONE. 2018;13(4):1–20. doi:10.1371/journal.pone.0195622.

[93] Bhattacharjya R, Tiwari A, Marella TK, Bansal H, Srivastava S. New paradigm in diatom omics and genetic manipulation. Bioresource Technology. 2021;325(January):124708. doi:10.1016/j.biortech.2021.124708.

[94] Tirichine L, Rastogi A, Bowler C. Recent progress in diatom genomics and epigenomics. Current Opinion in Plant Biology. 2017;36:46–55. doi:10.1016/j.pbi.2017.02.001.

[95] Sims PA, Mann DG, Medlin LK. Evolution of the diatoms: Insights from fossil, biological and molecular data. Phycologia. 2006;45(4):361–402. doi:10.2216/05-22.1.

[96] Harwood DM, Nikolaev V, Winter DM. Cretaceous records of diatom evolution, radiation and expansion. The Paleolontogical Society Papers. 2007;13:33–59. doi:10.1017/S1089332600.

[97] Snoeijs P, Notter M. Benthic diatoms as monitoring organisms for radionuclides in a Brackish-Water coastal environment. Journal of Environmental Radioactivity. 1993;18(1):23–52. doi:10.1016/0265-931X(93)90064-E.

[98] Heldal HE, Stupakoff I, Fisher NS. Bioaccumulation of 137Cs and 57Co by five marine phytoplankton species. Journal of Environmental Radioactivity. 2001;57(3):231–236. doi:10.1016/S0265-931X(01)00020-0.

[99] Uddin S, Behbehani M, Al-Ghadban AN, Sajid S, Vinod Kumar V, Al-Musallam L, et al. 210Po concentration in selected diatoms and dinoflagellates in the northern Arabian Gulf. Marine Pollution Bulletin. 2018;129(1):343–346. doi:10.1016/j.marpolbul.2018.02.051.

[100] Biswas RK, Choudhury AK. Diatoms: Miniscule biological entities with immense importance in synthesis of targeted novel bioparticles and biomonitoring. Journal of Biosciences. 2021;46(4). doi:10.1007/s12038-021-00222-x.

[101] Raven JA, Waite AM. The evolution of silicification in diatoms: Inescapable sinking and sinking as escape? New Phytologist. 2004;162(1):45–61. doi:10.1111/j.1469-8137.2004.01022.x.

[102] Chepurnov VA, Mann DG, Sabbe K, Vyverman W. Experimental studies on sexual reproduction in diatoms. International Review of Cytology. 2004;237:91–154. doi:10.1016/S0074-7696(04)37003-8.

[103] Armbrust EV. The life of diatoms in the world's oceans. Nature. 2009;459(7244):185–192. doi:10.1038/nature08057.

[104] Falciatore A, Bowler C. Revealing the molecular secrets of marine diatoms. Annual Review of Plant Biology. 2002;53(29):109–130. doi:10.1146/annurev.arplant.53.091701.153921.

[105] Parkinson J, Gordon R. Beyond micromachining: The potential of diatoms. Trends in Biotechnology. 1999;17(5):190–196. doi:10.1016/S0167-7799(99)01321-9.

[106] Kröger N, Poulsen N. Diatoms - From cell wall biogenesis to nanotechnology. Annual Review of Genetics. 2008;42:83–107. doi:10.1146/annurev.genet.41.110306.130109.

[107] Wang Y, Cai J, Jiang Y, Jiang X, Zhang D. Preparation of biosilica structures from frustules of diatoms and their applications: Current state and perspectives. Applied Microbiology and Biotechnology. 2013;97(2):453–460. doi:10.1007/s00253-012-4568-0.

[108] Rivasseau C, Farhi E, Compagnon E, de Gouvion Saint Cyr D, van Lis R, Falconet D, et al. Coccomyxa actinabiotis sp. nov. (Trebouxiophyceae, Chlorophyta), a new green microalga living in the spent fuel cooling pool of a nuclear reactor. Journal of Phycology. 2016;52(5):689–703. doi:10.1111/jpy.12442.

[109] Macaskie LE. The application of biotechnology to the treatment of wastes produced from the nuclear fuel cycle: Biodegradation and bioaccumulation as a means of treating radionuclide-containing streams. Critical Reviews in Biotechnology. 1991;11(1):41–112. doi:10.3109/07388559109069183.

[110] Patrick R, Palms J, Kreeger D, Harris C. Twenty-five-year study of radionuclides in the Susquehanna River via periphyton biomonitors. Health Physics. 2007;92(1):1–9. doi:10.1097/01.HP.0000228934.94734.3f.

[111] Sansone U, Belli M, Jeran Z, Kanivets VV, Radojko J. Suspended particle adhesion on aquatic plant surfaces implications for 137Cs and 133C uptake rates and water to plant concentration ratios. Journal of Environmental Radioactivity. 2002;59:257–271.

[112] Stevenson RJ, Pan Y, van Dam H. Assessing environmental conditions in rivers and streams with diatoms. The Diatoms: Applications for the Environmental and Earth Sciences, Second Edition. 2010; p. 57–85. doi:10.1017/CBO9780511763175.005.

[113] DREAL (Direction régionale de l'environnement dledlARA. Atlas des diatomées;. online. Available from: https://www.auvergne-rhone-alpes.developpement-durable.gouv.fr/atlas-des-diatomees-a3480.html.

[114] Antoine SE, Benson-Evans K. Teratological variations in the river Wye diatom flora, Wales, UK. Proceedings of the Eighth Diatom Symposium. 1984; p. 375–384.

[115] Hessen DO, De Lange HJ, Van Donk E. UV-induced changes in phytoplankton cells and its effects on grazers. Freshwater Biology. 1997;38(3):513–524. doi:10.1046/j.1365-2427.1997.00223.x.

[116] Falasco E, Bona F, Badino G, Hoffmann L, Ector L. Diatom teratological forms and environmental alterations: A review. Hydrobiologia. 2009;623(1):1–35. doi:10.1007/s10750-008-9687-3.

[117] Stoermer E, Andresen N. Atypical Tabularia in Coastal Lake Erie, USA. Fossil and recent phycological studies. 2006; p. 351–361.

[118] Hakansson H, Korhola A. Phenotypic plasticity in the diatom Cyclotella meneghiniana or a new species? Nova Hedwigia. 1998;66(1-2):187–196. doi:10.1127/nova.hedwigia/66/1998/187.

[119] Morin S. Bioindication des effets des pollutions metalliques sur les es de diatomees benthiques. Approches in situ et experimentales. [Ph.D. thesis]. Universite Sciences et Technologies - Bordeaux I; 2006.

[120] Lavoie I, Hamilton PB, Morin S, Kim Tiam S, Kahlert M, Gonçalves S, et al. Diatom teratologies as biomarkers of contamination: Are all deformities ecologically meaningful? Ecological Indicators. 2017;82:539–550. doi:10.1016/j.ecolind.2017.06.048.

[121] Gutiérrez A, Gordon R, Dávila LP. Deformation Modes and Structural Response of Diatom Frustules. Journal of Materials Science and Engineering with Advanced Technology. 2017;15(2):105–134. doi:10.18642/jmseat7100121810.

[122] Lai GG, Beauger A, Wetzel CE, Padedda BM, Voldoire O, Lugliè A, et al. Diversity, ecology and distribution of benthic diatoms in thermo-mineral springs in Auvergne (France) and Sardinia (Italy). PeerJ. 2019;7. doi:10.7717/peerj.7238.

[123] Straub F, Jeannin PY. Efficacité autoépuratoire de tracés aérien et karstique d'un effluent de station d'épuration (La Ronde, Jura suisse) : valeur indicative des diatomées. Symbioses. 2006;14:35–41.

[124] Audouze J, Vauclair S. An Introduction to Nuclear Astrophysics. 1st ed. Springer Dordrecht; 1980.

[125] Gueniot B, Munier-lamy C, Berthelin J. Geochemical Behavior of Uranium in Solis, Part I. Influence of the Pedogenetic Processes of the distribution of Uranium in Aerated Soils. J Geochem Expl. 1988;31:21–37.

[126] Garnier–Laplace J, Colle C, Morello M. Radionuclide fact sheet: Natural Uranium and the environment. Institut de Radioprotection et de Surete Nucleaire (IRSN) France; 2010.

[127] Zapecza OS, Szabo Z. Natural radioactivity in ground water. A Review, in Groundwater Quality: Hydrologic Conditions and Events. 1988; p. 50–57.

[128] Haridasan PP, Paul AC, Desai MVM. Natural radionuclides in the aquatic environment of a phosphogypsum disposal area. Journal of Environmental Radioactivity. 2001;53(2):155–165. doi:10.1016/S0265-931X(00)00121-1.

[129] Cowart JB, Burnett WC. The Distribution of Uranium and Thorium Decay Series Radionuclides in the Environment-A Review. Journal of Environmental Quality. 1994;23(4):651–662. doi:10.2134/jeq1994.00472425002300040005x.

[130] Kondev FG, Wang M, Huang WJ, Naimi S, Audi G. The NUBASE2020 evaluation of nuclear physics properties. Chinese Physics C. 2021;45(3). doi:10.1088/1674-1137/abddae.

[131] Kamal A. Nuclear physics. Springer Berlin, Heidelber; 2014.

[132] Krane K. Introductory Nuclear Physics. Wiley; 1988.

[133] Bertulani CA. Nuclear Physics in a Nutshell. Princeton University Press; 2007.

[134] Bateman, Harry. The solution of a system of differential equations occurring in the theory of radioactive transformations. In: Proceedings of the Cambridge Philosophical Society, Mathematical and physical sciences. vol. 11; 1910. p. 423–427. Available from: https://ocw.mit.edu/courses/earth-atmospheric-and-planetary-sciences/12-744-marine-isotope-chemistry-fall-2012/nuclear-systematics/MIT12_744F12_rd1910Btmn.pdf.

[135] Harvey BG. Introduction to nuclear physics and chemistry. Prentice-Hall chemistry series. Englewood Cliffs, N.J.: Prentice-Hall; 1962. Available from: file://catalog.hathitrust.org/Record/000440236http://hdl.handle.net/2027/mdp.39015004456102.

[136] Cetnar J. General solution of Bateman equations for nuclear transmutations. Annals of Nuclear Energy. 2006;33(7):640–645. doi:10.1016/j.anucene.2006.02.004.

[137] Gilmore GR. Practical Gamma-ray Spectrometry 2nd Edition. 2nd ed. Wiley; 2008.

[138] Knoll GF. Radiation Detection and Measurement. 3rd ed. Wiley; 2000.

[139] Turner JE. Atoms, Radiation, and Radiation Protection: Third Edition. Wiley; 2007.

[140] Jacob P, Debertin K, Miller K, Roed J, Saito K, Sanderson D. Basic Principles of Gamma-Ray Spectrometry. Reports of the International Commission on Radiation Units and Measurements. 1994;os-27(2):4–14. doi:10.1093/jicru_os27.2.4.

[141] Byun SH, et al. Radioisotopes and radiation methodology. Med Phys 4R06/6R03, version. 2014;15.

[142] Encyclopaedia Britannica. *Britannica kids*;. online. Available from: https://kids.britannica.com.

[143] NIST. *Photon cross sections database*;. online. Available from: https://physics.nist.gov/PhysRefData/Xcom/html/xcom1.html.

[144] NIST National Institut of Standards and Technology. *PSTAR Stopping power and range tables for protons*; accessed Nov 2022. online. Available from: https://physics.nist.gov/PhysRefData/Star/Text/PSTAR.html.

[145] NIST National Institut of Standards and Technology. *ASTAR Stopping power and range tables for helium ions*; accessed Nov 2022. online. Available from: https://physics.nist.gov/PhysRefData/Star/Text/ASTAR.html.

[146] NIST National Institut of Standards and Technology. *PSTAR Stopping power and range tables for electrons*; accessed Nov 2022. online. Available from: https://physics.nist.gov/PhysRefData/Star/Text/ASTAR.html.

[147] ICRU. ICRU Technical Report 60: Fundamental Quantities and Units for Ionizing Radiation; 1998.

[148] Franken NAP, ten Cate R, Krawczyk PM, Stap J, Haveman J, Aten J, et al. Comparison of RBE values of high- LET α-particles for the induction of DNA-DSBs, chromosome aberrations and cell reproductive death. Radiation Oncology. 2011;6(1):1–8. doi:10.1186/1748-717X-6-64.

[149] Asaithamby A, Chen DJ. Mechanism of cluster DNA damage repair in response to high-atomic number and energy

particles radiation. Mutation Research - Fundamental and Molecular Mechanisms of Mutagenesis. 2011;711(1-2):87–99. doi:10.1016/j.mrfmmm.2010.11.002.

[150] European Nuclear Society. Nuclear Glossary; accessed 16-11-2022. online. Available from: (https://www.euronuclear.org/glossary/radiation-weighting-factors).

[151] ICRP 60. Recommendations of the International Commission on Radiological Protection. ICRP Publication 60. Ann ICRP. 1991;21.

[152] ICRP 33. Relative Biological Effectiveness (RBE), Quality Factor (Q), and Radiation Weighting Factor (wR). Ann ICRP. 2003;92.

[153] Beaugelin-Seiller K. Environmental dosimetry - Radionuclide Fact Sheet; 2011.

[154] Kellerer AM. 2 - Fundamentals of Microdosimetry. In: KASE KR, BJÄRNGARD BE, ATTIX FH, editors. The Dosimetry of Ionizing Radiation. Academic Press; 1985. p. 77–162. Available from: https://www.sciencedirect.com/science/article/pii/B9780124004016500073.

[155] Cooper GM. The Cell: A Molecular Approach. 2nd edition. Sinauer Associates 2000; 2000.

[156] Gilson PR, Mcfadden G. Good things in small packages: the tiny genomes of chlorarachniophyte endosymbionts. BioEssays : news and reviews in molecular, cellular and developmental biology. 1997;19:167–173. doi:10.1002/bies.950190212.

[157] Sessions SK, College H. Genome Size. vol. 3. Elsevier Inc.; 2021.

[158] Carlin JL. Mutations Are the Raw Materials of Evolution. Nature Education Knowledge. 2011;3:10.

[159] Ward JF. DNA Damage Produced by Ionizing Radiation in Mammalian Cells: Identities, Mechanisms of Formation, and Reparability. Progress in Nucleic Acid Research and Molecular Biology. 1988;35(C):95–125. doi:10.1016/S0079-6603(08)60611-X.

[160] Hall EJ, Giaccia AJ. Radiobiology for the radiologist: Eighth edition. vol. 148; 2019.

[161] Water radiolysis: Influence of oxide surfaces on H2 production under ionizing radiation. Water (Switzerland). 2011;3(1):235–253. doi:10.3390/w3010235.

[162] Kumar A, Becker D, Adhikary A, Sevilla MD. Reaction of electrons with dna: Radiation damage to radiosensitization. International Journal of Molecular Sciences. 2019;20(16). doi:10.3390/ijms20163998.

[163] Siefermann KR, Liu Y, Lugovoy E, Link O, Faubel M, Buck U, et al. Binding energies, lifetimes and implications of bulk and interface solvated electrons in water. Nature Chemistry. 2010;2(4):274–279. doi:10.1038/nchem.580.

[164] ICRP 91. A Framework for Assessing the Impact of Ionising Radiation on Non-human Species. ICRP Publication 91. vol. 33; 2003.

[165] ICRP 103. The 2007 Recommendations of the International Commission on Radiological Protection. ICRP Publication 103. vol. 37; 2007.

[166] Kryshev II, Sazykina TG, Kryshev AI, Sanina KD. Risk Analysis using data from radioecological monitoring. Atomic Energy. 2009;106(6):332–339.

[167] Jones D, Domotor S, Higley K, Kocher D, Bilyard G. Principles and issues in radiological ecological risk assessment. Journal of Environmental Radioactivity. 2003;66:19–39. doi:10.1016/S0265-931X(02)00114-5.

[168] ICRP International Commission on Radiological Protection;. online. Available from: https://www.icrp.org/.

[169] BVSABR. ICRP concept on Protection of Environment. Annales de l'Association Belge de Radioprotection (BVSABR). 2018;43(1).

[170] Ruhm W, Clement C, Cool D, Laurier D, Bochud F, Applegate K, et al. Summary of the 2021 ICRP Workshop on the Future of Radiological Protection. Journal of Radiological Protection. 2022;42(2). doi:10.1088/1361-6498/ac670e.

[171] 108 I. Environmental Protection: the concept and use of reference animals and plans. ICRP Publication 108. Ann ICRP. 2008;38.

[172] 136 I. Dose coefficients for nonhuman biota environmentally exposed to radiation. ICRP Publication 136. Ann ICRP. 2017;46.

[173] Ulanowski A, Padilla-Alvarez R. IAEA CRP "Improving External Dosimetry for Terrestrial Animals and Plants";. online. Available from: https://www.iaea.org/projects/crp/k41023.

[174] Larsson CM. An overview of the ERICA Integrated Approach to the assessment and management of environmental risks from ionising contaminants. Journal of Environmental Radioactivity. 2008;99(9):1364–1370. doi:10.1016/j.jenvrad.2007.11.019.

[175] Larsson CM. The FASSET Framework for assessment of environmental impact of ionising radiation in European ecosystems - An overview. Journal of Radiological Protection. 2004;24(4 A). doi:10.1088/0952-4746/24/4A/001.

[176] Brown JE, Thørring H, Hosseini A. The ''EPIC" impact assessment framework e a deliverable report for EU Funded Project ICA2-CT-2000-10032; 2003.

[177] Brown JE, Jones SR, Saxén R, Thørring H, Vives i Batlle J. Radiation doses to aquatic organisms from natural radionuclides. Journal of Radiological Protection. 2004;24(4 A). doi:10.1088/0952-4746/24/4A/004.

[178] Vives i Batlle J, Copplestone D, Jones SR. Allometric methodology for the assessment of radon exposures to terrestrial wildlife. Science of the Total Environment. 2012;427-428:50–59. doi:10.1016/j.scitotenv.2012.03.088.

[179] Vives i Batlle J, Ulanovsky A, Copplestone D. A method for assessing exposure of terrestrial wildlife to environmental radon (222Rn) and thoron (220Rn). Science of the Total Environment. 2017;605-606:569–577. doi:10.1016/j.scitotenv.2017.06.154.

[180] Beresford NA, Barnett CL, Vives i Batlle J, Potter ED, Ibrahimi ZF, Barlow TS, et al. Exposure of burrowing mammals to 222Rn. Science of the Total Environment. 2012;431:252–261. doi:10.1016/j.scitotenv.2012.05.023.

[181] Vives i Batlle J, Jones SR, Copplestone D. A method for estimating 41Ar, 85,88Kr and 131m,133Xe doses to non-human biota. Journal of Environmental Radioactivity. 2015;144:152–161. doi:10.1016/j.jenvrad.2015.03.004.

[182] Copplestone D, Bielby S, Jones SR, Patton D, Daniel P, Gize I. Impact assessment of ionising radiation on wildlife. The Environment Agency R&D Publication 128. 2001; p. 1–222.

[183] Beaugelin-Seiller K, Jasserand F, Garnier-Laplace J, Gariel JC. EDEN: Software to calculate the dose rate of energy for the non-human biota, due to the presence of radionuclides in the environment. Environmental Studies. 2004;11:87–96.

[184] Yu C, Lepoire D, Kamboj S, Klett T, Arnish J, Cheng JJ, et al. RESRAD-BIOTA: A new code for evaluating environmental radiation doses to ecological receptors. Health Physics. 2003;84:S193–S194.

[185] Howard BJ, Beresford NA, Andersson P, Brown JE, Copplestone D, Beaugelin-Seiller K, et al. Protection of the environment from ionising radiation in a regulatory context-an overview of the PROTECT coordinated action project. Journal of Radiological Protection. 2010;30(2):195–214. doi:10.1088/0952-4746/30/2/S01.

[186] Zhang X, Yang Z, Qin C. Comparison and applicability analysis of models for estimating radiological dose rates of freshwater biota. IOP Conference Series: Earth and Environmental Science. 2018;108(4). doi:10.1088/1755-1315/108/4/042040.

[187] Ćujić M, Dragović S. Assessment of dose rate to terrestrial biota in the area around coal fired power plant applying ERICA tool and RESRAD BIOTA code. Journal of Environmental Radioactivity. 2018;188:108–114. doi:10.1016/j.jenvrad.2017.09.014.

[188] Beresford NA, Barnett CL, Jones DG, Wood MD, Appleton JD, Breward N, et al. Background exposure rates of terrestrial wildlife in England and Wales. Journal of Environmental Radioactivity. 2008;99:1430–1439. doi:10.1016/j.jenvrad.2008.03.003.

[189] Gomez-Ros JM, Prohl G, Taranenko V. Estimation of internal and external exposures of terrestrial reference organisms to natural radionuclides in the environment. Journal of Radiological Protection. 2004;24:A79–A88. doi:10.1088/0952-4746/24/4A/005.

[190] Hosseini A, Beresford NA, Brown JE, Jones DG, Phaneuf M, Thørring H, et al. Background dose-rates to reference animals and plants arising from exposure to naturally occurring radionuclides in aquatic

environments. Journal of Radiological Protection. 2010;30:235–264. doi:10.1088/0952-4746/30/2/S03.

[191] Thorring H, Brown JE, Hosseini A. Characterisation of background dose-rates for marine environments. Radioprotection. 2009;44:595–600. doi:https://doi.org/10.1051/radiopro/20095110.

[192] Beaugelin-Seiller K, Jasserand F, Garnier–Laplace J, Gariel JC. Modeling radiological dose in non-human species: principles, computerization, and application. Health Physics. 2006;90(5):485–493. doi:10.1097/01.HP.0000182192.91169.ed.

[193] Vassiliev ON. Monte Carlo Methods for Radiation Transport: Fundamentals and Advanced Topics; 2016.

[194] Incerti S, Kyriakou I, Bernal MA, Bordage MC, Francis Z, Guatelli S, et al. Geant4-DNA example applications for track structure simulations in liquid water: A report from the Geant4-DNA Project. Medical Physics. 2018;45(8):e722–e739. doi:10.1002/mp.13048.

[195] Kawrakow I. Accurate condensed history Monte Carlo simulation of electron transport. I. EGSnrc, the new EGS4 version. Medical Physics. 2000;27(3):485–498. doi:10.1118/1.598917.

[196] Bertolet A, Grilj V, Guardiola C, Harken AD, Cortés-giraldo MA, Baratto-roldán A. Experimental validation of an analytical microdosimetric model based on Geant4-DNA simulations by using a silicon-based microdosimeter. Radiation Physics and Chemistry. 2020;176(January):109060. doi:10.1016/j.radphyschem.2020.109060.

[197] Jan, S , Santin, G , Strul, D , Staelens, S , Assié, K , Autret, D , Avner, S , Barbier, R , Bardiès, M , Bloomfield, P M , Brasse, D , Breton, V , Bruyndonckx, P , Buvat, I , Chatziioannou, A F , Choi, Y , Chung, Y H , Comtat, C , Donnarieix, D , Ferr C. GATE: a simulation toolkit for PET and SPECT. Physics in Medicine and Biology. 2004;4543(19):4543. doi:10.1088/0031-9155/49/19/007.

[198] Jan S, Benoit D, Becheva E, Carlier T, Cassol F, Descourt P, et al. GATE V6: A major enhancement of the GATE simulation platform enabling modelling of CT and radiotherapy. Physics in Medicine and Biology. 2011;56(4):881–901. doi:10.1088/0031-9155/56/4/001.

[199] Bongrand A, Koumeir C, Villoing D, Guertin A, Haddad F, Métivier V, et al. A monte carlo determination of dose and range uncertainties for preclinical studies with a proton beam. Cancers. 2021;13(8). doi:10.3390/cancers13081889.

[200] Wang Y, Li Z, Zhang A, Gu P, Li F, Li X, et al. Microdosimetric calculations by simulating monoenergetic electrons in voxel models of human normal individual cells. Radiation Physics and Chemistry. 2020;166(July 2019):108518. doi:10.1016/j.radphyschem.2019.108518.

[201] Papadimitroulas P. Dosimetry applications in GATE Monte Carlo toolkit. Physica Medica. 2017;41:136–140. doi:10.1016/j.ejmp.2017.02.005.

[202] Clairand I, Bouchet LG, Ricard M, A, Villoing D, Marcatili S, et al. Internal Dosimetry with the Monte Carlo code GATE: validation using the ICRP/ICRU female reference computational mode. Physics in Medicine & Biology Phys Med Biol. 2017;62:1885–1904. doi:10.1088/1361-6560/62/5/1885.

[203] Agostinelli S, Allison J, Amako K, Apostolakis J, Araujo H, Arce P, et al. GEANT4 - A simulation toolkit. Nuclear Instruments and Methods in Physics Research, Section A: Accelerators, Spectrometers, Detectors and Associated Equipment. 2003;506(3):250–303. doi:10.1016/S0168-9002(03)01368-8.

[204] Allison J, Amako K, Apostolakis J, Araujo H, Dubois PA, Asai M, et al. Geant4 developments and applications. IEEE Transactions on Nuclear Science. 2006;53(1):270–278. doi:10.1109/TNS.2006.869826.

[205] Allison J, Amako K, Apostolakis J, Arce P, Asai M, Aso T, et al. Recent developments in GEANT4. Nuclear Instruments and Methods in Physics Research, Section A: Accelerators, Spectrometers, Detectors and Associated Equipment. 2016;835:186–225. doi:10.1016/j.nima.2016.06.125.

[206] Incerti S, Douglass M, Penfold S, Guatelli S, Bezak E. Review of Geant4-DNA applications for micro and nanoscale simulations. Physica Medica. 2016;32(10):1187–1200. doi:10.1016/j.ejmp.2016.09.007.

[207] Ivantchenko AV, Ivanchenko VN, Molina JMQ, Incerti SL. Geant4 hadronic physics for space radiation environment. International Journal of Radiation Biology. 2012;88(1-2):171–175. doi:10.3109/09553002.2011.610865.

[208] Freudenberg R, Wendisch M, Kotzerke J. Geant4-Simulations for cellular dosimetry in nuclear medicine. Zeitschrift fur Medizinische Physik. 2011;21(4):281–289. doi:10.1016/j.zemedi.2011.08.003.

[209] Geant4 , *examples*;. online. Available from: `https://geant4-userdoc.web.cern.ch/Doxygen/examples_doc/html/index.html`.

[210] Berman H, Henrick K, Nakamura H. Announcing the worldwide Protein Data Bank. Nature Structural Biology. 2003;10(12):980.

[211] Meylan S, Vimont U, Incerti S, Clairand I, Villagrasa C. Geant4-DNA simulations using complex DNA geometries generated by the DnaFabric tool. Computer Physics Communications. 2016;204:159–169. doi:10.1016/j.cpc.2016.02.019.

[212] Bernal MA, Bordage MC, Brown JMC, Davídková M, Delage E, El Bitar Z, et al. Track structure modeling in liquid water: A review of the Geant4-DNA very low energy extension of the Geant4 Monte Carlo simulation toolkit. Physica Medica. 2015;31(8):861–874. doi:10.1016/j.ejmp.2015.10.087.

[213] Incerti S, Baldacchino G, Bernal M, Capra R, Champion C, Francis Z, et al. The Geant4-DNA project The Geant4-DNA collaboration. International Journal of Modeling, Simulation, and Scientific Computing. 2010;1(2):157. doi:10.1142/S1793962310000122.

[214] Incerti S, Ivanchenko A, Karamitros M, Mantero A, Moretto P, Tran HN, et al. Comparison of GEANT4 very low energy cross section models with experimental data in water. Medical Physics. 2010;37(9):4692–4708. doi:10.1118/1.3476457.

[215] Francis Z, Villagrasa C, Clairand I. Simulation of DNA damage clustering after proton irradiation using an adapted DBSCAN algorithm. Computer Methods and Programs in Biomedicine. 2011;101(3):265–270. doi:10.1016/j.cmpb.2010.12.012.

[216] Francis Z, Stypczynska A. Clustering algorithms in radiobiology and DNA damage quantification. In: Data Security, Data Mining and Data Management: Technologies and Challenges. Nova Science Pub Inc; 2013. p. 1–29.

[217] Bibliotheque municipale, Commune de Chateldon. Extrait du Petit Thiernois; 1926.

[218] Jacquet C. Contribution a l'etude de la radioactivite des eaux minerales et du magnetisme des roches volcaniques du departement. In: Bulletin de l'Institut et Observatoire de physique du globe du Puy-de-Dôme. vol. 1. Paris : Presses universitaires de France, 1929-1948; 1929.

[219] ICRP 26. Recommendations of the Radiological Protection Commission on Radiological Protection. ICRP Publication 26. vol. 1; 1977.

[220] Hendee WR, Marc Edwards F. ALARA and an integrated approach to radiation protection. Seminars in Nuclear Medicine. 1986;16(2):142–150. doi:10.1016/S0001-2998(86)80027-7.

[221] Courtine F, Pilleyre T, Sanzelle S, Miallier D. Ge well detector calibration by means of a trial and error procedure using the dead layers as a unique parameter in a Monte Carlo simulation. Nuclear Instruments and Methods in Physics Research, Section A: Accelerators, Spectrometers, Detectors and Associated Equipment. 2008;596(2):229–234. doi:10.1016/j.nima.2008.07.155.

[222] Courtine F, Sanzelle S, Pilleyre T, Miallier D. Calibration of a germanium well-detector using 60Co: The effects of the angular correlation of the two gamma rays emitted in cascade, quantified with Monte Carlo simulations. Radiation Measurements. 2014;61:78–82. doi:10.1016/j.radmeas.2013.11.007.

[223] Pilleyre T, Sanzelle S, Miallier D, Faïn J, Courtine F. Theoretical and experimental estimation of self-attenuation corrections in determination of 210Pb by γ-spectrometry with well Ge detector. Radiation Measurements. 2006;41(3):323–329. doi:10.1016/j.radmeas.2004.11.007.

[224] Infoclimat. *Climatology and pluviometry database*;. online. Available from: `https://www.infoclimat.fr/climatologie/annee/2023/ferrieres-sur-sichon-cheval-rigon/valeurs/000P4.html`.

[225] IAEA. Sediment Distribution Coefficients and Concentration Factors for Biota in the Marine Environment. IAEA Technical Report 422. 2004;75(1):14–22.

[226] Onishi Y, Serne RJ, Arnold EM, Cowan CE. Critical review: Radionuclide transport, sediment transport, and water quality mathematical modeling; and radionuclide adsorption/desorption

mechanisms. Nuclear Regulatory Commission, Washington, DC (United States). Div. of Safeguards, Fuel Cycle and Environmental Research; Pacific Northwest Lab., Richland, WA (United States); 1981.

[227] US EPA. Understanding variation in partition coefficient, Kd, values. Volume II: review of geochemistry and available Kd values for cadmium, cesium, chromium, lead, plutonium, radon, strontium, thorium, tritium (3 h), and uranium. US EPA - United States Environmental Protection Agency. 1999;II(August):1–341.

[228] IAEA. Handbook of Parameter Values for the Prediction of Radionuclide Transfer in Terrestrial and Freshwater Environments. No. 472 in Technical Reports Series. INTERNATIONAL ATOMIC ENERGY AGENCY; 2010.

[229] Hosseini A, Thørring H, Brown JE, Saxén R, Ilus E. Transfer of radionuclides in aquatic ecosystems - Default concentration ratios for aquatic biota in the Erica Tool. Journal of Environmental Radioactivity. 2008;99(9):1408–1429. doi:10.1016/j.jenvrad.2008.01.012.

[230] Boyer P, Wells C, Howard B. Extended Kd distributions for freshwater environment. Journal of Environmental Radioactivity. 2018;192:128–142. doi:10.1016/j.jenvrad.2018.06.006.

[231] Sheppard S, Long J, Sanipelli B, Sohlenius G. Solid/liquid partition coefficients (Kd) for selected soils and sediments at Forsmark and Laxemar-Simpevarp; 2009. March.

[232] Kelleher K, Mcginnity P, Howard BJ, Boyer P, Vidal M, Bildstein OM. The use of the IAEA MARIS database in determining the variability of sediment distribution coefficients in the marine environment and potential implications for marine dispersion modelling. Journal of Radiological Protection. 2022;42(3). doi:10.1088/1361-6498/ac8a53.

[233] MARIS I. Marine Radioactivity Information System. In: Division of IAEA Environment Laboratories.; 2023. online. Available from: `https://maris.iaea.org`.

[234] OECD, Agency NE. Using Thermodynamic Sorption Models for Guiding Radioelement Distribution Coefficient (Kd) Investigations; 2001.

[235] Urso L, Hormann V, Diener A, Achatz M. Modelling partition coefficients of radium in soils. Applied Geochemistry. 2019;105(April):78–86. doi:10.1016/j.apgeochem.2019.04.014.

[236] Vandenhove H, Gil-García C, Rigol A, Vidal M. New best estimates for radionuclide solid-liquid distribution coefficients in soils. Part 2. Naturally occurring radionuclides. Journal of Environmental Radioactivity. 2009;100(9):697–703. doi:10.1016/j.jenvrad.2009.03.014.

[237] Ivanova K, Stojanovska Z, Badulin V, Kunovska B, Yovcheva M. Radiological impact of surface water and sediment near uranium mining sites. Journal of Radiological Protection. 2015;35(4):819–834. doi:10.1088/0952-4746/35/4/819.

[238] Galván J, Díaz I, Manjón G, Mantero J, Vioque I, Chakiri S. Distribution coefficients water sediment for uranium and polonium in the Moulouya River (eastern Morocco), a river affected by abandoned mines of lead and zinc. In: International Conference on Radioecological Concentration Processes; 2016. p. 1 – 6.

[239] Sahoo SK MS. Activity Ratio of Caesium, Strontium and Uranium with Site Specific Distribution Coefficients in Contaminated Soil near Vicinity of Fukushima Daiichi Nuclear Power Plant. Journal of Chromatography & Separation Techniques. 2014;05(06). doi:10.4172/2157-7064.1000250.

[240] US EPA. Understanding variation in partition coefficient, Kd, values. Volume III: review of geochemistry and available Kd values for americium, arsenic, curium, iodine, neptunium, radium, and technetium. US EPA - United States Environmental Protection Agency. 2004;III(July):1–188.

[241] Heydarizadeh P, Marchand J, Chenais B, Sabzalian MR, Zahedi M, Moreau B, et al. Functional investigations in diatoms need more than a transcriptomic approach. Diatom Research. 2014;29(1):75–89. doi:10.1080/0269249X.2014.883727.

[242] Tang W, Tang B, Li X, Wang Y, Li Z, Gao Y, et al. Cellular S-value evaluation based on real human cell models using the GATE MC package. Applied Radiation and Isotopes. 2021;168(October 2020):109509. doi:10.1016/j.apradiso.2020.109509.

[243] Salim R, Taherparvar P. Cellular S values in spindle-shaped cells: a dosimetry study on more realistic cell geometries using Geant4-

DNA Monte Carlo simulation toolkit. Annals of Nuclear Medicine. 2020;34(10):742–756. doi:10.1007/s12149-020-01498-z.

[244] Nikjoo H, Uehara S, Emfietzoglou D, Cucinotta FA. Track-structure codes in radiation research. Radiation Measurements. 2006;41(9):1052–1074. doi:https://doi.org/10.1016/j.radmeas.2006.02.001.

[245] Dingfelder M. Track-structure simulations for charged particles. Health physics. 2012;103(5):590–595. doi:10.1097/hp.0b013e3182621292.

[246] NIST National Institut of Standards and Technology. *Materials database*;. online. Available from: `https://materialsdata.nist.gov/`.

[247] Habchi C, Nguyen DT, Devès G, Incerti S, Lemelle L, Van Vang PL, et al. Three-dimensional densitometry imaging of diatom cells using STIM tomography. Nuclear Instruments and Methods in Physics Research, Section B: Beam Interactions with Materials and Atoms. 2006;249(1-2 SPEC. ISS.):653–659. doi:10.1016/j.nimb.2006.03.074.

[248] Miklasz KA, Denny MW. Diatom sinking speeds: Improved predictions and insight from a modified Stoke's law. Limnology and Oceanography. 2010;55(6):2513–2525. doi:10.4319/lo.2010.55.6.2513.

[249] Lu J, Sun C, Wang QJ. Mechanical Simulation of a Diatom Frustule Structure. Journal of Bionic Engineering. 2015;12(1):98–108. doi:10.1016/S1672-6529(14)60104-9.

[250] Li A, Zhang W, Ghaffarivardavagh R, Wang X, Anderson SW, Zhang X. Towards uniformly oriented diatom frustule monolayers: Experimental and theoretical analyses. Microsystems and Nanoengineering. 2016;2(December 2015). doi:10.1038/micronano.2016.64.

[251] Bertrand J, Coste C, Cohu RL, Renon Jp, Ector L. Étude préliminaire sur la présence de diatomées sur les lichens. Botany Letters. 2016;8107:1–23. doi:10.1080/23818107.2016.1156573.

[252] Browne E, Tuli JK. Nuclear Data Sheets for A = 234. Nuclear Data Sheets. 2007;108(3):681–772. doi:10.1016/j.nds.2007.02.003.

[253] Singh S, Jain AK, Tuli JK. Nuclear Data Sheets for A = 222. Nuclear Data Sheets. 2011;112(11):2851–2886. doi:10.1016/j.nds.2011.10.002.

[254] Singh B, Basunia MS, Martin M, McCutchan EA, Bala I, Caballero-Folch R, et al. Nuclear Data Sheets for A=218. Nuclear Data Sheets. 2019;160:405–471. doi:10.1016/j.nds.2019.100524.

[255] Kondev FG. Nuclear Data Sheets for A = 206. Nuclear Data Sheets. 2008;109(6):1527–1654. doi:10.1016/j.nds.2008.05.002.

[256] Morthekai P, Tiwari P, Murari MK, Singh P, Thakur B, Manoj MC, et al. Further investigations towards luminescence dating of diatoms. Radiation Measurements. 2022;156(June):106803. doi:10.1016/j.radmeas.2022.106803.

[257] European Commission. Radiation Protection, No.177 EU Scientific Seminar 2012 " Protection of the Environment "; 2014. November 2012.

[258] Agüero A, Alonzo F, Bjork M, Ciffroy P, Copplestone D, Garnier-Laplace J, et al.. ERICA DELIVERABLE 5: Derivation of Predicted-No-Effect-Dose-Rate values for ecosystems (and their sub-organisational levels) exposed to radioactive substances; 2006. Available from: https://wiki.ceh.ac.uk/download/attachments/115017395/FP6+ERICA+Deliverable+D5+-+28+Feb+06.pdf.

[259] Fisher NS, Teyssié JL, Krishnaswami S, Baskaran M. Accumulation of Th, Pb, U, and Ra in marine phytoplankton and its geochemical significance1. Limnology and Oceanography. 1987;32(1):131–142. doi:10.4319/lo.1987.32.1.0131.

[260] Copplestone D, Hingston J, Real A. The development and purpose of the FREDERICA radiation effects database. Journal of Environmental Radioactivity. 2008;99(9):1456–1463. doi:10.1016/j.jenvrad.2008.01.006.

[261] ICRP. BiotaDC v.1.5.2.;. online. Available from: http://biotadc.icrp.org/.

[262] Ulanovsky A, Copplestone D, Batlle JVI. ICRP Publication 136: Dose Coefficients for Non-human Biota Environmentally Exposed to Radiation. Annals of the ICRP. 2017;46(2):1–136. doi:10.1177/0146645317728022.

[263] Pröhl G, Brown J, Gomez-Ros J, Jones S, Woodhead D, Vives J, et al. Dosimetric models and data for assessing radiation exposure to biota. Deliverable 3 to the Project "FASSET" Framework for the assessment of Environmental Impact, contract No. Contract No FIGE-CT-2000-00102 Stockholm: Swedish Radiation Protection Authority. 2003;.

[264] WTD Wildlife Transfer Parameter Database;. online. Available from: https://www.wildlifetransferdatabase.org/panel.asp.

[265] Chambers DB, Osborne RV, Garva AL. Choosing an alpha radiation weighting factor for doses to non-human biota. Journal of Environmental Radioactivity. 2006;87(1):1–14. doi:10.1016/j.jenvrad.2005.10.009.

[266] Ulanovsky A, Pröhl G. A practical method for assessment of dose conversion coefficients for aquatic biota. Radiation and Environmental Biophysics. 2006;45(3):203–214. doi:10.1007/s00411-006-0061-4.

[267] Ulanovsky A, Pröhl G, Gómez-Ros JM. Methods for calculating dose conversion coefficients for terrestrial and aquatic biota. Journal of Environmental Radioactivity. 2008;99(9):1440–1448. doi:10.1016/j.jenvrad.2008.01.010.

[268] Garnier-Laplace J, Copplestone D, Gilbin R, Alonzo F, Ciffroy P, Gilek M, et al. Issues and practices in the use of effects data from FREDERICA in the ERICA Integrated Approach. Journal of Environmental Radioactivity. 2008;99(9):1474–1483. doi:10.1016/j.jenvrad.2008.04.012.

[269] Kulikov NV, Chebotina MY. Radioecology of freshwater biosystems. In: Ural Division of Academy Science. Sverdlovsk; 1988.

[270] Stewart GM, Fowler SW, Fisher NS. Chapter 8 The Bioaccumulation of U- and Th-Series Radionuclides in Marine Organisms. Radioactivity in the Environment. 2008;13(07):269–305. doi:10.1016/S1569-4860(07)00008-3.

[271] Fisher N, Burns K, Cherry R, Heyraud M. Accumulation and cellular distribution of 241 Am, 210Po, and 210Pb in two marine algae. Marine Ecology Progress Series. 1983;11:233–237. doi:10.3354/meps011233.

[272] Shannon LV, Cherry RD. Radium-226 in marine phytoplankton. Earth and Planetary Science Letters. 1971;11(1):339–343. doi:10.1016/0012-821X(71)90189-0.

[273] Pappa F, Patiris DL, Tsabaris C, Eleftheriou G, Androulakaki EG, Kokkoris M, et al. Comparison of MCNP and ERICA codes in two different marine areas. HNPS Proceedings. 2019;24:185. doi:10.12681/hnps.1863.

[274] Incerti S, Ivantchenko V, Karamitros M. Geant4 extended medical dna, *dnaphysics example*;. online. Available from: https://geant4-userdoc.web.cern.ch/Doxygen/examples_doc/html/ExampleDnaphysics.html.

[275] Geant4 extended medical dna examples, *clustering example*;. online. Available from: https://geant4-userdoc.web.cern.ch/Doxygen/examples_doc/html/Exampleclustering.html.

[276] The HDF5 group. HDF5 Hierarchical Data Format *version 5*;. online. Available from: https://www.hdfgroup.org/solutions/hdf5//.

[277] Kyriakou I, Incerti S, Francis Z. Technical note: Improvements in geant 4 energy-loss model and the effect on low-energy electron transport in liquid water. Medical Physics. 2015;42(7):3870–3876. doi:10.1118/1.4921613.

[278] Margis S, Magouni M, Kyriakou I, Georgakilas AG, Incerti S, Emfietzoglou D. Microdosimetric calculations of the direct DNA damage induced by low energy electrons using the Geant4-DNA Monte Carlo code. Physics in Medicine and Biology. 2020;65(4). doi:10.1088/1361-6560/ab6b47.

[279] Charlton DE. The deposition of energy in small cylindrical targets by high LET radiations. Radiation Protection Dosimetry. 1985;13(1-4):123–125.

[280] Stepiński D. Functional ultrastructure of the plant nucleolus. Protoplasma. 2014;251(6):1285–1306. doi:10.1007/s00709-014-0648-6.

[281] Krasovec M, Sanchez-Brosseau S, Piganeau G, Baer C. First Estimation of the Spontaneous Mutation Rate in Diatoms. Genome Biology and Evolution. 2019;11(7):1829–1837. doi:10.1093/gbe/evz130.

[282] Bowler C, Allen AE, Badger JH, Grimwood J, Jabbari K, Kuo A, et al. The Phaeodactylum genome reveals the evolutionary history of diatom genomes. Nature. 2008;456(7219):239–244. doi:10.1038/nature07410.

[283] Bowler C, Falciatore A. Phaeodactylum tricornutum. Trends in Genetics. 2019;35(9):706–707. doi:10.1016/j.tig.2019.05.007.

[284] Pampuch M, Walker EJL, Karas BJ. Towards synthetic diatoms: The Phaeodactylum tricornutum Pt-syn 1.0 project. Current

Opinion in Green and Sustainable Chemistry. 2022;35:100611. doi:10.1016/j.cogsc.2022.100611.

[285] Scala S, Carels N, Falciatore A, Chiusano ML, Bowler C. Genome properties of the diatom Phaeodactylum tricornutum. Plant Physiology. 2002;129(3):993–1002. doi:10.1104/pp.010713.

[286] Lewin JC. The taxonomic position of Phaeodactylum tricornutum. Journal of general microbiology. 1958;18(2):427–432. doi:10.1099/00221287-18-2-427.

[287] Martino AD, Meichenin A, Shi J, Pan K, Bowler C. Genetic and phenotypic characterization of Phaeodactylum tricornutum (Bacillariophyceae) accessions. Journal of Phycology. 2007;43(5):992–1009. doi:10.1111/j.1529-8817.2007.00384.x.

[288] Cavalier-Smith T. Skeletal DNA and the Evolution of Genome Size. Annual Review of Biophysics and Bioengineering. 1982;11(1):273–302. doi:10.1146/annurev.bb.11.060182.001421.

[289] Moeini H, Mokari M, Alamatsaz MH, Taleei R. Calculation of the initial DNA damage induced by alpha particles in comparison with protons and electrons using Geant4-DNA. International Journal of Radiation Biology. 2020;96(6):767–778. doi:10.1080/09553002.2020.1730015.

[290] Nikjoo H, O'Neill P, Wilson WE, Goodhead DT. Computational approach for determining the spectrum of DNA damage induced by ionizing radiation. Radiation Research. 2001;156(5 II):577–583. doi:10.1667/0033-7587(2001)156[0577:cafdts]2.0.co;2.

[291] Friedland W, Dingfelder M, Jacob P, Paretzke HG. Calculated DNA double-strand break and fragmentation yields after irradiation with He ions. Radiation Physics and Chemistry. 2005;72(2-3):279–286. doi:10.1016/j.radphyschem.2004.05.053.

[292] Semenenko VA, Stewart RD. Fast Monte Carlo simulation of DNA damage formed by electrons and light ions. Physics in Medicine and Biology. 2006;51(7):1693–1706. doi:10.1088/0031-9155/51/7/004.

[293] Semenenko VA, Stewart RD. A fast Monte Carlo algorithm to simulate the spectrum of DNA damages formed by ionizing radiation. Radiation Research. 2004;161(4):451–457. doi:10.1667/RR3140.

[294] Neary GJ, Horgan VJ, Bance DA, Stretch A. Further data on DNA Strand breakage by various radiation qualities. International Journal of Radiation Biology. 1972;22(6):525–537. doi:10.1080/09553007214551431.

[295] Frankenberg D, Brede HJ, Schrewe UJ, Steinmetz C, Frankenberg-Schwager M, Kasten G, et al. Induction of DNA double-strand breaks by 1H and 4He ions in primary human skin fibroblasts in the LET range of 8 to 124 keV/μm. Radiation Research. 1999;151(5):540–549. doi:10.2307/3580030.

[296] Jenner TJ, DeLara CM, O'Neill P, Stevens DL. Induction and rejoining of DNA double-Strand breaks in v79-4 mammalian cells following γ and αirradiation. International Journal of Radiation Biology. 1993;64(3):265–273. doi:10.1080/09553009314551421.

[297] Lampe N, Karamitros M, Breton V, Brown JMC, Sakata D, Sarramia D, et al. Mechanistic DNA damage simulations in Geant4-DNA Part 2: Electron and proton damage in a bacterial cell. Physica Medica. 2018;48(November 2017):146–155. doi:10.1016/j.ejmp.2017.12.008.

[298] Lampe N, Biron DG, Brown JMC, Incerti S, Marin P, Maigne L, et al. Simulating the impact of the natural radiation background on bacterial systems: Implications for very low radiation biological experiments. PLoS ONE. 2016;11(11):1–19. doi:10.1371/journal.pone.0166364.

[299] Lee H, Popodi E, Tang H, Foster PL. Rate and molecular spectrum of spontaneous mutations in the bacterium Escherichia coli as determined by whole-genome sequencing. Proceedings of the National Academy of Sciences of the United States of America. 2012;109(41). doi:10.1073/pnas.1210309109.

[300] Cannan W, Pederson D. Mechanisms and consequences of double-strand break formation in chromatin. Physiology & behavior. 2017;176(5):139–148. doi:10.1002/jcp.25048.Mechanisms.

[301] Rastogi RP, Madamwar D, Nakamoto H, Incharoensakdi A. Resilience and self-regulation processes of microalgae under UV radiation stress. Journal of Photochemistry and Photobiology C: Photochemistry Reviews. 2020;43:100322. doi:10.1016/j.jphotochemrev.2019.100322.

[302] Bray CM, West CE. DNA repair mechanisms in plants: Crucial sensors and effectors for the maintenance of genome integrity. New Phytologist. 2005;168(3):511–528. doi:10.1111/j.1469-8137.2005.01548.x.

[303] Baer CF. Does mutation rate depend on itself? PLoS Biology. 2008;6(2):0233–0235. doi:10.1371/journal.pbio.0060052.

[304] Jiang C, Mithani A, Belfield EJ, Mott R, Hurst LD, Harberd NP. Environmentally responsive genome-wide accumulation of de novo Arabidopsis thaliana mutations and epimutations. Genome Research. 2014;24(11):1821–1829. doi:10.1101/gr.177659.114.

[305] PubChem National Library of Medicine (US) - National Center for Biotechnology Information. Periodic Table of Elements; 2023. online. Available from: https://pubchem.ncbi.nlm.nih.gov/periodic-table/.

[306] NNDC National Nuclear Data Center. NUDAT3; retrieved 2023. online. Available from: https://www.nndc.bnl.gov/nudat3/indx_dec.jsp.

List of publications

- A. Beauger, O. Voldoire, C. E. Wetzel, E. Allain, F. Millan, V. Breton, **S. Kolovi**, and L. Ector, Biodiversity and Ecology of Diatoms in Mineral Springs of the Area of of Sainte Marguerite (Saint-Maurice-Ès-Allier, Massif Central, France), BIOM 1, 21 (2020), doi:10.18145/biom.v1i1.250.

- **S. Kolovi**, G.-R. Fois, S. Lanouar, P. Chardon, D. Miallier, G. Rivrais, E. Allain, L.-A. Baker, C. Bailly, A. Beauger, D.-G. Biron, Y. He, G. Holub, A.-H. Le Jeune, C. Mallet, H. Michel, G. Montavon, B. Schoefs, C. Sergeant, L. Maigne, and V. Breton, Radiation Exposure of Microorganisms Living in Radioactive Mineral Springs, EPJ Web Conf. 261, 04001 (2022), doi:10.1051/epjconf/202226104001.

- **S. Kolovi**, G.-R. Fois, S. Lanouar, P. Chardon, D. Miallier, G. Rivrais, E. Allain, L.-A. Baker, C. Bailly, A. Beauger, D.-G. Biron, Y. He, G. Holub, A.-H. Le Jeune, C. Mallet, H. Michel, G. Montavon, B. Schoefs, C. Sergeant, L. Maigne, and V. Breton, Radiation Exposure of Microorganisms Living in Radioactive Mineral Springs, HNPS Adv. Nucl. Phys. 28, 68 (2022), doi:10.12681/hnps.3585.

- A. Beauger, C. E. Wetzel, E. Allain, C. Bertin, O. Voldoire, V. Breton, L.-A. Baker, **S. Kolovi**, D. Biron, and L. Ector, Chamaepinnularia Salina (Bacillariophyta), A New Diatom Species from French Mineral Springs (Massif Central), Phytotaxa 538, 55 (2022), doi:10.11646/phytotaxa.538.1.5.

- L. A. Baker, A. Beauger, **S. Kolovi**, O. Voldoire, E. Allain, V. Breton, P. Chardon, D. Miallier, C. Bailly, G. Montavon, A. Bouchez, F. Rimet, C. Chardon, V. Vasselon, L. Ector, C. E. Wetzel, and D. G. Biron,

Diatom DNA Metabarcoding to Assess the Effect of Natural Radioactivity in Mineral Springs on ASV of Benthic Diatom Communities, Sci. Total Environ. 873, (2023), doi:10.1016/j.scitotenv.2023.162270.

- L. A. Baker, D. G. Biron, A. Beauger, **S. Kolovi**, J. Colombet, E. Allain, O. Voldoire, V. Breton, P. Chardon, T. Sime-Ngando, K. David, G. Montavon, H. Michel, and A. S. Pradeep Ram, Virus-to-Prokaryote Ratio in Spring Waters along a Gradient of Natural Radioactivity, Hydrobiologia (2023), doi:10.1007/s10750-023-05146-1.

- V. Breton, E. Allain, A. S. Pradeep Ram, C. Bailly, L. A. Baker, A. Beauger, D. G. Biron, E. Busato, H. Celle, P. Chardon, J. Colombet, K. David, G.-R. Fois, P.-J. Gauthier, Y. He, G. Holub, **S. Kolovi**, C. Landesman, A.-H. Le Jeune, L. Maigne, C. Mallet, J. Marchand, D. Miallier, H. Michel, G. Montavon, O. Peron, T. Pilleyre, B. Schoefs, C. Sergeant, H. Vesvres, and O. Voldoire, Impact of Radioactivity on Microorganisms Living in Mineral Springs, Radiat. Prot. Dosimetry, (2023 - Under review).

- **S. Kolovi**, G.-R. Fois, S. Lanouar, P. Chardon, D. Miallier, L. Baker, C. Bailly, A. Beauger, D.-G. Biron, K. David, G. Montavon, T. Pilleyre, B. Schoefs, V. Breton and L. Maigne, Simulation of the Radiation Exposure of Microorganisms Living in Naturally Radioactive Mineral Springs Using GATE and Geant4-DNA Monte Carlo Simulation Tools, PLoS One (2023 - Under review).

Appendices

Appendix A

Periodic table of elements

Figure A.1 Periodic table of elements [305]

Appendix B

Decay schemes

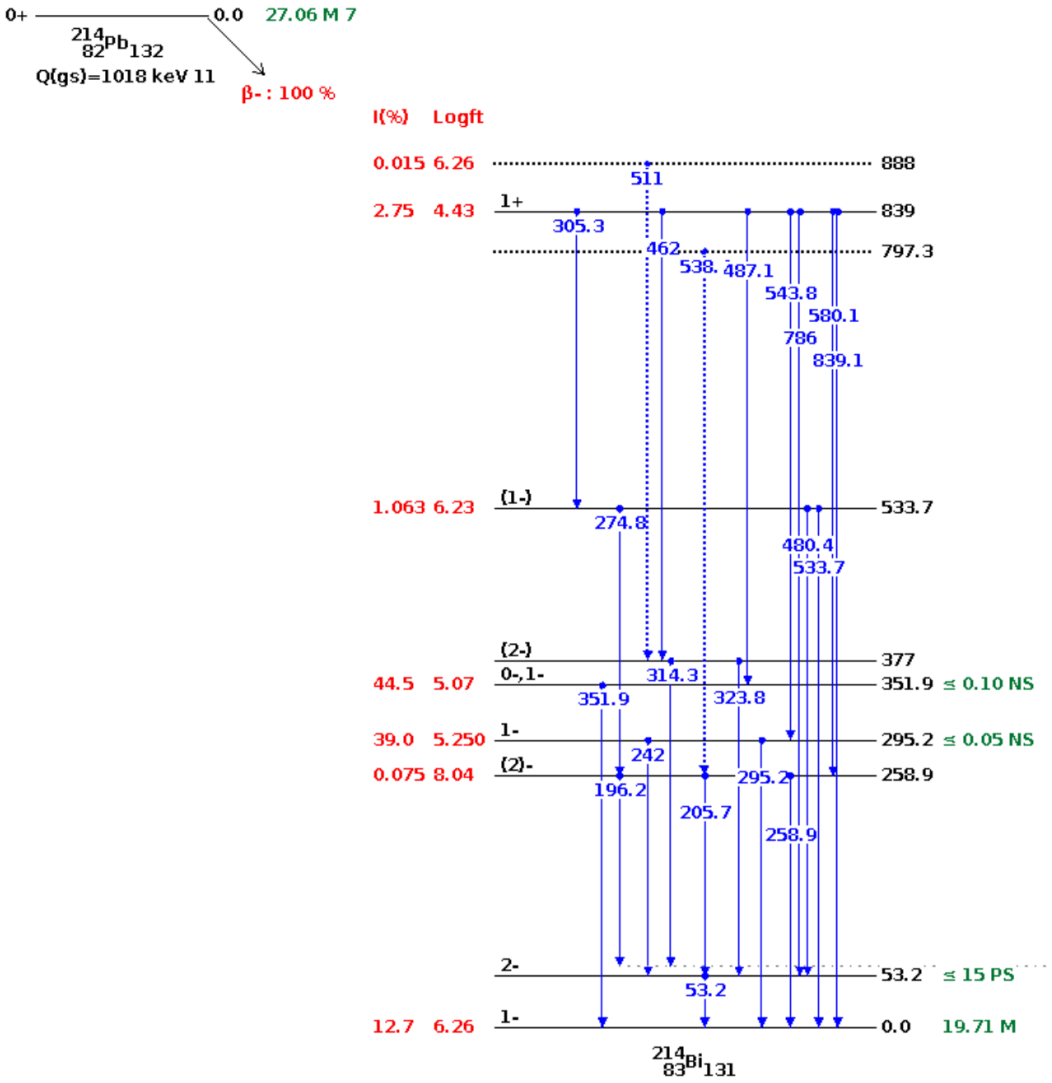

Figure B.1 ^{214}Pb partial decay scheme [306]

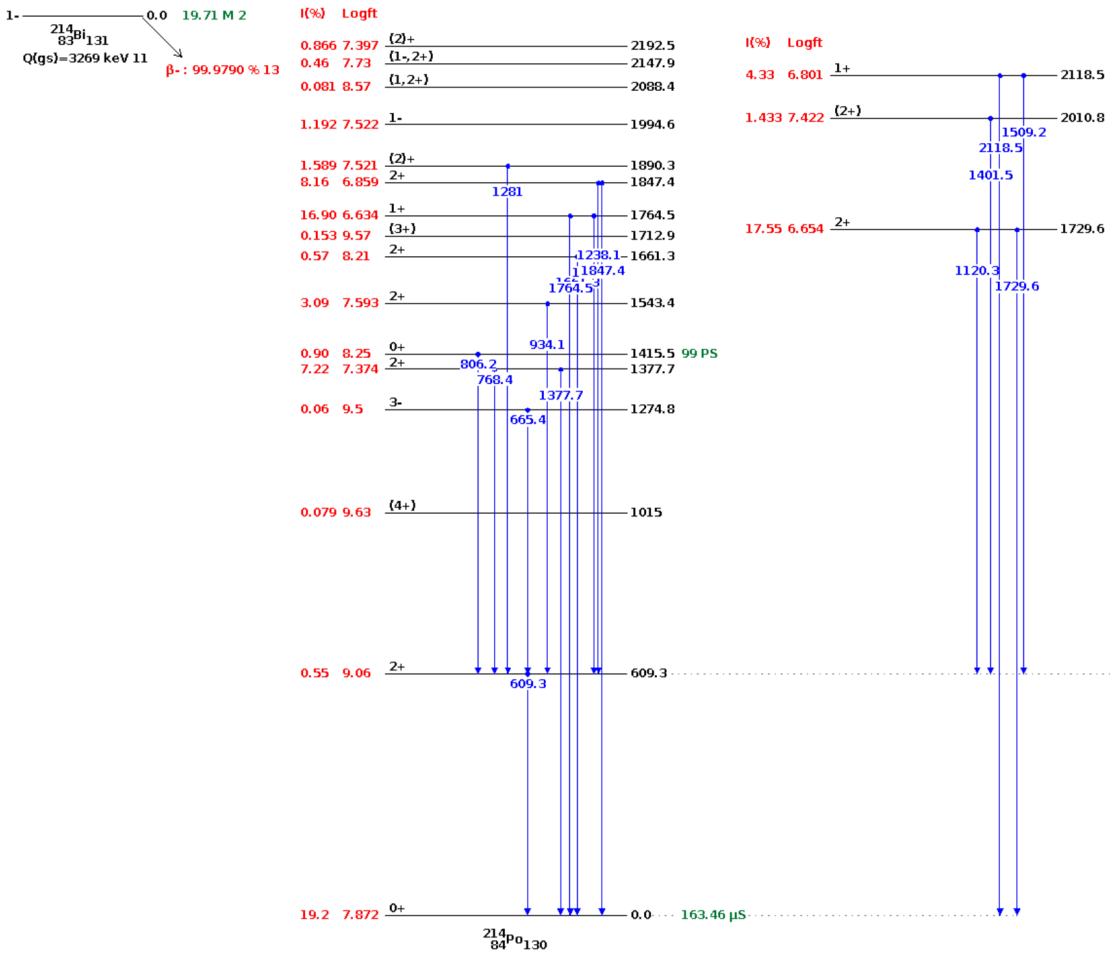

Figure B.2 ^{214}Bi partial decay scheme [306]

Appendix C

Sampling data

	Total Precipitation (mm)		^{222}Rn (Bq/L)			Conductivity (µS/cm)			Water temperature (°C)		
Date	**1 w prior to sampling**	**on date**	**M1**	**M2**	**Mariol**	**M1**	**M2**	**Mariol**	**M1**	**M2**	**Mariol**
18/04/2017	0.0	0.0	4108.0	-	-	-	-	-	-	-	-
30/05/2017	0.0	24.4	-	-	147.0	-	-	-	-	-	-
16/05/2018	61.2	0.0	4600.0	1737.0	147.0	512.0	493.0	767.0	11.3	10.3	17.3
18/01/2019	14.8	0.0	4561.0	-	-	-	-	-	-	-	-
08/04/2019	13.2	0.0	2780.0	2100.0	160.0	-	-	-	-	-	-
21/10/2019	72.8	0.8	3452.5	-	138.8	693.0	-	811.0	-	-	-
18/11/2019	18.0	1.8	1662.7	-	136.8	1343.0	1625.0	998.0	19.2	9.9	16.4
13/12/2019	30.2	8.4	761.7	1127.8	162.2	463.0	1468.0	819.0	9.6	9.3	17.1
10/01/2020	7.60	1.4	737.4	1866.1	134.1	362.0	1399.0	909.0	9.8	9.5	17.0
04/02/2020	23.6	3.2	796.4	1338.2	132.7	478.0	1568.0	817.0	9.8	9.4	16.7
23/06/2020	4.00	0.0	3746.4	2177.1	-	-	-	-	-	-	-
01/07/2020	1.20	1.8	-	-	139.1	-	-	-	-	-	-
28/07/2020	1.40	0.0	-	1448.7	-	-	-	-	-	-	-
16/09/2020	0.0	0.0	2610.3	1982.5	-	-	-	-	-	-	-
10/02/2021	53.6	2.0	1344.8	629.1	139.2	-	-	-	-	-	-
22/03/2021	20.8	0.0	3848.5	2212.1	130.3	-	-	-	-	-	-
21/04/2021	7.60	0.0	-	-	138.3	-	-	-	-	-	-
28/05/2021	13.2	0.0	2721.7	2440.3	-	-	-	-	-	-	-
08/09/2021	10.4	0.0	1610.3	2158.4	-	-	-	-	-	-	-

M1: Montagne 1, M2: Montagne 2, '-': absence of measurement

Appendix D

GATE macros

D.1 Energy deposition

D.1.1 Crystal SD

```
#Diatom_(microorganism_with_frustule)_in_benthic_mixture

#VISUALIZATION
#=============
#/vis/open OGLSQt
#/vis/viewer/set/viewpointThetaPhi 45 45
#/vis/viewer/flush
#/vis/viewer/zoom     50.0
#/vis/viewer/set/background 1 1 1 1
#/vis/viewer/set/background grey
#/vis/drawVolume
#/tracking/storeTrajectory 1
#/vis/scene/add/trajectories
#/vis/scene/endOfEventAction    accumulate 10
#/vis/reviewKeptEvents
#/vis/scene/add/text  1 0 0 mm 102 0 0 sediments
#/vis/scene/add/axes
#/vis/viewer/set/auxiliaryEdge true

#VERBOSE
#=======
/gate/verbose Physic 2
#/gate/verbose Cuts 2
#/gate/verbose SD 2
#/gate/verbose Actions 2
#/gate/verbose Actor 2
#/gate/verbose Step 2
/gate/verbose Error 2
/gate/verbose Warning 2
#/gate/verbose Output 2
#/gate/verbose Beam 2
#/gate/verbose Volume 2
```

```
#/gate/verbose Image 2
/gate/verbose Geometry 2
#/gate/verbose Core 2
#/run/verbose 2
#/event/verbose 2
#/tracking/verbose 2

#GEOMETRY
#========
#Materials
/gate/geometry/setMaterialDatabase data/GateMaterials_9.db

#World
/gate/world/setMaterial Vacuum
/gate/world/geometry/setXLength 1 m
/gate/world/geometry/setYLength 1 m
/gate/world/geometry/setZLength 1 m

#Scanner
/gate/world/daughters/name scanner
/gate/world/daughters/insert box
/gate/scanner/geometry/setXLength 5 cm
/gate/scanner/geometry/setYLength 5 cm
/gate/scanner/geometry/setZLength 5 cm
/gate/scanner/placement/setTranslation 0.0 0.0 0.0 cm
/gate/scanner/setMaterial G4_WATER
/gate/scanner/vis/setVisible 1
/gate/scanner/vis/setColor blue
/gate/scanner/vis/setLineStyle dashed

#Environment
/gate/scanner/daughters/name sedim
/gate/scanner/daughters/insert sphere
/gate/sedim/geometry/setRmin 0 um
/gate/sedim/geometry/setRmax 57.1 um
/gate/sedim/geometry/setPhiStart 0 deg
/gate/sedim/geometry/setDeltaPhi 360 deg
/gate/sedim/geometry/setThetaStart 0 deg
/gate/sedim/geometry/setDeltaTheta 360 deg
/gate/sedim/placement/setTranslation 0.0 0.0 0.0  cm
/gate/sedim/setMaterial Sediments
/gate/sedim/vis/setVisible 1
/gate/sedim/vis/setColor grey

#Frustule
/gate/sedim/daughters/name frustule
```

```
/gate/sedim/daughters/insert sphere
/gate/frustule/geometry/setRmin 0 um
/gate/frustule/geometry/setRmax 12 um
/gate/frustule/geometry/setPhiStart 0 deg
/gate/frustule/geometry/setDeltaPhi 360 deg
/gate/frustule/geometry/setThetaStart 0 deg
/gate/frustule/geometry/setDeltaTheta 360 deg
/gate/frustule/placement/setTranslation 0.0 0.0 0.0  cm
/gate/frustule/setMaterial Silicate
/gate/frustule/vis/setVisible 1
/gate/frustule/vis/setColor magenta

#Microorganism
/gate/frustule/daughters/name diatom
/gate/frustule/daughters/insert sphere
/gate/diatom/geometry/setRmin 0 um
/gate/diatom/geometry/setRmax 10 um
/gate/diatom/geometry/setPhiStart 0 deg
/gate/diatom/geometry/setDeltaPhi 360 deg
/gate/diatom/geometry/setThetaStart 0 deg
/gate/diatom/geometry/setDeltaTheta 360 deg
/gate/diatom/placement/setTranslation 0.0 0.0 0.0  cm
/gate/diatom/setMaterial G4_WATER
/gate/diatom/vis/setVisible 1
/gate/diatom/vis/setColor blue

#Nucleus
/gate/diatom/daughters/name nucleus
/gate/diatom/daughters/insert sphere
/gate/nucleus/geometry/setRmin   0 um
/gate/nucleus/geometry/setRmax   0.5 um
/gate/nucleus/geometry/setPhiStart 0 deg
/gate/nucleus/geometry/setDeltaPhi 360 deg
/gate/nucleus/geometry/setThetaStart 0 deg
/gate/nucleus/geometry/setDeltaTheta 360 deg
/gate/nucleus/placement/setTranslation 0.0 0.0 0.0  cm
/gate/nucleus/setMaterial                G4_WATER
/gate/nucleus/vis/setVisible     1
/gate/nucleus/vis/setColor               cyan

#CrystalSD
#=========
/gate/systems/scanner/level1/attach diatom
/gate/diatom/attachCrystalSD

#PHYSICS
```

```
#=======
/gate/physics/addPhysicsList emstandard_opt4

#CUTS
#====
/gate/physics/Gamma/SetCutInRegion      world 1 m
/gate/physics/Electron/SetCutInRegion   world 1 m
/gate/physics/Positron/SetCutInRegion   world 1 m

/gate/physics/Gamma/SetCutInRegion      scanner 5 cm
/gate/physics/Electron/SetCutInRegion   scanner 5 cm
/gate/physics/Positron/SetCutInRegion   scanner 5 cm

/gate/physics/Gamma/SetCutInRegion      sedim 0.1 um
/gate/physics/Electron/SetCutInRegion   sedim 0.1 um
/gate/physics/Positron/SetCutInRegion   sedim 0.1 um

/gate/physics/Gamma/SetCutInRegion      frustule 0.01 um
/gate/physics/Electron/SetCutInRegion   frustule 0.01 um
/gate/physics/Positron/SetCutInRegion   frustule 0.01 um

/gate/physics/Gamma/SetCutInRegion      diatom 0.01 um
/gate/physics/Electron/SetCutInRegion   diatom 0.01 um
/gate/physics/Positron/SetCutInRegion   diatom 0.01 um

/gate/physics/Gamma/SetCutInRegion     nucleus 0.001 um
/gate/physics/Electron/SetCutInRegion   nucleus 0.001 um
/gate/physics/Positron/SetCutInRegion   nucleus 0.001 um

/gate/physics/displayCuts

#ACTORS
#======
#StatisticsActor
/gate/actor/addActor SimulationStatisticActor stat
/gate/actor/stat/save output/statistics_Ra.txt

#INITIALIZATION
#==============
/gate/run/initialize

#SOURCE
#======
/gate/source/addSource sed_emission gps
/gate/source/sed_emission/gps/particle alpha
/gate/source/sed_emission/gps/energytype UserSpectrum
```

```
/gate/source/sed_emission/gps/setSpectrumFile data/238Uchain/226Ra.txt
/gate/source/sed_emission/gps/type Volume
/gate/source/sed_emission/gps/shape Sphere
/gate/source/sed_emission/gps/radius 57.1 um
/gate/source/sed_emission/gps/angtype iso
/gate/source/sed_emission/gps/centre 0 0.0 0 cm
/gate/source/sed_emission/gps/Forbid diatom_phys
/gate/source/sed_emission/gps/Forbid nucleus_phys
/gate/source/sed_emission/gps/Forbid frustule_phys
/gate/source/sed_emission/dump 3

#OUTPUT
#======
/gate/output/tree/enable
/gate/output/tree/addFileName output/edep_Ra.root
/gate/output/tree/hits/enable

#SEED
#====
/gate/random/setEngineName MersenneTwister
/gate/random/setEngineSeed auto

#MEASUREMENT SETTINGS
#====================
/gate/application/setTotalNumberOfPrimaries 1E8
/gate/application/start
```

D.1.2 Dose Actor

```
##Diatom_(microorganism_with_frustule)_in_benthic_mixture

#GEOMETRY
#========
#Materials
/gate/geometry/setMaterialDatabase data/GateMaterials_9.db

#World
/gate/world/setMaterial Vacuum
/gate/world/geometry/setXLength 1 m
/gate/world/geometry/setYLength 1 m
/gate/world/geometry/setZLength 1 m

#Water_box
/gate/world/daughters/name waterbox
/gate/world/daughters/insert box
/gate/waterbox/geometry/setXLength 5 cm
```

```
/gate/waterbox/geometry/setYLength 5 cm
/gate/waterbox/geometry/setZLength 5 cm
/gate/waterbox/placement/setTranslation 0.0 0.0 0.0 cm
/gate/waterbox/setMaterial G4_WATER
/gate/waterbox/vis/setVisible 1
/gate/waterbox/vis/setColor blue
/gate/waterbox/vis/setLineStyle dashed

#Environment
/gate/waterbox/daughters/name sedim
/gate/waterbox/daughters/insert sphere
/gate/sedim/geometry/setRmin 0 um
/gate/sedim/geometry/setRmax 57.1 um
/gate/sedim/geometry/setPhiStart 0 deg
/gate/sedim/geometry/setDeltaPhi 360 deg
/gate/sedim/geometry/setThetaStart 0 deg
/gate/sedim/geometry/setDeltaTheta 360 deg
/gate/sedim/placement/setTranslation 0.0 0.0 0.0  cm
/gate/sedim/setMaterial Sediments
/gate/sedim/vis/setVisible 1
/gate/sedim/vis/setColor grey

#Frustule
/gate/sedim/daughters/name frustule
/gate/sedim/daughters/insert sphere
/gate/frustule/geometry/setRmin 0 um
/gate/frustule/geometry/setRmax 12 um
/gate/frustule/geometry/setPhiStart 0 deg
/gate/frustule/geometry/setDeltaPhi 360 deg
/gate/frustule/geometry/setThetaStart 0 deg
/gate/frustule/geometry/setDeltaTheta 360 deg
/gate/frustule/placement/setTranslation 0.0 0.0 0.0  cm
/gate/frustule/setMaterial Silicate
/gate/frustule/vis/setVisible 1
/gate/frustule/vis/setColor magenta

#Microorganism
/gate/frustule/daughters/name diatom
/gate/frustule/daughters/insert sphere
/gate/diatom/geometry/setRmin 0 um
/gate/diatom/geometry/setRmax 10 um
/gate/diatom/geometry/setPhiStart 0 deg
/gate/diatom/geometry/setDeltaPhi 360 deg
/gate/diatom/geometry/setThetaStart 0 deg
/gate/diatom/geometry/setDeltaTheta 360 deg
/gate/diatom/placement/setTranslation 0.0 0.0 0.0  cm
```

```
/gate/diatom/setMaterial G4_WATER
/gate/diatom/vis/setVisible 1
/gate/diatom/vis/setColor blue

#Nucleus
/gate/diatom/daughters/name nucleus
/gate/diatom/daughters/insert sphere
/gate/nucleus/geometry/setRmin   0 um
/gate/nucleus/geometry/setRmax   0.5 um
/gate/nucleus/geometry/setPhiStart 0 deg
/gate/nucleus/geometry/setDeltaPhi 360 deg
/gate/nucleus/geometry/setThetaStart 0 deg
/gate/nucleus/geometry/setDeltaTheta 360 deg
/gate/nucleus/placement/setTranslation 0.0 0.0 0.0  cm
/gate/nucleus/setMaterial                G4_WATER
/gate/nucleus/vis/setVisible     1
/gate/nucleus/vis/setColor               cyan

#PHYSICS
#=======
/gate/physics/addPhysicsList emstandard_opt4

#CUTS
#====
#/gate/physics/setEMin 0.1 keV
#/gate/physics/setEMax 10 GeV
#/gate/physics/setDEDXBinning 350
#/gate/physics/setLambdaBinning 350

/gate/physics/Gamma/SetCutInRegion      world 1 m
/gate/physics/Electron/SetCutInRegion   world 1 m
/gate/physics/Positron/SetCutInRegion   world 1 m

/gate/physics/Gamma/SetCutInRegion      waterbox 5 cm
/gate/physics/Electron/SetCutInRegion   waterbox 5 cm
/gate/physics/Positron/SetCutInRegion   waterbox 5 cm

/gate/physics/Gamma/SetCutInRegion      sedim 0.1 um
/gate/physics/Electron/SetCutInRegion   sedim 0.1 um
/gate/physics/Positron/SetCutInRegion   sedim 0.1 um

/gate/physics/Gamma/SetCutInRegion      frustule 0.01 um
/gate/physics/Electron/SetCutInRegion   frustule 0.01 um
/gate/physics/Positron/SetCutInRegion   frustule 0.01 um

/gate/physics/Gamma/SetCutInRegion      diatom 0.01 um
```

```
/gate/physics/Electron/SetCutInRegion   diatom 0.01 um
/gate/physics/Positron/SetCutInRegion   diatom 0.01 um

/gate/physics/Gamma/SetCutInRegion     nucleus 0.001 um
/gate/physics/Electron/SetCutInRegion   nucleus 0.001 um
/gate/physics/Positron/SetCutInRegion   nucleus 0.001 um

/gate/physics/displayCuts

#ACTORS - OUTPUT
#===============
#Dose Actor - 1D
/gate/actor/addActor                   DoseActor diatom-d1
/gate/actor/diatom-d1/save  output/diat_frust_ext_9Ra.txt
/gate/actor/diatom-d1/attachTo              diatom
/gate/actor/diatom-d1/stepHitType           random
/gate/actor/diatom-d1/setPosition           0 0 0 cm
/gate/actor/diatom-d1/setResolution         1 1 1
/gate/actor/diatom-d1/enableEdep            true

#StatisticsActor
/gate/actor/addActor SimulationStatisticActor stat
/gate/actor/stat/save output/stat_226Ra.txt

#INITIALIZATION
#==============
/gate/run/initialize

#SOURCE
#======
/gate/source/addSource sed_emission gps
/gate/source/sed_emission/gps/particle alpha
/gate/source/sed_emission/gps/energytype UserSpectrum
/gate/source/sed_emission/gps/setSpectrumFile data/238Uchain/226Ra.txt
/gate/source/sed_emission/gps/type Volume
/gate/source/sed_emission/gps/shape Sphere
/gate/source/sed_emission/gps/radius 57.1 um
/gate/source/sed_emission/gps/angtype iso
/gate/source/sed_emission/gps/centre 0 0.0 0 cm
/gate/source/sed_emission/gps/Forbid diatom_phys
/gate/source/sed_emission/gps/Forbid nucleus_phys
/gate/source/sed_emission/gps/Forbid frustule_phys
/gate/source/sed_emission/dump 3

#SEED
#====
```

```
/gate/random/setEngineName MersenneTwister
/gate/random/setEngineSeed auto

#MEASUREMENT SETTINGS
#====================
/gate/application/setTotalNumberOfPrimaries 1e8
/gate/application/start

%\end{lstlisting}
```

D.1.3 Dose Actor - Internal Exposure

```
##Diatom_(microorganism_with_frustule)_in_benthic_mixture

#GEOMETRY
#========
#Materials
/gate/geometry/setMaterialDatabase data/GateMaterials_9.db

#World
/gate/world/setMaterial Vacuum
/gate/world/geometry/setXLength 1 m
/gate/world/geometry/setYLength 1 m
/gate/world/geometry/setZLength 1 m

#Water_box
/gate/world/daughters/name waterbox
/gate/world/daughters/insert box
/gate/waterbox/geometry/setXLength 5 cm
/gate/waterbox/geometry/setYLength 5 cm
/gate/waterbox/geometry/setZLength 5 cm
/gate/waterbox/placement/setTranslation 0.0 0.0 0.0 cm
/gate/waterbox/setMaterial G4_WATER
/gate/waterbox/vis/setVisible 1
/gate/waterbox/vis/setColor blue
/gate/waterbox/vis/setLineStyle dashed

#Environment
/gate/waterbox/daughters/name sedim
/gate/waterbox/daughters/insert sphere
/gate/sedim/geometry/setRmin 0 um
/gate/sedim/geometry/setRmax 57.1 um
/gate/sedim/geometry/setPhiStart 0 deg
/gate/sedim/geometry/setDeltaPhi 360 deg
/gate/sedim/geometry/setThetaStart 0 deg
/gate/sedim/geometry/setDeltaTheta 360 deg
/gate/sedim/placement/setTranslation 0.0 0.0 0.0  cm
```

```
/gate/sedim/setMaterial Sediments
/gate/sedim/vis/setVisible 1
/gate/sedim/vis/setColor grey

#Frustule
/gate/sedim/daughters/name frustule
/gate/sedim/daughters/insert sphere
/gate/frustule/geometry/setRmin 0 um
/gate/frustule/geometry/setRmax 12 um
/gate/frustule/geometry/setPhiStart 0 deg
/gate/frustule/geometry/setDeltaPhi 360 deg
/gate/frustule/geometry/setThetaStart 0 deg
/gate/frustule/geometry/setDeltaTheta 360 deg
/gate/frustule/placement/setTranslation 0.0 0.0 0.0  cm
/gate/frustule/setMaterial Silicate
/gate/frustule/vis/setVisible 1
/gate/frustule/vis/setColor magenta

#Microorganism
/gate/frustule/daughters/name diatom
/gate/frustule/daughters/insert sphere
/gate/diatom/geometry/setRmin 0 um
/gate/diatom/geometry/setRmax 10 um
/gate/diatom/geometry/setPhiStart 0 deg
/gate/diatom/geometry/setDeltaPhi 360 deg
/gate/diatom/geometry/setThetaStart 0 deg
/gate/diatom/geometry/setDeltaTheta 360 deg
/gate/diatom/placement/setTranslation 0.0 0.0 0.0  cm
/gate/diatom/setMaterial G4_WATER
/gate/diatom/vis/setVisible 1
/gate/diatom/vis/setColor blue

#PHYSICS
#=======
/gate/physics/addPhysicsList emstandard_opt4

#CUTS
#=========
/gate/physics/Gamma/SetCutInRegion      world 1 m
/gate/physics/Electron/SetCutInRegion   world 1 m
/gate/physics/Positron/SetCutInRegion   world 1 m

/gate/physics/Gamma/SetCutInRegion      waterbox 5 cm
/gate/physics/Electron/SetCutInRegion   waterbox 5 cm
/gate/physics/Positron/SetCutInRegion   waterbox 5 cm
```

```
/gate/physics/Gamma/SetCutInRegion      sedim 0.1 um
/gate/physics/Electron/SetCutInRegion   sedim 0.1 um
/gate/physics/Positron/SetCutInRegion   sedim 0.1 um

/gate/physics/Gamma/SetCutInRegion      frustule 0.01 um
/gate/physics/Electron/SetCutInRegion   frustule 0.01 um
/gate/physics/Positron/SetCutInRegion   frustule 0.01 um

/gate/physics/Gamma/SetCutInRegion      diatom 0.01 um
/gate/physics/Electron/SetCutInRegion   diatom 0.01 um
/gate/physics/Positron/SetCutInRegion   diatom 0.01 um

/gate/physics/displayCuts

#ACTORS - OUTPUT
#===============
# Dose Actor - 1D
/gate/actor/addActor                    DoseActor diatom-d1
/gate/actor/diatom-d1/save                    output/dose-diatom-d1.txt
/gate/actor/diatom-d1/attachTo                diatom
/gate/actor/diatom-d1/stepHitType             random
/gate/actor/diatom-d1/setPosition             0 0 0 cm
/gate/actor/diatom-d1/setResolution           1 1 1
/gate/actor/diatom-d1/enableEdep              true

#StatisticsActor
/gate/actor/addActor SimulationStatisticActor stat
/gate/actor/stat/save output/stat_226Ra.txt

#INITIALIZATION
#==============
/gate/run/initialize

#SOURCE
#======
/gate/source/addSource sed_emission gps
/gate/source/sed_emission/gps/particle alpha
/gate/source/sed_emission/gps/energytype UserSpectrum
/gate/source/sed_emission/gps/setSpectrumFile data/238Uchain/226Ra.txt
/gate/source/sed_emission/gps/type Volume
/gate/source/sed_emission/gps/shape Sphere
/gate/source/sed_emission/gps/radius 10 um
/gate/source/sed_emission/gps/angtype iso
/gate/source/sed_emission/gps/centre 0 0.0 0 cm

#SEED
```

```
#====
/gate/random/setEngineName MersenneTwister
/gate/random/setEngineSeed auto

#MEASUREMENT SETTINGS
#====================
/gate/application/setTotalNumberOfPrimaries 1E8
/gate/application/start
```

D.2 PhaseSpace

D.2.1 PhaseSpace at microorganism

```
#Diatom_(microorganism_with_frustule)_in_benthic_mixture

#GEOMETRY
#========
#Materials
/gate/geometry/setMaterialDatabase data/GateMaterials_9.db

#World
/gate/world/setMaterial Vacuum
/gate/world/geometry/setXLength 1 m
/gate/world/geometry/setYLength 1 m
/gate/world/geometry/setZLength 1 m

#Water_box
/gate/world/daughters/name waterbox
/gate/world/daughters/insert box
/gate/waterbox/geometry/setXLength 5 cm
/gate/waterbox/geometry/setYLength 5 cm
/gate/waterbox/geometry/setZLength 5 cm
/gate/waterbox/placement/setTranslation 0.0 0.0 0.0 cm
/gate/waterbox/setMaterial G4_WATER
/gate/waterbox/vis/setVisible 1
/gate/waterbox/vis/setColor blue
/gate/waterbox/vis/setLineStyle dashed

#Environment
/gate/waterbox/daughters/name sedim
/gate/waterbox/daughters/insert sphere
/gate/sedim/geometry/setRmin 0 um
/gate/sedim/geometry/setRmax 57.1 um
/gate/sedim/geometry/setPhiStart 0 deg
/gate/sedim/geometry/setDeltaPhi 360 deg
```

```
/gate/sedim/geometry/setThetaStart 0 deg
/gate/sedim/geometry/setDeltaTheta 360 deg
/gate/sedim/placement/setTranslation 0.0 0.0 0.0  cm
/gate/sedim/setMaterial Sediments
/gate/sedim/vis/setVisible 1
/gate/sedim/vis/setColor grey

#Frustule
/gate/sedim/daughters/name frustule
/gate/sedim/daughters/insert sphere
/gate/frustule/geometry/setRmin 0 um
/gate/frustule/geometry/setRmax 12 um
/gate/frustule/geometry/setPhiStart 0 deg
/gate/frustule/geometry/setDeltaPhi 360 deg
/gate/frustule/geometry/setThetaStart 0 deg
/gate/frustule/geometry/setDeltaTheta 360 deg
/gate/frustule/placement/setTranslation 0.0 0.0 0.0  cm
/gate/frustule/setMaterial Silicate
/gate/frustule/vis/setVisible 1
/gate/frustule/vis/setColor magenta

#Microorganism
/gate/frustule/daughters/name diatom
/gate/frustule/daughters/insert sphere
/gate/diatom/geometry/setRmin 0 um
/gate/diatom/geometry/setRmax 10 um
/gate/diatom/geometry/setPhiStart 0 deg
/gate/diatom/geometry/setDeltaPhi 360 deg
/gate/diatom/geometry/setThetaStart 0 deg
/gate/diatom/geometry/setDeltaTheta 360 deg
/gate/diatom/placement/setTranslation 0.0 0.0 0.0  cm
/gate/diatom/setMaterial G4_WATER
/gate/diatom/vis/setVisible 1
/gate/diatom/vis/setColor blue

#Nucleus
/gate/diatom/daughters/name nucleus
/gate/diatom/daughters/insert sphere
/gate/nucleus/geometry/setRmin   0 um
/gate/nucleus/geometry/setRmax   0.5 um
/gate/nucleus/geometry/setPhiStart 0 deg
/gate/nucleus/geometry/setDeltaPhi 360 deg
/gate/nucleus/geometry/setThetaStart 0 deg
/gate/nucleus/geometry/setDeltaTheta 360 deg
/gate/nucleus/placement/setTranslation 0.0 0.0 0.0  cm
/gate/nucleus/setMaterial                G4_WATER
```

```
/gate/nucleus/vis/setVisible     1
/gate/nucleus/vis/setColor               cyan

#PHYSICS
#=======
/gate/physics/addPhysicsList emstandard_opt4

#CUTS
#====
/gate/physics/Gamma/SetCutInRegion      world 1 m
/gate/physics/Electron/SetCutInRegion   world 1 m
/gate/physics/Positron/SetCutInRegion   world 1 m

/gate/physics/Gamma/SetCutInRegion      waterbox 5 cm
/gate/physics/Electron/SetCutInRegion   waterbox 5 cm
/gate/physics/Positron/SetCutInRegion   waterbox 5 cm

/gate/physics/Gamma/SetCutInRegion      sedim 0.1 um
/gate/physics/Electron/SetCutInRegion   sedim 0.1 um
/gate/physics/Positron/SetCutInRegion   sedim 0.1 um

/gate/physics/Gamma/SetCutInRegion      frustule 0.01 um
/gate/physics/Electron/SetCutInRegion   frustule 0.01 um
/gate/physics/Positron/SetCutInRegion   frustule 0.01 um

/gate/physics/Gamma/SetCutInRegion      diatom 0.01 um
/gate/physics/Electron/SetCutInRegion   diatom 0.01 um
/gate/physics/Positron/SetCutInRegion   diatom 0.01 um

/gate/physics/Gamma/SetCutInRegion     nucleus 0.001 um
/gate/physics/Electron/SetCutInRegion   nucleus 0.001 um
/gate/physics/Positron/SetCutInRegion   nucleus 0.001 um

/gate/physics/displayCuts

#ACTORS - OUTPUT
#===============
#PhaseSpace Actor
/gate/actor/addActor PhaseSpaceActor phase_space
/gate/actor/phase_space/attachTo diatom
/gate/actor/phase_space/save output/frustPhSp9_Ra.root

#StatisticsActor
/gate/actor/addActor SimulationStatisticActor stat
/gate/actor/stat/save output/statistics_Ra.txt
```

```
#INITIALIZATION
#==============
/gate/run/initialize

#SOURCE
#======
/gate/source/addSource sed_emission gps
/gate/source/sed_emission/gps/particle alpha
/gate/source/sed_emission/gps/energytype UserSpectrum
/gate/source/sed_emission/gps/setSpectrumFile data/238Uchain/226Ra.txt
/gate/source/sed_emission/gps/type Volume
/gate/source/sed_emission/gps/shape Sphere
/gate/source/sed_emission/gps/radius 57.1 um
/gate/source/sed_emission/gps/angtype iso
/gate/source/sed_emission/gps/centre 0 0.0 0 cm
/gate/source/sed_emission/gps/Forbid diatom_phys
/gate/source/sed_emission/gps/Forbid frustule_phys
/gate/source/sed_emission/gps/Forbid nucleus_phys
/gate/source/sed_emission/dump 3

#SEED
#====
/gate/random/setEngineName MersenneTwister
/gate/random/setEngineSeed auto

#MEASUREMENT SETTINGS
#====================
/gate/application/setTotalNumberOfPrimaries 1E8
/gate/application/start
```

D.2.2 PhaseSpace at nucleus

```
#Diatom(microorganism_with_frustule)_in_benthic_mixture

#GEOMETRY
#========
#Materials
/gate/geometry/setMaterialDatabase data/GateMaterials_9.db

#World
/gate/world/setMaterial Vacuum
/gate/world/geometry/setXLength 1 m
/gate/world/geometry/setYLength 1 m
/gate/world/geometry/setZLength 1 m

#Water_box
```

```
/gate/world/daughters/name waterbox
/gate/world/daughters/insert box
/gate/waterbox/geometry/setXLength 5 cm
/gate/waterbox/geometry/setYLength 5 cm
/gate/waterbox/geometry/setZLength 5 cm
/gate/waterbox/placement/setTranslation 0.0 0.0 0.0 cm
/gate/waterbox/setMaterial G4_WATER
/gate/waterbox/vis/setVisible 1
/gate/waterbox/vis/setColor blue
/gate/waterbox/vis/setLineStyle dashed

#Environment
/gate/waterbox/daughters/name sedim
/gate/waterbox/daughters/insert sphere
/gate/sedim/geometry/setRmin 0 um
/gate/sedim/geometry/setRmax 57.1 um
/gate/sedim/geometry/setPhiStart 0 deg
/gate/sedim/geometry/setDeltaPhi 360 deg
/gate/sedim/geometry/setThetaStart 0 deg
/gate/sedim/geometry/setDeltaTheta 360 deg
/gate/sedim/placement/setTranslation 0.0 0.0 0.0  cm
/gate/sedim/setMaterial Sediments
/gate/sedim/vis/setVisible 1
/gate/sedim/vis/setColor grey

#Frustule
/gate/sedim/daughters/name frustule
/gate/sedim/daughters/insert    sphere
/gate/frustule/geometry/setRmin 0 um
/gate/frustule/geometry/setRmax 12 um
/gate/frustule/geometry/setPhiStart 0 deg
/gate/frustule/geometry/setDeltaPhi 360 deg
/gate/frustule/geometry/setThetaStart 0 deg
/gate/frustule/geometry/setDeltaTheta 360 deg
/gate/frustule/placement/setTranslation 0.0 0.0 0.0  cm
/gate/frustule/setMaterial              Silicate
/gate/frustule/vis/setVisible   1
/gate/frustule/vis/setColor             magenta

#Microorganism
/gate/frustule/daughters/name diatom
/gate/frustule/daughters/insert sphere
/gate/diatom/geometry/setRmin 0 um
/gate/diatom/geometry/setRmax 10 um
/gate/diatom/geometry/setPhiStart 0 deg
/gate/diatom/geometry/setDeltaPhi 360 deg
```

```
/gate/diatom/geometry/setThetaStart 0 deg
/gate/diatom/geometry/setDeltaTheta 360 deg
/gate/diatom/placement/setTranslation 0.0 0.0 0.0  cm
/gate/diatom/setMaterial G4_WATER
/gate/diatom/vis/setVisible 1
/gate/diatom/vis/setColor blue

#Nucleus
/gate/diatom/daughters/name nucleus
/gate/diatom/daughters/insert sphere
/gate/nucleus/geometry/setRmin   0 um
/gate/nucleus/geometry/setRmax   0.5 um
/gate/nucleus/geometry/setPhiStart 0 deg
/gate/nucleus/geometry/setDeltaPhi 360 deg
/gate/nucleus/geometry/setThetaStart 0 deg
/gate/nucleus/geometry/setDeltaTheta 360 deg
/gate/nucleus/placement/setTranslation 0.0 0.0 0.0  cm
/gate/nucleus/setMaterial                G4_WATER
/gate/nucleus/vis/setVisible     1
/gate/nucleus/vis/setColor               cyan

#PHYSICS
#=======
/gate/physics/addPhysicsList emstandard_opt4

#CUTS
#====
/gate/physics/Gamma/SetCutInRegion      world 1 m
/gate/physics/Electron/SetCutInRegion   world 1 m
/gate/physics/Positron/SetCutInRegion   world 1 m

/gate/physics/Gamma/SetCutInRegion      waterbox 5 cm
/gate/physics/Electron/SetCutInRegion   waterbox 5 cm
/gate/physics/Positron/SetCutInRegion   waterbox 5 cm


/gate/physics/Gamma/SetCutInRegion      sedim 0.1 um
/gate/physics/Electron/SetCutInRegion   sedim 0.1 um
/gate/physics/Positron/SetCutInRegion   sedim 0.1 um

/gate/physics/Gamma/SetCutInRegion     frustule 0.01 um
/gate/physics/Electron/SetCutInRegion   frustule 0.01 um
/gate/physics/Positron/SetCutInRegion   frustule 0.01 um

/gate/physics/Gamma/SetCutInRegion      diatom 0.01 um
/gate/physics/Electron/SetCutInRegion   diatom 0.01 um
```

```
/gate/physics/Positron/SetCutInRegion   diatom 0.01 um

/gate/physics/Gamma/SetCutInRegion     nucleus 0.001 um
/gate/physics/Electron/SetCutInRegion   nucleus 0.001 um
/gate/physics/Positron/SetCutInRegion   nucleus 0.001 um

/gate/physics/displayCuts

#ACTORS - OUTPUT
#===============
#PhaseSpace Actor
/gate/actor/addActor PhaseSpaceActor phase_space
/gate/actor/phase_space/attachTo nucleus
/gate/actor/phase_space/save output/frustnucleusPhSp9_Ra.root

#StatisticsActor
/gate/actor/addActor SimulationStatisticActor stat
/gate/actor/stat/save output/statistics_Ra.txt

#INITIALIZATION
#==============
/gate/run/initialize

#SOURCE
#======
/gate/source/addSource diatomPhSp phaseSpace
/gate/source/diatomPhSp/addPhaseSpaceFile data/frustPhSp9_Ra.root
/gate/source/diatomPhSp/setPhaseSpaceInWorldFrame

#SEED
#====
/gate/random/setEngineName MersenneTwister
/gate/random/setEngineSeed auto

#MEASUREMENT SETTINGS
#====================
#Total_number_of_primaries_in_the_PhaseSpace_file
/gate/application/setTotalNumberOfPrimaries 2685222
/gate/application/start
```

Appendix E

GATE deposited energy distributions to diatoms for ^{222}Rn in the benthic mixture for different Physics Lists

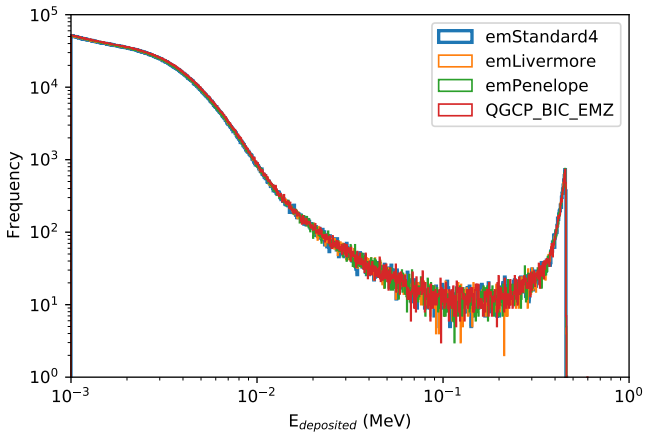

(a) Total deposited energy distribution

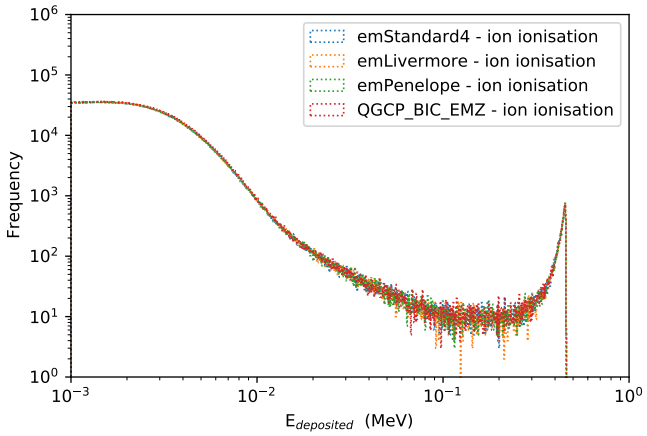

(b) Ion ionisation

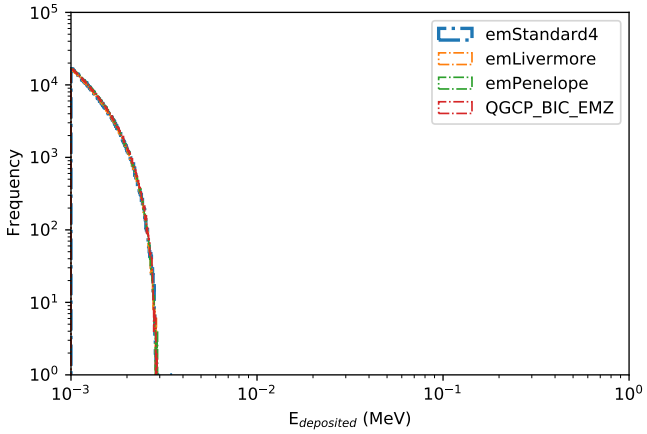

(c) e- ionisation

Figure E.1 Deposited energy distributions to diatoms for ^{222}Rn in the benthic mixture for different Physics Lists

Appendix F

Geant4-DNA HDF5 implementation

F.1 G4UserH5PhaseSpaceReader.cc

```
/*
Copyright (C) 2015 Jaafar EL Bakkali
<><><><><><><><><><><><><><><><><><><><>

Permission is hereby granted, free of charge, to any person obtaining a copy
of this software and associated documentation files (the "Software"), to deal
in the Software without restriction, including without limitation the rights
to use, copy, modify, merge, publish, distribute, sublicense, and/or sell
copies of the Software, and to permit persons to whom the Software is furnished
to do so, subject to the following conditions:

The above copyright notice and this permission notice shall be included in all
copies or substantial portions of the Software.

THE SOFTWARE IS PROVIDED "AS IS", WITHOUT WARRANTY OF ANY KIND, EXPRESS OR
IMPLIED, INCLUDING BUT NOT LIMITED TO THE WARRANTIES OF MERCHANTABILITY,
FITNESS FOR A PARTICULAR PURPOSE AND NONINFRINGEMENT. IN NO EVENT SHALL THE
AUTHORS OR COPYRIGHT HOLDERS BE LIABLE FOR ANY CLAIM, DAMAGES OR OTHER
LIABILITY, WHETHER IN AN ACTION OF CONTRACT, TORT OR OTHERWISE, ARISING FROM,
OUT OF OR IN CONNECTION WITH THE SOFTWARE OR THE USE OR OTHER DEALINGS IN
THE SOFTWARE.
<><><><><><><><><><><><><><><><><><><><><><>
 For documentation
 see http://G4PhspH5.sourceforge.net
  - 13/02/2015: public version 1.0
<><><><><><><><><><><><><><><><><><><><><><>
*/


#include "G4UserH5PhaseSpaceReader.hh"
#include "G4RunManager.hh"
#include "G4ParticleTable.hh"
#include "G4ParticleDefinition.hh"
```

```
#include "G4SystemOfUnits.hh"
#include "Randomize.hh"
#include "Randomize.hh"
#include "Randomize.hh"
#include "Randomize.hh"
#include "G4PrimaryParticle.hh"
#include "G4PrimaryVertex.hh"
#include "H5Cpp.h"
#ifndef H5_NO_NAMESPACE
#ifndef H5_NO_STD
    using std::cout;
    using std::endl;
#endif  // H5_NO_STD
#endif

#include "H5Cpp.h"

#ifndef H5_NO_NAMESPACE
    using namespace H5;
#endif

using namespace H5;

 static int    incr=-1,
               PHASE_SPACE_TIME_REUSED=1,
               ID_OF_NEXT_EVENT=0;
        int    INDEX_OF_CURRENT_DATA=0,
               event_data_length=0;

 G4UserH5PhaseSpaceReader::PhspData  *  dump_PhspData ;
 G4UserH5PhaseSpaceReader::EventData *  dump_EventData ;
 bool a=true;

G4UserH5PhaseSpaceReader::G4UserH5PhaseSpaceReader()
: G4VPrimaryGenerator()

{

}

 void G4UserH5PhaseSpaceReader::INITIALIZE()
{
    READ_BEAM_DATA();
    this-> NUMBER_OF_SIMULATED_HISTORIES=myBeamData[0].NUMBER_OF_HISORIES;
    READ_EVENT_DATA();
    READ_PHASE_SPACE_FILE();
```

```
}
G4UserH5PhaseSpaceReader::~G4UserH5PhaseSpaceReader()
{

}

/*implementation of GENERATE_PRIMARY_VERTEX method*/
void G4UserH5PhaseSpaceReader::GeneratePrimaryVertex(G4Event*anEvent)
{
    if (a==true) incr++ ;
    G4cout<<"a = "<<a<<G4endl;

    Event_ID = dump_EventData[incr]. EVENT_ID;
    G4cout<<"Event_ID =
     "<<Event_ID<< " incr = "<<incr<<G4endl;

    Number_of_Entries = dump_EventData[incr].NUMBER_OF_ENTRIES;
    G4cout<<"Number_of_Entries =
     "<<Number_of_Entries<<G4endl;

    G4cout<<"NUMBER_OF_SIMULATED_HISTORIES =
     "<<NUMBER_OF_SIMULATED_HISTORIES<<G4endl;

    if (anEvent->GetEventID()< this-> NUMBER_OF_SIMULATED_HISTORIES)

    {
        a=true;
                {
                    GENERATE_NEW_PARTICLE(incr,anEvent);
                }
    }
}

/*implementation of GENERATE_NEW_PARTICLE method*/
void G4UserH5PhaseSpaceReader::GENERATE_NEW_PARTICLE(int incr,G4Event*&
↪   anEvent){
    this->energy           *=MeV;
    this->pos_x            *=mm;
    this->pos_y            *=mm;
    this->pos_z            *=mm;
    this->dir_x            *=mm;
    this->dir_y            *=mm;
    this->dir_z            *=mm;
for ( INDEX_OF_CURRENT_DATA=0+incr;
    INDEX_OF_CURRENT_DATA<Number_of_Entries+incr;
    INDEX_OF_CURRENT_DATA++){
```

```
     G4cout<<"eventID = "<<Event_ID<<G4endl;

     this->particle_pdge   = dump_PhspData[INDEX_OF_CURRENT_DATA]. PART_PDGE;
     this->particle_weight = dump_PhspData[INDEX_OF_CURRENT_DATA]. PART_WEIGHT;
     this->energy          = dump_PhspData[INDEX_OF_CURRENT_DATA].
↪  PART_KINETIC;
     this->pos_x           = dump_PhspData[INDEX_OF_CURRENT_DATA]. PART_POS_X;
     this->pos_y           = dump_PhspData[INDEX_OF_CURRENT_DATA]. PART_POS_Y;
     this->pos_z           = dump_PhspData[INDEX_OF_CURRENT_DATA]. PART_POS_Z;
     this->dir_x           = dump_PhspData[INDEX_OF_CURRENT_DATA]. PART_DIR_X;
     this->dir_y           = dump_PhspData[INDEX_OF_CURRENT_DATA]. PART_DIR_Y;
     this->dir_z           = dump_PhspData[INDEX_OF_CURRENT_DATA]. PART_DIR_Z;
    G4ParticleDefinition*  partDef=GET_PARTICLE_DEFINITION(
↪  this->particle_pdge);
    G4float   partMass = partDef->GetPDGMass();
    G4float partEnergy = this->energy+ partMass;
    G4float  partMom = std::sqrt( partEnergy*partEnergy - partMass*partMass );
    G4float  particle_time =0;
    G4cout<<"Ekine = "<<energy<<G4endl;

    G4ThreeVector particle_position(this->pos_x,this->pos_y,this->pos_z);

    G4PrimaryParticle * particle = new
↪  G4PrimaryParticle(GET_PARTICLE_DEFINITION( this->particle_pdge),
        partMom*this->dir_x,partMom*this->dir_y,partMom*this->dir_z);
    particle->SetWeight(this->particle_weight);
     // Create the new primary vertex and set the primary to it
    G4PrimaryVertex * vertex = new G4PrimaryVertex(particle_position,
↪  particle_time);
    vertex->SetPrimary(particle);
    // And finally set the vertex to this event
    anEvent->AddPrimaryVertex(vertex);
}// end for
ID_OF_NEXT_EVENT=ID_OF_NEXT_EVENT+Number_of_Entries+1;
}

/*implementation of GET_PARTICLE_DEFINITION method*/
 G4ParticleDefinition*  G4UserH5PhaseSpaceReader::GET_PARTICLE_DEFINITION(int&
↪  PDGE)
{
G4String particleName               =     "";

G4ParticleTable* particleTable      =
   G4ParticleTable::GetParticleTable();

G4ParticleDefinition* particle_def  =
```

```
   particleTable->FindParticle(particleName="gamma");

    switch (PDGE)
     {
     case -11:
                    particle_def     =
                        particleTable->FindParticle(particleName="e+");
         break;
     case 11:
                    particle_def     =
                        particleTable->FindParticle(particleName="e-");
         break;
     case 22:
                    particle_def     =
                        particleTable->FindParticle(particleName="gamma");
         break;
    case 1000020040:
                    particle_def     =
                       particleTable->FindParticle(particleName="alpha");
        break;
    case 2212:
                    particle_def     =
                       particleTable->FindParticle(particleName="proton");
        break;
     }

return particle_def;
}

 /*implementation of READ_EVENT_DATA method*/
 void G4UserH5PhaseSpaceReader::READ_EVENT_DATA()
 {
      // DECLARATION OF STRINGS OF MEMBERS OF DATASET NAMED "EventData"
      const std::string DatasetName_event("EventData");
      const std::string MEMBER_ENTERIES("_ENTERIES");
      const std::string MEMBER_EVENTID("_EVENTID");
      H5File file(  this->FileName, H5F_ACC_RDONLY );
      DataSet dataset_event = file.openDataSet( DatasetName_event );
      H5::CompType mtype_event( sizeof(EventData) );
      // GET NUMBER OF DATA IN DATASET NAMED EventData
     G4int data_event_size=dataset_event.getSpace().getSimpleExtentNpoints();
     dump_EventData = new EventData[data_event_size];
     event_data_length=data_event_size;
     mtype_event.insertMember(MEMBER_ENTERIES,
         HOFFSET(EventData, NUMBER_OF_ENTRIES),      H5::PredType::NATIVE_INT);
     mtype_event.insertMember(MEMBER_EVENTID,
```

```
          HOFFSET(EventData, EVENT_ID),
↪  H5::PredType::NATIVE_INT);
     dataset_event.read( dump_EventData, mtype_event );

 }

 /*implementation of :SET_PHASE_SPACE_FILE_NAME method*/
void G4UserH5PhaseSpaceReader::SET_PHASE_SPACE_FILE_NAME( G4String _FileName)
 {
 this->FileName=_FileName;
 }

void G4UserH5PhaseSpaceReader::READ_BEAM_DATA()
 {
     const std::string FileName(this->FileName);
     const std::string DatasetName_histories("BeamData");
     const std::string MEMBER_HISTORIES("_NUMBER_OF_HISTORIES");
     H5File file( FileName, H5F_ACC_RDONLY );
     DataSet dataset_histories = file.openDataSet( DatasetName_histories );
     H5::CompType mtype_histories( sizeof(BeamData) );
     mtype_histories.insertMember(MEMBER_HISTORIES,
        HOFFSET(BeamData, NUMBER_OF_HISORIES),      H5::PredType::NATIVE_INT);
     dataset_histories.read( myBeamData, mtype_histories );

 }

 /*implementation of READ_PHASE_SPACE_FILE method*/
void G4UserH5PhaseSpaceReader::READ_PHASE_SPACE_FILE()
{
     const std::string DatasetName("PhspData");
     const std::string MEMBER_PART_PDGE("_PART_PDGE");
     const std::string MEMBER_PART_WEIGHT("_PART_WEIGHT");
     const std::string MEMBER_PART_POS_X("_PART_POS_X");
     const std::string MEMBER_PART_POS_Y("_PART_POS_Y");
     const std::string MEMBER_PART_POS_Z("_PART_POS_Z");
     const std::string MEMBER_PART_DIR_X("_PART_DIR_X");
     const std::string MEMBER_PART_DIR_Y("_PART_DIR_Y");
     const std::string MEMBER_PART_DIR_Z("_PART_DIR_Z");
     const std::string MEMBER_PART_KINETIC("_PART_KINETIC");

     // LOAD PHASE SPACE HDF5-BASED FORMAT FILE
     H5File file( this->FileName, H5F_ACC_RDONLY );
     DataSet dataset = file.openDataSet( DatasetName );
     H5::CompType mtype2( sizeof(PhspData) );

    // GET NUMBER OF DATA IN DATASET NAMED PhspData
```

```
    G4int data_size  = dataset.getSpace().getSimpleExtentNpoints();
    dump_PhspData    = new PhspData[data_size];
    mtype2.insertMember(MEMBER_PART_WEIGHT,
        HOFFSET(PhspData, PART_WEIGHT),   H5::PredType::NATIVE_FLOAT);
    mtype2.insertMember(MEMBER_PART_POS_X,
        HOFFSET(PhspData, PART_POS_X),    H5::PredType::NATIVE_FLOAT);
    mtype2.insertMember(MEMBER_PART_PDGE,
        HOFFSET(PhspData, PART_PDGE),     H5::PredType::NATIVE_INT);
    mtype2.insertMember(MEMBER_PART_POS_Y,
        HOFFSET(PhspData, PART_POS_Y),    H5::PredType::NATIVE_FLOAT);
    mtype2.insertMember(MEMBER_PART_POS_Z,
        HOFFSET(PhspData, PART_POS_Z),    H5::PredType::NATIVE_FLOAT);
    mtype2.insertMember(MEMBER_PART_DIR_X,
        HOFFSET(PhspData, PART_DIR_X),    H5::PredType::NATIVE_FLOAT);
    mtype2.insertMember(MEMBER_PART_DIR_Y,
        HOFFSET(PhspData, PART_DIR_Y),    H5::PredType::NATIVE_FLOAT);
    mtype2.insertMember(MEMBER_PART_DIR_Z,
        HOFFSET(PhspData, PART_DIR_Z),    H5::PredType::NATIVE_FLOAT);
    mtype2.insertMember(MEMBER_PART_KINETIC,
        HOFFSET(PhspData, PART_KINETIC),  H5::PredType::NATIVE_FLOAT);
    dataset.read( dump_PhspData, mtype2 );

}

void G4UserH5PhaseSpaceReader::SET_PARAMETERS(G4String _PHASE_SPACE_NAME) {

   SET_PHASE_SPACE_FILE_NAME(_PHASE_SPACE_NAME);
}
```

F.2 G4UserH5PhaseSpaceReader.hh

```
/*
Copyright (C) 2015 Jaafar EL Bakkali
<><><><><><><><><><><><><><><><><><><><><><><><><><><><><><><><><><><><><><><><><><>

Permission is hereby granted, free of charge, to any person obtaining a copy
of this software and associated documentation files (the "Software"), to deal
in the Software without restriction, including without limitation the rights
to use, copy, modify, merge, publish, distribute, sublicense, and/or sell
copies of the Software, and to permit persons to whom the Software is furnished
to do so, subject to the following conditions:

The above copyright notice and this permission notice shall be included in all
copies or substantial portions of the Software.
```

```
THE SOFTWARE IS PROVIDED "AS IS", WITHOUT WARRANTY OF ANY KIND, EXPRESS OR
IMPLIED, INCLUDING BUT NOT LIMITED TO THE WARRANTIES OF MERCHANTABILITY,
FITNESS FOR A PARTICULAR PURPOSE AND NONINFRINGEMENT. IN NO EVENT SHALL THE
AUTHORS OR COPYRIGHT HOLDERS BE LIABLE FOR ANY CLAIM, DAMAGES OR OTHER
LIABILITY, WHETHER IN AN ACTION OF CONTRACT, TORT OR OTHERWISE, ARISING FROM,
OUT OF OR IN CONNECTION WITH THE SOFTWARE OR THE USE OR OTHER DEALINGS IN
THE SOFTWARE.
<><><><><><><><><><><><><><><><><><><><><><><><><><><><><><><><><><><><><><><><>
 For documentation
 see http://G4PhspH5.sourceforge.net
  - 13/02/2015: public version 1.0
<><><><><><><><><><><><><><><><><><><><><><><><><><><><><><><><><><><><><><><><>
*/


#ifndef G4UserH5PhaseSpaceReader_h
#define G4UserH5PhaseSpaceReader_h 1

#include "G4VPrimaryGenerator.hh"
#include "G4ParticleGun.hh"
#include "globals.hh"

class G4Event;
class G4ParticleDefinition;

class G4UserH5PhaseSpaceReader : public G4VPrimaryGenerator
{
  public:
    G4UserH5PhaseSpaceReader();
     ~G4UserH5PhaseSpaceReader();

    // method from the base class
   //virtual void GeneratePrimaries(G4Event*);

public:

  void GeneratePrimaryVertex(G4Event* anEvent);   // Mandatory

  void INITIALIZE();

  void SET_PARAMETERS(G4String);


    typedef struct
    {
       int    PART_PDGE;
```

```
        float  PART_WEIGHT
                 ,PART_POS_X
                 ,PART_POS_Y
                 ,PART_POS_Z
                 ,PART_DIR_X
                 ,PART_DIR_Y
                 ,PART_DIR_Z
                 ,PART_KINETIC;


     }PhspData;

      typedef struct
      {
          G4int    EVENT_ID,
                   NUMBER_OF_ENTRIES;


      }EventData;

   typedef struct
   {
      G4int    NUMBER_OF_HISORIES;

   }BeamData;
  //
   PhspData tmp;
   EventData tmp_event;
   //
   BeamData  myBeamData[1];
   private:
      G4int particle_pdge,Event_ID, particle_weight,Number_of_Entries,
       NUMBER_OF_SIMULATED_HISTORIES;
      G4float particle_time,pos_x, pos_y, pos_z, dir_x,dir_y,dir_z,energy;
      G4String FileName;

   void GENERATE_NEW_PARTICLE(int incr,G4Event*& anEvent);
   void READ_EVENT_DATA();
   void SET_PHASE_SPACE_FILE_NAME( G4String  _FileName);
   void READ_BEAM_DATA();
   void READ_PHASE_SPACE_FILE();
   G4ParticleDefinition* GET_PARTICLE_DEFINITION(int& PDGE);


};
```

```
//xxxxxxxxxxxxxxxxxxxxxxxxxxxxxxxxxxxxxxxxxxxxxxxxxxxxxxxxxxxxxxxxxxxxxxxxxxxxxxxxxxxxxxxxxxxxxxx

#endif
```

F.3 PrimaryGeneratorAction.cc

```
//
// ********************************************************************
// * License and Disclaimer                                           *
// *                                                                  *
// * The  Geant4 software  is  copyright of the Copyright Holders  of *
// * the Geant4 Collaboration.  It is provided  under  the terms  and *
// * conditions of the Geant4 Software License,  included in the file *
// * LICENSE and available at  http://cern.ch/geant4/license .  These *
// * include a list of copyright holders.                             *
// *                                                                  *
// * Neither the authors of this software system, nor their employing *
// * institutes,nor the agencies providing financial support for this *
// * work  make  any representation or  warranty, express or implied, *
// * regarding  this  software system or assume any liability for its *
// * use.  Please see the license in the file  LICENSE  and URL above *
// * for the full disclaimer and the limitation of liability.         *
// *                                                                  *
// * This  code  implementation is the result of  the  scientific and *
// * technical work of the GEANT4 collaboration.                      *
// * By using,  copying,  modifying or  distributing the software (or *
// * any work based  on the software)  you  agree  to acknowledge its *
// * use  in  resulting  scientific  publications,  and indicate your *
// * acceptance of all terms of the Geant4 Software license.          *
// ********************************************************************
//
// This example is provided by the Geant4-DNA collaboration
// Any report or published results obtained using the Geant4-DNA software
// shall cite the following Geant4-DNA collaboration publication:
// Med. Phys. 37 (2010) 4692-4708
// The Geant4-DNA web site is available at http://geant4-dna.org
//
//
/// \file PrimaryGeneratorAction.cc
/// \brief Implementation of the PrimaryGeneratorAction class

#include "PrimaryGeneratorAction.hh"
#include "G4RunManager.hh"
#include "G4ParticleTable.hh"
#include "G4ParticleDefinition.hh"
#include "G4SystemOfUnits.hh"
```

```
#include "Randomize.hh"
#include "G4UserH5PhaseSpaceReader.hh"
#include "H5Cpp.h"

//....oooOOOOOooo........oooOOOOOooo........oooOOOOOooo........oooOOOOOooo......

PrimaryGeneratorAction::PrimaryGeneratorAction()
: G4VUserPrimaryGeneratorAction()

{

   theG4UserH5PhaseSpaceReader = new G4UserH5PhaseSpaceReader();
theG4UserH5PhaseSpaceReader-> SET_PARAMETERS("PhSp.h5");


   theG4UserH5PhaseSpaceReader->INITIALIZE();

}

//xxxxxxxxxxxxxxxxxxxxxxxxxxxxxxxxxxxxxxxxxxxxxxxxxxxxxxxxxxxxxxxxxxxxxxxxxxxxxxx
//------------------------------------------------------------------------------
//xxxxxxxxxxxxxxxxxxxxxxxxxxxxxxxxxxxxxxxxxxxxxxxxxxxxxxxxxxxxxxxxxxxxxxxxxxxxxxx


PrimaryGeneratorAction::~PrimaryGeneratorAction()
{
    if (theG4UserH5PhaseSpaceReader) delete theG4UserH5PhaseSpaceReader;

}

//xxxxxxxxxxxxxxxxxxxxxxxxxxxxxxxxxxxxxxxxxxxxxxxxxxxxxxxxxxxxxxxxxxxxxxxxxxxxxxx
//------------------------------------------------------------------------------
//xxxxxxxxxxxxxxxxxxxxxxxxxxxxxxxxxxxxxxxxxxxxxxxxxxxxxxxxxxxxxxxxxxxxxxxxxxxxxxx
void PrimaryGeneratorAction::GeneratePrimaries(G4Event* anEvent)
{

    theG4UserH5PhaseSpaceReader->GeneratePrimaryVertex(anEvent);

}


//xxxxxxxxxxxxxxxxxxxxxxxxxxxxxxxxxxxxxxxxxxxxxxxxxxxxxxxxxxxxxxxxxxxxxxxxxxxxxxx
//------------------------------------------------------------------------------
//xxxxxxxxxxxxxxxxxxxxxxxxxxxxxxxxxxxxxxxxxxxxxxxxxxxxxxxxxxxxxxxxxxxxxxxxxxxxxxx
```

Appendix G

GATE dose rates in the Auvergne mineral springs

Spring	^{222}Rn (Bq/L)	External DR (µGy/h)	^{226}Ra (Bq/kg)	External DR (µGy/h)	^{210}Po (Bq/L)	External DR (µGy/h)	^{238}U (Bq/kg)	External DR (µGy/h)
Bard 1	5.90	$1.36 \cdot 10^{-2}$	-	-	$<1.00 \cdot 10^{-2}$	-	-	-
Bard 2	$1.00 \cdot 10^{1}$	$2.30 \cdot 10^{-2}$	$2.19 \cdot 10^{3}$	$5.37 \cdot 10^{-1}$	$<1.00 \cdot 10^{-2}$	-	$<2.70 \cdot 10^{2}$	-
Chemin	$1.22 \cdot 10^{2}$	$2.80 \cdot 10^{-1}$	$1.08 \cdot 10^{4}$	2.64	$<1.00 \cdot 10^{-2}$	-	$<3.60 \cdot 10^{2}$	-
Combris	$2.70 \cdot 10^{2}$	$6.22 \cdot 10^{-1}$	$3.86 \cdot 10^{3}$	$9.46 \cdot 10^{-1}$	$1.54 \cdot 10^{-1}$	$3.35 \cdot 10^{-4}$	$<2.50 \cdot 10^{2}$	-
Croizat	$2.89 \cdot 10^{1}$	$6.65 \cdot 10^{-2}$	-	-	$8.80 \cdot 10^{-2}$	$1.91 \cdot 10^{-4}$	-	-
Daguillon	$5.45 \cdot 10^{2}$	1.25	$2.30 \cdot 10^{4}$	5.63	$<1.00 \cdot 10^{-2}$	-	$<3.10 \cdot 10^{2}$	-
Dourioux	$3.85 \cdot 10^{3}$	8.86	$6.00 \cdot 10^{2}$	$1.47 \cdot 10^{-1}$	$3.00 \cdot 10^{-2}$	$6.53 \cdot 10^{-5}$	$2.60 \cdot 10^{2}$	$4.99 \cdot 10^{-2}$
Estreys	$1.44 \cdot 10^{3}$	3.31	$1.94 \cdot 10^{3}$	$4.75 \cdot 10^{-1}$	$2.70 \cdot 10^{-2}$	$5.87 \cdot 10^{-5}$	$<8.60 \cdot 10^{1}$	-
Font Salee	$3.95 \cdot 10^{1}$	$9.09 \cdot 10^{-2}$	$6.70 \cdot 10^{2}$	$1.64 \cdot 10^{-1}$	$<1.00 \cdot 10^{-2}$	-	$<1.10 \cdot 10^{2}$	-
Giraudon	$1.66 \cdot 10^{1}$	$3.82 \cdot 10^{-2}$	$4.17 \cdot 10^{3}$	1.02	$<1.00 \cdot 10^{-2}$	-	$<2.40 \cdot 10^{2}$	-
Graviers	$2.92 \cdot 10^{1}$	$6.72 \cdot 10^{-2}$	$2.67 \cdot 10^{4}$	6.55	$<1.00 \cdot 10^{-2}$	-	$<4.40 \cdot 10^{2}$	-
Mariol*	$1.39 \cdot 10^{2}$	$3.19 \cdot 10^{-1}$	$1.96 \cdot 10^{4}$	4.80	$2.50 \cdot 10^{-2}$	$5.44 \cdot 10^{-5}$	$<1.10 \cdot 10^{2}$	-
Montagne 1*	$3.45 \cdot 10^{3}$	7.94	$8.61 \cdot 10^{3}$	2.11	$1.95 \cdot 10^{-1}$	$4.24 \cdot 10^{-4}$	$<2.70 \cdot 10^{2}$	-
Montagne 2*	$1.13 \cdot 10^{3}$	2.59	$5.97 \cdot 10^{3}$	1.46	$6.60 \cdot 10^{-2}$	$1.44 \cdot 10^{-4}$	$<1.70 \cdot 10^{2}$	-
Ours	$2.21 \cdot 10^{1}$	$5.08 \cdot 10^{-2}$	$5.21 \cdot 10^{4}$	12.77	$<1.00 \cdot 10^{-2}$	-	$<4.80 \cdot 10^{2}$	-
Par	2.20	$5.06 \cdot 10^{-3}$	-	-	$<1.00 \cdot 10^{-2}$	-	-	-
Poix	$6.00 \cdot 10^{-1}$	$1.40 \cdot 10^{-3}$	$3.00 \cdot 10^{1}$	$7.35 \cdot 10^{-3}$	$1.18 \cdot 10^{-1}$	$2.57 \cdot 10^{-4}$	<7.60	-
Rocs Bleus	$2.01 \cdot 10^{1}$	$4.62 \cdot 10^{-2}$	$5.60 \cdot 10^{2}$	$1.37 \cdot 10^{-1}$	$<1.00 \cdot 10^{-2}$	-	$<8.60 \cdot 10^{1}$	-
Sail	$1.01 \cdot 10^{3}$	2.31	$8.40 \cdot 10^{2}$	$2.06 \cdot 10^{-1}$	$<1.00 \cdot 10^{-2}$	-	$<7.70 \cdot 10^{1}$	-
Saladis	$1.02 \cdot 10^{1}$	$2.35 \cdot 10^{-2}$	$1.19 \cdot 10^{3}$	$2.92 \cdot 10^{-1}$	$<1.00 \cdot 10^{-2}$	-	$<7.50 \cdot 10^{1}$	-
Salins	$1.19 \cdot 10^{1}$	$2.74 \cdot 10^{-2}$	$7.50 \cdot 10^{2}$	$1.84 \cdot 10^{-1}$	$3.92 \cdot 10^{-1}$	$8.53 \cdot 10^{-4}$	$3.00 \cdot 10^{2}$	$5.76 \cdot 10^{-2}$
Salut	6.90	$1.59 \cdot 10^{-2}$	$9.51 \cdot 10^{3}$	2.33	$<1.00 \cdot 10^{-2}$	-	$<3.80 \cdot 10^{2}$	-
Saulcee	$9.17 \cdot 10^{1}$	$2.11 \cdot 10^{-1}$	$1.93 \cdot 10^{4}$	4.72	$1.68 \cdot 10^{-1}$	$3.65 \cdot 10^{-4}$	$<3.60 \cdot 10^{2}$	-
Tennis	$1.77 \cdot 10^{2}$	$4.06 \cdot 10^{-1}$	$2.16 \cdot 10^{4}$	5.30	$<1.00 \cdot 10^{-2}$	-	$<2.80 \cdot 10^{2}$	-
Tete de Lion	$1.33 \cdot 10^{2}$	$3.05 \cdot 10^{-1}$	$1.59 \cdot 10^{4}$	3.89	$<1.00 \cdot 10^{-2}$	-	$<3.30 \cdot 10^{2}$	-
Trois sauts	$5.78 \cdot 10^{2}$	1.33	$2.08 \cdot 10^{3}$	$5.10 \cdot 10^{-1}$	$<1.00 \cdot 10^{-2}$	-	$<2.00 \cdot 10^{2}$	-

Spring	^{222}Rn (Bq/L)	Internal DR (μGy/h)	^{226}Ra (Bq/kg)	Internal DR (μGy/h)	^{210}Po (Bq/L)	Internal DR (μGy/h)	^{238}U (Bq/kg)	Internal DR (μGy/h)
Bard 1	5.90	$2.27 \cdot 10^{-3}$	-	-	$<1.00 \cdot 10^{-2}$	-	-	-
Bard 2	$1.00 \cdot 10^{1}$	$3.84 \cdot 10^{-3}$	$2.19 \cdot 10^{3}$	$9.49 \cdot 10^{-1}$	$<1.00 \cdot 10^{-2}$	-	$<2.70 \cdot 10^{2}$	-
Chemin	$1.22 \cdot 10^{2}$	$4.68 \cdot 10^{-2}$	$1.08 \cdot 10^{4}$	4.67	$<1.00 \cdot 10^{-2}$	-	$<3.60 \cdot 10^{2}$	-
Combris	$2.70 \cdot 10^{2}$	$1.04 \cdot 10^{-1}$	$3.86 \cdot 10^{3}$	1.67	$1.54 \cdot 10^{-1}$	$6.08 \cdot 10^{-5}$	$<2.50 \cdot 10^{2}$	-
Croizat	$2.89 \cdot 10^{1}$	$1.11 \cdot 10^{-2}$	-	-	$8.80 \cdot 10^{-2}$	$3.48 \cdot 10^{-5}$	-	-
Daguillon	$5.45 \cdot 10^{2}$	$2.09 \cdot 10^{-1}$	$2.30 \cdot 10^{4}$	9.96	$<1.00 \cdot 10^{-2}$	-	$<3.10 \cdot 10^{2}$	-
Dourioux	$3.85 \cdot 10^{3}$	1.48	$6.00 \cdot 10^{2}$	$2.60 \cdot 10^{-1}$	$3.00 \cdot 10^{-2}$	$1.19 \cdot 10^{-5}$	$2.60 \cdot 10^{2}$	$1.27 \cdot 10^{-1}$
Estreys	$1.44 \cdot 10^{3}$	$5.52 \cdot 10^{-1}$	$1.94 \cdot 10^{3}$	$8.41 \cdot 10^{-1}$	$2.70 \cdot 10^{-2}$	$1.07 \cdot 10^{-5}$	$<8.60 \cdot 10^{1}$	-
Font Salee	$3.95 \cdot 10^{1}$	$1.52 \cdot 10^{-2}$	$6.70 \cdot 10^{2}$	$2.90 \cdot 10^{-1}$	$<1.00 \cdot 10^{-2}$	-	$<1.10 \cdot 10^{2}$	-
Giraudon	$1.66 \cdot 10^{1}$	$6.37 \cdot 10^{-3}$	$4.17 \cdot 10^{3}$	1.81	$<1.00 \cdot 10^{-2}$	-	$<2.40 \cdot 10^{2}$	-
Graviers	$2.92 \cdot 10^{1}$	$1.12 \cdot 10^{-2}$	$2.67 \cdot 10^{4}$	$1.16 \cdot 10^{1}$	$<1.00 \cdot 10^{-2}$	-	$<4.40 \cdot 10^{2}$	-
Mariol*	$1.39 \cdot 10^{2}$	$5.33 \cdot 10^{-2}$	$1.96 \cdot 10^{4}$	8.48	$2.50 \cdot 10^{-2}$	$9.88 \cdot 10^{-6}$	$<1.10 \cdot 10^{2}$	-
Montagne 1*	$3.45 \cdot 10^{3}$	1.33	$8.61 \cdot 10^{3}$	3.73	$1.95 \cdot 10^{-1}$	$7.70 \cdot 10^{-5}$	$<2.70 \cdot 10^{2}$	-
Montagne 2*	$1.13 \cdot 10^{3}$	$4.33 \cdot 10^{-1}$	$5.97 \cdot 10^{3}$	2.59	$6.60 \cdot 10^{-2}$	$2.61 \cdot 10^{-5}$	$<1.70 \cdot 10^{2}$	-
Ours	$2.21 \cdot 10^{1}$	$8.49 \cdot 10^{-3}$	$5.21 \cdot 10^{4}$	22.59	$<1.00 \cdot 10^{-2}$	-	$<4.80 \cdot 10^{2}$	-
Par	2.20	$8.45 \cdot 10^{-4}$	-	-	$<1.00 \cdot 10^{-2}$	-	-	-
Poix	$6.00 \cdot 10^{-1}$	$2.30 \cdot 10^{-4}$	$3.00 \cdot 10^{1}$	$1.30 \cdot 10^{-2}$	$1.18 \cdot 10^{-1}$	$4.66 \cdot 10^{-5}$	<7.60	-
Rocs Bleus	$2.01 \cdot 10^{1}$	$7.72 \cdot 10^{-3}$	$5.60 \cdot 10^{2}$	$2.43 \cdot 10^{-1}$	$<1.00 \cdot 10^{-2}$	-	$<8.60 \cdot 10^{1}$	-
Sail	$1.01 \cdot 10^{3}$	$3.86 \cdot 10^{-1}$	$8.40 \cdot 10^{2}$	$3.64 \cdot 10^{-1}$	$<1.00 \cdot 10^{-2}$	-	$<7.70 \cdot 10^{1}$	-
Saladis	$1.02 \cdot 10^{1}$	$3.92 \cdot 10^{-3}$	$1.19 \cdot 10^{3}$	$5.16 \cdot 10^{-1}$	$<1.00 \cdot 10^{-2}$	-	$<7.50 \cdot 10^{1}$	-
Salins	$1.19 \cdot 10^{1}$	$4.57 \cdot 10^{-3}$	$7.50 \cdot 10^{2}$	$3.25 \cdot 10^{-1}$	$3.92 \cdot 10^{-1}$	$1.55 \cdot 10^{-4}$	$3.00 \cdot 10^{2}$	$1.46 \cdot 10^{-1}$
Salut	6.90	$2.65 \cdot 10^{-3}$	$9.51 \cdot 10^{3}$	4.12	$<1.00 \cdot 10^{-2}$	-	$<3.80 \cdot 10^{2}$	-
Saulcee	$9.17 \cdot 10^{1}$	$3.52 \cdot 10^{-2}$	$1.93 \cdot 10^{4}$	8.35	$1.68 \cdot 10^{-1}$	$6.64 \cdot 10^{-5}$	$<3.60 \cdot 10^{2}$	-
Tennis	$1.77 \cdot 10^{2}$	$6.79 \cdot 10^{-2}$	$2.16 \cdot 10^{4}$	9.38	$<1.00 \cdot 10^{-2}$	-	$<2.80 \cdot 10^{2}$	-
Tete de Lion	$1.33 \cdot 10^{2}$	$5.10 \cdot 10^{-2}$	$1.59 \cdot 10^{4}$	6.88	$<1.00 \cdot 10^{-2}$	-	$<3.30 \cdot 10^{2}$	-
Trois sauts	$5.78 \cdot 10^{2}$	$2.22 \cdot 10^{-1}$	$2.08 \cdot 10^{3}$	$9.01 \cdot 10^{-1}$	$<1.00 \cdot 10^{-2}$	-	$<2.00 \cdot 10^{2}$	-